UNIVERSITAT DE BARCELONA

Development of tunable bioinks to fabricate 3D-printed *in vitro* models:

a special focus on skeletal muscle models with potential applications in metabolic alteration studies

Andrea García Lizarribar

Tesi doctoral

Development of tunable bioinks to fabricate 3D-printed *in vitro* models:

a special focus on skeletal muscle models with potential applications in metabolic alteration studies

Andrea García Lizarribar

Josep Samitier Martí

UNIVERSITAT DE BARCELONA

Development of tunable bioinks to fabricate 3D-printed *in vitro* models:

a special focus on skeletal muscle models with potential applications in metabolic alteration studies

Programa de Doctorat de Biomedicina

Universitat de Barcelona

Tesis realitzada en el Institut de Bioenginyeria de Catalunya (IBEC)

PhD candidate

Andrea García Lizarribar

Director

Josep Samitier Martí

IBEC Institute for Bioengineering of Catalonia

EXCELENCIA SEVERO OCHOA

UNIVERSITAT DE BARCELONA

Table of contents

Table of figures

1. Introduction

2. Methods

3. Results

Chapter 1

Introduction

1. Tissue engineering

The term *tissue engineering* was coined in 1993 by Langer and Vacanti as “an interdisciplinary field which applies the principles of engineering and life sciences toward the development of biological substitutes that restore, maintain, or improve tissue function” [1]. For decades, engineering customized tissues to replace or restore damaged ones have raised many interests to overcome the well-known drawbacks of organ and tissue transplantation. In regenerative medicine, cellular or acellular templates can be designed for their consequent implantation to repair segments of organs. However, there is still a long way to achieve complete organs due to their structural complexity and cellular diversity.

Nowadays, tissue engineering has taken another course to develop *in vitro* engineered functional models of healthy or pathological tissues. *In vitro,* organs-on-a-chip or engineering living models aim to provide a reliable and approachable template to study the biochemical events and overcome the disadvantages of animal testing and traditional monolayer cultures.

1.1. Current experimental models

1.1.1. *In vivo* models

Ethical issues concerning the study of human embryology, as well as the scarce resources of human biological samples, led to the use of animals for *in vivo* experiments. During history, a selected group of animals were established as models, each one presenting its advantages. The most common non-mammalian models are Zebrafish (*Danio rerio*), *Caenorhabditits elegans* nematode and *Drosophila melanogaster* fruitfly [2]. These models are transparent and small organisms, which makes them very suitable for *in vivo* study of developmental processes and molecular mechanisms during adulthood. The genetic modification of these models is relatively easy, as their genome is fully sequenced and small, particularly in the case of *C. elegans* (97 Mb) and *D. melanogaster* (180 Mb). The embryos of these models grow rapidly, furthermore, *C. elegans* females are self-fertilizing hermaphrodite, and *D. melanogaster* and zebrafish have high fecundity. Thus, they provide a high number of mutant individuals compared to other animal models and greater experimental replicates.

Despite the obvious advantages of these transparent and small animal models, their capability to recapitulate the biochemical processes cannot be compared with the similarities between mammals. Rodents share 85% of genes with humans, in contrast to 70% of zebrafish. Furthermore, there are several structural and developmental discrepancies between zebrafish and mammals [2].

Mice are the most used mammal models to study human biology and diseases. The fecundity rate is lower than non-mammalian models and they need more complex facilities and care. However, the genome of the mouse is highly identical to humans, and they provide a close overview of the molecular and biological processes in humans. The use of mice for experimental studies goes back

to thousands of years [3], during which the response of mice to certain stimuli has been studied in deep. Such knowledge is nowadays used to perform behavioral tests, where changes in mouse organism (i.e. disease, mutations, or drug administration) result in an altered response of mice to physical challenges as running, learning, and escaping from danger. Furthermore, animals can be dissected after tests to analyze the affected tissues using countless molecular techniques. Regarding the extended use of mouse models, there are currently thousands of species-specific reagents available. Together with their body size, lifespan and short gestation mice are ideal subjects for preclinical studies in comparison to bigger mammals. Mice are relatively easy to genetically modify, thus there are plenty of disease models that aim to resemble the pathologic phenotype. However, many of them fail to fully recapitulate the disease in humans. Using skeletal muscle tissue as an example, genetically modified *dmx* models of Duchenne Muscular Dystrophy (DMD) were designed by disrupting the codification of dystrophin, however, mice present mild pathology and lack of fat infiltration [4].

Animal use in research requires complex facilities approved by competent authorities. Qualified workers for animal testing, breeding, and care together with certified devices and materials notably increase the experimental costs. Furthermore, ethical issues concerning the generation of disease models must be considered, as they are meant to endure the pathology since birth and, then enough individuals must be sacrificed to obtain statistically relevant results.

1.1.1. *In vitro* models

As an alternative to animal experiments, *in vitro* models are used as non-costly, feasible, and less complex platforms. Experiments can be performed using tissue explants, cell monolayer cultures, and 3D cultures. Tissue explants or *ex vivo* experiments have been used to study cell-cell and cell-pathogen interactions, as well as to preserve the structural complexity and cell diversity. For instance, human lymphoid tissue explants were used to study the pathogenesis of VIH, and muscle explants highlighted the complex structure and function of neuromuscular junctions [5]. However, the lifespan of excised muscles is very short, as the extraction of the organ from its natural environment triggers the activation of molecular signals related to death and apoptosis that can lead to the misrepresentation of the results [6]. Muscle explants provide information about adult and mature differentiated tissues. Nevertheless, the acquisition of those samples requires biopsies in humans or animal sacrifices, thus they still present ethical and procedural issues found in *in vivo* experiments.

Monolayer cell cultures are expansions of single-cell suspensions obtained from enzymatically digested organs. Today, cells have been isolated from almost all tissue types and cultured on flat surfaces. This type of culture is the most simple, fast, and rentable approach to develop *in vitro* experimental models. Usually, cells are isolated from the original tissue and termed primary cells. The multipotency and proliferative nature of the original tissue will determine the division and differentiation capability of primary cells. Most adherent primary cells of adults

(i.e. neurons and muscle cells) are terminally differentiated and present a limited number of divisions. Primary cells have been genetically modified to skip senescence and maintain an unlimited proliferative capability. In this way, immortalized cell lines of many cell types and species have been established. They provide less phenotypic and genotypic variations than primary cells, however, they can present altered functionality as a result of immortalization [7]. Primary cells have also been modified to generate induced pluripotent stem cells (iPSCs). In this case, cells are "de-differentiated" to a pluripotent state in which they have unlimited proliferation and the capability to re-differentiate into other tissue types. iPSCs can be derived from patients that present a specific pathology, therefore, they can be used for personalized clinical studies and medical diagnosis. iPSC commitment to a particular tissue is a long and complex process. It can be achieved through direct reprogramming by the upregulation of key genes, or through directed differentiation by the sequential modification of medium signals that emulate the organogenesis process [8]. Although direct reprogramming is faster, both approaches are extremely complex, long, and still present some drawbacks related to low production yield and genetic instability, which hamper their use in clinics [9]. Consequently, many *in vitro* studies chose primary and immortalized cells due to their simplicity.

In vitro experiments of monolayer cell cultures provided countless contributions to the biomedical field. However, two-dimensional (2D) cultures do not fully recapitulate the features of native tissue. Several studies in the literature revealed that 2D cultures presented altered morphology and function when compared to native tissue [10-12]. Soares *et al*. showed discrepancies between 2D and 3D cultures of cardiac tissue in morphology, adhesion junctions, presence of myofibrils, and protein expression. In that study, they demonstrated that 3D engineered tissue was closer to *in vivo* models than 2D cultures [12]. Moreover, many authors reviewed the benefits of engineering tissue-mimicking 3D culture systems [13-15]. In physiological conditions, cells establish interactions with others and their surrounding extracellular matrix (ECM). Those interactions are involved in processes that regulate signaling, metabolism, migration, proliferation, differentiation, and apoptosis. Each tissue has a characteristic three-dimensional (3D) architecture and cell distribution, which are essential for the correct functioning of the organ.

Considering those needs, tissue engineering aims to combine several disciplines to develop 3D cultures that resemble the physical, chemical and biological properties of the native tissue. 3D cultures can be achieved by scaffold-free techniques and biomaterial-based approaches. Scaffold-free approaches are based on the self-assembly of cells to form multilayered sheets, strands, and spheroids. Shimizu *et al.* used "cell sheet engineering" to attach multiple layers of cell sheets and obtain 3D cultures of cardiomyocytes [17]. To that end, cells can be cultured on detachable thermoresponsive surfaces [16]. Multilayered cultures are also obtained using magnetic cell sheets. Cells are labeled with magnetic particles and grown in a monolayer. Once formed, cell sheets are detached and manipulated using magnetic fields [17]. Magnetically labeled cells have been also used to develop muscle strands used as drug testing platforms [18]. As an alternative

method, Akkouch *et al*. fabricated hollow alginate strands filled with highly dense cell pellets [19].

Due to their manipulability, spheroids are the most popular approach for scaffold-free 3D cultures. There are several methods to achieve spherical cultures of single or multiple cells, as antiadhesive culture plates or hanging drops [20, 21]. Scaffold-free approaches provide 3D cultures of densely packed single or multiple cell types. However, cells need an initial time until they secrete enough ECM to merge between them as a single unit, and the resultant tissue usually presents poor mechanical properties. Due to their high cell density and fabrication methods, scaffold-free techniques have limited scalability, as fabrication of large structures will be time-consuming and nutrient diffusion to the core would be compromised.

Biomaterial-based approaches provide more versatility to design 3D cultures. Biomaterials are preparations of biocompatible pure or mixed polymers. They act as ECMs supporting the proliferation, migration, and differentiation of tissues in 3D. Dimensions and shape of 3D templates can be customized using electrospinning, freeze-drying, micromolding, or 3D-bioprinting techniques, thus the scalability is only limited by the nutrient diffusion capability of the engineered tissue. The biochemical and physical properties of biomaterials can be tuned, as well as the final composition of the mixture, which brings the opportunity to meet the needs of native tissue. Furthermore, they can be chemically modified to show biochemical cues and engineer a system to control the release of biomolecules. Altogether, biomaterial-based tissue engineering provides a wide window of possibilities to customize 3D cultures as tissue-resembling templates.

1.2. Biomaterial-based tissue engineering models

Researchers are increasingly transferring experiments from 2D to 3D cultures due to its benefits and better resemblance to native tissue. Biomaterial-based tissue models are good candidates for regenerative medicine and to develop *in vitro* models. In regenerative medicine, models can be fabricated as acellular scaffolds that promote the infiltration of host cells to repair damaged sections or as carriers of biomolecules to activate signaling pathways. In contrast, biomaterial-based *in vitro* models must portray *ex vivo* the structure and functions of the original tissue. To that end, optimal cell sources, biomaterials and manufacturing strategies must be selected for each type of tissue model. Some approaches of biomaterial-based engineered tissues and their advantages have been reported in the literature.

1.2.1. Epithelial models

Skin models are one of the most studied systems, probably due to their simpler spatial organization. In 1976, the first models were based on the culture of keratinocytes on decellularized dermis of human or porcine skin [22,23]. Later, collagen hydrogels with embedded fibroblasts were used as artificial dermis to support the growth of keratinocytes [24,25]. However, collagen hydrogels present high degradation rates and weak mechanical properties. Indeed, tensile forces of

encapsulated fibroblasts can deform and contract collagen hydrogel. To improve mechanical strength and reduce degradability of artificial dermis, collagen has been combined with electrospun polymers as silk fibroin, poly(ε-caprolactone) (PCL) and poly (lactic-co-glycolic acid) (PLGA) [26-28].

Another strategy to automate the manufacturing process of skin models is the use of 3D bioprinting approaches. Extrusion bioprinting allowed layer-by-layer deposition of fibroblasts embedded into biopolymer mixtures of alginate, gelatin and fibrinogen as a 3D dermis with subsequent culturing of keratinocytes. Using 3D bioprinting they obtained large-scale skin models that presented defined dermis and epidermis compartments [29].

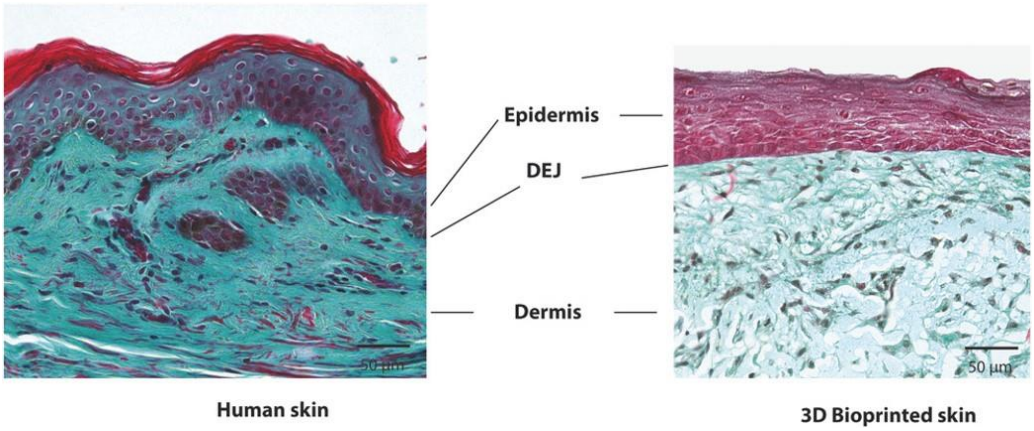

Figure 1.15. Optical microscopy images of normal human skin and bioprinted skin after 26 d of culture. Tissues were stained with Masson's Trichrome [29].

Skin models are nowadays used for regenerative medicine. They substitute damaged skin sections after wounds or burns [30]. Nevertheless, *in vitro* skin models have gained much interest as disease models and drug screening platforms. Several commercial skin models are currently being used by the cosmetic industry to avoid animal testing. Skin disease models are mainly focused on wound healing, infection, inflammation and cancer [31]. They were used to study the damage of UV radiation exposure, the importance of cell-cell and cell-ECM interactions in melanoma and to create innervated immune-competent skin systems [32-34].

1.2.2. Models of the nervous system

The nervous system is composed of the central nervous system (CNS) and peripheral nervous system (PNS). CNS is formed by the brain and the spinal cord, while PNS consists of peripheral nerves that exchange information between body organs and CNS. Due to the high complexity of the brain, *in vitro* models of CNS are focused on specific anatomical structures as the cortex, blood-brain barrier (BBB), optical nerve, and spinal cord. Brain stiffness is extremely soft, ranging

from 0 to 2 kPa, and the main components of natural ECM are glycosaminoglycans as hyaluronic acid (HA). Therefore, choosing the optimum material to meet brain features and obtain stable 3D cultures can be difficult [35]. Although it is not present in the brain, collagen I demonstrated valuable properties for neuronal and glial commitment. Collagen allowed the differentiation of neural stem cells into neurons, astrocytes, and oligodendrocytes [36]. They showed polarity, neurotransmitters, ion channels/receptors, and excitability [37]. Seidlits *et al*. used photocrosslinkable HA (HAMA) to guide the differentiation into neurons or glial cells by modulating the stiffness of 3D culture [38]. As part of natural ECM, HA has excellent properties to support neural growth and differentiation. Regarding the weakness and degradability of collagen and HA, agarose, polyethyleneglycol (PEG), and silk were explored for neural applications [39-41].

In contrast to CNS, PNS has greater regenerative capability. However, it has a limited self-recovery that tissue engineering aims to overcome. Peripheral nerves are myelinated by Schwann cells in stiffer ECMs composed of collagen, fibronectin and laminin. 2D cultures have demonstrated limited neurite outgrowth, lack of myelination, altered action potential and voltage-gated channels [42]. In this line, different strategies have been proposed to develop engineered peripheral nerve models with proper topographical and biochemical stimuli. Malheiro *et al.* fabricated aligned electrospun PEOT/PBT scaffolds to align Schwann cells (SC), promoting the myelinization of motoneurons encapsulated in fibrin matrices [43]. Similarly, aligned scaffolds of poly-L-lactic acid (PLA) and collagen were engineered to improve cell infiltration and uniaxial growth in cut nerves [45,46].

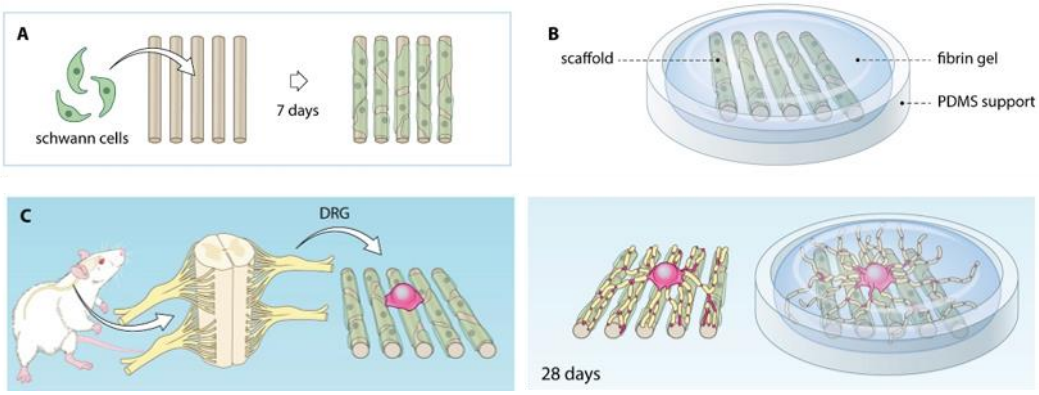

Figure 1.16. Illustration of PN model fabrication process. A) Formation of Bands of Büngner (BoB); B) Overview of the model components; C) DRG/SC co-culture procedure [43].

In vitro engineered 3D nerve models provided more reliable platforms than 2D models for preclinical studies, drug screening and modeling neurodegenerative diseases. Furthermore, nerve tissue engineering provided templates that recapitulate the architecture and biochemical cues of native tissue to enhance neurite growth and reconnection.

1.2.3. Models of the digestive system

Pharmacokinetics describes the interaction of drugs in the body through absorption, distribution, metabolism and excretion (ADME), which mainly occur in the digestive tract, liver and kidney. To obtain feasible, non-costly platforms and reduce the use of animals, several studies fabricated engineered systems of organs related to ADME processes. Villi-like structures have been fabricated to promote the hierarchical organization of the different cell types of the intestine, where stem cells are located in crypts and differentiation grade gradually increases towards the villus [47]. Microvilli have been modeled using micromolds of collagen, Matrigel® and decellularized intestine [48-50], and using 3D bioprinting approaches [51]. Those 3D models better replicated the intestine ADME processes than monolayer cultures and were used to recapitulate the diseased tissue *in vitro*.

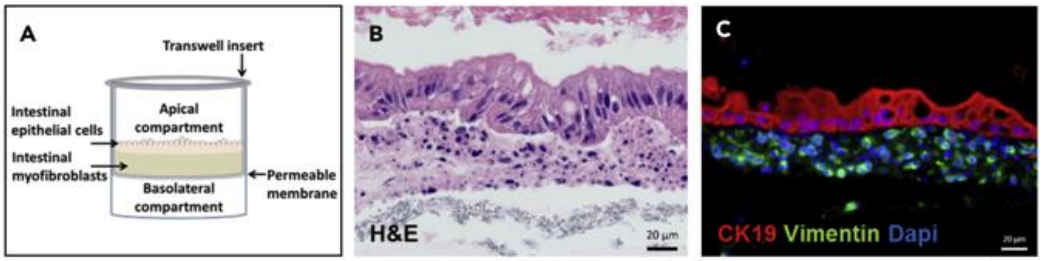

Figure 1.17. Engineered intestine model. A) A bilayered architecture is achieved by bioprinting an interstitial layer containing adult human intestinal myofibroblasts (IMF) followed by adult human intestinal epithelial cells (hIEC). The vimentin-expressing interstitial cells and CK19-expressing epithelial compartments remain separate over 17 days in culture (B, C).

Continuing with organs related to ADME, the liver has the role of metabolizing most of the compounds coming from the blood, thus it is in charge of metabolizing drugs into more hydrophilic excretable compounds. The liver structure is more complex and is composed of many different cell types. Glucose uptake, glycolysis, aminoacid synthesis and bile acid production are performed by perivenous cells, while gluconeogenesis, glucose delivery, oxygen uptake and fatty acid oxidation are driven by periportal cells. Those cells and functions are distributed in the outer or the core zones of lobular structures depending on their oxygen requirements [52]. To emulate lobular structures and their central bile duct, several studies have used spheroids [53-54], as they provide a gradient concentration of oxygen, unlike monolayer cultures. In this line, Haque *et al*. developed hepatocyte microspheres of alginate-chitosan with immune isolation for transplantation [55]. Similar to the liver, kidney organoids have been differentiated to develop *in vitro* nephrons as the functional unit of the kidney [56]. Mimicking human native tissue function *in vitro* through the optimization of the architecture, composition and stimuli of those 3D models will lead to improved ADME platforms and more efficient preclinical studies by connecting different organs with microfluidics.

1.2.4. Tumor models

Tumor interaction with its microenvironment is considered essential for its progression, metastasis evolution and drug resistance. There is increasing evidence that tumor interaction with stromal cells and ECM plays an important role in extravasation, invasion, migration, stemness maintenance, angiogenesis and immunosurveillance evasion [57]. To study tumor behavior *in vitro*, engineered models can be designed to provide interactions with stromal cells, vasculature and matrices in a 3D network that mimics the structure of the native tumor. Several studies denoted that tumor cell behavior in monolayer cultures was fundamentally different from 3D cultures. It was seen that 3D cultures downregulated EGFR/AKT signaling pathway related to proliferation and protein synthesis [10,58], which demonstrated decreased sensitivity to anti-EGFR treatments (cisplatin and cetuximab) [59]. However, it is important to take into consideration the composition and physical properties of biomaterials used to mimic tumor ECM. Pavlou *et al.* demonstrated that collagen hydrogels supplemented with laminin, fibronectin and bone granules resulted in an increased invasion, malignant metabolic reprogramming and different responses to chemotherapeutic agents in osteosarcoma cells. Those models better recapitulated *in vivo* drug responses, which could help to define suitable treatments for osteosarcoma patients [60]. In this line, hard stiffness collagen matrices decelerated the proliferation rate of breast tumor cells and incremented their resistance to placlitaxel, which corresponded more to *in vivo* results. In contrast, soft matrices presented proliferation and sensitivity similar to 2D cultures [62]. In light of those recent studies, choosing a suitable biomaterial for each type of tumor is of great importance to recapitulate their microenvironment and mimic their progression *in vivo*. To that end, biomaterial composition, physical properties and biochemical cues must be considered.

1.2.5. Musculoskeletal models

The musculoskeletal system comprises bones, cartilage, tendons, ligaments and skeletal muscle. It is in charge of body shape, support and locomotion. Mainly, tissue injuries are derived from mechanical loading, repetitive motions and maintained static positions [63]. Muskuloskeletal system functions are possible by the interconnection between tissues, as bone-tendon and tendon-muscle. In this context, there is a transition between tissues with opposite features, ranging from hard vascularized and self-regenerating bone to soft and avascularized cartilage [63].

Collagen I is one of the main components of the ECM in the musculoskeletal system. Although their composition is similar, the architectural arrangement differs among tissues. Cartilage is stiffer in the superficial zone than in the deep zone. The horizontal orientation of collagen fibers on the surface makes the tissue more resistant to bone friction, while the core is composed of vertical fibers. In bone,

collagen I is densely packed in parallel fibers of 30-80 nm linked to hydroxyapatite (HPA) reservoirs. Therefore, they combine the harness of minerals and the flexibility of natural polymers [64]. Tendons are hierarchically packed collagen fibers of 35-500 nm. They form elongated bundles aligned towards the muscle contraction axis, which provides tensile strength and connects muscles to bones [65]. Consequently, collagen I in muscle is similarly aligned, however, it envelopes muscle fascicles forming more amorphous and disorganized meshes [66]. ECM organization and composition provide each tissue with different stiffness according to their function, which can be classified from the stiffest to the softest as follows: bone> tendon > cartilage >muscle [67].

Considering the specificities of tissues in the musculoskeletal system, many *in vitro* models have been developed. Human bone marrow stromal cells and monocytes were committed to osteoblasts and osteoclasts in mineralized scaffolds of silica/collagen and PMMA [68,69]. Numerous studies demonstrated that intermittent mechanical loading of collagen hydrogels promoted the alignment of matrix fibers and induced tenogenesis [70,71].

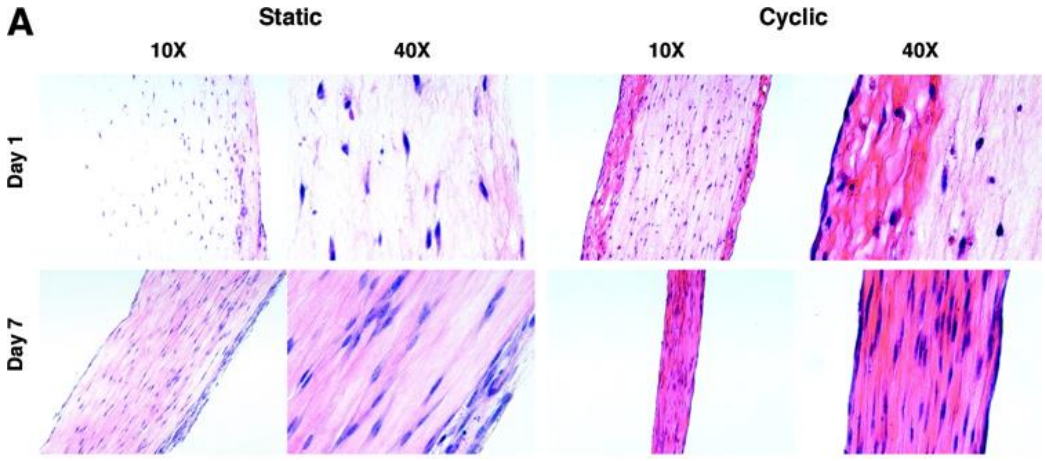

Figure 1. 18. Engineered tendon models. Histology of collagen constructs with mesenchymal stem cells harvested after 1 and 7 days of static and cyclic loading. Longitudinal 5-μm-thick sections are histologically stained with (A) hematoxylin and eosin [70].

Muscle tissue development is driven by multiple physical, mechanical and biological factors. Mechanical loading of tendons together with suitable biochemical was found to induce the alignment of myoblasts and promote myogenesis signaling [72]. Together with tensile strength, muscle contraction activity was correlated to fiber maturation and sarcomerogenesis [73]. To achieve complete skeletal muscle models, mechanical tension and electrical stimulation systems were combined with fibrin-based engineered 3D muscles [74]. They showed aligned differentiated fibers with sarcomeric structures. Fibrin-based *in vitro* muscles were also cocultured with motoneurons to emulate the native stimulation through neuromuscular junctions (NMJ) [75]. Those *in vitro* platforms showed potential applications in drug screening and disease modeling. In contrast to 2D cultures,

3D models provided *in vitro* skeletal muscle tissue with characteristics closely resembling *in vivo* tissue, as elongated fiber morphology, alignment, sarcomerogenesis, contractile activity and genetic expression.

These examples evidence the numerous advantages of 3D engineered tissues over traditional monolayer cultures. Engineered tissues combine bioactive matrices, external physicochemical stimuli and multiple cell types to recapitulate the microenvironments and architecture of native tissues. Furthermore, biomaterials can be combined with additive manufacturing techniques to automatize and scale the fabrication of tissue-engineered models. However, there is still a long way to achieve engineered tissues that comprise all the cellular and extracellular components of the original tissues, support their long-term maintenance, and perform all the functions, while they provide an automated, scalable and feasible fabrication.

Developing a system that mimics the features of a natural tissue requires deep knowledge of the functions, architecture, cell diversity and interaction between them and with other components of the body. One of the most challenging tissues in 3D modeling is the skeletal muscle. As mentioned before, its development is strongly influenced by the 3D architecture, mechanical forces, cell orientation and the stimuli of neighbor tissues as PNS. The existence of those components in the *in vitro* system determines the level of maturation and functionality of muscle tissue. Indeed, few examples of biomaterial-based strategies fulfilled all the requirements to establish tissue-resembling skeletal muscle *in vitro* models, and many of them did not achieve functional contractile models. To enlighten the steps and factors involved in skeletal muscle development and how they are translated to 3D cultures, the following sections will be focused on the intricacies of myogenesis and fabrication of skeletal muscle tissue models.

2. Skeletal muscle tissue

2.1. Skeletal muscle structure

Skeletal muscle is one of the largest organs in the musculoskeletal system, which comprises around 40% of the total body mass [76]. It participates in the regulation of body temperature and is involved in body homeostasis through its interaction with other organs [77]. Myokines secreted by the muscle are necessary for fat and glucose reservoir regulation, vascularization, appetite control, and regulation of the immune system [78]. It is well known that low or disrupted muscle activity is associated with metabolic diseases and has a pivotal role in the prognostic of cancer patients [78-81].

Muscles are in charge of body movements that enable predation, escaping in the face of danger and vital activities as breathing, chewing and heart beating. The locomotion is powered by a contractile basic unit, the sarcomere, which is evolutionarily conserved among bilaterians (i.e. vertebrates, insects) and some non-bilaterian phyla (cnidarians and ctenophores) [82]. Sarcomeres are an alternation of thin actin and thick myosin filaments

that are sequentially repeated and form the characteristic striated ultrastructure. The basic actomyosin machinery is prior to the animal kingdom and has independently evolved in every phylum. The next section is focused on the ultra- and molecular structure of the striated skeletal muscle tissue in vertebrates.

2.1.1. Skeletal muscle macrostructure

Muscles are physiological fractals composed of packed elongated fibers surrounded by connective tissue. In the outer layer, the epimysium envelopes a set of fascicles, which are, at the same time, individually surrounded by perimysium. Inside the muscle fascicles, the endomysium envelops muscle fibers individually.

Muscle connective tissue is mainly composed of collagen fibers, whose composition and orientation are related to the hierarchical classification [66]. The composition and structural patterning of perimysium are similar to tendons, which are mainly formed by collagen I. In contrast, endomysium presents mesh-like conformation of equal parts of collagen I and III. This theory suggests that perimysium blends into the tendon, which helps to transmit muscle contraction to the adjacent locomotor apparatus and ensures the orientation of muscle fascicles.

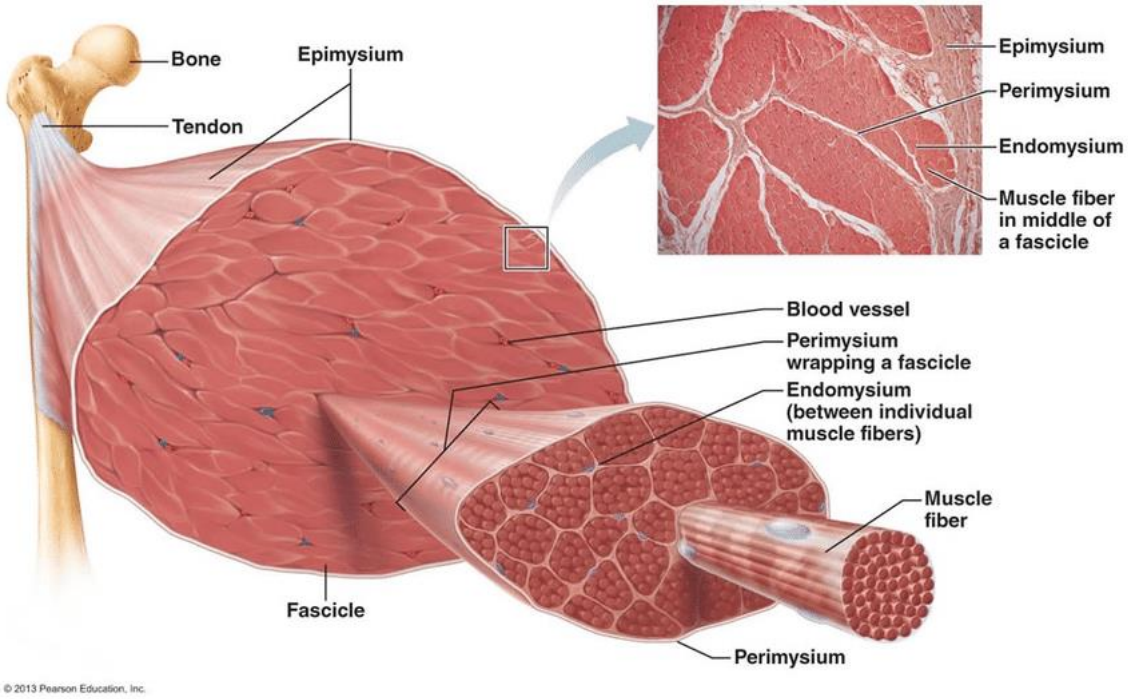

Figure 1.19. Structure of the skeletal muscle tissue. Marieb & Hoehn, Anatomy & Physiology, 7th Edition | Pearson. Retrieved May 29, 2021, from https://www.pearson.com/us/higher-education/program/Marieb-Modified-Mastering-A-P-with-Pearson-e-Text-Standalone-Access-Card-for-Anatomy-Physiology-7th-Edition/PGM2092383.htmlMarieb/Human anatomy and PhysiologyCopyright ©Pearson Education, Inc.

Muscle fibers result from the fusion of multiple myocytes that share the cytoplasm in a multinucleated syncytium. The cytoskeleton of that syncytium is mainly organized in myofibrils, which are bundles of sarcomere reiterations. Muscle fibers are surrounded by the basal lamina or basement membrane that

provides them with mechanical support and envelopes the plasmatic membrane of the fiber, called sarcolemma. The sarcolemma is one of the aftereffects of the evolution of the muscle fibers towards a fast and coordinated contractile machinery in vertebrates. Sarcolemma invaginates into the interior of the muscle fibers to form the T-tubules. Those structures help to the propagation of membrane depolarization to the second tubular system in the fiber, the terminal cisternae of the sarcoplasmic reticulum (SR). The coupling of two SR cisternae with one central T-tubule is called a triad and is located between the Z-disks and the M-line. Nuclei, mitochondria, lysosomes and other organelles are distributed between the sarcolemma and the myofibrils.

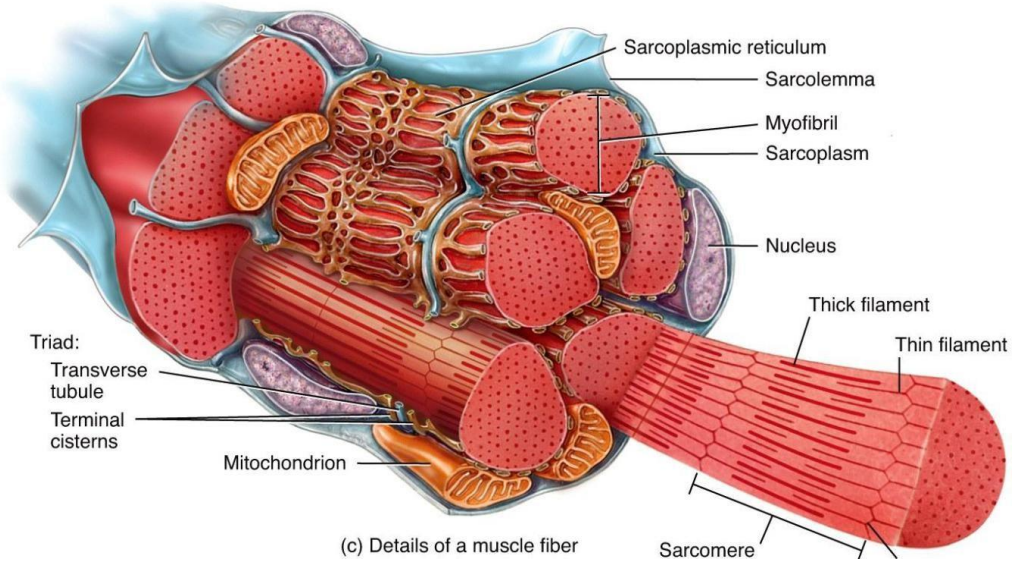

Figure 1.20. Structure of a muscle fiber composed of several myofibrils and surrounded by the cell sarcolemma (membrane) and endomysium (connective tissue). Marieb & Hoehn, Anatomy & Physiology, 7th Edition | Pearson. Retrieved May 29, 2021, from https://www.pearson.com/us/higher-education/program/Marieb-Modified-Mastering-A-P-with-Pearson-e-Text-Standalone-Access-Card-for-Anatomy-Physiology-7th-Edition/PGM2092383.html.

2.1.2. Skeletal muscle molecular structure

Sarcomeres are the basic unit of contractile machinery. Myosin thick filaments are in the center of the sarcomere and intercalated with actin thin filaments. Actin is closer to the Z disk, which delimitates the sarcomere length on each side. In histology, actomyosin arrangement is classified in central A band and two flanking I bands. The A band comprises the myosin filament and the section overlapped with actin. The central section of the A band that only contains myosin is called H zone and can be distinguished as a clear band. In the middle of the H band, the myosin presents a darker line called M line, where the tails of the myosin dimers and functional and structural proteins converge. Structural proteins as titin, link the myosin filaments to the Z disks. Conversely, actin is directly connected to the Z disks configuring the I band. As in the A band, there is a clear

band where actin and myosin are not overlapped. The Z disk appears as a dark line in the middle of the I band, due to the high protein gathering. Z disks are the limits of each sarcomere and mostly contain structural proteins, as α-actinin and ZASP, that preserve the actomyosin arrangement.

The repetitive unit of the thin filaments consists of seven actin monomers, one tropomyosin (Tm) and one troponin (Tn), which is extended to the actin total length. Tm and Tn give structural stability to the actin filament, but their main function is focused on the regulation of myosin coupling to the actin during contraction. Tn is a multimeric complex formed by Troponin C (TnC), the Ca^{2+} binding subunit; Troponin T (TnT), the Tm binding subunit; and Troponin I (TnI), the inhibitory subunit. Under high Ca^{2+} concentration conditions, the molecules bind to the TnC, which changes its spatial conformation and consequently modifies the TnT three-dimensional structure. TnT conformation change displaces the Tm chains and uncovers the myosin binding site of the actin filament, allowing the myosin coupling.

Myosin is formed by protein hexamers of two long coiled-coil tails, each one containing a flexible neck with two light chains and a heavy chain head in the end [83]. The heavy chain heads are the motor of myosin. They contain an ATPase domain and an actin-binding domain. Myosin head recognizes the actin-binding domain and pulls the filament shortening the I band of the sarcomere. After the contraction, an ATP molecule is bound to the ATPase domain and myosin is uncoupled from actin. The ATP is then hydrolyzed allowing the head to bound to the actin again and complete the cycle. This process explains the sliding filament theory proposed by Huxley [84], where the increased overlapping of actin and myosin filaments leads to fiber contraction.

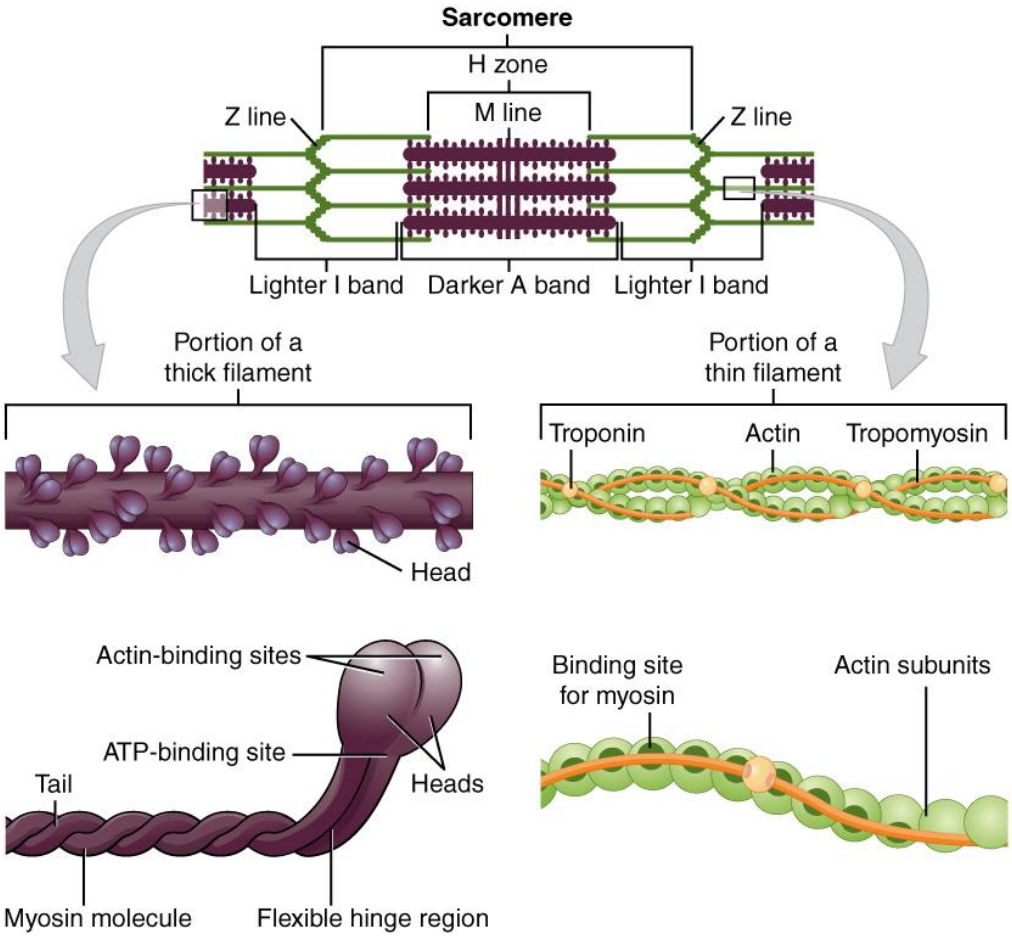

Figure 1.21. Schematic structure of sarcomere and the thick and thin filaments. Skeletal Muscle - Anatomy and Physiology | OpenStax. Retrieved May 29, 2021, from https://openstax.org/books/anatomy-and-physiology/pages/10-2-skeletal-muscle.

2.2.Skeletal muscle functions: muscle contraction

The main function of skeletal muscle tissue is body locomotion. Skeletal muscle contraction force is transmitted through the tendons and coordinated with the additional components of the musculoskeletal system to produce an accurate movement.

Muscle contraction in skeletal muscle tissue is induced by signals transmitted from the central nervous system (CNS). The CNS sends a synaptic signal to the peripheral nervous system (PNS) composed of the spinal cord and peripheral nerves (afferent and efferent). The signal passes from the ventral horn of the spinal cord to the motoneurons or efferent nerves, which directly innervate the muscle fibers [85]. Synapsis between the terminal end of motoneurons end and muscle fibers is known as the neuromuscular junction (NMJ). The Ach molecules released in the synaptic cleft bind to the acetylcholine receptors of the muscle membrane (sarcolemma) and open the influx of Na^+ ions [87]. The increment of cations in the fiber cytosol depolarizes the membrane that propagates as a potential action (PA). If the PA is enough, high quantities of Ca^{2+} are released from the sarcoplasmic reticulum to the cytosol, which activates Ca^{2+}-dependant proteins like TnC allowing muscle contraction [88].

2.3. Muscle fiber classification

In the past, skeletal muscle was classified into two categories depending on its phenotype, type of metabolism and contractile properties [89]. Slow-twitch fibers showed high mitochondria number and high oxidative enzyme activity and myoglobin content, which provide the characteristic red color of the slow fibers. Fast fibers, on the contrary, were distinguished for their lower myoglobin and mitochondria content, white color and more glycolytic metabolism. Fatigability studies also demonstrated that slow muscles were less fatigable and thus, used for sustained exercise or body posture, while fast fibers performed strong and short contractions, but were more fatigable. However, around 1970 some studies, as those using electron microscopy, revealed the heterogeneity of fast fibers [90]. They observed mitochondria-rich and poor fibers with large sarcoplasmic reticulum, which was characteristic of the fast fibers. Furthermore, all the fibers classified as slow showed thick Z disks, while those presenting large SR showed thin Z disks regardless of their high or low mitochondria number.

The same year, enzyme histochemistry revealed different myosin ATPase activity among the fast fibers, which led to the outcoming of two new fast fiber subtypes: 2A and 2B. Together with other physiological analyses, fibers were classified as slow oxidative (type I, fatigue-resistant), fast-twitch oxidative glycolytic (type 2A, less fatigable) and fast-twitch glycolytic (type 2B, fatigable).

Since 1980, the use of monoclonal antibodies against myosin heavy chain (MyHC), gel electrophoresis and transcriptomics made it possible to identify the fast-twitch 2X subtype and confirmed that each myosin ATPase was encoded by different genes [91]. In combination with physiological analysis, they showed that 2A fast fiber behavior was closer to that found in slow fibers and that 2X fast fiber contractility and fatigue were between 2A and 2B fibers. Thus, anti-myosin monoclonal antibodies became the gold standard for the identification of the muscle fiber subtypes. Four main fibers were determined according to their contraction rate: type I < type 2A < type 2X < type 2B, encoded in skeletal muscle by *MYH7*, *MYH2*, *MYH1* and *MYH4* respectively.

2.3.1. Fiber plasticity in adult muscles

Skeletal muscle has extraordinary adaptability to external changes. Myosin composition and fiber metabolism change during muscle development and regeneration. But muscle fibers also respond to environmental changes and adapt their functioning to the new requirements in adulthood.

The changes of the muscle fibers are limited by the fiber type baseline. It is well known that exercise boosts fiber remodeling to a more oxidative state. In rats and mice, voluntary wheel exercise resulted in the transition from 2B glycolytic fibers to 2X and 2A more oxidative fast fibers [92]. In humans, endurance training is known to increase the transition of 2X fibers to 2A. However, those transitions are limited to the fast fibers, and the transformation from fast to slow type is small or inexistent. In highly trained humans, fast fibers have shown the same oxidative metabolism as slow fibers and the same mitochondria content [93]. In contrast, slow fibers after endurance training are transformed into a faster phenotype.

However, those changes are not caused by myosin heavy chain modifications and they are not detectable by histochemical fiber typing. The switch of the slow fibers to a faster type allows them to respond to the exercise requirement contraction velocity, while they maintain their efficiency of energy use [94]. The slow to fast transition is generally reported in experiments that involve decreased neuromuscular activity. Hind-limb suspension, microgravity and denervation promote the transition from 2A to 2B fibers, or 2X in the case of humans [95]. However, the transition from slow type I to fast fibers has only been reported after severe spinal cord injury or prolonged spinal cord isolation. Therefore, the plasticity of fast fibers is greater than slow fibers, and changes take place following a determined sequence from faster and more glycolytic fibers to slow and oxidative fibers: MyHC-2B (*Myh4*) ↔ MyHC-2X (*Myh1*)↔ MyHC-2A (*Myh2*) ↔ MyHC-I (*Myh7*).

2.4. Skeletal muscle development: myogenesis

In embryogenesis, the zygote undergoes a development process called gastrulation to generate the embryo. The totipotent cells of the zygote divide into a 64-cell stage blastula, which contains an empty core. Blastula enters the gastrulation process, where the totipotent cell layer is fold and cells are specialized into three germ layers named ectoderm, mesoderm and endoderm. Each layer is committed to the development of different organs, and this transformation is governed by molecular signaling between compartments. Among others, the ectoderm is differentiated into the epidermis, brain nerves and pigment cells. The endoderm is specialized into lung, thyroid and digestive cells. Finally, the mesoderm is the progenitor of tubule cells, red blood cells and cardiac, smooth and skeletal muscle cells.

2.4.1. Hierarchical gene expression in early myogenesis

Myogenesis is the formation of muscle tissue that takes place both during the embryo development from the myotome precursor cells or in adulthood from satellite cells. During the myogenesis, the gene expression pattern of precursor cells is sequentially changed for their commitment to new myoblasts and subsequent myocytes.

Both during embryogenesis and in adult muscle regeneration *Pax3* and *Pax7* play an essential role in maintaining the cell multipotency and preserving the satellite cell pool. Myogenesis begins with the expression of highly conserved myogenic regulatory factors (MRFs) that drive the precursor cells to an irreversible myogenic differentiation [96]. The four major MRFs are myogenic factor 5 (*Myf5*), myoblast determination protein D (*MyoD*), myogenin (*Myog*) and MRF4 (*Myf6*). These transcription factors contain a DNA binding domain and a helix-loop-helix that associates with E protein to activate gene promoters. The first upregulated MRF is *Myf5* that helps in the formation of the myotome during embryogenesis and the differentiation to myoblasts in satellite cells. *MyoD* is upregulated after *Myf5* and both initiate the transcription of late differentiation genes. However, the differentiation to fused myofibers is only completed with the upregulation of myogenin (*Myog)*. *MyoD* enhances the expression of *Myog*, which

maintains the expression of *MyoD* in a feedback manner and together upregulates the transcription of late differentiation genes [97]. Therefore, *Myf5* and, more remarkably, *MyoD* are known as "commitment" or "specification" factors and are key for the definition of the muscle lineage. Whereas *Myog* is defined as a "differentiation" factor and is essential to enhance the transcription of genes for the formation and maturation of myofibers [98]. MRF4 plays a transient role similar to *Myf5* and *MyoD*.

Thus, myogenesis is a sequential process of genes suffering transient upregulation peaks that upregulate the expression of downstream genes. *Sox3/Sox7* is downregulated after the expression of *Myf5* and *MyoD*. Then, *Myog* reaches its maximum expression, while *MyoD* is gradually decreased. *Myog* starts an irreversible process downregulating the genes involved in the cell cycle and division and upregulating the expression of genes for muscle fiber fusion, sarcomerogenesis and contraction as myosin heavy chains, α-actinin, titin and dystrophins.

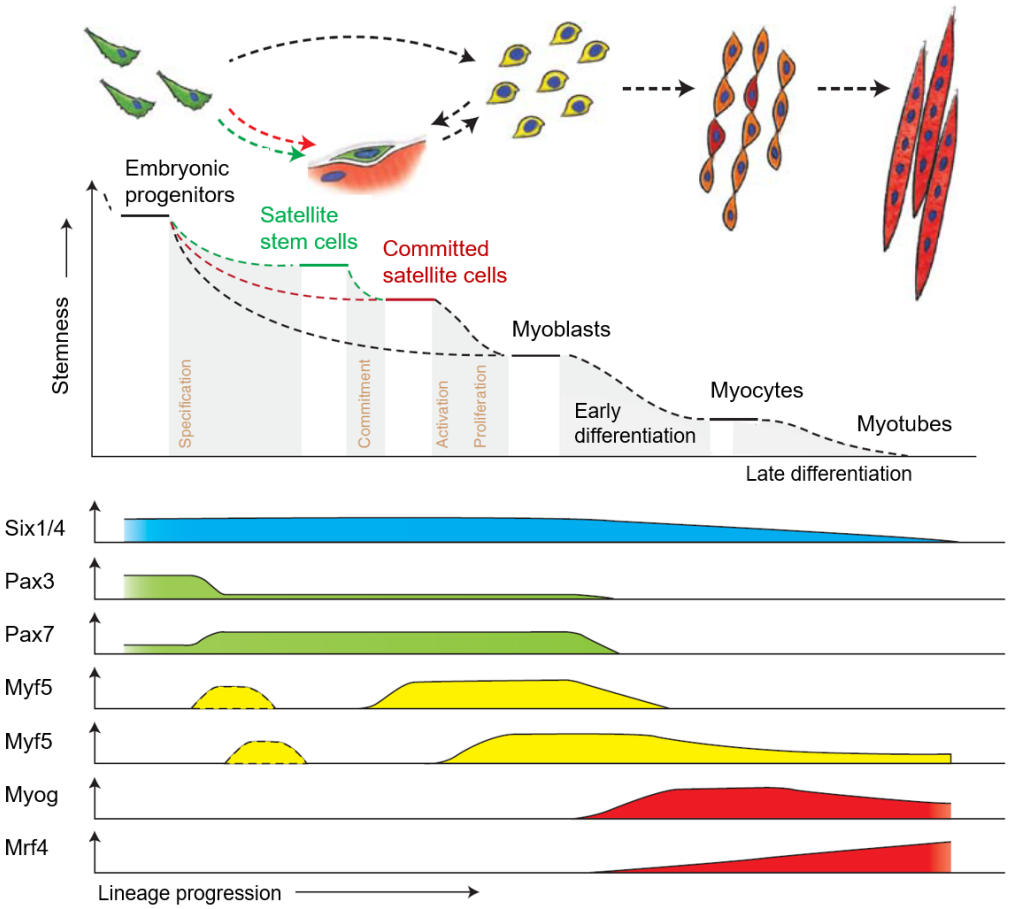

Figure 1.22. Hierarchy of transcription factors regulating progression through the myogenic lineage. Muscle progenitors that are involved in embryonic muscle differentiation skip the quiescent satellite cell stage and directly become myoblasts. Some progenitors remain as satellite cells in postnatal muscle and form a heterogeneous population of stem and committed cells. Activated committed satellite cells (Myoblasts) can eventually return to the quiescent state. Six1/4 and Pax3/7 are master regulators of early lineage specification, whereas Myf5 and MyoD commit cells to the myogenic program. Expression of the terminal differentiation genes, required for the fusion of myocytes

and the formation of myotubes, is performed by both myogenin (MyoG) and MRF4 [96].

2.4.2. Skeletal muscle fiber formation and late maturation

Myogenesis and consecutive muscle fiber maturation are driven by molecular signaling and transitions in gene expression. However, there are additional processes that are key for the formation of functional skeletal muscle fibers.

2.4.2.1. Cell-cell contact for myotube syncytium formation

Muscle fibers are the result of the fusion of multiple mononucleated myoblasts. *In vitro* studies demonstrated that myoblast migration is guided in response to chemotactic factors [99]. Positive migratory factors promote cell migration increasing the probability of cell-cell contact. Negative migratory factors slow down the cell motility facilitating cell-cell recognition and adhesion. *In vitro* experiments also reveal that multinucleated myotubes are formed in ordered steps [100]. First, myoblasts differentiate into mononuclear elongated myocytes that are fused with neighbor ones to form nascent myotubes. After, more myoblast fuse to the nascent myotubes and increase the syncytium myonuclei content to finally become a mature myotube. To make those contacts possible, the capability of the myoblasts to proliferate is crucial, as high cell density increase the chance of cell-cell contact and myoblast fusion. Furthermore, in scenarios where cell division is lowered or compromised as aging and pathophysiologic fibrosis, the muscle regeneration process fails and fibrotic tissue is formed instead [101].

2.4.2.2. Mechanical tension and sarcomerogenesis

The fusion of myoblasts into multinucleated myotubes in embryogenesis is followed by the formation of sarcomere units to provide the muscle fibers with powerful and coordinated contractions. Sarcomerogenesis begins once the myotubes are attached to the tendons [72]. In *Drosophila* embryogenesis, myotubes migrate and elongate to reach the tendons at the ends of the longitudinal axis. During this phase, myotubes are contracted while tendons elongate generating a high mechanical tension along the longitudinal axis [102]. The mechanical tension guides the newly formed myotubes towards the longitudinal axis, which finally determines the contraction axis. Together with the myotube positioning, the mechanical tension induces the actomyosin rearrangement into sarcomeres, thus it is essential for the formation of the contractile units. The assembly of the first sarcomeres results in the progressive concatenation of more sarcomere units to complete the entire length of muscle fibers. Afterward, muscle fibers grow in width and length until they reach the mature state [103]. Muscle fibers are finally packed into fascicles and surrounded by connective tissue.

2.5. Skeletal muscle diseases

Muscle disorders can be classified into inherited and acquired. Hereditary myopathies are grouped into muscular dystrophies, congenital myopathies and metabolic myopathies [104]. Muscular dystrophies are progressive diseases with a poor prognosis. Most of them have been studied in deep, and their molecular genetic aspects are well understood. These include X-linked dystrophinopathies (i.e. Duchenne Muscular Dystrophy (DMD)) and the autosomal dominant disorder myotonic muscular dystrophy [105]. Congenital myopathies are slowly progressive and relatively benign. In contrast to dystrophies, they are characterized by structural changes of some muscle elements [106]. Metabolic myopathies show altered cellular energy metabolism, which includes glycogen storage diseases, fatty acid oxidation defects, and mitochondrial disorders [107].

Acquired myopathies are non-hereditary muscle disorders that include toxic, immune-mediated, infectious, endocrine, electrolyte myopathies and myopathies associated with systemic disease. Toxic myopathies are caused by the ingestion or injection of substances like alcohol, medical drugs (statins, chloroquine, diuretics, corticosteroids, omeprazole, etc.) [108]. Infectious myositis are less common and may be caused by several bacteria, fungi, parasites and viral agents [109]. Endocrine myopathies are those associated with thyroid and parathyroid dysfunction, adrenal dysfunction and diabetes [110]. Lastly, systemic diseases as amyloidosis, sarcoidosis, vitamin D deficiency and paraneoplastic syndrome result in muscle atrophy and malfunction. Among paraneoplastic syndromes, cancer cachexia (CC) is one of the harshest and frequent myopathies [111].

Cachexia is severe and progressive muscle atrophy that ends in a significant loss of body mass and is responsible for 20% of death in cancer patients [112]. Pro-inflammatory cytokines, as interleukins (i.e. IL-6), tumor necrosis factors (i.e. TNFα)114 and Interferon type II (INFγ) are known to impede muscle differentiation and induce protein degradation and myotube atrophy [113,114]. Other inflammatory cytokines as Myostatin (Mstn) and ActivinA (ActA), which are part of the transforming growth factor β (TGFβ), act as an autocrine signal causing a strong downregulation in myogenesis [115]. Cancer cells secreted components as microRNAs have also been studied as strong cachexia promoters [116, 117]. miRNAs can be free in the serum or enclosed in extracellular vesicles (EVs) secreted by tumor cells, which can modulate the gene expression of the receptor muscle cell. The above-mentioned inflammatory cytokines unbalance the protein turnover in muscle cells via NFκB, p38/C/EBPβ and JAK/STAT pathways, which activate the E3 ubiquitin ligases as Atrogin-1 (*Fbxo32*) and muscle RING finger containing protein 1 (MuRF1, *Trim63*) [118]. These enzymes ubiquitinylate muscle structural protein as myosin heavy chains (MHCs) that are later degraded by ubiquitin-proteasome complex. Other pathways as Akt/mTOR and those related to autophagy are also modulated in cancer cachexia, however, they are less studied than those related to the ubiquitin-proteasome pathway [118]. Due to their significant role in CC, proteolytic pathways and their upstream processes are the main targets of drug screening studies in cachexia [112,118]. However, most drugs fail in clinical phases due to the poor recapitulation of the human phenotype in the current animal models and lack of studies on the molecular basis of cancer cachexia [118].

3. Skeletal muscle tissue engineering

Skeletal muscle tissue engineering (SMTE) aims to recapitulate the original tissue through the combination of muscle cells, alone or encapsulated in biomaterials, with external physical and biochemical factors. Considering muscle architecture and function, engineered 3D systems must consist of at least 1) a 3D template that enhances high cell proliferation to facilitate myoblast fusion and promote differentiation, 2) a mechanism that aligns muscle fibers towards the contraction axis and 3) a system to induce muscle contraction. Some of the requirements of the biomaterials and the engineered system to develop skeletal muscle tissue will be discussed in the following sections.

3.1. Properties of biomaterials for skeletal muscle tissue engineering

Generation of *in vitro* muscle tissue requires an initial template that guides cells towards the three spatial dimensions. 3D templates must meet the needs of the muscle precursor cells to proliferate, migrate, differentiate and be functional.

3.1.1. Biocompatibility and bioactivity

Biomaterials must be designed to support cell survival and avoid the overactivation of apoptotic pathways and rejection. Nevertheless, the surface of the materials must not be inert. Indeed, a biomaterial that mimics the native ECM must interact with the cells and serve them as a template to develop the tissue *in vitro*.

Since cells contact with the biomaterial, they activate a response corresponding to the characteristics of the surface. In the case of adherent cells like myoblasts, they need to interact with molecular structures of the surface via integrin receptors to establish focal adhesions. Cells use the focal adhesions to migrate, divide and differentiate. These cell-ECM interactions also activate intracellular signaling pathways known as mechanotransduction processes. Those processes modulate the gene expression and influence the response of the cells to the surrounding biomaterial [121]. Thus, biomaterials must contain short aminoacid adhesion motifs as RGD, found in fibronectin, laminin or vitronectin proteins, or DGEA and GFOGER, found in collagen. Furthermore, the density of adhesion motifs has also a relevant influence on cell behavior. If the distance between motifs is too long, the cell cytoskeleton will be highly deformed to bind with the closest point, while if the adhesion points are very close, the deformation of the cells will be minimal. In these two cases, the deformation of the cells and changes in the cytoskeleton will activate opposite mechanotransduction pathways [122]. Indeed, focal adhesion kinases play an important role in the induction of MyoD expression, myoblasts fusion and costamerogenesis in C2C12 cell line [123].

3.1.2. Swelling, porosity and diffusion

One of the most important features of biomaterials is their capability to allow the influx of nutrients, water and gases into the core of the structure. If the consumption of nutrients by the cells is higher than the influx rate, the cells in the core of the biomaterial will experience nutrient starvation and hypoxia. Engineered tissues that lack vascularization must take care of the diffusion properties of the biomaterial, as it will be determinant for the correct nutrient supply to the encapsulated cells. Physical laws governing the diffusion phenomenon strongly depend on the surface properties of biomaterials and the porosity of the polymer mesh.

3.1.2.1. Swelling

In tissue engineering, the principal solvent of nutrients and gases is water. Therefore, the surface of the biomaterial must preferentially be thermodynamically compatible with water. When material and a solvent present the same polarity, the latter interacts with the surface and penetrates the mesh pores until they reach a maximum uptake value. This phenomenon is termed swelling, which indicates the water absorption rate of the biomaterials. During swelling, solvent molecules increase the mobility of polymer chains that expand and allow the penetration of more solvent molecules. If the surface polarity is opposite to the solvent, as water and hydrophobic surfaces, the repulsion forces will impede the influx of the solvent to the core.

Opposite to the osmotic forces, elasticity forces determine the deformation limit of the biomaterial during the water absorbance. If the elasticity forces are too weak, high swelling rates and polymer chain expansion result in the deformation, instability and disaggregation of the hydrogel [19]. An equilibrium between osmotic and elastic forces ensures a good water absorption rate and the stability of the 3D mesh.

3.1.2.2. Porosity and pore size

Biomaterial swelling rate and diffusion depend on the surface properties, however, they are also influenced by the pore size and porosity. In terms of pore size, biomaterials can be classified into four groups [124]. Non-porous materials work as flat substrates, where molecules are adsorbed to the surface. Microporous materials present pore sizes between 100-1000 Å. The swelling rates are slow and the diffusion is dependent on the size of the solute. The size range of the microporous materials is between 0.1 and 1 µm. In this regime, the swelling rates are very fast and diffusion is independent of the solute size. Finally, in the super-porous materials, the solvent flow is free through the > 1µm size pores.

Pore size limits the dimensions of the particles that can penetrate the biomaterial mesh. Nevertheless, porosity and pore connectivity are equally important in terms of diffusion. The porosity corresponds to the ratio between the total pore volume and the apparent volume of the biomaterial. Materials with big pore sizes but low porosity present low pore density, meaning that most of the structure volume is filled with material and scarce cavities. Low porosity implies

less solid/liquid surface contact and lower diffusion. Regarding pore connectivity, they can be classified into two types [125]. Closed pores that are inaccessible to the outside fluids and open pores that communicate with the external media. Inside the open pores, they are classified as through pores, which cross the material from one point in the surface to another one; and blind pores, which are only open to the surface by one side. In tissue engineering, open through pores are the best choice, as they provide channels by which nutrients and detritus can be exchanged with the external medium across all the biomaterial.

3.1.3. Mechanical properties

Biomaterials for muscle tissue engineering are usually hydrogel preparations composed of highly hydrophilic polymers. These porous hydrogels mostly behave as elastomeric foams when are subjected to compression forces, where three regions can be distinguished [126]. First, a short linear elastic regime, where the bending of the whole system is calculated, including polymer chains, cavities and the infiltrated water. Second, a plateau regime, where the struts buckle and the pores collapse. Third, a densification regime in which all the pores are collapsed and polymer chains are reoriented according to the applied pressure. Compression tests analyze the stress-strain curves resulting from those regions and provide information about the stiffness of the material. In every linear regime, the slope can be easily extracted, called Young's Modulus. This value is expressed in kPa and corresponds to the amount of force needed for a certain material deformation. For the sake of simplicity, in variable models as hydrogels, Young's Modulus is calculated from the slope of the linear elastic regime.

Many studies support that the stiffness of biomaterials strongly influences cell behavior. Adhesion structures, cell spreading, migration, cytoskeleton arrangement and morphology are influenced by the stiffness [127-129]. Furthermore, substrate elasticity was shown to induce the formation of different lineages in mesenchymal stem cells (MSC) [130]. They showed that soft stiffness materials (0.1-1 kPa) promote the MSC differentiation to neural lineage, while cells in intermediate stiffness (8-17 kPa) express myogenic genes and those in hard stiffness (25-40 kPa) present a more osteogenic phenotype. Those experiments suggest that biomaterials with tissue-like stiffness provide better development of the engineered tissue.

In muscle tissue, substrates with intermediate stiffness (8-12 kPa) promoted the formation of sarcomeres in C2C12 differentiated myotubes, while softer or harder stiffness did not show an organized actomyosin cytoskeleton [131,132]. Since myotubes transmit actomyosin contraction through their attachments to the matrix, substrate stiffness is crucial for muscle function. Therefore, muscle tissue engineering must consider the use of biomaterials with tissue-like stiffness, which is widely accepted to be close to 12 kPa [67,130,133].

3.1.4. Degradation kinetics

Degradation is the process where polymer chains are cleaved into smaller oligomers or subproducts. It can be triggered by physicochemical processes, as hydrolysis or oxidation, or enhanced by cellular and enzymatic activity. In physicochemical processes, porosity, pore architecture, swelling and chemical composition of the environment are some factors influencing biopolymer degradation [134]. Medium pH changes the degradation rate, as in PLGA scaffolds, where acid medium increases biomaterial degradation rate [135]. Similarly, it was reported that the frequency of culture medium replacement has a strong effect on the degradation of polymer blends [136]. The degradation byproducts can acidify de medium and compromise cell viability [137]. Furthermore, polymer biomaterial degradation results in the loss of mechanical properties, which can induce changes in the gene expression of cultured cells. In the last phase of degradation, scaffolds suffer a physical breakdown that impedes cell attachment and loses 3D conformation. Therefore, biomaterials for tissue engineering should present a degradation rate that keeps the integrity of the 3D structure while promoting cell proliferation and secretion of new ECM.

3.2. Biomaterials for skeletal muscle tissue engineering

In the last decade, there has been a growing interest in the use of biomaterials for the generation of *in vitro* muscle grafts. Biomaterials must meet the physicochemical properties that recapitulate the muscle tissue and contain biochemical cues to promote the growth and differentiation of myoblasts in 3D. There is a vast variety of polymers used in the literature, and they can be obtained from natural or synthetic sources.

3.2.1. Synthetic polymers

Synthetic polymers have attracted the attention of the tissue engineering community due to their versatility. The surface of synthetic polymers can be conjugated with biologically relevant molecules, like growth factors. Conjugations can be engineered to obtain a controlled release of biochemical signals or to promote cell adhesion. Furthermore, the manufacturing process can be modified to modulate some physical properties of the biomaterials. Synthetic polymers can be classified into hydrophobic and hydrophilic.

3.2.1.1. Hydrophobic polymers

Polyesters are the most common polymers in tissue engineering. Poly(ε-caprolactone) (PCL) is a highly resistant hydrophobic thermopolymer. Although it is biodegradable, PCL scaffolds have been used for long-term *in vivo* implants, as their integrity was preserved for up to two years [138]. In muscle engineering, electrospun PCL scaffolds promoted the alignment of myoblasts and provided them with mechanical support [139]. However, the elastic modulus was far from native tissue, thus PCL was more indicated to support the growth of tendons [140]. Poly-L-lactic acid (PLLA) and poly(lactic-co-glycolic acid) (PLGA) are also biodegradable thermopolymers, but their degradation rate is faster than PCL. PLLA and PLGA were successfully used for the generation of electrospun

membranes that driven the alignment of the myoblasts and enhanced muscle differentiation [141-145]. To improve the electrical conductivity of PLLA, fibers were modified with Au nanoparticles, showing advantageous properties for muscle development [143]. However, they noticed that those biomaterials doubled the yield stress of muscle tissue. Levenberg *et al*. mixed PLLA and PLGA to generate implantable porous sponges where myoblasts embedded in Matrigel® were cocultured with endothelial cells [146].

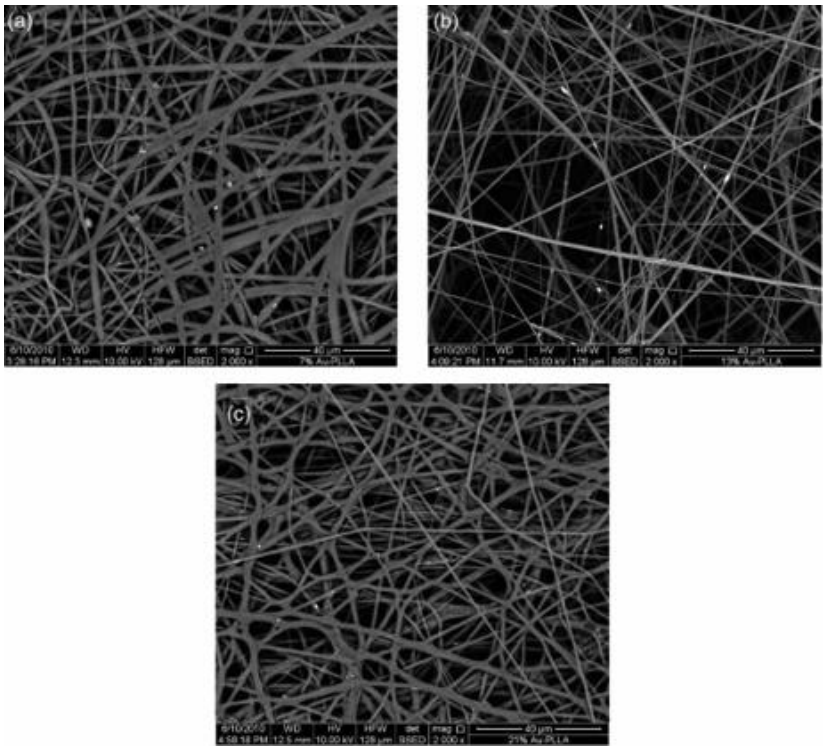

Figure 1.23. SEM images displaying the gold within the electrospun fibers (magnification, equation image 5000) for: (a) 7% Au–PLLA; (b) 13% Au–PLLA; (c) 21% Au–PLLA scaffolds [143].

Polyurethanes (PUs) are elastomers notably more flexible than the abovementioned polyesters, which makes them more suitable for muscle tissue engineering. Furthermore, they have tunable mechanical properties, which can be adapted to meet skeletal muscle needs [147]. PUs contain several moieties that provide them with biodegradable capability and offer the possibility to add multiple chemical and biological cues. The versatility of PUs has led to several manufacturing options, as electrospun fibers or cast foams after their dissolution in organic solvents, or printed at high temperature [140,147-150].

Polyesters and polyurethanes are mostly hydrophobic thermopolymers, therefore they are only malleable when subjected to high temperatures or dissolved in organic solvents. Organic solvents are evaporated during the manufacturing process; however, the remaining traces could compromise the viability of cells. High melting temperature impedes the encapsulation of cells inside these biomaterials, and their hydrophobic nature hinders the nutrient diffusion into the polymer mesh.

3.2.1.2. Hydrophilic polymers and hydrogels

Hydrophobic properties of synthetic polymers can be adapted to biomedical applications by the conjugation of amphiphilic polymers like poly(ethylene) glycol (PEG). PEG is both water and organic solvent-soluble and its application in the pharmaceutical industry is well known. PEG is used to encapsulate hydrophobic drugs in aqueous systems and reduce the immunologic response in the host in a process called PEGylation [151]. These amphiphilic polymers are extremely soluble in water [152], therefore, they need to form copolymers with additional molecules to synthesize stable hydrogels. PEGs with high molecular weights are known as PEO and are frequently conjugated with PPO to form triblock copolymers (PEO-PPO-PEO) known as poloxamers and pluronics. In muscle tissue engineering, pluronics are used as sacrificial scaffolds to mold softer biomaterials [153,154]. However, they cannot be in culture for extended periods due to their cytotoxicity.

Hydrogels based on PEG can be designed to offer different crosslinking methods. Crystallization, hydrogen bonding and host-guest interactions are some of the crosslinking strategies [155-157], nonetheless, photopolymerization is one of the most common methods used for muscle engineering. Hydroxyl groups of PEG can be functionalized with acrylic groups to obtain PEG-diacrylate (PEGDA). In the presence of free radicals, vinyl groups of PEGDA are highly reactive and form covalent bonds. To obtain PEGDA crosslinked hydrogels, photoinitiators are used as the main source of free radicals. In presence of long-wavelength UV light, photoinitiators as Irgacure 2959, Lithium phenyl (2,4,6-trimethylbenzoyl) phosphinate (LAP) and 2,2-Dimethoxy-2-phenylacetophenone (DMPA) generate free radicals that react with vinyl groups of PEGDA. Photocrosslinking reaction establishes covalent bonds between different polymer chains to create an interconnected PEGDA mesh. Among others, reaction kinetics is ruled by the type of photoinitiator, UV light source and the number of available reactive groups, thus photocrosslinking method provides highly versatile hydrogels with tunable physical properties [158]. In the literature, PEGDA has been used to generate highly porous foams for skeletal muscle development, photocrosslinked hydrogels with myogenic functionalizations or as delivery particles for muscle regeneration [159-162].

In recent studies, synthetic polymers are combined with polyacrylamides to produce electroactive hydrogels to enhance muscle contraction. Polyacrylamides are stimuli-responsive polymers whose physical properties can be modulated with changes in pH, temperature or electrical field. Browe *et al.* combined acrylic acid (AA) with PEGDA to fabricate bioactuator sheets that contracted with electrical stimulation [163]. PAA was also combined with the conductive polymer polyaniline (PANi) to obtain hydrogels with improved electrical properties and controlled porosity [164]. In another study, Villa *et al.* used poly(N-isopropylacrylamide) (NIPAAM) as thermoresponsive polymer to fabricate detachable skeletal muscle sheets165.

Synthetic polymers are attractive materials for skeletal muscle tissue engineering due to their tunability, reproducibility and inexpensive manufacturing. They can be easily functionalized and their inert nature impedes the adhesion of undesirable proteins. However, inert nature is also related to the low availability of cell adhesion points. Cell adhesion to surfaces is mediated by the interaction of receptors of the membrane. To initiate the adhesion process, receptors must recognize at least a sequence of Arg-Gly-Asp (RGD) [166]. RGD adhesion motifs work with synergistic aminoacid sequences, as PHSRN, to reinforce the adhesion and preserve an adequate structural conformation. Synthetic polymers lack adhesion motifs and they are commonly functionalized with RGD groups [166]. Nevertheless, they do not fully recapitulate the structural protein complex of focal adhesions found in natural polymers. Furthermore, degradation byproducts of some synthetic polymers can include toxic substances that compromise cell viability and generate a proinflammatory response. Despite some synthetic polymers are hydrophilic and used as hydrogels for tissue engineering, most of them are not suitable for the encapsulation of cells during the manufacturing process. Scaffold fabrication with thermopolymers requires the use of organic solvents and critical temperatures. These scaffolds are mainly fabricated with electrospinning or 3D-printing methods, and cells are cultured on the surface, thus generating monolayer cultures.

3.2.2. Natural polymers

Natural polymers are highly biocompatible and contain native cues that promote cell attachment, proliferation and differentiation. They are highly hydrophilic with excellent mechanical properties as hydrogels for soft tissue engineering. Furthermore, breakdown byproducts are less toxic and easier to metabolize by the organisms than those derived from synthetic polymers. In contrast to synthetic polymers, they are less chemically tunable, however, most of them contain a chemically reactive group. Natural polymers can be extracted from different sources. Cell interaction with biopolymers that are naturally present in their native environment will be more effective than foreign polymers. Therefore, in this section, they will be classified as mammal or non-mammal derived polymers.

3.2.2.1. Polymers from mammal sources

Collagen

Collagen is one of the most abundant polymers of soft, semi-rigid and rigid connective tissues. In skeletal muscle tissue, collagens I and III are the major components of endo-, peri- and epimysium [66]. Collagen I is an amphoteric protein with triple helix conformation formed by hydrophilic and hydrophobic aminoacids. This conformation is sensitive to pH changes because hydrophobic aminoacids can interact with aqueous medium out of the isoelectric point range. For that reason, collagen can be extracted in a soluble form both by acid and basic

treatments, which determines the final composition [167]. In neutral aqueous solutions, collagen restores the native conformation and shifts to a gel state.

Due to its close relationship with muscle ECM, type I collagen has been extensively used in muscle engineering. Muscle precursor cells are usually embedded in collagen to fabricate *in vitro* models by mold casting, micropatterning or 3D bioprinting [168,169]. However, the collagen extraction process can produce toxic compounds and complete neutralization must be ensured before cell encapsulation. This means that collagen must be rapidly manipulated and refrigerated before its complete gelation. Furthermore, collagen gelation is a poorly controllable self-assembly process, which limits the control of mechanical properties.

Fibrin

Fibrin has been used as an alternative to improve the mechanical properties of collagen matrices. In contrast to collagen, degradation and crosslinking degree of fibrin can be controlled through the precursor concentration and medium ionic strength. Fibrin is the result of the coagulation reaction of fibrinogen and thrombin. Fibrinogen is a water-soluble glycoprotein composed of 2 Aα, 2Bβ and 2γ monomers, whose N-terminal end in the central region of the macromolecule named E nodule [170]. E nodule conformation is stabilized by A (FpA) and B (FpB) fibrinopeptides. During wound healing, thrombin plasma protease is activated by the coagulation cascade. Thrombin cleaves FpA and FpB releasing the active sites of Bβ and Aα in the E nodule that interact with the D nodule of adjacent fibrinogen molecules. Continuous aggregation of fibrin protofibrils leads to the formation of a gel-like insoluble substance that forms the clot.

Fibrinogen has been widely used in surgery as a bioadhesive and haemostatic sealant [171]. Despite the scarce presence of fibrin in the skeletal muscle ECM, it became one of the most used biopolymers for muscle *in vitro* models. Engineered muscles based on fibrin templates showed excellent capabilities to support myoblast growth and differentiation. Differentiated muscle fibers showed a mature differentiation state with sarcomeric patterning and contractility, which were also used to emulate muscle diseases *in vitro* [172-175].

Gelatin

Gelatin was also araised as an alternative to the inconveniences of collagen. Gelatin is the product of the irreversible denaturation of collagen, thus keeping most of the biochemical cues and properties of its predecessor. The denaturation process determines the properties and composition of gelatin [176]. The most common method for collagen denaturation is based on a thermal process mixed with a hydrolytic process in alkali or acidic medium. This process breaks the strongest covalent bonds obtaining type B gelatin in alkali processes and type A in acidic ones. Type B gelatin contains fewer impurities and higher carboxyl groups.

Once collagen is denatured, the thermosensitive nature of gelatin avoids its gelation at physiological temperature. Moreover, the gelation state and viscosity of this polymer can be controlled through temperature. However, it is necessary to find an alternative crosslinking method to fabricate suitable templates for *in vitro* muscle culture. Chemical crosslinking of gelatin can be performed using glutaraldehyde (GTA), methanal (formaldehyde), dextran dialdehyde, carbodiimide (i.e. EDC/NHS), ethylene glycol diglycidyl ether and hexamethylene diisocyanate [177-181]. However, unreacted products of chemical crosslinking can compromise cell viability and induce inflammation. As an alternative, physical crosslinking provides a more tunable a controllable method. To that end, gelatin is chemically modified with methacrylic groups that interact in the presence of a photoinitiator activated by UV light. The amino groups of the polypeptide chain react with methacrylic anhydride, providing them with a vinyl group. As explained in section 7.2.1.2., photosensitive initiators (i.e. LAP and I2959) irradiated with 365 nm wavelength UV light generate free radicals that bind vinyl groups of different gelatin methacryloyl chains (GelMA). Although natural polymers are less tunable than synthetic polymers, using this approach it is possible to monitor different parameters of the fabrication process (i.e. irradiation time, methacrylation degree and photoinitiator concentration) that affect the physical properties of the final biomaterial. GelMA versatility and stability in physiological conditions are some of the reasons why it has been increasingly used in muscle tissue engineering [183-185]. GelMA is one of the most common bioinks used for 3D extrusion bioprinting [160,186]. As a thermoresponsive biomaterial, the viscosity can be controlled by temperature to obtain a highly bioprintable biomaterial.

Hyaluronic acid

Hyaluronic acid (HA) is a polysaccharide ubiquitously distributed in vertebrate ECM. In muscle tissue, HA promotes cell proliferation and migration for regeneration, while impedes differentiation [187]. Calve *et al.* experiments demonstrated that HA has an important role in myogenesis and hypertrophy enhancing the growth and recruitment of muscle precursor cells and preventing premature fusion [188]. HA contains several chemical moieties that can be modified for polymer functionalization. Together with its poor mechanical properties and fast degradation, HA in literature is commonly found chemically and physically crosslinked and in combination with other biomaterials [140,189]. Chemical crosslinking methods include the generation of amide bonds between amino and carboxyl groups using carbodiimide, modification of hydroxyl groups (i.e. ester and ether bonds) and modification of -$NCOCH_3$ group. As in previously mentioned polymers, amino and carboxyl groups can be methacrylated to obtain photocrosslinkable HA (i.e. HAMA, GMHA) [189].

Keratin

Keratin is a cysteine-rich protein found in the epidermal appendageal of vertebrates as hair, horns, nails, wool, quills, feathers and reptile scales. They can be classified as hard and soft keratins according to their sulfur content. Hard keratins are strongly packed thanks to the high content of disulfide bonds, while soft keratins present more amorphous conformations due to the lower content of sulfur groups and higher presence of weak bonds [190]. Structural conformation also determines keratin solubility, however, any of the keratin forms in nature are fully soluble in water [191]. To obtain water-soluble keratins, they can be modified in the extraction process using a reductive or an oxidative treatment. Oxidative extraction to keratose (KSO) caps the cysteine residues with sulfonic acid groups, which impedes the formation of disulfide bonds. In contrast, keratin reduction to kerateine (KTN) preserves cysteine chemical structure [190]. In tissue engineering, hydrogels with a controlled KSO/KTN ratio are prepared to control the degradation rate of the scaffolds. Those hydrogels with high KSO content are degraded in weeks, while high KTN content hydrogels last for months [190]. KSO/KTN hydrogels can be mixed with growth factors for a controlled release in muscle tissue regeneration [192-194]. In those studies, keratin hydrogels are solubilized and intracutaneously delivered through injection. These biomaterials have demonstrated excellent myogenic properties and successful recovery of volumetric muscle loss (VML). Despite the good outcomings of keratin use in muscle development, pure keratin biomaterials have poor mechanical properties and brittle structure.

Decellularized ECM

Despite mammal-derived natural biomaterials present many biochemical properties that benefit the growth and differentiation of engineered tissues, so far there is not any biopolymer that encloses all the features of native ECM, as molecular signaling and architecture.

Decellularized ECM (dECM) emerged as a tool to develop native tissue resembling biomaterials with low induction of inflammation and rejection [195]. To date, several animal sources have been used to obtain dECM, but porcine is one of the most extended due to its similarities to humans in composition and architecture [196]. Human dECM has also been successfully extracted, however, sources are limited and hampers the scalability of the biomaterial. Decellularization processes must be designed to remove cells while preserving the molecular composition and arrangement. Nowadays, two main protocols based on the use of mild detergents or detergent-enzymatic treatments are the most used [196]. They successfully isolated muscle ECM, however, those treatments could alter the biochemical cues and physical properties, thus changing the cell-ECM interaction. Although complete preservation of ECM properties is still a challenge, muscle dECM demonstrated exceptional capabilities as biomaterials for tissue engineering. Fresh dECM were used as implantable hydrogels that promote cell migration and infiltration for the recovery of VML [197].

Poor mechanical properties and fast degradation are some of the limitations of dECM for SMTE. Choi and colleagues used gelatin as a self-healing sacrificial material to obtain high-resolution bioprinted structures [198]. However, once gelatin was dissolved, scaffolds experienced a fast degradation. To improve post-printing mechanical stability, Kim *et al.* developed a promising photocrosslinkable dECM [199]. Nevertheless, dECM composition can vary from batch to batch, thus the degree of substitution is difficult to control. Furthermore, dECM biomaterials are poorly reproducible and physical properties change between sample individuals. To obtain more controllable dECM biomaterials, they are often combined with synthetic polymers [200, 201].

3.2.2.2. Natural polymers from alternative sources

The natural polymers listed above are originated from mammal sources. Mammal-derived biomaterials contain biochemical cues that are recognized by cells for adhesion. However, the recognition and remodeling result in the degradation of the initial biomaterial to be substituted by a cell-secreted matrix. As stated before, the degradation of biomaterials in tissue engineering must be equilibrated to the degradation rate. To that aim, natural polymers from alternative sources make biomaterials more resistant to cell degradation. Like synthetic polymers, non-mammal polymers present fewer cell-recognizable cues, thus hampering the degradation of the biomaterial.

Alginate

Alginate is a polysaccharide extracted from the cell wall of brown algae (*Phaeophyceae*). Alginate is formed by blocks of (1,4)-linked β-D-mannuronate (M) and α-L-guluronate (G) residues, and only the G blocks are known to participate in reversible crosslinking with divalent cations. Ca^{2+} ions interact with two carboxyl groups of adjacent alginate chains that fold around the cations creating the named “egg-box” crosslinking [204]. The type of salt used as crosslinker will determine the gelation time, thus the ionic crosslinking process can be modulated [205]. However, irreversible ionic bonds can compromise biomaterial stability. Furthermore, soluble ions are known to activate signaling pathways as messengers to regulate cell physiological function. Excitable cells, as neurons and muscles, are particularly sensitive to Ca^{2+} ions, which are involved in proliferation, differentiation, secretion, mobility and contraction [206].

As an alternative to ionic crosslinking, alginate photocrosslinking provides controllable gelation rate and mechanical properties [207]. Carboxyl groups of polysaccharide monomers can be modified with aminoethyl methacrylate (AEMA) to generate potentially reactive groups in the presence of an active photoinitiator. Photocrosslinkable alginate is known as alginate methacrylate (AlgMA) and has been used in many biomedical applications, as cell-laden injectable scaffolds, replacement of nucleus pulposus, chemotherapeutic delivery and tissue engineering [208-211]. AlgMA prepolymer is a promising candidate

for 3D bioprinting techniques given its thixotropic behavior. Thixotropic materials, also known as shear-thinning, present decreased viscosity under shear stress, as in printing needles, which is recovered after their release, which improves the printability of viscous materials [211]. In tissue engineering, it showed good biocompatibility and supported the growth and differentiation of skeletal muscle [160].

Cellulose

Cellulose demonstrated excellent properties as hydrogels for biomedical applications. It is non-costly, chemically tunable and biocompatible. Cellulose is a polysaccharide with crystalline and amorphous conformation given by different arrangements of β (1→4) D-glucose monomers. Enzymatic machinery of mammalian is not able to hydrolyze β (1→4) bonds, hence is resistant to cell degradation [212].

Cellulose fibers can be extracted from plants or produced by bacteria. Differences are based on crystalline structure, as plant cellulose presents more amorphous groups and is complemented with hemicellulose and lignin. In contrast, bacterial cellulose is pure and more crystalline. Furthermore, microfibril arrangement can be modified using different strains and culture conditions to obtain cellulose with different lengths and physical properties. In general, microfibrils of bacterial cellulose are smaller and form highly porous matrixes with significant water retention [213].

Cellulose, like other polysaccharides, is susceptible to chemical modifications thanks to the carboxyl groups. They can be conjugated with ether groups to obtain water-absorbent polymers as methylcellulose, ethylcellulose, hydroxypropyl cellulose and carboxymethyl cellulose (CMC) [214]. Water-soluble cellulose is commonly used for the generation of hydrogels. Soluble cellulose forms weak bonds (i.e. Van der Waals and H bonds) that give them a viscous aspect and interesting properties for pharmacologic and biomedical applications. However, to obtain lasting hydrogels, cellulose can be crosslinked by several chemical methods. Citric acid was combined with CMC and PEG to create superabsorbent hydrogels for wound healing and drug delivery [215,216]. Leonardis *et al.* used 1,4-Butanediol diglycidyl to obtain injectable CMC for soft tissue augmentation in patients [217]. Bacterial cellulose cultured with muscle cells demonstrated improved muscle bundles and epithelial tissue after implantation. To reinforce cellulose crosslinking and improve hydrogel durability, CMC was chemically modified with AEMA to obtain photocrosslinkable CMC methacrylate (CMCMA) with tunable physical properties [160,218].

Agarose

Agarose is a byproduct of agar, which is present in red seaweeds. Agar is a mixture of two polysaccharides, a linear component known as agarose and the amorphous component agaropectin, whose removal results in a more neutral

hydrogel with improved gelation properties [219]. Agarose is composed of agarobiose disaccharide subunits, which form helical arrangements by H bonds and electrostatic interactions. Those interactions are thermally reversible and depend on the molecular weight of the chains, which present melting temperatures ranging from 30 and 90 °C [219]. Agarose hydrogels are therefore stable at physiological conditions and have demonstrated good biocompatibility as substrates for cell culture or molds for cell-laden hydrogel shaping [220-223]. However, Pollot *et al.* published a detailed study comparing the properties of fibrin, collagen, alginate and agarose, where agarose presented the highest Young's modulus and was the most brittle. They showed reduced expression of muscle differentiation genes in agarose, thus suggesting that it is not the best choice for SMTE [224].

Silk

Silk is a structural protein produced mainly by silkworms and spiders, however, there are few studies focused on the use of spider silk for biomedical applications225. Silkworm silk is divided into two components, silk fibroin (SF) and silk sericin (SS). SF is hydrophobic and provides toughness and strength to the fibers, while SF acts as a hydrophilic gumming agent with elastic properties. Differences in the composition of SF and SS determine the solubility, mechanical properties and degradation of silk.

Many studies have been published using silk matrices for skeletal muscle tissue engineering due to its cytocompatibility, mechanical properties and slow degradability. A great percentage is focused on the combination and functionalization of silk with electroactive molecules to improve biomaterial conductivity [226,227]. Chaturvedi *et al.* analyzed the growth and differentiation of human muscle myoblasts in silk foams from different sources. They concluded that those silk foams resembling the muscle tissue stiffness were the more promising for SMTE [228]. Due to their low solubility in water, most of the engineered cell substrates are based on foams and electrospinning [226-230], where cells are cultured after their synthesis. Therefore, obtaining silk hydrogels can be challenging, and they need to be combined with hydrophilic polymers in a semi-interpenetrating network [231].

Chitosan

Chitosan is the deacetylated form of chitin, a polysaccharide mainly found in fungi and the exoskeleton of invertebrates as insects, arachnids, crustaceans and mollusks. Partial deacetylation of chitin ends in a more amorphous and hydrophilic copolymer of N-acetylglucosamine and N-glucosamine residues [232]. The degree of deacetylation determines the mechanical properties and solubility of the biomaterial [233].

Chitosan is biocompatible, biodegradable and allows many chemical modifications thanks to its amine and hydroxyl groups. Since decades, chitosan

has been used for biomedical applications due to its antimicrobial properties [234]. Furthermore, it was explored as a biomaterial to engineer bone, cartilage, cornea, skin, intervertebral disk and tendon using solvent casting, thermally induced phase separation, gas foaming, electrospinning and grafted to hydrophilic polymers to form hydrogels [232]. Some studies combined chitosan with synthetic polymers to engineer electrospinned aligned substrates to enhance muscle tissue growth and differentiation [235, 236]. However, they are not suitable materials for the formation of hydrogels. Similar to silk, the hydrophilic nature and toughness of chitosan limited its use in soft tissue engineering.

3.3.Muscle fiber alignment

Skeletal muscle tissue is arranged in a tubular, unidirectional and parallel conformation. The specialized organization of muscle fibers provides a strong and coordinated contraction for optimized movements. Fiber alignment is one of the most important issues in muscle *in vitro* models and many solutions have been proposed to this end. Many strategies are based on the fabrication process of the engineered muscle. However, techniques are limited by the type of biomaterial since they can be incompatible with some fabrication processes. The following subsections summarize the most used techniques and biomaterials for muscle fiber alignment.

3.3.1. Directional topographical cues

The surface of culturing substrates can be modified to drive the attachment of myoblasts in a particular orientation. Several studies take advantage of the hydrophilic/hydrophobic properties of the surface to promote linear and unidirectional growth of myoblasts. Junkin *et al*. demonstrated that cells replicated the substrate geometry and propagated position signals by local autocatalytic alignment feedback. To emulate muscle conformation, they generated hydrophilic striped patterns with selective plasma treatment of the surface [237]. Vajanthri *et al.* coated a glass coverslip with hydrophilic OTS and fabricated aligned tracks with a subsequent APTES coating. Hydrophilic APTES hampered cell attachment, which was condensed in the uncovered OTS lines [238].

Differential cell attachment can be achieved using physical topographical cues. Wavy surfaces present elongated grooves where cells are easily laid. After attachment, cells grow towards the “valley” following the less energetic path. As myoblasts proliferate, unidirectional topography is transmitted to the nearby cells resulting in an aligned culture. Aligned topography can be obtained using wrinkled polydimethylsiloxane (PDMS) stamp. This elastomer was subjected to unidirectional strain with subsequent toughening by oxidation. When the tension was released, PDMS autoassembled into a wavy topography [239]. Surface micropatterning was also achieved using soft-lithography techniques. Crosslinkable materials as PDMS and GelMA were poured on top of a solid mold [240, 241]. After crosslinking, poured material replicated the groovy topography

of the mold. The topography of molds can be designed using computer-aided design (CAD) software and transferred to the mold by different techniques as photolithography and 3D printing. Molds have a micrometric accuracy and allow to control the dimensions of grooves and ridges, which notably influenced myoblast alignment, growth and differentiation [242]. Another intelligent strategy to generate aligned patterns was exposed by Velasco-Mallorquí *et al.* In this work, aligned pores of GelMA-CMCMA cryogels were used to drive the proliferation of myoblasts. To that end, they used a unidirectional gradual freeze-drying method that produced tubular pores inside the scaffold [218].

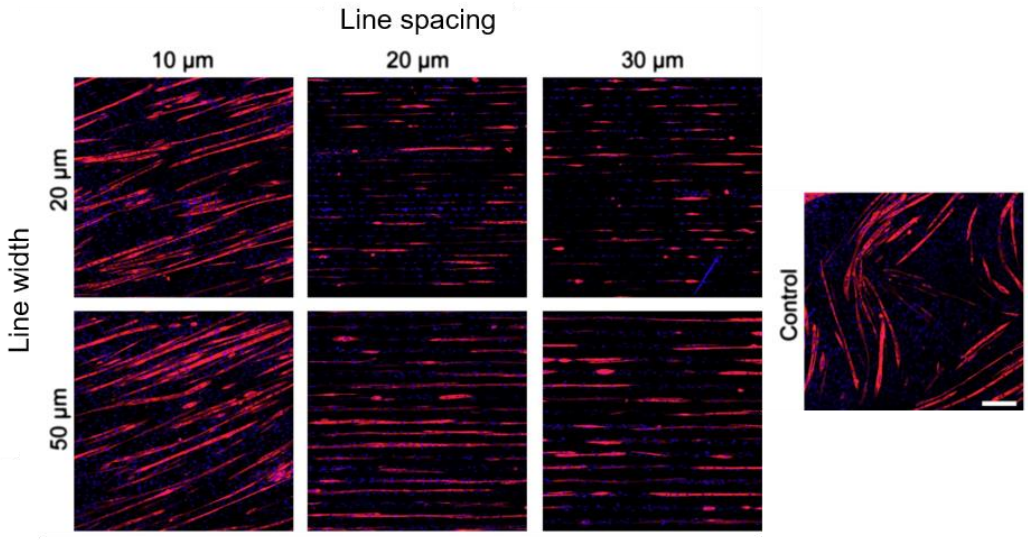

Figure 1.24. Systematic variation of the width and spacing of micropatterned fibronectin (FN) lines resulted in distinct changes in the differentiation and alignment of C2C12 myoblasts into myotubes. FN line width was varied as 20 and 50 µm and line spacing was varied as 10, 20 and 30 µm, with inclusion of an isotropic control. Differentiated myotubes were labeled for MHC (red) and nuclei with DAPI (blue). At the 10 µm spacing, myotubes were able to overgrow the gap between FN lines and form a sheet that was aligned off-axis to the underlying FN pattern. At the larger spacings of 20 and 30 µm, the myotubes remained restricted to the patterned FN area. Scale bar is 200 µm [242].

Although micrometric topographic cues successfully enclosed myoblast into aligned patterns, the scientific community made a step forward to emulate muscle tissue topography. In native tissue, nanometric polymer fibers of ECM are the ones that guide myoblasts towards the contraction axis. To emulate the nanometric aligned topography, many studies used aligned electrospun nanofibers of natural, synthetic and hybrid polymers. To improve the attachment of muscle precursor cells in electrospun scaffolds, PCL was mixed with decellularized bovine muscle ECM, chitosan and collagen [200, 235, 243]. However, PCL scaffolds presented a Young's Modulus in the order of MPa, which is much higher than native muscle stiffness (kPa). McQueen *et al.* developed a methodology to fabricate electrospun scaffolds of gelatin nanofibers [244], and Smoak *et al.* achieved electrospun nanofibers from decellularized muscle ECM [245]. Natural polymers from ECM sources have a better resemblance to native tissue and improved biochemical properties, however, they need strong chemical crosslinking to avoid fast

degradation, which led to higher mechanical properties that exceeded the stiffness of muscle.

Directional topographical cues drive myoblast proliferation towards aligned patterns. These techniques improve cell bundling, fusion and differentiation into aligned fibers. However, they lack the three-dimensional nature of physiological muscle, since scaffolds are fabricated as substrates for the on-top culture of myoblasts.

3.3.2. Micropatterning and micromolding

3D aligned structures of cell-embedded biomaterials can be achieved through micropatterning or micromolding. In these techniques, cells are mixed with uncrosslinked pre-polymers and patterned by photolithography or soft lithography. Prepolymers must be mixed with cells in a liquid state and crosslink after their fabrication to preserve the patterned structure. Therefore, these methods require biomaterials with inducible crosslinking. Furthermore, they must be highly biocompatible and present appropriate physical properties to ensure viability, proliferation and migration of encapsulated cells.

Gelatin, as a product of collagen, contains most of the biochemical signals present in muscle ECM. As a thermosensitive material, it can be found as a liquid at mild temperatures, thus it can be mixed with cells at physiological temperatures. Aubin *et al.* chose GelMA to encapsulate C2C12 mouse myoblasts into striped 3D patterns. Using UV light, liquid GelMA prepolymer was crosslinked across transparent sections of a photomask with lines. Physical confinement of myoblasts in lines forced them to proliferate and align towards the longitudinal axis [183]. Ortega *et al.* combined GelMA with CMCMA to diminish the degradation rate by C2C12. The liquid prepolymer was pressured against a grooved PDMS stamp and irradiated with UV light. GelMA-CMCMA lines promoted the differentiation of myotubes over biosensors to monitor secreted inflammatory factors [269].

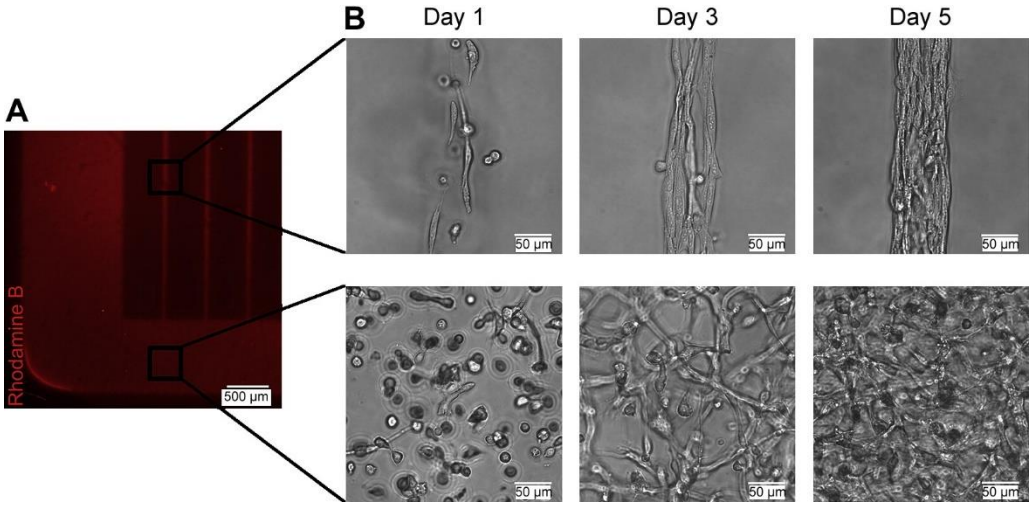

Figure 1.25. Cell morphology and organization as a function of time in patterned and unpatterned 5% GelMA hydrogel microconstructs. (A) Rhodamine B stained GelMA hydrogel construct shows the patterned and unpatterned regions. (B) Representative phase contrast images of 3T3-fibroblasts (10 × 106 cells/mL) encapsulated in patterned (top row) and unpatterned regions [183].

Fibrin is one of the most used biomaterials for muscle engineering due to the high myoblast survival, proliferation and differentiation to fibers. Moreover, crosslinking degree can be controlled by modulating the activity of thrombin. In some studies, fibrin was mixed with commercial Matrigel® to fabricate micromolded engineered muscles [202, 203]. Neal *et al*. used a tube-shaped mold of gelatin and thrombin as a sacrificial material. At physiological temperature, gelatin melted and released thrombin that crosslinked the fibrin bundle from the inner core. In the experiments of Bian *et al*., hydrogel mixture was directly poured on a mesoscopic pillar array. This system generated interconnected biomaterial lines, which was suggested to be advantageous to coordinate muscle contractions.

Cell alignment through micropatterning and micromolding is suitable for highly myogenic soft biomaterials as fibrin and dECMs. They showed fusion of myoblast into multinucleated aligned fibers with sarcomere patterning, indicating that bundles reached an advanced maturation state [202]. However, those techniques have limited scalability, as dimensions are determined by the micrometric structure of molds.

3.3.3. Mechanical stress

One of the most successful methods for the alignment of muscle fibers *in vitro* is mechanical stress or passive tension. This method aims to mimic the strain transmitted from tendons to muscle tissue during growth. As explained previously, unidirectional tension of aligned tendon fibers organizes myoblasts towards the longitudinal axis of contraction. In this case, cells are subjected to an artificial unidirectional tension that induces the alignment of both the polymer fibers that comprise the 3D matrix and the encapsulated cells. Mechanical stress can be

active or passive. In the active form, cyclic strain is applied to 3D engineered muscles. Kim *et al.* used the previously described mold casting into sacrificial materials to obtain muscle bundles that were subjected to different frequencies of cyclic stretching [202]. They demonstrated that 0.23 Hz strain was the most effective condition to enhance the contraction force of muscle bundles [74]. As an alternative strategy, engineered muscles were fixed to dynamic hooks that were connected to a motorized stretching device [223, 246].

Alignment by passive tension is a simple and spontaneous process, thus it is one of the most used methods in muscle engineering. Passive tension is produced by the mechanical forces exerted by the encapsulated muscle cells [247]. Focal adhesions and cell migration movements deform the polymer fibers of ECM. Cell traction forces pull ECM fibers radially, which increment with cell number and results in the contraction of biomaterials. If the matrix is anchored between two opposite points, cell forces will be counteracted by the resistance force of the anchors. As resistance forces are pulling in opposed directions from central mechanical forces, biomaterial fibers are reoriented towards the longitudinal direction of the force. Consequently, muscle fibers are aligned towards the anchored points.

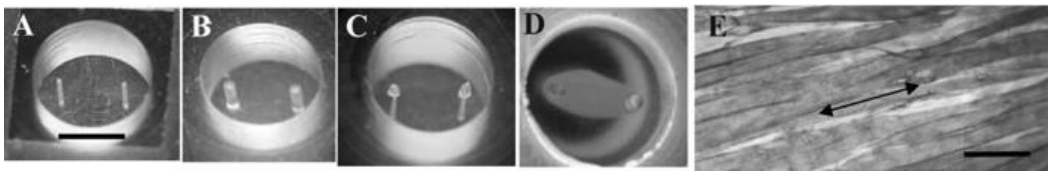

Figure 1.26. Tissue engineering miniature bioartificial muscles (mBAMs) on flexible PDMS microposts. (A) 165-μm radius μposts, scale bar of 4 mm; (B) 350-μm radius μposts; (C) μposts with caps. (D) mBAM at day 4–5 after casting in the 7-mm diameter microwell on 350-μm radius; (E) A 7–8-day-old mBAM whole-mount stained for sarcomeric tropomyosin (dark gray color) showing well-organized myofibers. Double-headed arrow indicates the long axis of the mBAM. Scale bar, 20 μm [248*]*.

To use the passive tension strategy, muscle precursor cells are encapsulated in a hydrogel that is poured over an anti-adherent surface that contains two cell-adherent opposite pillars. As cells proliferate, hydrogel tends to contract towards the core of the culture plate. However, opposite forces of pillars generate a bundle of aligned muscle fibers between them. To achieve this effect, hydrogels must be composed of elastic and soft polymers that allow the deformation of the matrix while bearing the tension without reaching the breaking point. Most biomaterials used for passive tension are mixtures of fibrin or collagen with Matrigel®. In the literature, this method was applied to murine and human cells. Khodabukus *et al.* encapsulated isolated human myoblasts that were successfully differentiated into bundles of aligned muscle fibers [120]. Muscle bundles were contractile and showed sarcomere formations. Regarding the clinical potential of hiPSC, several works used passive tension to achieve differentiated human muscle bundles showing striated morphology and contractility [168, 249]. Some of them developed high throughput platforms with several units of double pillars to do simultaneous testing of human skeletal muscle bundles [249]. Other applications

include soft robotics, where authors took advantage of muscle contractions to act as bioactuators of small mobile robots [172, 250]. To that end, Cvetkovic *et al.* encapsulated C2C12 in a mixture of collagen/fibrin and Matrigel®. The hydrogel was poured between two connected 3D printed posts that formed a "U"-like biobot. Posts provided a uniaxial constrain for muscle alignment while transmitted contraction force to the 3D printed holder. Controlled contractions of biobot resembled the crawling movements of inchworms [172].

Although passive mechanical stress for muscle alignment led to promising engineered muscle models, it must be considered that the used biomaterials, as fibrin and collagen, have poor mechanical properties and fast degradation rates. During muscle fiber growth cells can generate excessive tension and break the bundles. Furthermore, contraction activity facilitates the bundle fracture. Furthermore, this system presents limited control over model dimensions, as bundle dimensions depend on the hydrogel volume and distance between pillars.

3.3.4. 3D bioprinting

Among the numerous techniques to obtain uniaxial structures, 3D bioprinting has gained much attention due to its benefits for skeletal muscle tissue engineering. Bioprinting is used to fabricate complex 3D structures with a controlled deposition of biomaterials. 3D model shape and dimensions are previously designed using computer-aided design (CAD) software, which makes 3D bioprinting automatable, reproducible and scalable. The current bioprinting methods are inkjet-based, light-assisted and extrusion bioprinting. Inject-based bioprinting is used with low viscosity biomaterials (<15 mPa · s) that are deposited as droplets with the help of a heater or a piezoelectric actuator. Light-assisted bioprinting is suitable for photocrosslinkable biomaterials. A pool of soluble prepolymer is crosslinked layer-by-layer after the localized irradiation with light, mainly 365 nm UV light. The height of each layer is limited by the resolution of the used technique, which can be stereolithography appearance (SLA), digital light processing (DLP), liquid crystal display (LCD) and two-photon.

So far, extrusion bioprinting is the most used technique for skeletal muscle engineering. It is low cost and suitable for biomaterials with a wide range of viscosities. Biomaterials are loaded into printing syringes and extruded through a needle with pressurized air. Extrusion bioprinting has several tunable parameters. The size and shape of the printing fiber are determined by the morphology and diameter of the nozzle. However, those parameters are also modified by printing pressure and rate. Despite the versatility of the printing process, biomaterial printability is the key parameter that determines the success of the fabrication.

In terms of extrusion printing, there is a lack of parameters to define the concept of printability, partly because it depends on a set of physical properties that differ among biomaterials [251, 252]. However, it is generally accepted that low printable materials are released as drops through the nozzle and spread in the printing surface, thus resulting in a collapsed and undefined structure. In contrast, highly printable materials faithfully replicate nozzle dimensions, keep the shape

of printing fiber and allow the building of multilayered designs with high definition. This concept was evidenced by Ouyang *et al*., who observed that in thermosensitive polymers as gelatin, fabrication temperature and polymer concentration were key to assess good printable properties. They demonstrated that under-gelled materials were extruded as drops and over-gelation resulted in irregular printing fibers and broken printing pattern [253]. As an attempt to establish a general equation for printability, Paxton *et al.* developed a two-step assessment protocol. The first step was focused on the drop or fiber formation properties of the dispensed material and the layer stacking or merging. In the second assessment, they established a "window of printability" where they analyzed the rheological properties of the biomaterial that matched good printable properties at the first step. One of the main insights of this work was the relevance of polymer concentration in bioink printability [254].

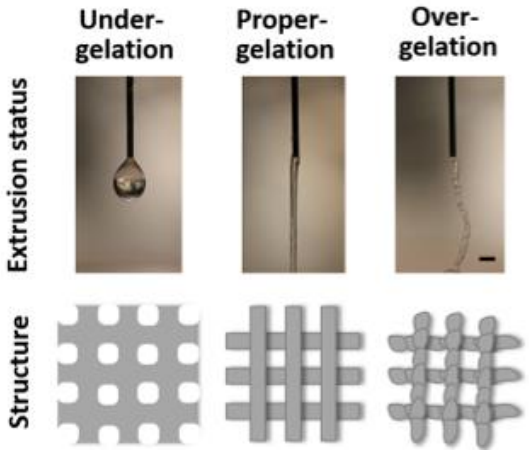

Figure 1.27. Bioink printability assessment under different printing parameter combinations. (A) Evaluation of printability (Pr) under three typical gelation statuses, namely under-, proper- and over-gelation [253].

In those studies, printability was associated with viscoelastic properties [251-254]. High polymer concentrations yield biomaterials with high viscosity and good printability. However, excessive polymer concentration impedes mass transport, cell deposition of ECM and cell proliferation and migration [255]. Furthermore, Blaeser *et al.* demonstrated that high viscous materials increased extrusion pressure and shear stress, which compromised cell viability [256]. In parallel, several studies using 3D bioprinting for skeletal muscle engineering confirmed that controlled shear stress of extrusion printing needle enhanced myoblast alignment towards printing direction [257, 258]. It has been demonstrated that raised pressure in needles incremented shear stress between biomaterial and needle walls, consequently forcing the alignment of polymer fibers towards printing direction and driving uniaxial cell growth [259, 260]. Altogether, biomaterials for biomedical purposes should be defined as *bioprintable.* Meaning that they have suitable printability to build high-resolution 3D models, while they promote cell proliferation and tissue growth. This concept was also defined by Kyle *et al.* as the "biofabrication window" [252].

Most bioprintable materials are based on hydrogels due to their capability to sustain a high viability of encapsulated cells. In 3D bioprinting of muscle models, as in other approaches, the use of fibrin is widely extended. However, like many other soft biomaterials, fibrin lacks the "printable" side. To improve its extrudability, fibrin has been combined with gelatin, HA, and glycerol for implantable human and mouse 3D muscle constructs [261, 262]. Bioink promoted the alignment and differentiation of mouse and human myoblasts into muscle myotubes, whose maturation was completed upon subcutaneous implantation into mice. Despite its benefits for muscle growth, this formulation results in soft bioinks with poor mechanical properties. To achieve defined printing lines, extremely soft biomaterials must be shaped using sacrificial bioinks. Highly printable removable bioinks can be used as molds to shape cell-laden hydrogels. Thermosensitive biomaterials as Pluronic F-127 and gelatin are good sacrificial bioinks [261, 262]. They can be removed by washing steps at the corresponding melting point temperatures. Gelatin was also used as a self-healing material to improve printability of soft materials. To that end, muscle dECM was mixed with C2C12 myoblasts and extruded inside a gelatin pool containing PVA. Gelatin deformed and adapted to the extruded dECM fiber shape, which impeded its expansion and increased the line resolution [198]. Printing inside reservoirs with crosslinking agents induces the immediate crosslinking of extruded bioink, which increases the mechanical stability and avoids the collapse of printed fiber. Kim *et al*. extruded myoblast embedded in collagen bioink into a KCl and Glycine pool to induce collagen fiber assembly [169].

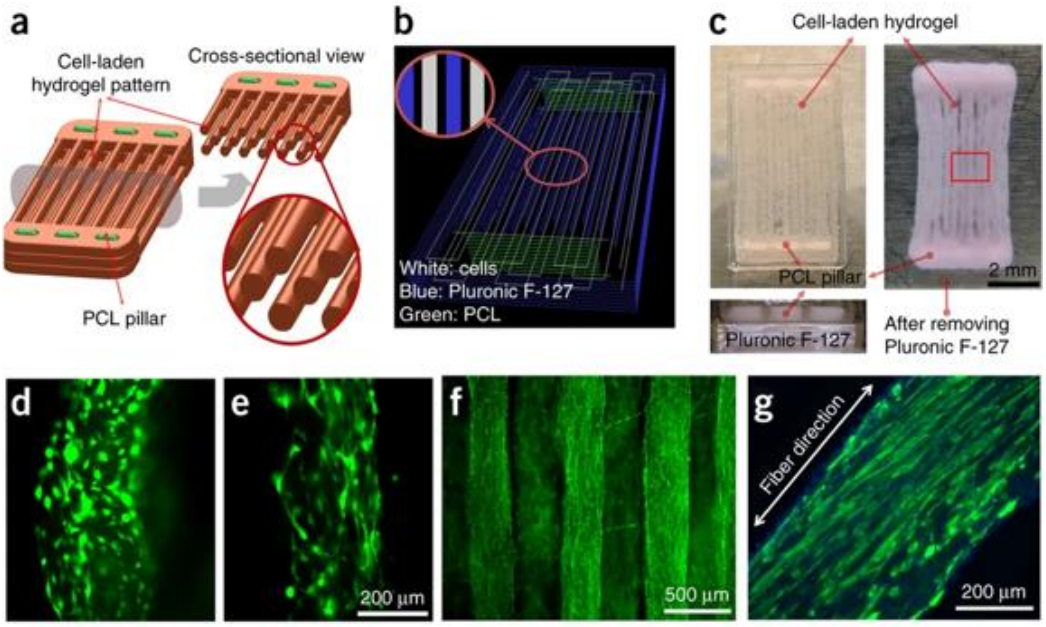

Figure 1.28. Bioprinted skeletal muscle bundles. (a) Designed fiber bundle structure for muscle organization. (b) Visualized motion program for 3D printing muscle construct. Lines of green, white and blue indicate the dispensing paths of PCL, cell-laden hydrogel and sacrificial material, respectively. (c) 3D patterning outcome of designed muscle organization (left) before and (after) removing the sacrificial material (Pluronic F127). The printed construct was cross-linked with thrombin solution to induce gelation of fibrinogen and the uncrosslinked sacrificial material was removed by dissolving with cold medium. Calcein staining of constructs without PCL pillar (d) and with PCL pillar (e and f). (g)

Immunofluorescent staining for myosin heavy chain of the 3D printed muscle organization after 7-d differentiation. The encapsulated myoblasts aligned along the longitudinal direction of the fiber structure [261].

To reduce the volume of sacrificial materials during fabrication and accelerate the crosslinking process, sacrificial materials can be printed together with cell-laden bioinks using coaxial needles. Fast crosslinking bioinks can be extruded in a core needle surrounded by a crosslinker solution. In this way, Costantini *et al*. extruded low viscous alginate solutions that were instantaneously crosslinked in the nozzle with a Ca^{2+} solution. Viscoelastic properties of extruded fibers allowed the deposition of multiple layers with a high definition [257]. Despite the efforts to obtain highly myogenic bioprintable inks, the poor mechanical properties and degradability of soft biomaterials limit their culture time and stability. Furthermore, washing steps of sacrificial materials extend the fabrication time.

Biomaterials with higher viscosity as gelatin have been used as printable sacrificial materials, nevertheless, they can be used as cell-laden bioinks. Myogenic properties, thermosensitivity and photocrosslinkability make GelMA an excellent candidate for the generation of bioprinted skeletal muscle models [186, 263, 264]. Viscoelastic properties of GelMA can be controlled with temperature to achieve highly printable bioinks. An appropriate gelation state ensures the preservation of the nozzle shape in the deposited fibers. Furthermore, extruded GelMA can be photocrosslinked layer-by-layer to avoid fiber merging and decrease the degradation rate. Hence, the printing and crosslinking process of GelMA can be automated by the bioprinter device, offering a more straightforward fabrication of bioprinted muscle models.

3.4.Electrical stimulation in muscle engineering

Skeletal muscle tissue is innervated by afferent and efferent motor neurons. Efferent motoneurons transmit synaptic signals from CNS to muscles. The signal is transmitted by neurotransmitters that induce cell membrane depolarization, which propagates as an action potential and activates muscle contraction. Muscle excitation enhances myoblast differentiation, cytoskeleton organization and function. Hence, contractile activity is key for muscle development and maintenance.

Several attempts have been made to recapitulate the neuromuscular junction *in vitro*. Most of the NMJ models are based on the coculturing or on-top culturing of neuromotors and engineered muscles. Several studies cocultured motoneurons were with engineered muscle on fibrin/Matrigel® hydrogels and stimulated them with glutamate to induce contraction. However, they presented low contraction force, probably due to the early differentiation state of motoneurons [267, 268]. Furthermore, cocultures can result in medium incompatibilities between cell types. As an alternative, motoneurons were genetically modified to be optically excitable. To that end, engineered muscles of collagen/Matrigel and motoneurons were separately differentiated in compartmentalized microfluidic chambers. After neurite outgrowth and neuromuscular junction formation, neuromotors were stimulated with light pulses to induce muscle contraction [75]. This

approach allowed better control over contraction frequency than chemical induction. However, this technique requires the genetic modification of cells and the width and amplitude of light pulses can be difficult to monitor.

Alternative studies used electrical pulses to mimick the neural stimulation. Frequency, pulse width and pulse amplitude (or voltage) can be modulated according to the needs of the *in vitro* system. There is a wide range of electrical parameters in the literature due to the differences in the electrical pulse stimulation (EPS) setup. Potential differential (V) is influenced by system resistance, which can be given by medium conductivity, biomaterial conductivity, the distance between electrodes and electrode geometry. Ortega *et al*. molded engineered muscle lines of GelMA-CMCMA on top of interdigitated electrodes. Due to the proximity of electrodes and biomaterial, they established 5 V and 1 Hz pulses to avoid electrode overburn [269]. Nevertheless, most studies used non-flat electrodes to ensure a homogeneous electrical field in the 3D engineered muscle. Ito *et al.* tested voltages, frequencies and widths ranging from 2 to 10 V, 2 to 10 ms and 0.5 to 2 Hz. They found that electrical pulses of 6 V, 4 ms and 1 Hz in 20 mm wells notably improved muscle contraction force [270]. In a study by Cvetkovic *et al.,* they fabricated swimming biobots with muscle actuators. They used 20 V, 50 ms and 1-4 Hz in 10 mm spaced electrodes, since they observed tetanic contraction in frequencies above 10 Hz [172].

In conclusion, electrical parameters must be adapted according to the EPS system to ensure contraction induction. EPS provides better control of muscle contraction and has demonstrated a beneficial role in engineered muscle differentiation. Khodabukus *et al.* demonstrated that EPS increased fiber size, improved sarcomerogenesis, upregulated expression of sarcomeric proteins and increased force generation [120]. Similarly, Langelaan *et al.* showed improved sarcomerogenesis after EPS, however, they did not observe such upregulation of sarcomeric protein genes. Although EPS improves engineered muscle maturation, medium hydrolysis must be carefully considered, as it can increase the production of ROS and dramatically decrease cell viability. As a solution, several studies used biphasic pulses that alternated the electron flux bidirectionally and diminished the production of reactive species [120, 172].

Chapter 2

Aims of the thesis

Bioprinting is an attractive tool for skeletal muscle tissue engineering due to the automatic deposition of cell-laden bioinks, control of the architecture and dimensions of 3D cultures, enhanced reproducibility and faster fabrication. However, there is a lack of suitable biomaterials that combine good printability properties and advanced tissue maturation. Consequently, most 3D bioprinted skeletal muscle tissue models have been used to fabricate premature implants for *in vivo* assays, where muscle maturation is completed after implantation to treat volumetric muscle loss (VML) [199, 261]. *In vitro* bioprinted muscle models have been mainly used for basic research [186, 262]. However few studies showed improved differentiation and muscle contraction capability [265]. Moreover, none of them used highly printable materials, thus impeding the fabrication of multilayered constructs due to their low viscosity [265, 266]. As a result, the potential applications of current 3D bioprinted models are limited. Indeed, there are no 3D bioprinted skeletal muscle models approved for preclinical applications and disease modeling.

The main goal of the thesis is to develop printable biomaterials to fabricate *in vitro* models of healthy and diseased tissues using 3D bioprinting techniques. This project is focused on recapitulating the physiological conditions of skeletal muscle tissue and neuroblastoma and highlight the advantages of 3D cultures over traditional monolayer cultures. To that aim, the thesis is divided into the following sub-objectives:

I. Development of highly printable biomaterials with tunable physical properties and suitable post-printing stability for the development of *in vitro* engineered tissues.

II. Modulation of the physical properties and composition of GelMA-AlgMA bioink to obtain 3D printed cultures that induce the differentiation of skeletal muscle tissue.

III. Evaluation and improvement of muscle tissue differentiation *in vitro* and validation of the functionality of the bioprinted model.

IV. Analysis of the potential applications of bioprinted muscle as a model to study metabolic alterations like muscle wasting in cancer cachexia.

V. Adaptation of the physical properties and composition of GelMA-AlgMA bioink to develop neuroblastoma models and study the effects of matrix stiffness.

Chapter 3

Methodology

1. Fabrication of photocrosslinkable biomaterials and characterization of the physical properties

1.1. Synthesis of polymer precursors

Gelatin (Sigma-Aldrich, USA) was modified to a 50% and 80% degree of methacrylation [271]. Briefly, gelatin was dissolved in PBS 1X at a concentration of 10% w/v. 1.25% and 5% (v/v) of methacrylic anhydride (Sigma-Aldrich, USA) was carefully added to the solution drop by drop to reach 50% and 80% of methacrylation respectively. One hour later, the reaction was stopped by adding an excess of PBS 1X and dialyzed against Milli Q water with 6–8 kDa MWCO membranes (Spectra/por, Spectrumlabs, USA). Water was changed every 4 h for 4 days. Gelatin methacryloyl (GelMA) was lyophilized and stored at −20 °C. Sodium carboxymethylcellulose (CMC) and sodium alginate (alginate, Alg) (Sigma-Aldrich) were methacrylated at a maximum degree of methacrylation as previously described [207, 272]. The methacrylation reaction was performed by mixing a solution of 1% w/v of the polymer in 50 mM MES buffer at pH 6.5 with 20 mM EDC, 10 mM N-hydroxysuccinimide and 10 mM 2-aminoethylmethacrylate (Sigma-Aldrich). The reaction was stopped after 24 h with the addition of acetone (Panreac, Spain) and filtered using a vacuum flask. The precipitate was dissolved in PBS 1X and dialyzed against Milli Q water with 3.5 kDa MWCO membranes (Thermofisher, USA). Finally, the solutions of methacrylated polymers (CMCMA and AlgMA) were lyophilized and stored at −20 °C.

1.2. Analysis of the degree of methacrylation

For 1H nuclear magnetic resonance, gelatin, GelMA, CMC, CMCMA, alginate, and AlgMA were dissolved in D_2O and analyzed on a Varian Inova 500 (Varian, USA). All samples were measured with a relaxation delay of 1 s for 64 scans.

To perform 2,4,6-Trinitrobenzenesulfonic acid (TNBS) assay, GelMA with 50% and 80% methacrylation degree were diluted in different concentrations. Three samples of each concentration and condition were measured. Five different concentrations of gelatin 10% (w/v) were placed in the well, in a concentration range from 2000 µg/ml to 31,25 µg/ml. Also, 3 samples per concentration were placed. Once all these concentrations were set and placed in the well plate, 50 µL/well of the TNBS 0,01% in bicarbonate buffer was added and incubated for 2 hours at room temperature under agitation. The reaction was stopped with 25 µL/well of HCl 1M. Once the assay was over, the absorbance was read at 335 nm.

The degree of methacrylation was calculated with the following definition:

$$\%\ of\ methacrylation = \left(\frac{Abs_{gel} - Abs_{GelMA}}{Abs_{GelMA}}\right) * 100\%$$

Where Abs_{gel} corresponded to the absorbance of the gelatin at a specific concentration and Abs_{GelMA} to the absorbance of the methacrylated gelatin at a specific concentration.

1.3. Preparation of composite hydrogels solutions

The polymer precursors (GelMA, CMCMA, AlgMA, and PEGDA) were mixed at different concentrations and diluted in PBS 1X containing the photoinitiator. Final concentrations of photoinitiator, either 2-Hydroxy-4′-(2-hydroxyethoxy)-2-methylpropiophenone (I2959) (Sigma-Aldrich) or lithium phenyl (2,4,6-trimethylbenzoyl) phosphinate (LAP) (TCI EUROPE N.V., Belgium) were fixed at 0.4% or 0.1% w/v. Polymer solutions were placed at 40 °C for 1 h to obtain homogeneous solutions. Polymer solutions were prepared to obtain final concentrations of 5% or 1% w/v GelMA and 1% w/v CMCMA, AlgMA, or PEGDA.

For the fabrication of skeletal muscle models, GelMA-AlgMA composite biomaterial was optimized. Stock solutions of LAP photoinitiator were prepared in growth medium and added to final concentrations of 0.05%, 0.02% and 0.01% in w/v%. In those samples containing fibrin, 5 mg/ml of fibrinogen from bovine plasma was added to the mixture and crosslinked with 0.25UI/ml of thrombin from bovine plasma. All hydrogels were fabricated using a 3D bioprinter (3D Discovery BioSafety, RegenHU, Switzerland; 365 nm, 3 W/cm^2) with the UV light source.

1.4. Swelling analysis of composite hydrogels

The prepolymer solutions were prepared as described above. Samples for swelling analysis were prepared by placing 300 µl of the prepolymer solution in a 48 well-plate. After exposing the prepolymer solution to UV light hydrogels were rinsed with PBS and their initial weight was measured. Then, the wet weight was determined after 1, 3, and 7 d in PBS, after a wipe with tissue paper to remove the excess water. The wet weight increase ratio (ΔW) of the hydrogels was determined by the following equation:

$$\Delta W = \frac{W_S - W_i}{W_i}$$

Here, W_i and W_S represent the weight of composite hydrogels after fabrication and the weight after swelling in PBS, respectively. To calculate the mass increase, each water content value was normalized with the initial weight of the sample. Maximum swelling was calculated as the average of swelling values on the plateau region of the swelling curves.

1.5. Degradation kinetics

Hydrogels were fabricated as described above for the swelling analysis. Hydrogels were removed from the 48 well-plate and left swelling for 3 d in a 6 well-plate. A total of 3 mL of 10 UI/ml of collagenase IV (Thermofisher) in PBS was poured on the hydrogels and they were incubated at 37 °C, under 100 rpm shaking conditions. Disks were weighted at different timepoints until their complete degradation. The percent hydrogel remaining (% W_r) was determined by the following equation:

$$\% W_r = \frac{W_t}{W_i} \cdot 100$$

Here, W_t represents the weight of hydrogel composites after collagenase incubation.

1.6. Analysis of the mechanical properties

Uniaxial compression tests of hydrogels were performed using a Zwick Z0.5 TN instrument (Zwick-Roell, Germany) with a 5 N load cell. Hydrogels were fabricated following the same procedure as for the swelling analysis. After reaching equilibrium swelling, cylindrical hydrogels were cut using a 6 mm diameter biopsy punch. Real hydrogel diameters and heights were measured before the experiment. Samples were tested at room temperature up to 30% final strain (deformation), using the following parameters: 0.1 mN preload force and 20% min^{-1} strain rate. Stress-strain graphs were obtained from load-deformation measurements. Values for the compressive modulus were calculated from the slope of the linear region corresponding to 10–20% strain. For each hydrogel formulation, three samples were prepared, and measurements were performed in triplicate.

1.7. Pore size quantification

Cylinder-shaped hydrogels, 10 mm in diameter, were fabricated as described above for pore size quantification. Then, they were left swelling in Milli-Q water for 3 d to reach the same hydrogel architecture as cell encapsulation experiments and be comparable with them After that, dehydration was carried out by sequential immersion in graded ethanol solutions in Milli-Q water: 30%, 50%, 70%, 80%, 90%, and 96% v/v for 5–15 min each and twice for 100% ethanol. Then, samples were placed in the chamber of a critical point dryer (K850, Quorum Technologies, UK), sealed, and cooled. Ethanol was replaced completely by liquid CO2, and by slowly heating. CO2 achieved gas phase equilibrium at 35 °C and 85.06 atm and was slowly drained. This technique allowed dehydration of the hydrogels while avoiding their collapse. After critical point drying, hydrogels were imaged by ultrahigh resolution scanning electron microscopy (Nova NanoSEM 230, FEI Company, The Netherlands) operating in low vacuum mode (0.5 mbar of water vapor pressure). Scanning electron microscopy (SEM) images were used to quantify the pore size distribution using ImageJ free software (http://rsb.info.nih.gov/ij, National Institutes of Health, USA).

1.8. Porosity

Overall porosity was calculated as the percentage of macropore volume over the total volume of the disk, using the following formula:

$$Porosity\ (\%) = \frac{\frac{W_S - W_D}{\rho_{H_2O}}}{\pi \cdot d^2 \cdot h} \cdot 100$$

Where W_S is the weight of the disk at maximum swelling and W_D is the weight of the disk after the removal of the water in macropores. The macropore volume is calculated using

the water density (ρ_{H2O}). The total volume of the biomaterial disk is calculated as the volume of a cylinder, where *d* is the diameter, and *h*, the height.

2. Culture and fabrication of skeletal muscle models

2.1. Cell cultures in monolayer

2.1.1. Skeletal muscle myoblasts

C2C12 myoblasts were purchased from ATCC. They were cultured in growth medium (GM) based on high glucose and glutamine Dulbecco's modified Eagle medium supplemented with fetal bovine serum (10% v/v), penicillin/streptomycin (1% v/v) and sodium pyruvate (1% v/v) at 37ºC with 5% CO2. For differentiation experiments in 2D cultures, medium was switched to DMEM supplemented with calf serum (2% v/v), HEPES buffer (2% v/v), penicillin/streptomycin (1% v/v) and L-glutamine (1% v/v), named as DM. Human skeletal muscle myoblasts (HSMM) were purchased from Lonza (Switzerland). They were cultured in SkBM™-2 basal medium (Lonza) supplemented with SkGM™-2 SingleQuots™ Supplement Pack (Lonza) containing hEGF, dexamethasone, FBS, L-glutamine and gentamicin/amphotericin-b. For differentiation in 2D cultures, the medium was switched to SkBM™-2 basal medium supplemented with horse serum (2% v/v) and penicillin/streptomycin (1% v/v).

2.1.2. Colon cancer cells

For cachexia experiments, LS174T human colon cancer cell line was purchased from ATCC and cultured in EMEM (ATCC) supplemented with FBS (10% v/v) and penicillin/streptomycin (1% v/v). HCT116 human colon cancer cell line was purchased from ATCC and cultured in high glucose with L-glutamine DMEM supplemented with FBS (10% v/v) and penicillin/streptomycin (1% v/v). Both cell lines were expanded to 80% confluency. Then, the medium was changed to C2C12 GM and cells were incubated for 48h. The medium was collected and centrifuged for 10 min at maximum rpm. The resulting supernatant was stored at -20 °C and used as conditioned medium (CM).

2.2. 3D culture of C2C12 myoblasts embedded in casted composite hydrogels

To promote myotube formation, a differentiation medium was used, based on DMEM high glucose and L-glutamine, supplemented with 2% Horse Serum (HS) (Thermofisher) 1% Penicillin/Streptomycin, and 2.5% HEPES (Thermofisher). To fabricate cell-laden hydrogels, one volume of prepolymer solutions of GelMA-CMCMA, GelMA-AlgMA, GelMA-PEGDA and pristine GelMA was mixed with one volume of a suspension of C2C12 cells to a final density of 1×10^7 cells/ml. Blends of prepolymer and cells were

then placed in a cylindrical mold of 6 mm inner diameter and 750 μm height. Cell-laden solutions were photocrosslinked by 5 s or 25 s exposure to UV light at 3 W/cm^2. This was followed by immersion of the cell-laden hydrogels in growth media to remove the unreacted reagents.

2.3. Extrusion bioprinting of C2C12 and myogenic differentiation in composite biomaterials

Prepolymer solutions and C2C12 cell suspension were mixed as previously described to obtain a 5% w/v GelMA solution with or without 1% of either PEGDA, CMCMA, or AlgMA in PBS containing 0.1% w/v LAP. Solutions were introduced in a 3cc printing syringe (Nordson Corporation, USA) and placed in the direct dispensing head of the bioprinter (3DDiscovery BioSafety). All of the printing processes were performed in a cooling chamber at 10 °C. The printing rate was 7 mm/s and printing pressure varied according to the loaded prepolymer solution. 2.5, 2.5, 3, and 5 bar in the case of GelMA, GelMA-CMCMA, GelMA-AlgMA, and GelMA-PEGDA, respectively. To promote myotube formation and alignment, cell-laden hydrogel architecture was designed as an array of 20 filaments in a 16 mm diameter circle (BioCAD v1.0 software, regenHU Ltd., Switzerland), and converted to computer-aided design (CAD) files. CAD files were opened in the 3D DISCOVERY HMI software interface (regenHU Ltd., Switzerland). Constructs were made by the extrusion of two layers, through a nozzle of 200 μm inner diameter, and then were photocrosslinked by a 5 s exposure to UV light (365 nm) into a 6 well-plate. After that, hydrogels were immersed in the growth medium and changed three times to remove unreacted reagents. After 5 d, growth medium was switched to differentiation medium.

2.4. Bioprinting and differentiation of mouse and human ring models

Previously prepared GelMA-AlgMA biomaterial mixtures were tempered to 37ºC and mixed with C2C12 or HSMM to a final density of $10 \cdot 10^6$ cels/ml and $15 \cdot 10^6$ cels/ml respectively. Biomaterials with encapsulated cells were loaded in 3 cc bioprinting syringes (Nordson, USA) and placed in the extrusion head of the 3D Discovery bioprinter (RegenHU, Switzerland). Ring-shaped models of 4.5 mm diameter and 5 layers were designed with BioCAD software. CAD files were transferred to 3D DISCOVERY HMI software interface. Rings were printed using 200 μm inner diameter tips (Nordson) at 2 bars pressure, 18 °C and 2 mm/s printing rate. Each layer was photocrosslinked for 4 seconds of UV light. Crosslinked rings were immediately submerged in growth medium and changed after 24h to remove the unreacted products. Medium was changed daily. For differentiation in 3D cultures, C2C12 and HSMM were maintained in complete growth mediums, unless specified otherwise.

3. Biological characterization of skeletal muscle models

3.1. Cell viability

3.1.1. Multifactorial analysis to assess cell viability in different fabrication conditions of pristine GelMA

The alamarBlue assay (Thermofisher) was performed by following the manufacturer's protocols. A multifactorial screening was assessed to test the synergic effect of GelMA concentration, photoinitiator concentration of both I2959 and LAP, and UV exposure time, on the cell viability. Prepolymers were prepared at 1% or 5% w/v of GelMA. Photoinitiators were used at 0.1% and 0.4% w/v. Cell-laden hydrogels (20 µl amounts) (10^6 C2C12 cells mL^{-1}) were poured into wells of a 96 well-plate. After UV exposure, samples were rinsed with growth medium to remove unreacted reagents and cultured for 24 h. Then, samples were incubated with alamarBlue solution at 10% v/v in growth media for 3 h at 37 °C. Finally, the absorbance was read at 570 nm (λ1) and 600 nm (λ2). The percentage of reduction (cell viability) was determined by the following equation:

$$\%\, Reduction = \frac{(\varepsilon_{OX})\lambda_2 \cdot A\lambda_1 - (\varepsilon_{OX})\lambda_1 \cdot A\lambda_2}{(\varepsilon_{RED})\lambda_2 \cdot A'\lambda_1 - (\varepsilon_{RED})\lambda_1 \cdot A'\lambda_2} \cdot 100$$

Here, ε_{OX} and ε_{RED} represent the molar extinction coefficient of alamarBlue oxidized form. A and A', represent the absorbance of the samples and the negative control, respectively. Statistical comparison was performed using a 24 ANOVA multifactorial analysis by StatGraphics Centurion software.

3.1.2. C2C12 survival in GelMA based composite hydrogels

The viability of C2C12 cells encapsulated in GelMA-CMCMA, GelMA-AlgMA, GelMA-PEGDA and pristine GelMA was studied after 1 and 7 d using the live/dead assay kit and Hoechst (Thermofisher). Fluorescence images were captured using confocal microscopy (TCS SPE, Leica, Germany) and processed by MATLAB software (Supporting Information). Survival percentage was calculated as the fraction of living cells in respect to the total cell number. Additionally, cell morphology within the hydrogels was studied through the immunostaining of nuclei and filamentous actin (F-actin). For this purpose, hydrogels were fixed in 10% formalin solution (Sigma-Aldrich) 7 d after fabrication. Then, hydrogels were washed with PBS and cells were permeabilized with Block-Perm solution: 0.2% v/v Triton X-100 (Sigma-Aldrich) and 1% w/v BSA (Sigma-Aldrich) in PBS for 1 h. Afterward, hydrogels were washed in PBS and incubated in 100 nm Rhodamine Phalloidin 480 (Cytoeskeleton, USA) solution overnight. After washing with PBS, nuclei were counterstained with DAPI (300 nm, Thermofisher) for 15 min. Hydrogels were mounted and stored at 4 °C before observation by confocal microscopy.

3.1.3. Mouse and human myoblast viability in GelMA-AlgMA-Fibrin bioprinted rings

Bioprinted muscle rings were cultured for 3 days and stained for 30 minutes at 37°C with LIVE/DEAD® Viability/Cytotoxicity Kit for mammalian cells (Thermofisher). Rings were washed twice with DPBS 1X and images were immediately acquired with LSM 800 confocal microscope (Zeiss, Germany). Live and dead cell percentages from 400 µm width stacks were calculated using FIJI free software. Live/Dead images were used to study the morphology of the cells and determine the adhesion to the biomaterials. Cell contour was thresholded and circularity degree was calculated with particle analyzer macro of FIJI. Frequency distribution histograms were generated with Prism (GraphPad Software Inc., USA).

3.2. Myotube alignment and fusion index analysis

Z-stack images obtained by confocal microscopy were processed using ImageJ software. Myosin heavy chain (MHC) staining was used for the analysis of the fusion index and myotube alignment. Myotube alignment was assessed by measuring the angle formed between the myotubes and the longitudinal axis of the printed pattern. The fusion index was calculated by dividing the number of nuclei within the myotubes by the total number of counted nuclei and this was expressed as a percentage. Three samples for each condition were used and more than 100 myotubes were analyzed for each sample.

3.3. Study of myoblast proliferation

Bioprinted rings with encapsulated myoblasts were cultured in growth medium for 8 days. The medium of the rings differentiated with the 2D culture protocol was switched to DM, while those rings following the new differentiation protocol were maintained in GM. Rings were collected on days 1, 3, 6, 8, 10, 13 and 15, washed 3 times with DPBS 1X and weighted. Rings were digested in a solution of papain (0.25% UI/ml, Worthington Biochemical Corp., USA), L-cystein (0.24 mg/ml, Sigma) and EDTA (2mM, Sigma) in DPBS 1X for 1h at 65 °C under orbital shaking. λ-DNA standard curves and samples were diluted in TE Buffer 1X and 100 ul were added to 96-well plate (black flat bottom, Corning Inc., USA). Dilutions were reacted with 100 ul of Quant-iT PicoGreen® dsDNA kit reagent (Thermofisher). Fluorescence was measured with Infinite M200 PRO Multimode Microplate reader (Tecan, Switzerland). The µg/ml of DNA of a known number of myoblasts was calculated to obtain the number of cells per ml. To avoid the effect of the ring size variability, samples were normalized by the ring weight, and proliferation was represented as the number of cells per gram of biomaterial.

3.4. Characterization of muscle differentiation

3.4.1. Study of the protein expression by fluorescence immunostaining

Bioprinted muscle rings were differentiated for 13 days in culture. Rings were fixed for 30 minutes with 4% formaldehyde solution in DPBS 1X, followed by blocking and permeabilization in FBS (10% v/v), BSA (2% w/v) and Triton X-100 for 1h. Myosin heavy chain and α-actinin were stained with MF20 (1:500, Thermofisher) and ACTN2 (1:250, Thermofisher) primary antibodies in 1:1 DPBS1X and blocking-permeabilizing solution overnight at 4°C. Primary antibodies were conjugated with Alexa Fluor donkey anti-mouse 568 (1:100, Thermofisher) and Alexa Fluor goat anti-rabbit 647 (1:500, Thermofisher) in 1:1 DPBS1X and blocking-permeabilizing solution overnight at 4°C. Subsequently, samples were stained with Cytopainter Phalloidin-ifluor 488 (1:1000, Abcam, UK) and Hoescht 33342 (1:1000, Thermofisher) for 1.5h at room temperature, followed by 3 washing steps in DPBS1X. Fluorescence images were acquired with a confocal microscope. F-actin coverage was calculated with FIJI.

3.4.2. Analysis of the genetic expression by RTqPCR

To study the transcriptomic profile of 2D and 3D cultures, samples were mechanically homogenized in TRIzol™ Reagent (Thermofisher). RNA was extracted by chloroform (Sigma) phase-separation protocol and precipitated with 2-propanol (Sigma), followed by ethanol (Sigma) washing steps and dissolution in nuclease-free water (Sigma). cDNA retrotranscription was performed using Ready-To-Go You-Prime First-Strand Beads (GE Healthcare, USA) and random primers (Thermofisher). Polymerase chain reaction (PCR) solutions were prepared with PowerUp™ SYBR™ Green Master Mix. Genetic expression was analyzed with StepOnePlus™ Real-Time system (Applied Biosystems, USA) and fold expression was calculated as $2^{\Delta C_{\tau Control} - \Delta C_{\tau Sample}}$. Human and mouse primer sequences detailed in Table 1 were extracted from PrimerBank Database (https://pga.mgh.harvard.edu/primerbank/).

Table 1. PrimerBank ID numbers of primers used for RTqPCR experiments.

Gene	PrimerBank ID
m-*Rpl7*	31981515a1
m-*Myf5*	6678982a1
m-*Myod1*	6996932a1
m-*Myog*	162287254c3
m-*Actn2*	31981445a1
m-*Tnnc2*	6678371a1

m-*Myh4*	67189166c2
m-*Myh1*	26334227a1
m-*Myh2*	21489941a1
m-*Myh7*	18859641a1
m-*Fbxo32*	13385848a1
m-*Trim63*	21523717a1
m-*Fbxo31*	31981581a1
m-*Fis1*	13384998a1
h-MYF5	156104905c1
h-MYOD1	77695919c1
h-MYOG	115387121c1
h-ACTN2	161377421c3
h-MYH4	110611902c1
h-MYH1	115527081c2
h-MYH2	153792662c3
h-MYH7	115496168c3

4. Study of the functionality and metabolic alterations of skeletal muscle fibers in bioprinted rings

4.1. Electric stimulation system

Muscle rings were anchored in bioprinted silicon pillars. To fabricate the pillars, DOWSILTM 1700 Clear W/C (DOW Inc., USA) silicon was prepared and loaded into 3cc bioprinting syringes. The stimulation platform was composed of 4 pillars aligned in the vertical axis of each well of a 6-well cell culture plate (Thermofisher). Pillars of 5 x 1 mm and 5 layers were printed at equal intervals in 24 x 24 mm glass slides with 580 µm tips, 2 bar pressure and 2mm/s printing rate at room temperature. Coverslips with pillars were crosslinked overnight at 60ºC and then placed into 6-well plates. Differentiated muscle rings were fit and immobilized in the pillars. C-dish covers (IonOptix, USA) were used for electric stimulation. C-dish was connected to LPA05 amplifier (N4L, UK) that received the signal from WW5061 waveform generator (Tabor Electronics, Israel). Signal was monitored with DSO3062A Oscilloscope (Agilent Technologies, USA). Muscle rings were stimulated 1h during 3 consecutive days with 20V, 1Hz and 2ms biphasic square pulse (**Figure 2.*1***.). Contraction amplitude was obtained from recorded life videos and calculated using MUSCLEMOTION macro [**¡Error! No se encuentra el origen de la referencia.**] in ImageJ software.

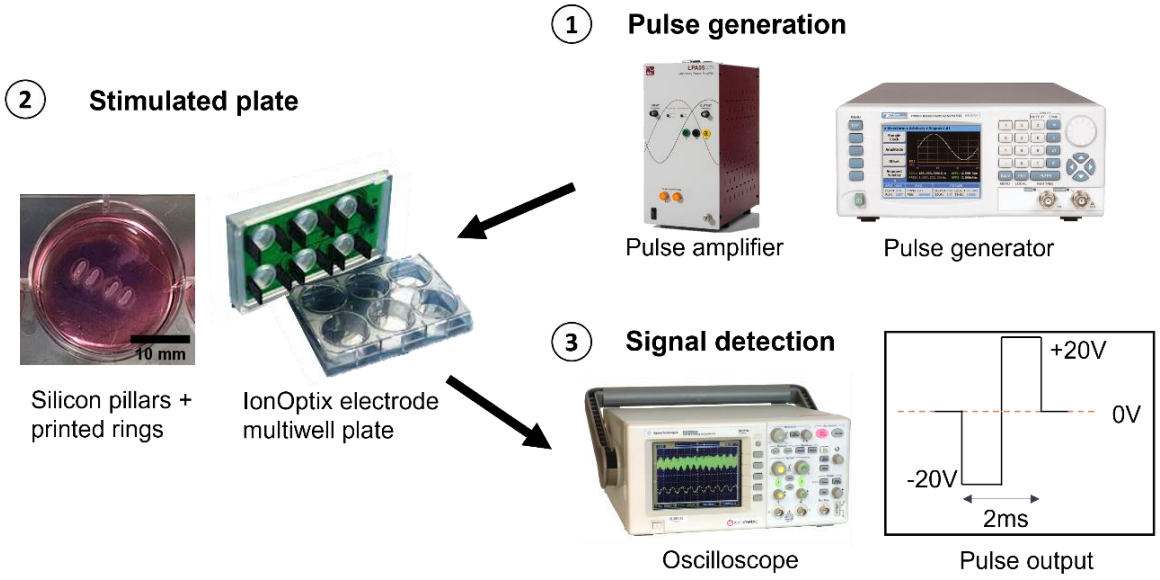

Figure 2.1. Schematic diagram of the electrical pulse stimulation system (EPS). (1) Biphasic square pulses are generated and amplified x10. (2) The signal is transmitted to the electrodes attached to the lid of a 6-well plate. On each well, 4 silicon pillars hold bioprinted rings with encapsulated muscle precursor cells. (3) The output signal in the plate is monitored with the oscilloscope.

4.2. Effect of EPS and aminoacid (AA) supplementation in protein synthesis

Bioprinted rings with encapsulated C2C12 were differentiated in GM. Once muscle fibers were formed, the medium was changed to RPMI (Gibco, Thermo Fisher) supplemented with AA-depleted FBS at t= 0 min. At t= 45 min, EPS was activated in the corresponding samples and stimulated for 1h. When completed (t=105min), the medium was changed to fresh RPMI or RPMI supplemented with AAs. Rings were incubated for 15 minutes and immediately washed with PBS 1X and fixed in 4% formaldehyde for 45 minutes. Samples were embedded in paraffin by the histology department of the Parc Científic de Barcelona. Deparaffination and antigen retrieval in citrate buffer was performed by the histopathology unit of the Centro Nacional de Investigaciones Oncológicas (CNIO). Afterward, immunostaining was conducted at the metabolism and cell signaling group of the CNIO. Briefly, samples were permeabilized in 0.5% Triton X-100 for 2h and blocked in 2% BSA for 2h at RT. Slides were then incubated O/N at 4°C in anti-Phospho-S6 Ribosomal Protein (Ser235/236) 1:200 (CST, USA). Finally, slides were stained with Alexa-Fluor goat anti-rabbit 1:300 for 2h at RT and with DAPI 1:5000 for 20 min at RT.

The composition of aminoacid supplementation is not provided due to property rights.

4.3. Extracellular flux analysis

Extracellular flux analysis assay was conducted in a Seahorse XFe24 flux analyzer at the department of Biochemistry and Molecular Biology of the Universitat de Barcelona. XFe24 sensor cartridges were calibrated overnight at 37 ºC in Seahorse XF calibrant solution. Bioprinted muscle fibers were rinsed with Seahorse XF calibrant solution supplemented with 25 mM glucose and 2mM L-glutamine adjusted to pH 7.4. Rings were placed in the bottom of Seahorse XFe24 culture microplates and fixed for 15 minutes at 37 ºC with 50 µl of Matrigel® (Corning Inc.). Fixed rings were washed again and incubated for 1h at 37 ºC on supplemented Seahorse medium. For the metabolic flux assay, solutions of 5 µM Oligomycin, 0.5 µM FCCP and a mixture of 2 µM Antimycin and 1 µM Rotenone were prepared, all purchased from Sigma. For data normalization, mtDNA and gDNA were extracted using PureLink™ Genomic DNA Mini Kit (Invitrogen). The mtDNA/gDNA ratio of each sample was analyzed with RTqPCR at the department of Biochemistry and Molecular Biology of the Universitat de Barcelona.

To evaluate the effect of anti-inflammatory compounds, differentiated bioprinted muscle rings were acclimated to 5mM D-glucose (Sigma-Aldrich) complete DMEM for 24h. Then, rings were treated with 150 µg/ml of plant extract (PE) and 1.3 µg/ml of isolated active ingredient (IAI) for 24h in low glucose medium. Extracellular flux analysis and data normalization were performed as described above using 1 µM of FCCP. To exclude values of non-cellular oxygen consumption, bioprinted rings with dead cells were used as blanks. The chemical names of compounds are not specified due to property rights.

4.4. Development of skeletal muscle models for cancer cachexia

4.4.1. *In vivo* models

In vivo models were developed in the department of Translational Oncology at the Instituto de Investigación Hospital 12 de Octubre (i+12). Male C57BL/6J mice, 6-8 weeks old, were obtained from Charles River RMS Spain and used in this study. The Bioethical Committee of the Universidad Autónoma de Madrid and the competent authority approved the experimental protocol. All animal manipulations were made following the European Union guidelines. Mice were maintained on regular dark-light cycle, with free access to food and water during the whole experimental period. After 2 weeks of local animal care facility adaptation, animals were randomly divided into two groups: Control inoculated mice and tumor-bearing mice.

In tumor cells inoculation, B16F10 melanoma cells were cultured in RPMI 1640 medium (Gibco) supplemented with 10% fetal bovine serum (HyClone) and antibiotic (Lonza) at 37ºC and 5% of CO_2. For inoculation, cells were removed from culture flasks by adding 0.05% of trypsin solution, centrifuged and re-suspended in sterile PBS to obtain a solution containing $1x10^6$ cells/ml. Cell viability was determined by trypan blue exclusion. Finally, C57BL/6J mice were subcutaneously injected with a solution of $5x10^4$ cells in a final volume of 100 µl (50 µl of cell

solution mixed with 50 µl of Matrigel- Corning), into the right flank. As a negative, control mice were inoculated with 50 µl of PBS mixed with 50 µl of Matrigel.

Animals were monitored at least three times a week for body weight, tumor dimensions and health condition and euthanized 24 days after tumor cells inoculation. The day of sacrifice, blood was withdrawn from anesthetized mice (using sevoflurane) by cardiac puncture and collected in heparinized tubes, then centrifuged (1,500 g, 10 min 4ºC) to obtain plasma. Quadriceps were rapidly excised and frozen in liquid nitrogen.

4.4.2. *In vitro* models

In vitro models were developed using both C2C12 monolayers (2D) and bioprinted muscle rings (3D). As explained in section 2.1.2., colon cancer cells were expanded and cultured in C2C12 growth medium for 48h at 80% of confluency. Afterward, conditioned medium (CM) was collected, centrifuged and stored at -20 °C. To obtain CC *in vitro* models, differentiated fibers in 2D and 3D were cultured in cancer cells-conditioned medium (CM) and control medium for 72h.

4.5. Analysis of soluble inflammatory factors in conditioned mediums

The composition of inflammatory factors secreted by HCT116 and LS174T cell lines was studied using the Human Inflammation Array C2 from RayBiotech (USA). Membranes were incubated with the CM collected after 72h following the commercial protocol. To analyze the concentration of TNFRI in plasma of tumor-bearing and healthy mice, samples were diluted 1:10 and incubated in Mouse sTNFRI ELISA Kit (RayBiotech) as described by manufacturers.

4.6. Extracellular vesicles isolation and treatment of bioprinted rings

The supernatant of LS174T and HCT116 colon cancer cells were collected as explained previously, except that GM was supplemented with 10% of exosome-depleted FBS (Gibco). Microvesicles and exosomes were collected with ultracentrifugation steps by the Microenvironment and Metastasis group of CNIO. LS and HCT yielded 1.01 µg/µl and 0.55 µg/µl of protein respectively in isolated exosomes. The size of LS and HCT exosomes was characterized, which presented 183 nm and 130 nm average diameters. 10µg of exosomes protein were labeled with SYTO™ RNASelect™ green fluorescent (Invitrogen) during 30 min at 37°C/5% CO_2 at a final dye concentration of 10 µM. Exosome Spin Columns (MW 3000) (Invitrogen) were used to remove unincorporated dye from exosome labeling. The same volume of PBS without exosomes was also treated with SYTO RNA and Exosome Spin Columns to serve as a control. 10 µg of labeled exosomes in PBS, or the same volume of PBS as control, were incubated with monolayer cultures of differentiated C2C12 myotubes for 2h at 37°C/5% CO2. To evaluate the effect

of exosomes in the gene expression of differentiated fibers, 10 μg of exosomes were directly incubated without labeling step. In this case, exosome incubation was prolonged to 72h, after, the genetic expression was analyzed by RTqPCR as described previously.

5. Fabrication and analysis of neuroblastoma bioprinted models

5.1. Neuroblastoma cell culture

SK-N-BE(2), SH-SY5Y human NB cell lines were chosen from a variety of available cell lines, since MYCN-amplified and ALK-mutated tumors represent 64% of high risk neuroblastoma (50 and 14%, respectively). SK-N-BE(2), SH-SY5Y cell line was acquired from American Type Culture Collection (ATCC, Manassas, VA, USA). NB cells were expanded in supplemented IMDM medium (Gibco, Life Technologies, Waltham, MA, USA) at 37°C and 5% CO_2 atmosphere. Two-dimensional cell cultures were grown in 8-well Cell Culture Slides (SPL Life Sciences, Waltham, MA, USA), until they reached 60% confluence before immunocytochemistry (ICC) analysis. Bioinks for 3D culture were formed by mixing SK-N-BE(2) or SH-SY5Y cells with the prepolymer solution at 37 ◦C to a final suspension of 2×10^6 cels/ml. Hydrogels were cultured from 2 to 12 weeks in supplemented IMDM medium replaced every 2 or 3 days before immunohistochemistry (IHC) analysis, which was performed at the Translational Research of Pediatric Solid Tumours group of the Instituto de Investigación Sanitaria INCLIVA.

5.2. Bioprinting of neuroblastoma models

To encapsulate neuroblastoma cell lines, GelMA-AlgMA biomaterial was used. Prepolymer solutions were placed at 50 °C overnight to obtain homogeneous solutions. Prepolymer solutions were prepared to obtain final concentrations of 5% w/v GelMA and 0%, 1% and 2% w/v AlgMA according to the desired initial stiffness level (the higher the alginate percentage, the stiffer the hydrogel).

To create the bioinks, cells were cultured and trypsinized. The resulting pellet was resuspended with the prepolymer solution at 37 °C to a 2.5×10^6 cell density. The bioink was loaded in a bioprinting syringe and gelled at −20 °C for 3 minutes before printing. All hydrogels were fabricated using a 3D bioprinter (3DDiscovery BioSafety, regenHU, Switzerland; 365 nm, 3 W/cm^2) polymerized with a UV light source as previously explained. Cell-laden gelled bioinks were printed applying an air pressure extrusion system, using a 150 μm nozzle. The bioprinter generated 0.4 mm spaced bioink rows to make 5 × 5 mm layers. Successive layers were photocrosslinked by 5 s exposure to UV light at 3 W/cm^2 and printed perpendicularly to generate a 1 mm-high 5-layer network. Next, hydrogels were immersed in growth media to remove unreacted reagents, and then cultured for 2 and 4 weeks before analysis.

5.3. Paraffin embedding, histochemical analysis and optical microscopy quantification

Histochemistry of samples and analysis was performed by the group of translational research of pediatric solid tumors of INCLIVA (Valencia). Hydrogels were collected and placed in Tissue-Tek Paraform biopsy cassettes (Sakura Finetek, USA), fixed in 4% formaldehyde and automatically embedded in paraffin (Leica EG1150H; Leica Microsystems; Wetzlas, Germany). Paraffin-embedded samples were cut into 3 μm sections. Hematoxylin-eosin staining (HE) was performed for morphology. Automated IHC and ICC stains (Autostainer Link 48; Dako, Glostrup, Denmark) using anti-Ki67 (prediluted), anti-PTBP1 (dil. 1/400), anti-Bax (dil. 1/50) and anti-Bcl2 (prediluted) antibodies, all from Dako (Agilent Technologies, USA), were quantified by optical microscopy. For IHC and ICC markers, cells stained in blue indicated negative cells while brown staining was considered a positive result. Samples were examined and interpreted using the following criteria: - Negative (<1% positive cells); + Low positive (1–20% positive cells); ++ Intermediate positive (20–50% positive cells); +++ High positive (>50% positive cells). Ki67 was analyzed automatically using Pannoramic Viewer (PV) software (3DHISTECH), and their number of positive cells was determined by applying the NuclearQuant module. HistoQuant module of PV was applied in VN-stained sections to obtain the areas of each VN intensity expression. All data obtained from PV modules were validated with the pathologist's morphological assessment of the digital image. Digitally obtained data and subsequent pathologist evaluation differed by only 5–10%.

6. Statistical analysis

All data collected were presented as the mean ± standard deviation (SD) using GraphPad Prism software (GraphPad, USA). A p-value lower than 0.05 was considered statistically significant. Data is presented as mean ± SD, *p-value < 0.05, **p-value < 0.005 and ***p-value < 0.0005 in column t-test, one-way and two-way ANOVA.

Chapter 4

Results and analysis

1. Development of lasting photocrosslinkable bioinks to fabricate 3D *in vitro* models by extrusion bioprinting methods

1.1. Fabrication and characterization of GelMA bioinks and its combination with CMCMA, AlgMA and PEGDA

To ensure the formation of homogeneous biopolymer matrices and reduce the fabrication time, the crosslinking method was unified. To that end, gelatin, alginate and cellulose were chemically modified with methacrylic groups to obtain photocrosslinkable materials.

Nuclear magnetic resonance (NMR) confirmed the presence of methacrylic groups in alginate (Figure 3.1**¡Error! No se encuentra el origen de la referencia.**) and cellulose (Figure 3.2), whose percentage was assumed to be 45% and 25% [207,272], as stated in previous work. Gelatin methacrylation was modulated to obtain 53% and 82% degrees, which was confirmed by TNBS colorimetric assay.

GelMA was used as the main component of composite biomaterials, thus its composition and fabrication were optimized according to cell viability and stability of the structure. Cell viability was measured with alamarBlue reduction signaling that indicated the cell metabolic activity (Figure 3.3). GelMA methacrylation degree did not show significative effect. GelMA concentration was set to 5% (w/v). It was found that higher concentrations compromised cell viability and required higher printing pressure at a printing temperature of 18°C. Sometimes resulted in overgelled bioinks that clogged the printing nozzle. Although concentrations lower than 5% initially presented higher viability, their fast degradation rates resulted in their complete dissolution after 3 days in culture. 5s UV exposure time was necessary to obtain fully crosslinked hydrogels and avoid cytotoxicity, since higher exposure times dramatically decreased cell viability. Photoinitiator concentration also had a significant impact on cell viability, thus 0.1% was chosen as the lowest concentration of I2959 that yielded crosslinked hydrogels. However, 0.1% I2959 resulted in poor crosslinked hydrogels with low stability. To evaluate the efficacy of different photoinitiators, I2959 crosslinking dynamics were compared with LAP. The extinction coefficient of LAP at 365 nm UV light is notably higher than I2959, therefore, hydrogels showed higher crosslinking degree and stability, however, viability was reduced.

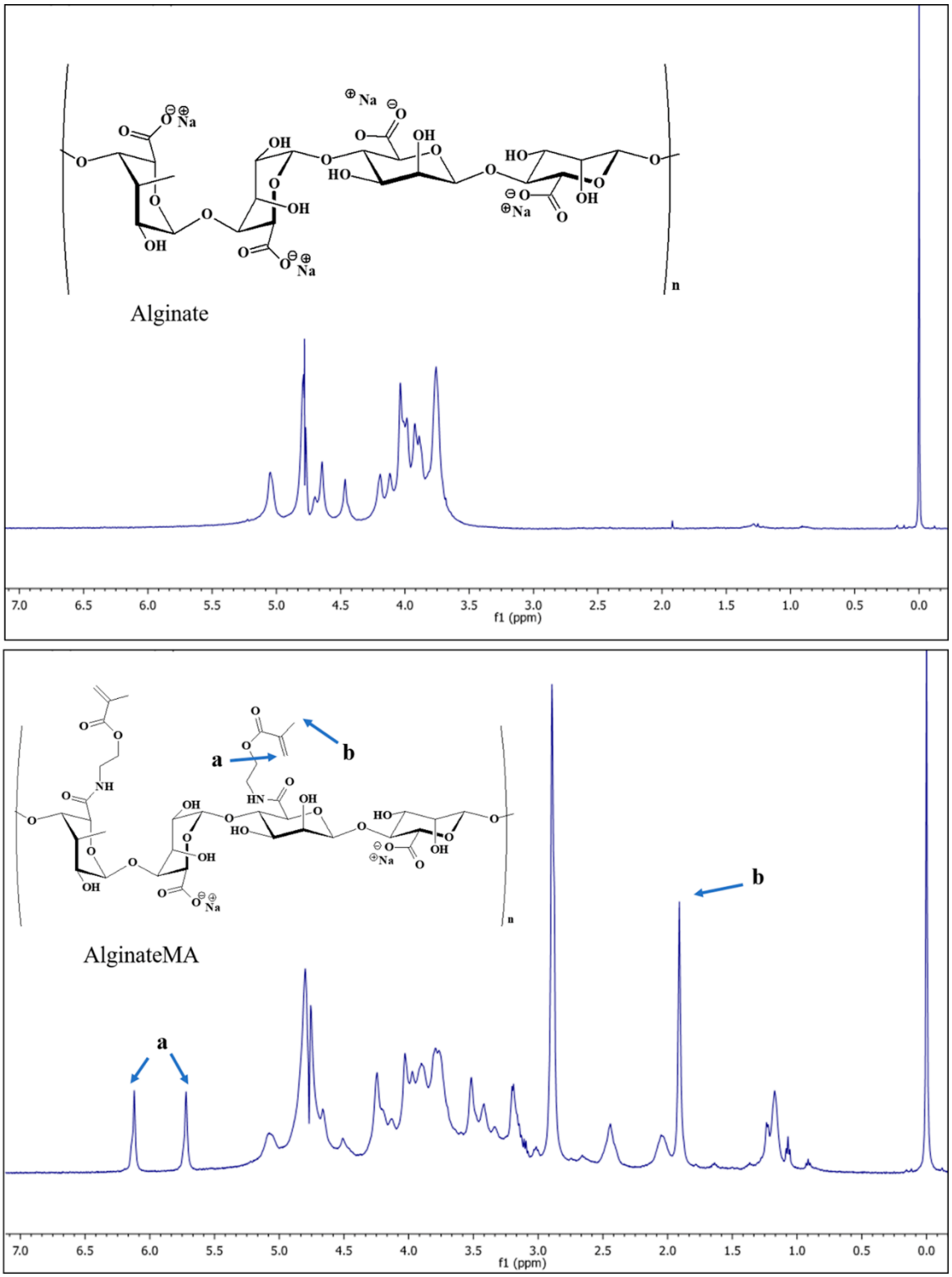

Figure 3.1. ^{1}H NMR spectra of methacrylated alginate and alginate without chemical modification in D_2O.

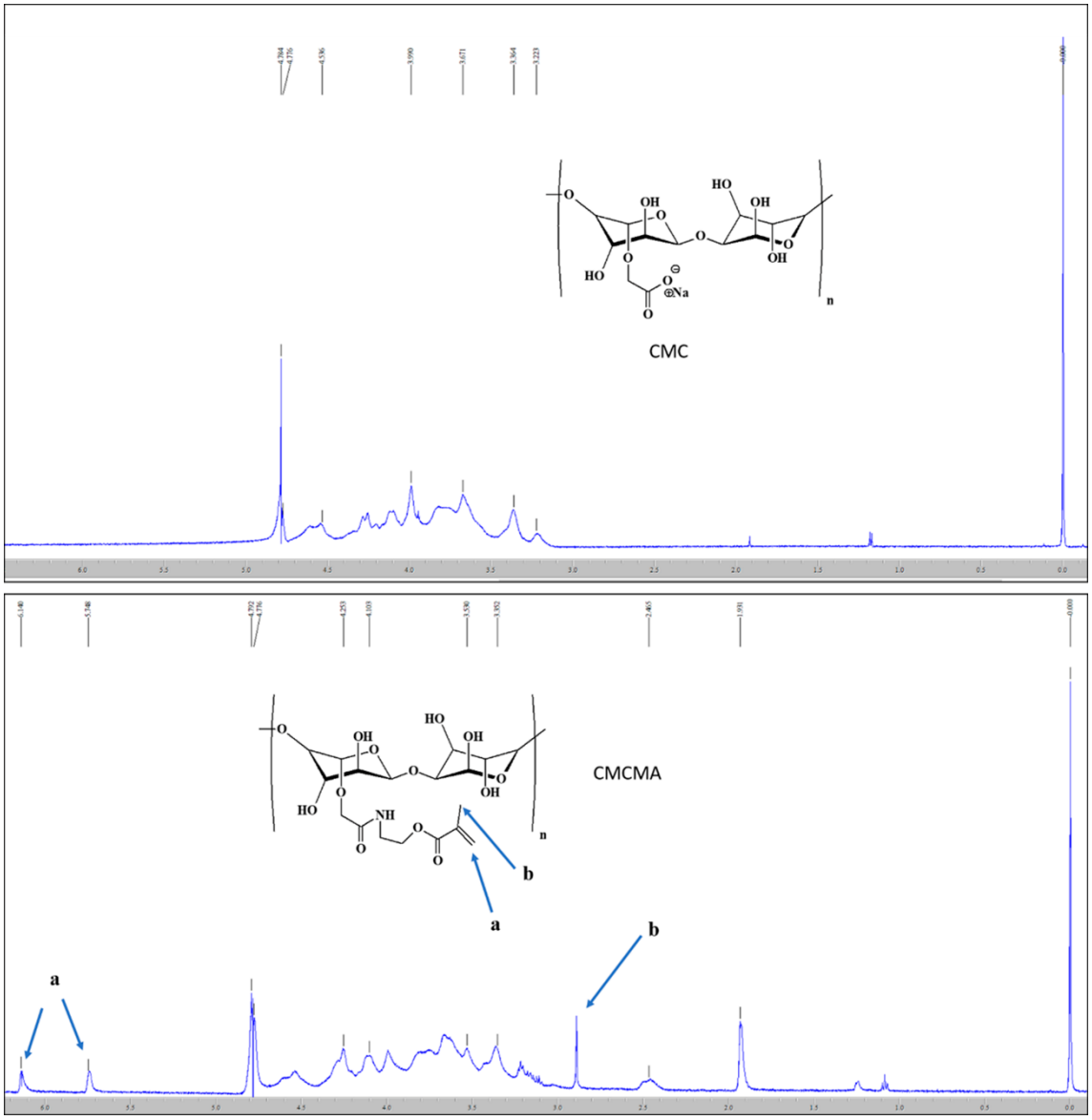

Figure 3.2. ^{1}H NMR spectra of methacrylated CMC and CMC without chemical modification in D_2O.

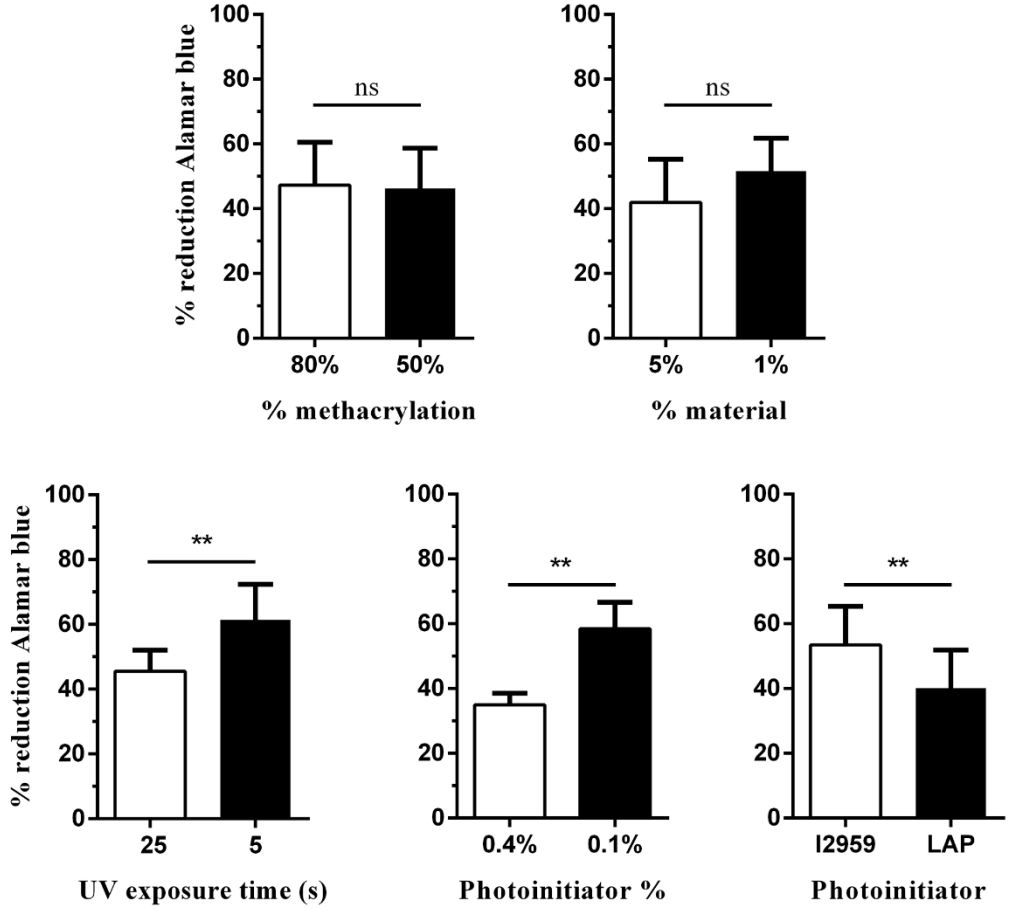

Figure 3.3. Setting of photocrosslinking parameters. Effect of % of methacrylation, GelMA concentration (% material), UV exposure time, photoinitiator concentration, and photoinitiator type on the C2C12 viability. Cell viability was examined using the alamarBlue test. Values are represented as percentage reduction (mean ± SD, t-test **p-value < 0.01, n = 12).

Composites of 5% GelMA with 1% AlgMA, CMCMA and PEGDA supplemented with 0.1% LAP resulted in turgid 3D structures after 5s of UV light exposure (Figure 3.4a, up). In contrast, composites photocrosslinked with I2959 showed collapsed structures with poor reproducibility of the 3D structure (Figure 3.4a, down). Secondary polymers provided GelMA with different physical properties. Swelling of composite biomaterials was higher than pristine GelMA, where GelMA-CMCMA and GelMA-AlgMA reached the highest values, followed by GelMA-PEGDA and GelMA (Figure 3.4b). The degradation rate of swelled composites by collagenase was significantly slowed down Degradation rate increased as follows (Figure 3.4c): GelMA-AlgMA < GelMA-PEGDA < GelMA-CMCMA < GelMA. The stiffness of composites was strongly influenced by the type of photoinitiator and UV exposure time (Figure 3.4d). In general terms, GelMA-AlgMA was presented as the stiffest material, followed by GelMA, GelMA-PEGDA and GelMA-CMCMA. Samples with I2959 photoinitiator showed significantly lower stiffness. Indeed, 5s UV exposure time resulted in poorly crosslinked hydrogels with Young's modulus below 1 kPa. When those samples were photocrosslinked for 25s, the stiffness increased at least by two-fold. LAP photoinitiator yielded well-cured hydrogels after 5s of UV light. GelMA-AlgMA showed the highest

compressive modulus (5.53 ± 2.01 kPa). GelMA-PEGDA (2.89 ± 0.46 kPa) and GelMA (3.02 ± 1.13 kPa) presented similar stiffness and GelMA-CMCMA was the softest biomaterial (1.96 ± 0.16 kPa). When hydrogels were irradiated for 25 s, GelMA-AlgMA compressive modulus was increased to 9 kPa and GelMA to 4 kPa. The stiffness of GelMA-PEGDA and GelMA-CMCMA was not significantly changed.

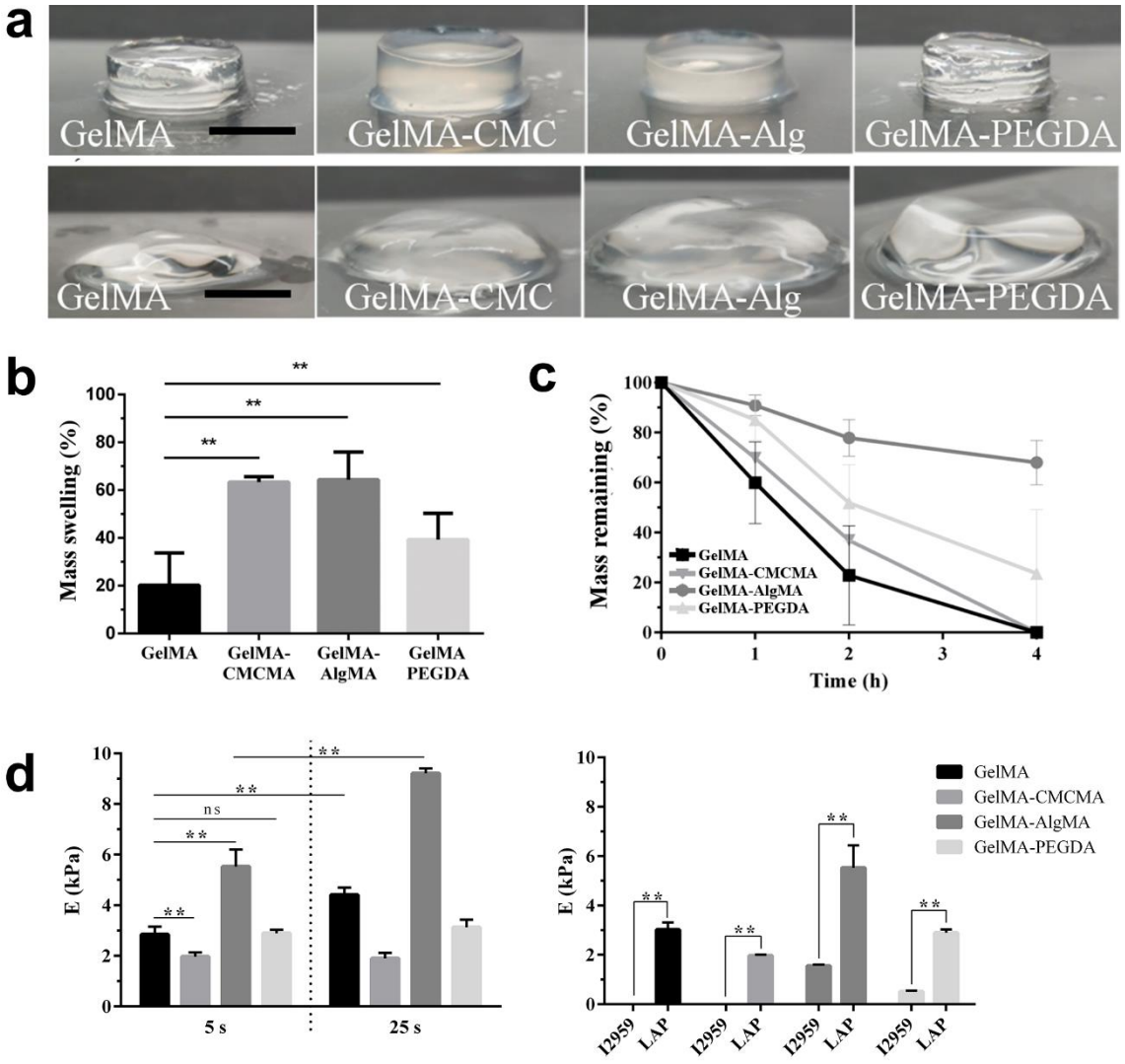

Figure 3.4. Physical properties of composite biomaterials. a) Disc-shaped hydrogels after 5 s of UV light exposure fabricated using LAP (up) and I2959 (down) photoinitiators. b) Maximum swelling values of composite biomaterials in mass % reached after 24h (mean ± SD, One-way ANOVA, **p-value < 0.01, n = 6). c) Percentage mass of the remaining profile showing the effect of the composite on the decrease in the wet weight of hydrogels (mean ± SD, n = 4) incubated in a 1.5 U mL−1 collagenase type II solution. d) Characterization of the mechanical properties of the composite hydrogels. Young's moduli of GelMA and the three composites photocrosslinked with I2959 and LAP for 5 s and 25 s (mean ± SD, Two-way ANOVA, **p-value < 0.01, n = 3).

The pore size of composite hydrogels was analyzed using SEM (Figure 3.5a). The images revealed that the fibrillar structure of the gelatin was not affected by the addition of the other polymers. These images were therefore used to determine the pore size

distribution. Among the different composite hydrogels, no significant differences were found in the range of the small pores (<20 nm). However, GelMA-PEGDA hydrogels showed a significant reduction in the number of pores with diameters > 200 nm ($5 \cdot 10^5$ nm^2) (Figure 3.5b). GelMA-PEGDA hydrogel presented a homogenous structure in terms of pore sizes and pore distribution. The structure is more packed as we can see in Figure 3.5a, and the total amount of pores > 200 nm was below 0.05% of the total pores, thus pore area distribution frequency was significantly lower.

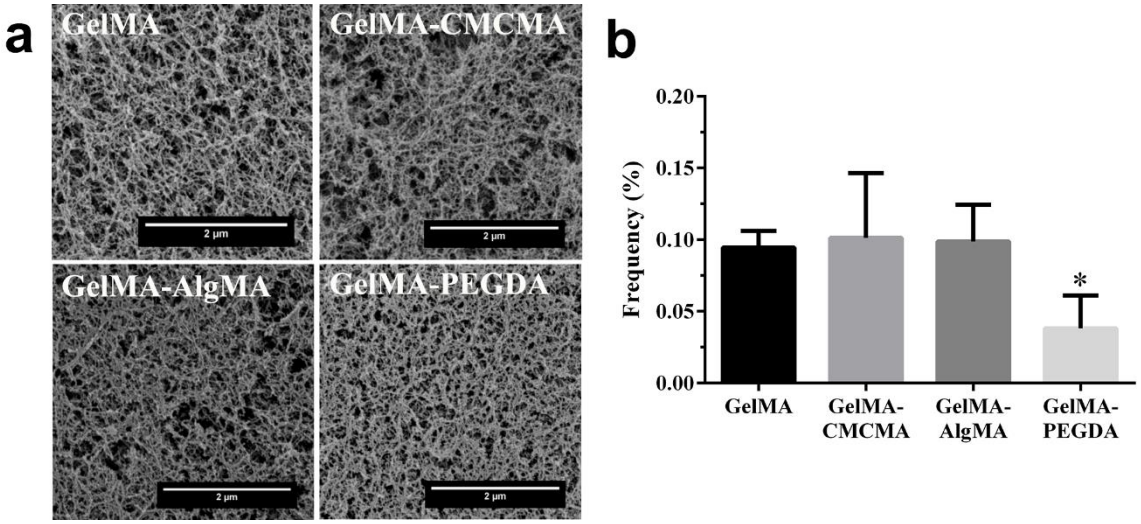

Figure 3.5. Porosity of composite biomaterials. a) Scanning electron microscopy (SEM) images of GelMA, GelMA-CMCMA, GelMA-AlgMA, and GelMA-PEGDA. b) The fraction of pores above 200nm from the total pore population, expressed as percentages (mean ± SD, One-way ANOVA, *p-value < 0.05).

In this study, the first experiments were focused on the fabrication and characterization of the main component of composite biomaterials, the GelMA. High and low methacrylation degrees of gelatin were studied. TNBS assays confirmed that 50% and 80% of methacrylation were achieved, which was in concordance with the results obtained by Nichol *et al*. [273].

As gelatin methacryloyl (GelMA) presented many adjustable parameters, the first experiments were focused on the setting of material %, UV exposure time, photoinitiator %, type of photoinitiator and methacrylation % based on the viability of C2C12 mouse myoblasts and bioink printability.

Previous studies showed that GelMA concentrations above 5% (w/v) compromised cell viability and proliferation [257]. In agreement with those experiments, alamarBlue reduction results indicated that cell viability was not significantly affected in samples with 1% and 5%. However, it was found that 5% GelMA provided optimum printability at 18 ºC, while lower concentrations yielded under-gelated structures [274].

The methacrylation degree of GelMA did not have negative effects on cell viability, thus the lowest degree of substitution was chosen to preserve the highest number of native motifs. UV exposure time, photoinitiator concentration and type of photoinitiator were

the most relevant factors for cell viability. Many works reported that long-wavelength (365 nm) UV light did not induce genetic mutations [275]. However, parallel studies demonstrated that long exposure times can decrease cell viability [276]. Discrepancies between studies may be due to variability in UV light setup specifications, which provide different UV light dosages (mW/cm^2). Indeed, some studies attributed cell death to the heat produced after long exposure times [277].

Using the UV light system of RegenHU 3D discovery bioprinter, it was determined that the limit dosage time of UV exposure was below 25 s, since it dramatically decreased cell viability. To diminish the collateral effects of UV light, 5s was set as the minimum time to obtain crosslinked GelMA hydrogels. However, using I2959 photoinitiator instead of LAP resulted in poorly stable and collapsed GelMA structures after 5s of UV light. The extinction coefficient of LAP at 365 nm is much higher than I2959 [278]. Therefore, LAP provided a higher crosslinking degree with a lower concentration, which was of great interest considering the negative effect of photoinititator (PI) concentration in cell viability. It was found that increasing PI% from 0.1% to 0.4% (w/v) severely decreased cell viability. Photoinitiator cytotoxicity has been associated with the formation of toxic monomers after UV-light exposure [279], thus 0.1% was established as the minimum concentration of LAP to obtain crosslinked hydrogels of 5% GelMA after 5s of UV light exposure.

1.2.3D bioprinting of composite biomaterials with embedded C2C12 mouse myoblasts to obtain highly aligned muscle fibers *in vitro*.

In the literature, composite biomaterials based on gelatin showed reduced cell confluence when combined with more than 1% (w/v) of the secondary polymer [280]. Together with the results obtained previously, composite biomaterials for this study were formulated with 5% GelMA, 1% of the secondary polymers (AlgMA, CMCMA and PEGDA) and 0.1% LAP.

To study myoblast viability and behavior in composite biomaterials, C2C12 immortalized myoblasts were encapsulated, poured into 6mm diameter PDMS molds and exposed for 5s to UV light (Figure 3.6a). Live/dead assay at day 1 revealed that GelMA-CMCMA and GelMA-AlgMA achieved the 80% of viability found in pristine GelMA between 0 and 100 µm deepness. In contrast, GelMA-PEGDA viability was reduced to 30% (Figure 3.6b).

To evaluate cell migration and morphology after 7 days in culture, F-actin and nuclei were stained (Figure 3.6c). Confocal images revealed dense cultures of elongated C2C12 in GelMA, GelMA-CMCMA and GelMA-AlgMA, suggesting that cells proliferated, migrated and established new cell-cell contacts. In contrast, C2C12 confluency in GelMA-PEGDA hydrogels was very low and they mostly showed round morphology. In casted hydrogels, structures deepness had a significant effect on cell viability. It was found that viability was dramatically reduced in structures of 100-300µm thickness (Figure 3.6b). C2C12 viability in GelMA and GelMA-AlgMA was 20% lower, while in

GelMA-CMCMA suffered a 10% of reduction and viability in GelMA-PEGDA was not altered.

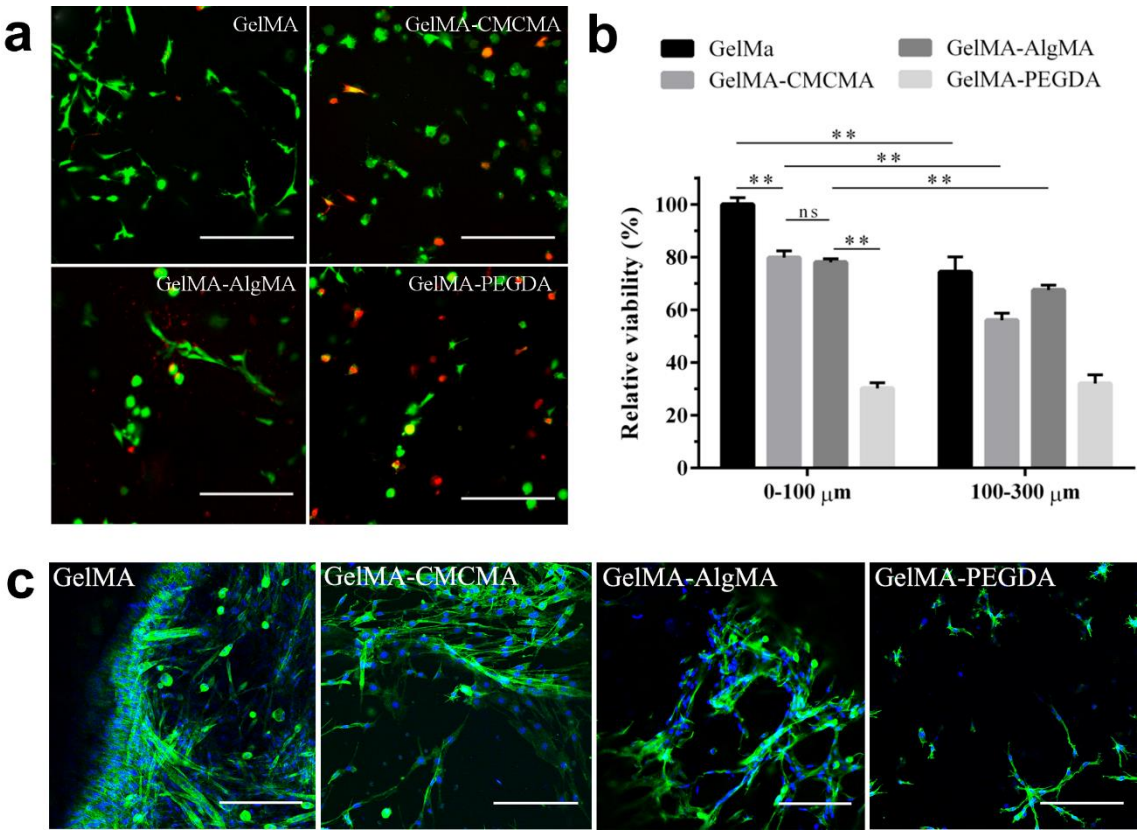

Figure 3.6. C2C12 viability and proliferation in the composite hydrogels. a) Representative images of the live/dead staining (dead in red and live in green) in the range of the first 100 µm depth. b) Cell viability in composite hydrogels represented as the living cells over the total cell number (mean ± SD, Two-way ANOVA, **p-value < 0.01) relative to GelMA hydrogels. c) Confocal microscopy pictures of C2C12 cells inside composite hydrogels. F-actin in green and nuclei in blue. Scale bar = 200 µm.

GelMA-AlgMA, GelMA-CMCMA and GelMA-PEGDA were tested as bioinks for skeletal muscle tissue models. To achieve a relevant height (about 200 µm) two layers were printed (Figure 3.7a). Printing fidelity was evaluated as the percentage change in width, compared to nozzle inner diameter (Figure 3.7b). After printing, filament width was expanded about 30% concerning the nozzle inner diameter, but this fact did not impair the fabrication of isolated filaments. With this method, bioprinted structures were successfully made using GelMA, GelMA-CMCMA, GelMA-AlgMA, and GelMA-PEGDA. Filaments of ± 200 µm in height and about 250 µm in width were achieved (Figure 3.7a).

C2C12 cells were cultured in growth medium until high confluence was reached (5 days) and then, growth medium was switched to a differentiation medium. After 11 days, GelMA scaffolds were nearly flat, and the structure was lost, due to the cell activity (degradation) while the composite hydrogels preserved their 3D structure. To observe the

morphology of the cells and distribution in the hydrogels, cells were stained with phalloidin, DAPI and anti-myosin heavy chain (MHC) (Figure 3.7c). In all cases, C2C12 cells were able to proliferate embedded in the composites and displayed myotube formation. The analysis of protein expression by immunostaining showed that MHC was present in all the constructs, indicating that composite biomaterials supported the differentiation of C2C12 myoblasts in the bioprinted pattern.

The effect of the 3D structures on guiding cell alignment was confirmed by the analysis of myotube orientation (Figure 3.7d). Patterned composite hydrogels exhibited unidirectional orientation of myotubes instead of a random, unorganized mesh as seen in the images obtained from the unpatterned hydrogels (Figure 3.6c). In contrast to pristine GelMA, three composites increased myotube alignment to 85%, which were oriented towards printing direction (Figure 3.7e). Wider filaments (400 µm) showed a significant decrease in cell alignment in the core of printed fibers, while cells in the contour kept the alignment towards the printing direction.

To evaluate the quality of differentiation in the patterned scaffolds, the fusion index was determined as the percentage of nuclei associated with myotubes compared to the total number of nuclei in each sample (Figure 3.7f). C2C12 fused into myotubes in GelMA hydrogel after 11 days of culture. GelMA-CMCMA, GelMA-AlgMA and GelMA-PEGDA also promoted myogenesis. Furthermore, the fusion index of those composites was slightly higher than GelMA. However, GelMA-PEGDA showed a lower number of myotubes. As previously mentioned, GelMA 3D structures tended to degrade after several days, due to cell metabolism, making it difficult to find significant 3D areas comparable with the scaffolds made of composite materials.

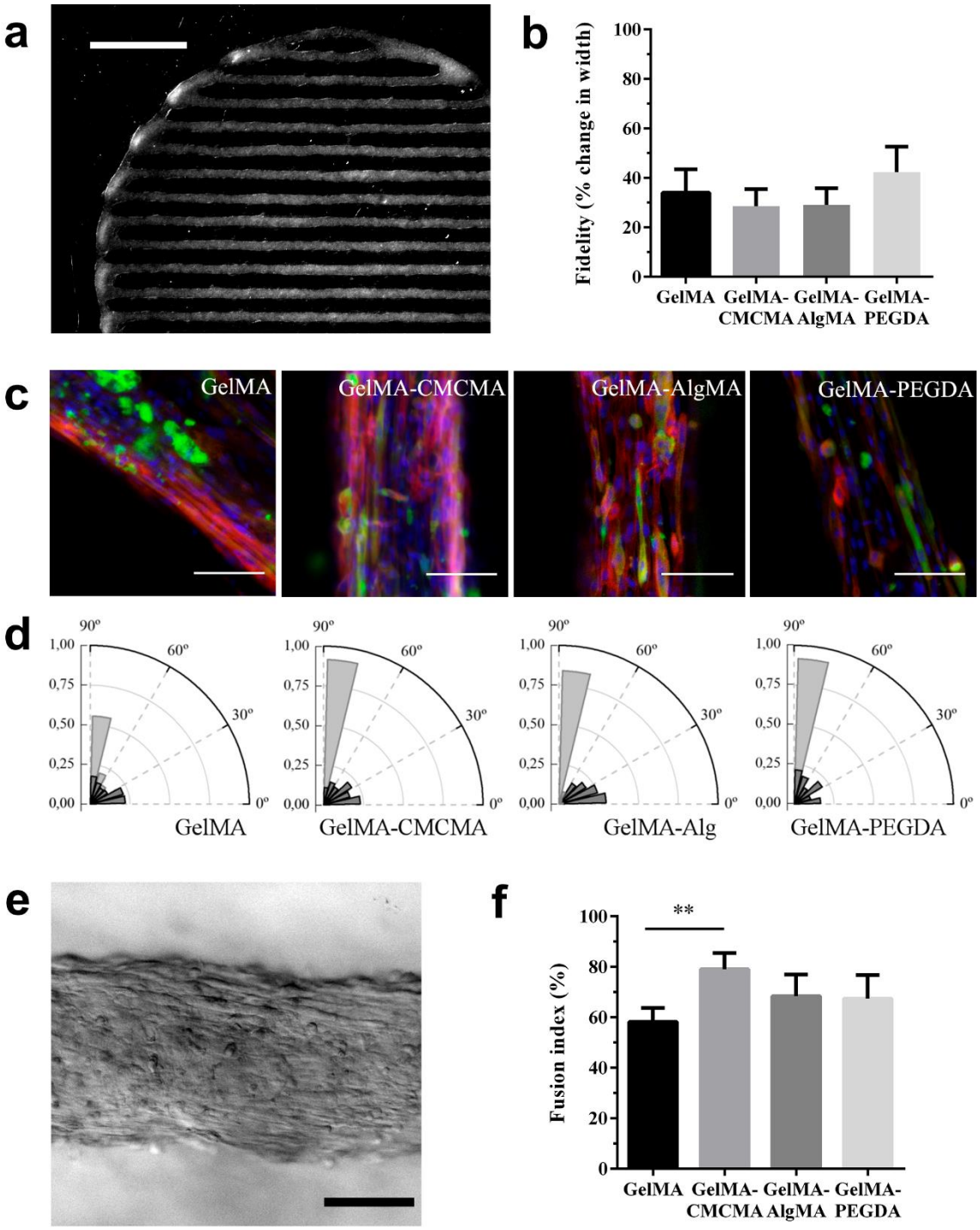

Figure 3.7. C2C12 myotube formation in bioprinted composite hydrogels. a) Example of the top view image of the bioprinted composite hydrogels after fabrication. Scale bar = 2 mm. b) Percentage change in width of composite hydrogels after printing compared to nozzle inner diameter (mean ± SD, One-way ANOVA). c) Confocal microscopy pictures of C2C12 cells encapsulated in the composite hydrogel structures after 11 days of culture. F-actin in red, MHC in green, and nuclei in blue. Scale bar = 200 µm. d) Normalized histograms (bin = 10°) depicting the distribution of the angles between cell cytoskeleton fibers (light gray) inside non-patterned hydrogels (dark gray) and in 3D printed hydrogels. C2C12 inside the bioprinted hydrogels show high degree of alignment (>75%) following the pattern direction, while inside cylinder-shaped hydrogels are randomly distributed. e) Bright-field image of elongated cells encapsulated in composite hydrogel

after 11 days in culture. Scale bar = 200 µm. f) Fusion index percentage (mean ± SD, **p-value < 0.01) of the C2C12 myotubes encapsulated in the bioprinted composite hydrogels.

Composite biomaterials modified the physical properties of pristine GelMA. They increased the biomaterial resistance to the enzymatic activity of matrix metalloproteinases. Among the three composites, GelMA-AlgMA showed the lowest degradation rate. In this line, GelMA-AlgMA presented the highest compressive modulus (5.53 ± 2.01 kPa). The higher stiffness of GelMA-AlgMA could be caused by the ionic crosslinking of alginate with the divalent cations of the medium [204]. GelMA-PEGDA did not significantly change GelMA stiffness, while GelMA-CMCMA decreased the compressive modulus. CMCMA was the biomaterial with the lowest methacrylation degree, which probably reduced the number of CMCMA-CMCMA and GelMA-CMCMA bonds. Furthermore, the presence of a poorly crosslinked interpenetrating network can hamper GelMA crosslinking [281], resulting in softer biomaterials.

It was found that UV exposure time and photoinitiator type significantly influenced biomaterial stiffness. In general terms, I2959 yielded softer biomaterials, while longer UV exposure times yielded stiffer composites. Those results suggested that biomaterial stiffness could be modulated by changing the crosslinking time and the type of photoinitiator.

Alginate, cellulose and polyethylenglycol are highly hydrophilic biopolymers. When combined with GelMA, they increased the water absorbance at maximum swelling. Altogether, each composite showed different physical properties, which could be suitable to develop different types of *in vitro* models. Furthermore, photocrosslinkable materials provide high tunability, since several parameters as UV exposure time, material composition, type of photoinitiator and its concentration can be modulated to achieve the properties of interest.

Crosslinked composites demonstrated different physical properties, however, all of them demonstrated high printability. Bioprinting process was performed at 18 °C, which was set as the suitable temperature for the printing of 5% GelMA according to similar studies [282]. The addition of a secondary material did not compromise GelMA printability, which allowed the fabrication of straight lines with minimal variation in width due to post-printing expansion.

To evaluate the suitability of composite biomaterials as bioinks for skeletal muscle tissue engineering, C2C12 mouse myoblasts were encapsulated and printed. Similar to previous reports of GelMA [274], composite biomaterials supported the attachment and proliferation of muscle precursor cells. Myoblasts differentiated into multinucleated myotubes with upregulated expression of myosin heavy chain (MHC). MHC is overexpressed during myogenesis to form thick filaments. Therefore, high expression of MHC indicated that GelMA-AlgMA, GelMA-CMCMA and GelMA-PEGDA supported the differentiation of muscle myoblasts. Indeed, faster degradation of pristine GelMA resulted in a lower fusion index due to the instability of 3D cultures.

The alignment of muscle fibers is essential to recapitulate the architecture of skeletal muscle tissue. Confocal images of bioprinted muscle cultures revealed an alignment

efficacy of 85% towards printing direction. The printing of thicker lines decreased the alignment efficacy in the core, suggesting that, in needles with inner diameters >200µm, the shear stress effect was more relevant in the outline. The morphology of the cell culture is also influenced by the spatial patterning shape in an autocatalytic manner [237]. During proliferation, cells near the geometric outline are aligned by contact guidance, which transmits the orientation to the nearby cells that followed the same alignment pattern. However, the highest biomaterial line widths slowed down the pattern shape transmission from the outline to the core. Aubin *et al.* showed that micromolded GelMA lines above 100 µm presented unaligned morphology [183]. Nevertheless, it is important to consider that using needles with an inner diameter lower than 200 µm can compromise cell viability due to increased pressure and shear stress [283, 284]. In our experiments, the combination of bioprinting shear stress with needle diameters of 200 µm achieved highly defined lines that kept the viability and alignment of myoblasts.

Although composite biomaterials showed differentiated skeletal muscle fibers, they presented diminished viability in comparison with pristine GelMA. It was seen that hydrogels with more than 5% (w/v) GelMA decreased cell spreading and viability [273]. In concordance with those studies, results indicated that viability decreased by 20% after the addition of 1% of CMCMA and AlgMA. It was studied that the increment in polymer concentration resulted in scaffolds with lower porosity, which reduced cell viability and proliferation, increased hypoxia and hampered differentiation [124,285]. Therefore, changes in the lower cell viability could be caused by a reduced porosity due to higher material concentration. SEM images revealed a significant decrease in GelMA-PEGDA pore size, whose viability was dramatically dropped down to 30%. Most of the protocols to fabricate PEGDA yield more than 90% of acrylation degree, which provides a high number of potentially photoactivable bonds, while CMCMA and AlgMA only yielded 25% and 45%. Some studies demonstrated that a high number of acrylic groups increased crosslinking degree and reduced porosity and cell viability [286]. Therefore, the significant reduction in pore size of GelMA-PEGDA could be due to a combination of increased material content and a higher crosslinking degree. Consequently, GelMA-PEGDA composite biomaterial was the less suitable candidate for skeletal muscle tissue engineering. Despite GelMA-AlgMA and GelMA-CMCMA allowed better cell survival, it was found that the number of live cells significantly decreased in structures thicker than 100 µm. The results suggested that the low porosity could slow down or impede nutrient diffusion and waste removal in the deepest regions of the biomaterial, thus hampering cell survival [287].

GelMA-AlgMA and GelMA-CMCMA showed improved durability in culture, high water absorbance and supported the differentiation of myoblasts into myotubes with a lower decrease in cell viability. They were good candidates for skeletal muscle engineering. However, they did not fulfill the viscoelastic requirements for skeletal muscle tissue. *Engler* et al. demonstrated the importance of biomaterial stiffness for the commitment of precursor cells [130]. They stated that muscle progenitor cells only achieved high maturation in biomaterials that resemble the mechanical properties of the native skeletal muscle tissue. Only those fibers cultured on biomaterials of 12 kPa stiffness showed the formation of sharped sarcomere structures [131]. Considering the skeletal muscle tissue requirements, GelMA-CMCMA was not the most suitable biomaterial due to its low stiffness (1.96 kPa). In contrast, AlgMA increased GelMA

stiffness to 5.53 kPa. Nevertheless, it was not high enough to recapitulate the stiffness of skeletal muscle tissue.

2. GelMA-AlgMA composite bioink optimization to induce skeletal muscle differentiation in 3D-printed human and mouse models

2.1. Increment of GelMA-AlgMA porosity and stiffness to obtain skeletal muscle tissue-resembling bioinks

Skeletal muscle tissue models require biomaterials that resemble native ECM mechanical properties and promote high cell proliferation to obtain fused and packed fibers. Among previously developed composite biomaterials, GelMA-AlgMA was chosen as the best candidate for muscle engineering due to its mechanical properties and capability to sustain muscle growth. Nevertheless, there was a clear need to improve biomaterial porosity and match the stiffness of skeletal muscle tissue.

There are several strategies to modulate the stiffness of biomaterials. Higher material concentrations are known to increase biomaterial stiffness. It was seen that doubling GelMA concentration resulted in a significant increase in the compressive modulus [273]. However, it can change the printing properties of composite biomaterials. Therefore, AlgMA concentration was modulated to control GelMA-AlgMA composite stiffness. In agreement with previous studies [280], doubling AlgMA concentration significantly increased the stiffness. The addition of 1% and 2% of AlgMA increased the Young's modulus from 1.5 kPa to 7.1 kPa and 20.3 kPa respectively (Figure 3.8a). GelMA-AlgMA 2% better recapitulated skeletal muscle stiffness. Nevertheless, the expression of MHC protein in immunostained images of differentiated C2C12 was higher in GelMA with 1% AlgMA and presented a higher density of myotubes. Whereas the expression of MHC and myotube content in 0% and 2% AlgMA was notably lower (Figure 3.8c).

Afterward, the effect of material % in the porosity was studied. The analysis of GelMA-AlgMA pore sizes evidenced that the highest AlgMA concentration decreased biomaterial pore size. Frequency histograms of the pore areas in biomaterials with 0%, 1% and 2% AlgMA showed decreased medians in higher AlgMA content (Figure 3.8b). Interquartile regions in 2% AlgMA were the most biased towards the small pore fraction. These observations confirmed that increasing the concentration of biopolymers reduce the porosity and suggested that low porosity compromise cell viability, proliferation and differentiation. On the contrary, biomaterials without AlgMA experienced fast degradation and most of the cells showed round morphology.

Therefore, there was a need to find a strategy to obtain tissue-like stiffness materials, resistant to degradation, and improve the matrix porosity to promote nutrient diffusion and cell migration.

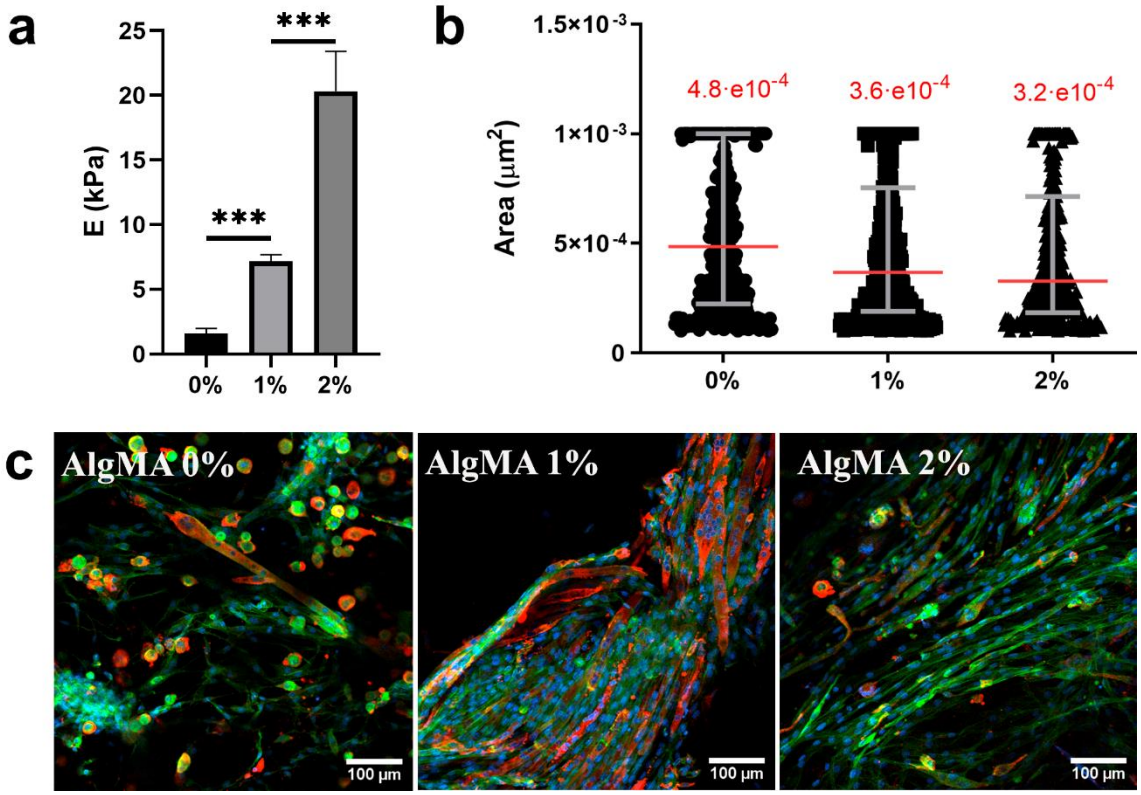

Figure 3.8. AlgMA concentration modulation in GelMA-AlgMA biomaterial. a) Young's Modulus of GelMA with 0% AlgMA, 1% AlgMA and 2% AlgMA (mean value ± SD, One-way ANOVA, p-value *** < 0.0001, n=9). b) Pore area frequency distribution of GelMA-AlgMA 0%, 1% and 2% obtained from SEM images. The interquartile range is presented in grey and the median values in red. c) Confocal images of F-actin (green), MHC (red) and nuclei (blue) in C2C12 differentiated in GelMA-AlgMA 0%, 1% and 2%. Scale bar 100 µm.

Alternative strategies to modulate the physical properties of photocrosslinkable materials are focused on the modulation of the crosslinking degree. Nichol *et al.* fabricated GelMA with low, medium and high methacrylation degrees, which modulated the porosity, stiffness and degradation of the biomaterials [273]. Duchi *et al.* modulated GelMA/HAMA physical properties by tuning the concentration of photoinitiator [288]. They showed that lower LAP concentration decreased biomaterial stiffness. In their study, they also confirmed that high concentrations of LAP were cytotoxic, particularly after their exposure to UV-light.

To increase the porosity of GelMA(5%)-AlgMA(1%), LAP photoinitiator concentration was decreased to 0.05, 0.02 and 0.01% (w/v) (Figure 3.9). Overall porosity was calculated as the volume of macropores over the total physical volume of the 3D structure. Decreasing LAP % increased overall porosity (Figure 3.9b). 0,05% LAP porosity (13.12 ± 4.3) was two-fold lower than 0.02% (21.22 ± 5.7). Similarly, 0.01% LAP porosity achieved a 44.56±1.6% porosity. Those results were confirmed with SEM images (Figure 3.9a), where 0.01% biomaterials presented the highest pore diameters. Swelling showed a similar trend to overall porosity, in which the lowest concentration of LAP presented the highest swelling % (Figure 3.9c). Samples with 0.1% (64.37±11.5)

and 0.05% LAP (66.73±3.3) did not show significative differences, while 0.02% and 0.01% LAP swelling increased to 104.73±10% and 152.77±2.1% respectively.

Porosity and swelling improvement after LAP % reduction was followed by an increased biomaterial degradation (Figure 3.9d) and reduced stiffness (Figure 3.9e). The degradation index between 0.05% (1±0.04) and 0.02% (0.99±0.04) was not significantly different, however, the degradation index of 0.01% (1.22±0.009) was 22% higher, and resulted in samples with low post-printing stability and durability. Similarly, 0.05% LAP samples presented the highest compressive modulus (7.2 kPa), which was similar to biomaterials with 0.1% LAP (7.6 kPa). In contrast, Young's modulus of 0.02% and 0.01% were progressively reduced to 4.1 kPa and 2.8 kPa respectively.

In conclusion, LAP concentration modulation changed the physical properties of GelMA-AlgMA biomaterial. It was found that reducing LAP from 0.1% to 0.02% significantly increased biomaterial porosity, pore size and water absorbance. As expected, it also increased biomaterial degradation, however, 0.02% LAP was stable in culture conditions, while 0.01% LAP was not suitable for long-term 3D culture. Increased porosity in GelMA-AlgMA with 0.02% LAP could improve nutrient diffusion and cell viability. However, those composites displayed lower stiffness (4.1 kPa) than the original composites of GelMA-AlgMA (7.6 kPa), which were even farther from the elastic modulus of skeletal muscle tissue.

To improve the mechanical properties of soft biomaterials, the addition of a low concentration of crosslinked fibrin was explored. Fibrin is one of the most used biomaterials in skeletal muscle tissue engineering due to its viscoelastic properties, high viability and demonstrated capability to support skeletal muscle differentiation [172-175].

Fibrin notably increased the compressive modulus (Figure 3.9e). The stiffness increased 40% in the softest biomaterials (0.01% LAP), which achieved 4.7 kPa. The compressive moduli in biomaterials with 0.02% and 0.05% LAP increased a 64%, which resulted in 11,4 kPa and 21 kPa respectively. In concordance with the changes in the stiffness, the degradation index of biomaterials was also affected after the addition of fibrin (Figure 3.9d). Fibrin diminished a 20% the degradation rate of the hardest biomaterials (0.05% and 0.02% LAP), whereas there were no significant changes in biomaterials with 0.01% LAP. In terms of the overall porosity and swelling, fibrin addition did not present notable alterations in biomaterials with 0.05% and 0.02% LAP, while they were reduced in samples with 0.01% LAP (Figure 3.9b and c).

In the light of previous results, the addition of a small concentration (0.5 w/v%) of fibrin to GelMA-AlgMA constituted an impressive rise in the stiffness. In biomaterials with 0.02% LAP, the stiffness was increased from 4.1 to 11.4 kPa. Consequently, GelMA-AlgMA-fibrin with 0.02% LAP more closely resembled the stiffness of the native skeletal muscle tissue, which has been seen to enhance muscle differentiation [131]. Different concentrations of LAP resulted in biomaterials out of range of the muscle tissue stiffness.

Fibrin also improved the resistance to degradation in biomaterials with 0.02% LAP, which is of great interest to fabricate long-lasting *in vitro* models. In agreement with previous experiments, an increment in biomaterial stiffness together with a decrease in

the degradation rate could be related to a decrease in porosity and swelling. However, the results did not show significant differences in biomaterials 0.02% LAP after fibrin addition, meaning that fibrin content was low enough to preserve the porous mesh of GelMA-AlgMA. In contrast, 0.01% LAP samples with fibrin presented decreased porosity and swelling in comparison with pure GelMA-AlgMA, which suggested that the hydrogel cohesion was governed by thrombin crosslinking rather than photocrosslinking. In fact, the degradation rate in 0.01% LAP samples with fibrin was not significantly diminished, probably due to the higher sensitivity of fibrin bonds to hydrolysis and enzymatic activity than the covalent bonds of photocrosslinked GelMA-AlgMA. Altogether, GelMA-AlgMA-Fib formulation with 0.02% LAP demonstrated a significant improvement concerning the first formulation of GelMA-AlgMA composite biomaterial. The new formulation provided higher porosity, improved swelling and good stability for long-term 3D culture. More importantly, its compressive modulus (11.4 kPa) recapitulated the stiffness of native skeletal muscle tissue (≈ 12kPa).

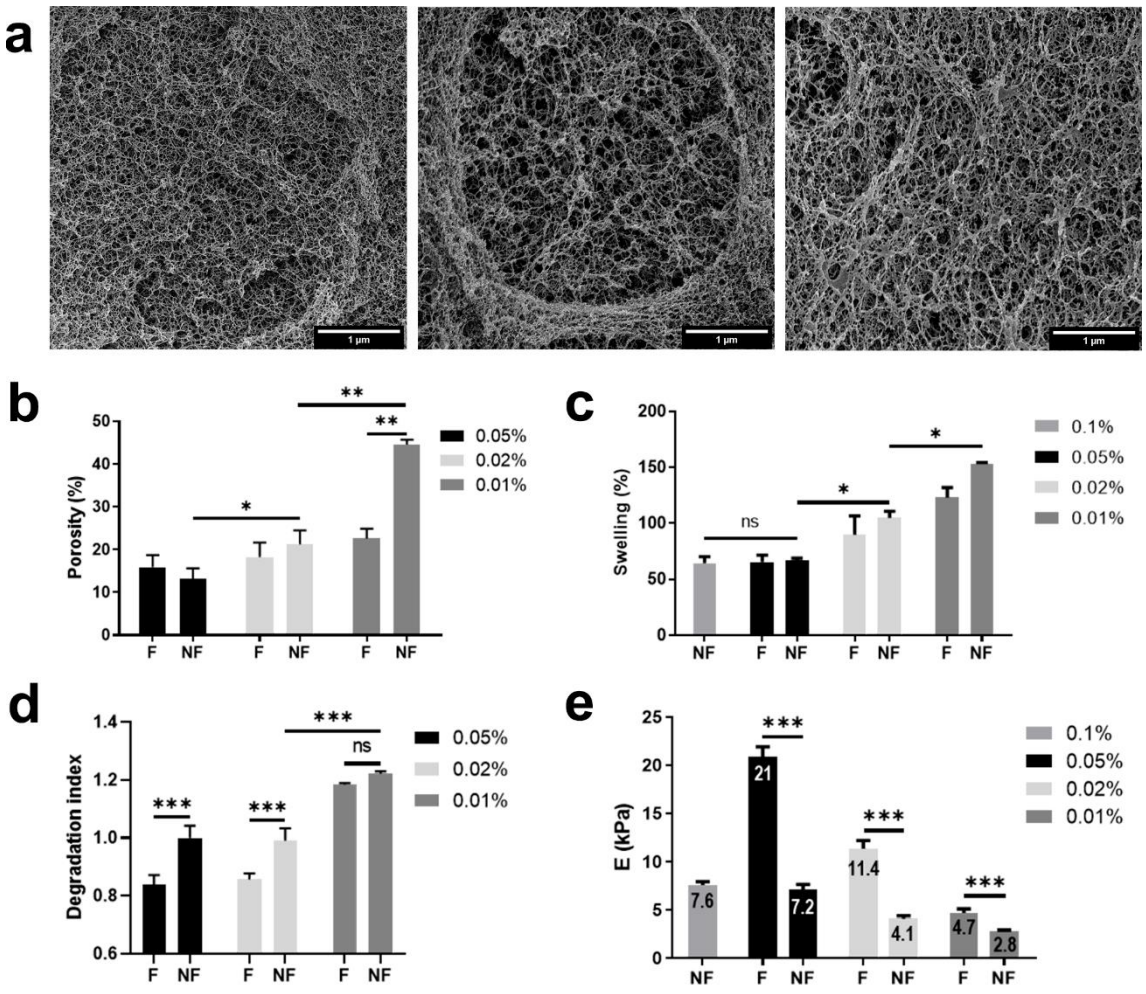

Figure 3.9. Modulation of the physical properties of GelMA-AlgMA biomaterial. a) SEM images of GelMA-AlgMA biomaterials with 0.05%, 0.02% and 0.01% w/v of LAP. Scale bar 1 µm. Physical properties of the six GelMA-AlgMA biomaterials with (F) or without (NF) fibrin at different concentrations of LAP, including b) overall porosity (%) (n=3), c) swelling (%) (n=4),

d) degradation index in collagenase (n=4) and e) compressive modulus E (kPa) (n=9). Mean ± SD, Two-way ANOVA, *p-value < 0.05, **p-value < 0.005 and ***p-value < 0.0005.

To study the effects of the physical properties of the new GelMA-AlgMA formulations in cell behavior, bioactivity and biocompatibility were analyzed. To that end, the viability and adhesion of C2C12 in the three formulations of GelMA-AlgMA (0.05, 0.02 and 0.01% LAP) alone or with fibrin were evaluated after 3 days in culture.

The cell adhesion was analyzed with cell circularity score (Figure 3.10a). Spherical morphology is indicative of the lack of focal adhesions between cells and ECM, while elongated morphology appears when cells establish attachments with the surrounding surfaces [289, 290]. Cell interaction with ECM is necessary for most of the cell functions as migration, division and differentiation [291]. Therefore, cells that do not display interactions with ECM remain in a latent state until they activate the apoptotic machinery [292].

Spherical cells were scored as 1, which were considered unable to perform cell-ECM contacts. Oppositely, fully elongated cells (score 0) were assumed to establish focal adhesions with the biomaterial. Results indicated that a reduction in LAP concentration increased cell adhesion. Frequency histograms of cell circularity in biomaterials with 0.05% LAP showed data distribution biased towards high circularity scores. The median was set at a score of 0.8, and 0.7 in samples with fibrin. However, samples without fibrin showed a higher frequency of cells with low circularity. The highest frequency of cells in 0.02% LAP biomaterials was distributed at the score of 0.4, regardless of the fibrin content. Biomaterials with 0.01% LAP were completely degraded after 3 days in culture (Figure 3.10b), thus only samples containing fibrin were analyzed. The median in 0.01% LAP was at a score of 0.2, indicating that most cells presented elongated morphology.

Considering that 0.02% LAP was the most resistant biomaterial with the lowest circularity score, they were used to study cell viability. After 3 days in culture, 90% of C2C12 cells survived in 0.02% LAP biomaterials regardless of fibrin addition (Figure 3.10d and 10e). In previous results, GelMA-AlgMA with 0.1% LAP showed 70% of cell viability in structures of 100-300µm. In contrast, LAP % reduction to 0.02% increased cell viability to 90% and 88% in NF and F structures up to 400 µm height (Figure 3.10c).

In agreement with the previous hypothesis, LAP concentration reduction showed a high impact on cell morphology and viability. The circularity and viability of C2C12 were similar between pure GelMA-AlgMA biomaterials and those containing fibrin, which suggested that stiffness was not the main factor involved in cell-ECM interaction. Instead, biomaterial porosity seemed to be correlated with cell adhesion and morphology. The results confirmed that highly porous biomaterials as 0.01% LAP provided matrices with bigger cavities where cells can elongate, find new attachment points, and interact with nearby cells. Consequently, their chances to form a dense population of myoblasts that promote their fusion into fibers are greater. However, 0.01% LAP samples were not suitable for long-term cultures. In contrast, 0.02% LAP were durable and presented also a high number of elongated cells after 3 days in culture. GelMA-AlgMA with 0.02% LAP yielded 90% of live cells regardless of fibrin addition, which was a notable improvement

regarding the previous composition with 0.1% that only reached viability of 70%. In the previous formulation containing GelMA-AlgMA and 0,1% LAP, it was seen that 3D culture deepness severely affected cell viability. In contrast, the viability in the new composition was measured in structures higher than 300 µm, where viability remained constant from the cells in the outline to the cells in the core. High porosity in GelMA-AlgMA and GelMA-AlgMA-Fib with 0.02% LAP probably improved medium changeover with the biomaterial core, which could improve nutrient diffusion and waste removal. Considering the previous results, GelMA-AlgMA-fibrin with 0.02% LAP was the best candidate for skeletal muscle tissue engineering, due to its durability, porosity, viability and tissue-like stiffness.

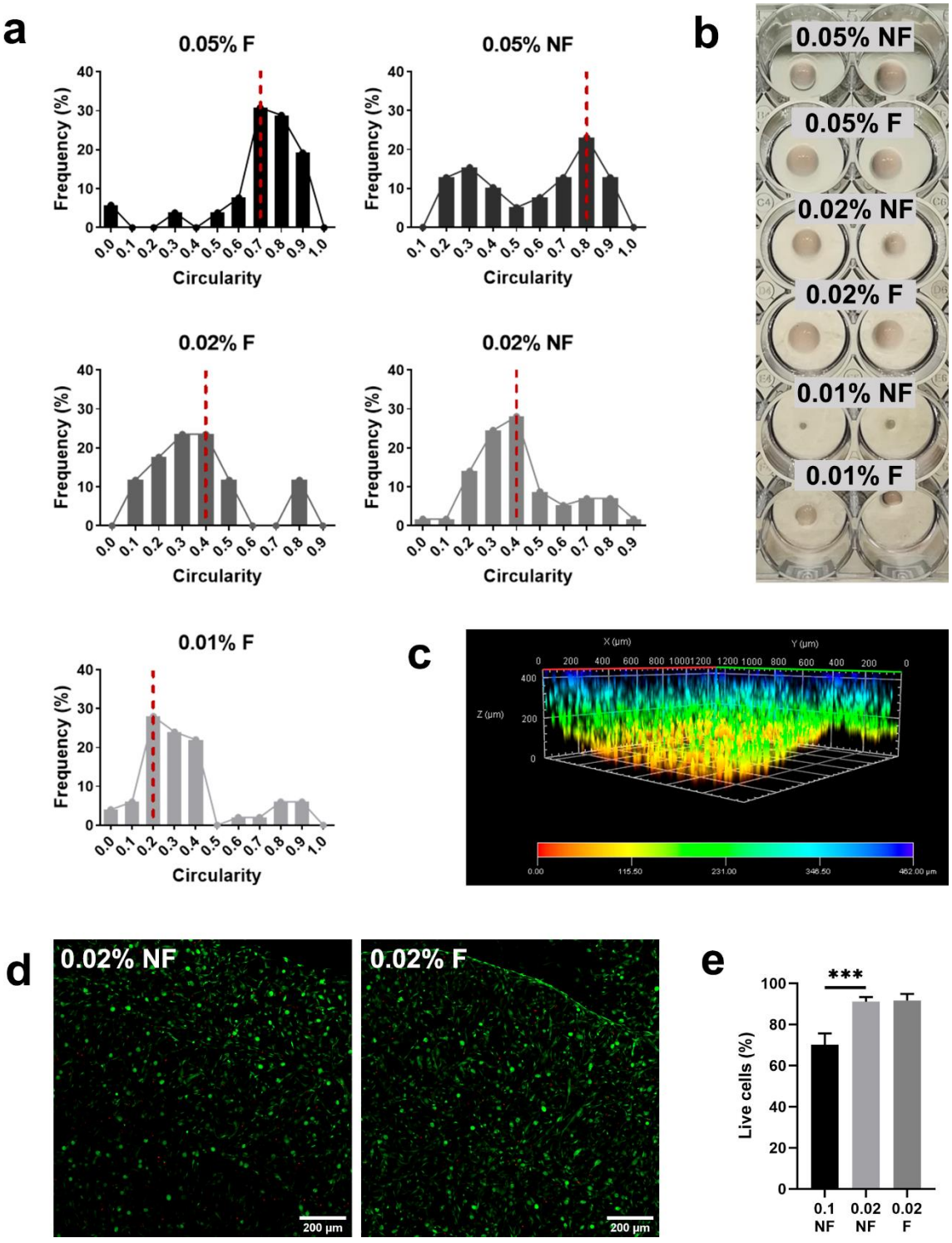

Figure 3.10. Viability and morphology of C2C12 in GelMA-AlgMA with fibrin (F) or without fibrin (NF) and with 0.05%, 0.02% and 0.01% (w/v) LAP photoinitiator. a) Frequency (%) of cells with different circularity score ranged from 0 (elongated) to 1 (circular). Distribution median is represented as red dashed line. b) Top view of C2C12 3D drops after 3 days of culture in GelMA-AlgMA with different percentages of LAP and fibrin. c) 3D reconstruction of calcein staining positive cells (live) C2C12 cultured in GelMA-AlgMA-Fib + 0.02% LAP for 3 days. The Z scale is ranged from 0 to 400 µm and cell location deepness is represented in color scale. d) Immunostaining of live (green) and dead (red) cells in 0.02% LAP biomaterial without (NF) and with fibrin (F) after 3 days in culture. Scale bar = 200 µm. e) Viability of C2C12 after 3 days in

culture in 0.02% LAP biomaterial with (F) and without (NF) fibrin in comparison with the viability showed by previously developed biomaterial with 0.1% LAP. All 3D cultures were thicker than 100 µm. Data is presented as mean ± SD, one-way ANOVA ***p-value < 0.0005, n=5.

The addition of new components to a bioink can alter its printability. Once GelMA-AlgMA-fibrin with 0.2% LAP was chosen as the best candidate for skeletal muscle tissue engineering, the printability of the new composite biomaterial was evaluated.

Fibrin crosslinking is naturally initiated by thrombin. Thrombin cleavage of fibrinopeptides triggers the spontaneous assembly of fibrinogen monomers into fibrin fibers, which form a water-insoluble mesh [170]. Fibrin polymerization is characterized by the formation of clots, which are known to obstruct the needles during the extrusion process in 3D bioprinting [293]. Consequently, many authors chose the prepolymerized form fibrinogen for bioprinting experiments, which was crosslinked after or during the extrusion process [261, 293, 294]. To unify and simplify the fabrication process in this thesis, a printable formulation of fibrin was studied.

Images in Figure 3.11a showed that thrombin concentrations higher than 0.5 UI/ml induced clot formation. At 0.25 UI/ml, thrombin generated a less hydrophobic fibrin matrix [295], which resulted in homogeneous hydrogels that did not present fiber/water phase separation. The resulting GelMA-AlgMA-fibrin biomaterial was extruded with pressurized air through the bioprinting needle, which kept fiber shape after its release, thus demonstrating high printability (Figure 3.11b). The combination of the new formulation with extrusion printing methods presented a highly printable biomaterial that did not require post-printing steps of crosslinking and washing, thus shortening the fabrication time.

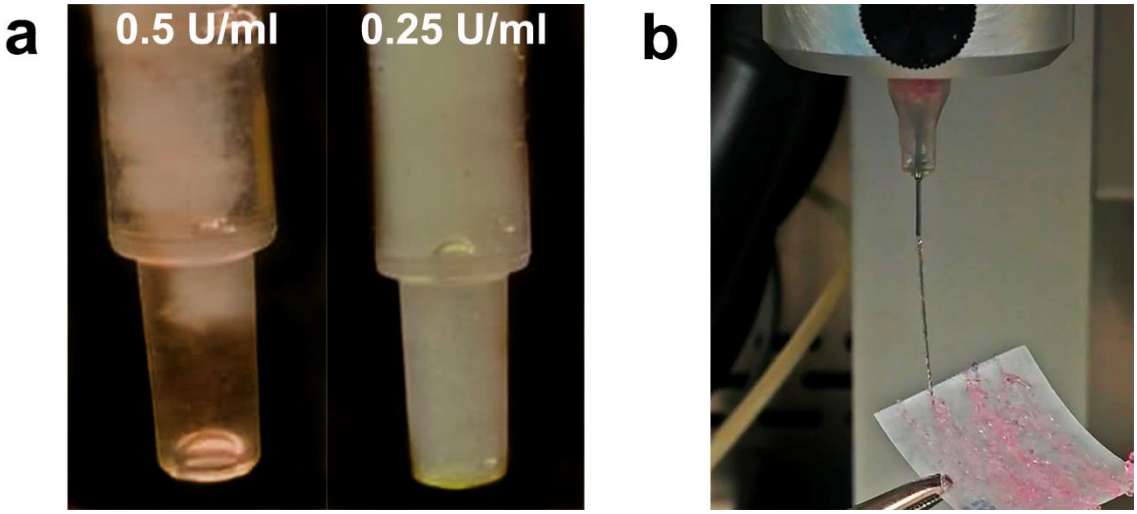

Figure 3.11. Thrombin concentration setting to obtain bioprintable ink. a) Front view of 1ml syringes loaded with GelMA-AlgMA-Fib 0.02% LAP with 0.5 U/ml and 0.25 U/ml thrombin. b) Front view of the extrusion process of GelMA-AlgMA-Fib with 0.25 UI/ml in the 3D bioprinter. The biomaterial fiber is extruded through a 200 µm inner diameter straight needle.

2.2.Development of mouse skeletal muscle *in vitro* models

To engineer skeletal muscle tissue *in vitro* models, C2C12 mouse myoblasts were encapsulated in 4,5 mm diameter and 1 mm height bioprinted rings (Figure 3.12a). The ring shape was designed with the aim to obtain easy-handling structures that enable their anchorage into pillars. This system aimed to facilitate the live monitoring of the bioprinted rings and generate passive tension in the elastic biomaterial.

Previously, the differentiation of C2C12 myoblasts in the original GelMA-AlgMA (0.1 % LAP) composite biomaterial was studied, where it was found the formation of several fused myotubes. After the formulation of the new composite based on GelMA-AlgMA-Fib with 0.02% LAP, the myogenic properties of the biomaterial were studied. C2C12 myoblasts were encapsulated and ring models were printed. Traditionally, the differentiation of myoblasts into fused myotubes is triggered by a shift in the medium. Medium containing high serum concentration (10 v/v%, growth medium, GM) is switched to a low serum medium (2 v/v%, differentiation medium, DM) that induces the fusion of the multinucleated syncytium. To evaluate the myogenic properties of the GelMA-AlgMA-fibrin biomaterial, the proliferation and differentiation of the myoblasts cultured in DM and GM were studied. After cells reached high confluency (± 8 days), GM was switched to DM if corresponded. After 15 days in culture, immunostaining images of bioprinted rings cultured in DM showed a low number of multinucleated fibers. Furthermore, there was a high number of damaged fibers, which presented detached round morphology (Figure 3.12b). Actin staining revealed that only 40% of the surface was covered by muscle cells when cultured in DM (Figure 3.12c). In contrast, myoblasts cultured in GM showed 85% of actin coverage, where myoblasts formed dense populations of packed muscle fibers (Figure 3.12b).

Many differentiation processes are accompanied by a slowdown in the proliferation rate. As could be expected, medium shift to DM slowed down cell proliferation, which started a falling tendency (Figure 3.12d). Oppositely, muscle cells maintained in GM showed an increasing trend.

To evaluate the differentiation state of each culture type, the genetic expression of muscle fibers in DM and GM after 15 days was compared (Figure 3.12e). Muscle fiber differentiation is characterized by the upregulation of sarcomeric structural proteins meant to form the contractile machinery unit, the sarcomere. *Actn2* (encoding for α-actinin), *Myh4* and *Myh7* (encoding for fast and slow myosin heavy chain), and *Tnnc2* (encoding for fast troponin c) are some genes upregulated during differentiation last stages of muscle differentiation. Genetic expression of *Actn2, Myh7* and *Myh4* in bioprinted rings cultured in DM and GM presented similar values, indicating that both treatments induced the differentiation of C2C12 myoblasts.

The expression of sarcomeric proteins in bioprinted rings cultured in GM was confirmed in the immunostaining images, which revealed the formation of fused multinucleated fibers with upregulated expression of myosin heavy chain (MHC) and α-actinin (Figure 3. 13a).

The upregulation of sarcomeric proteins in GelMA-AlgMA-fibrin cultured in GM suggested that serum starvation was not required for myoblasts differentiation. Distler *et al*. revealed similar results, where medium with high serum content promoted the

differentiation of mature muscle fibers in ADA-GEL biomaterial, while low serum treatment resulted in round and amorphous morphologies [260]. They suggested that using high serum medium for 3D cultures could be of great importance to ensure correct nutrient supply to cells in the biomaterial core.

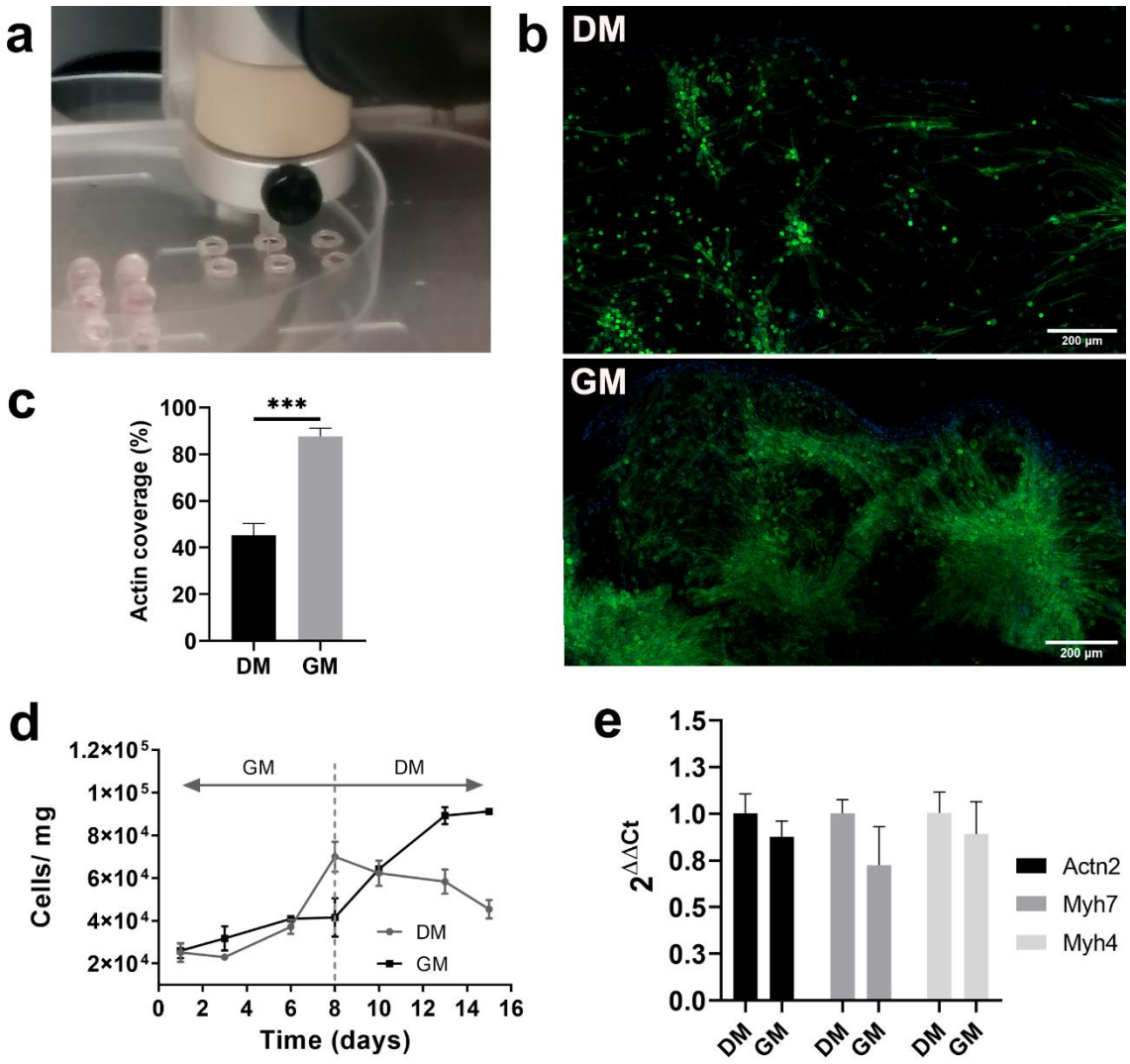

Figure 3.12. Study of the differentiation protocol in GelMA-AlgMA-Fib bioprinted rings with encapsulated C2C12. a) 3D bioprinting of C2C12 embedded ring models of GelMA-AlgMA-Fib. b) Immunostaining of C2C12 cells after 15 days in bioprinted rings cultured in differentiation medium (DM, 2% serum) and growth medium (GM, 10% serum). Nuclei are stained in blue and green corresponds to F-actin that was used to calculate the actin coverage of the 3D surfaces in c) (mean ± SD, t-test, *** p-value < 0.0005, n=4). Scale bar = 200 µm. d) Proliferation of C2C12 cells in bioprinted rings cultured in DM and GM calculated as the number of cells per mg of biomaterial. Dashed gray line indicates the medium shift to DM if corresponded. e) RTqPCR analysis of the fold expression ($2^{\Delta\Delta Ct}$) of Actn2, Myh7and Myh4 muscle differentiation genes in DM and GM after 15 days of culture (mean ± SD, One-way ANOVA, **p-value < 0.005, n=4).

Several authors studied the relevance of cell density in myoblast differentiation [296, 297]. In highly confluent cultures, close cell-cell contact induced myoblast differentiation and growth arrest via CDKI p21 upregulation [296]. Yoshiko *et al*. demonstrated that highly confluent monolayer cultures of C2C12 in GM showed improved differentiation by the regulation of proliferating/differentiating cells with an autocrine/paracrine loop of IGF, bFGF and TGF-β1 [298]. Regarding the high proliferation rate in bioprinted rings cultured in GM, myoblast differentiation could be induced by the high cell density.

To study the role of GelMA-AlgMA-Fib biomaterial interaction and cell density in myoblast differentiation, highly confluent monolayer cultures and 3D cultures treated with GM were compared. To that end, the genetic expression of myogenic regulatory factors and sarcomeric structural proteins was analyzed (Figure 3. 13b). MRFs like *Myf5* and *MyoD* are transcription factors upregulated during the myoblast stage, that induce the upregulation of *Myog*, an MRF characteristic of the early stage of myoblast differentiation. *Myog* is one of the transcription factors that induce the upregulation of sarcomeric proteins (*Actn2*, *Tnnc2*, *Myh4* and *Myh7*) and the formation of multinucleated mature muscle fibers. C2C12 monolayer culture in GM showed upregulated expression of early MRFs and low or negligible expression of sarcomeric proteins. In contrast, C2C12 cultured for 7 days in GelMA-AlgMA-fibrin presented downregulated expression of early MRFs and upregulated expression of *Myog* and sarcomeric proteins. The results demonstrated that GelMA-AlgMA-fibrin biomaterial played an important role in myogenesis, because it promoted the differentiation of myoblasts since the first days of encapsulation.

All in all, GelMA-AlgMA-Fib biomaterial allowed the encapsulation and printing of ring-shaped skeletal muscle mouse models and promoted the development of dense packed differentiated muscle fibers. Furthermore, confocal images showed muscle fibers aligned towards the printing direction (Figure 3. 13a), which confirmed that the extrusion bioprinting technique promotes cell alignment.

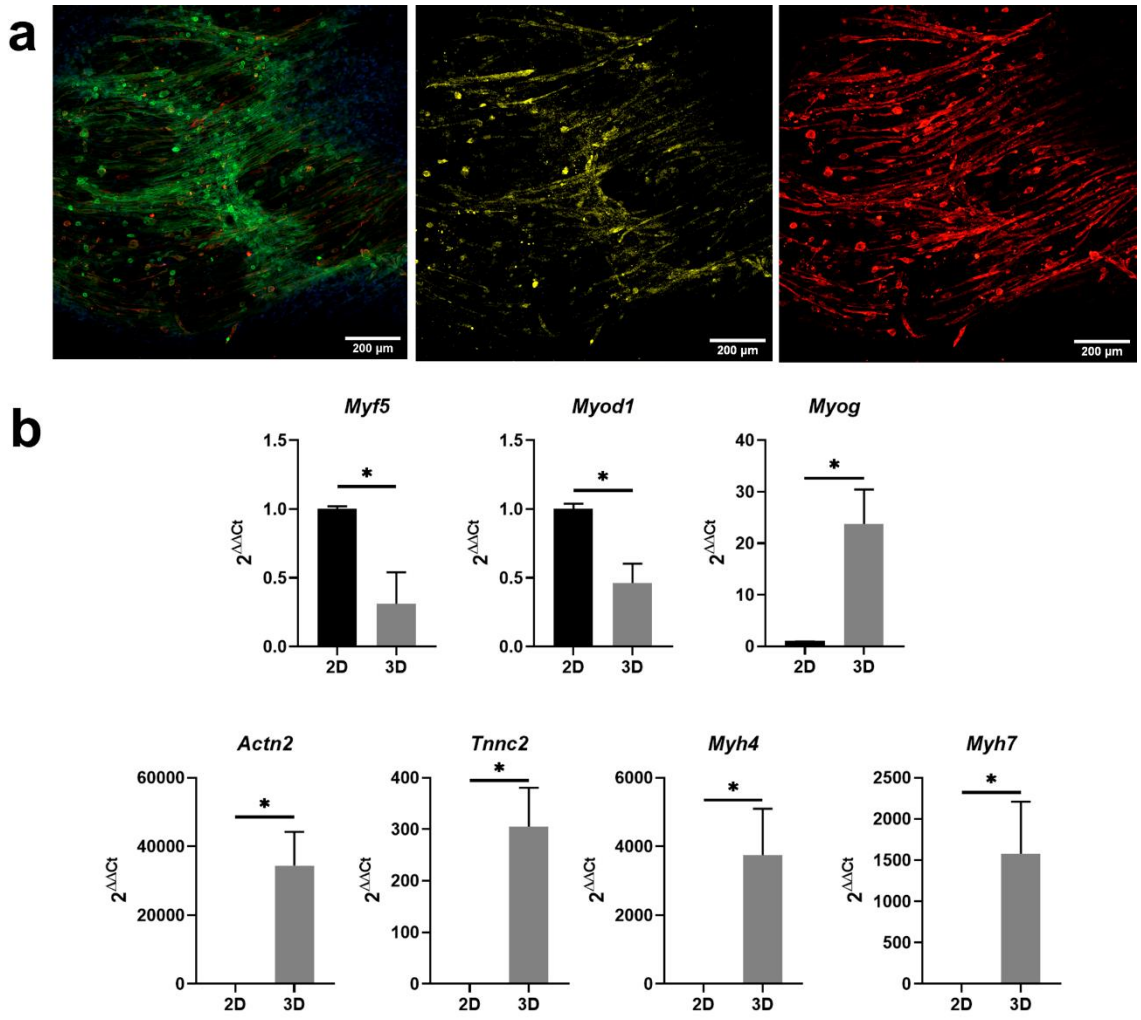

Figure 3. 13. Bioprinted muscle rings mouse model differentiation. a) C2C12 in bioprinted rings after 15 days of culture in GM showing differentiated fibers expressing α-actinin (yellow) and MHC (red). F-actin (green) and nuclei (blue) are also stained. Scale bar = 200 µm. b) Fold expression of myoblast stage (Myf5 and Myod1), early differentiation stage (Myog) and late differentiation stage (Actn2, Tnnc2, Myh4 and Myh7) genes in monolayer (2D) and bioprinted rings (3D) cultured in GM for 7 days (mean ± SD, Unpaired t-test *p-value < 0.05, n=4).

2.3.Development of human skeletal muscle *in vitro* models

Human skeletal muscle tissue is obtained from biopsies, which limits the size of the sample and can be harmful to patients. Developing human *in vitro* models can reduce the extraction of muscle samples from patients and overcome the limitations of sample sources. To explore the potential of GelMA-AlgMA-fibrin biomaterial to develop human muscle bioprinted models human skeletal muscle myoblasts (HSMM) were encapsulated and extruded by the bioprinter to obtain ring models. Same as in murine models, bioprinted rings were cultured in medium with high serum concentration (10% serum, GM) to study the myogenic properties of GelMA-AlgMA-fibrin he myogenic properties of GelMA-AlgMA-fibrin in human myoblasts.

Calcein staining revealed homogeneous distribution of elongated cells after 3 days in culture (Figure 3.14a). This cell morphology indicated that GelMA-AlgMA-fibrin composite supported the adhesion and migration of human primary myoblasts, which is essential for tissue development. Furthermore, the staining showed a viability of 80%. The number of live cells was homogeneously distributed along the 3D structure, and there was no evidence of nutrient starvation in the core of the bioprinted ring. The results confirm that the new formulation of GelMA-AlgMA-fibrin provides good support for myoblast culture in 3D structures with considerable thickness. The proliferation studies showed a constant number of cells in the bioprinted rings during 15 days of culture, which indicated a low rate of proliferation (Figure 3.14b). C2C12 are immortalized cells with an unlimited proliferation capability. The hyperactive proliferation of C2C12 probably results in a mixed population of new myoblasts and differentiated myotubes, which could explain the growing proliferation in murine models. In contrast, primary cells as HSMM have limited proliferation. Furthermore, muscle cells committed to a differentiated state loss their proliferative capability [299]. Considering the results obtained in murine bioprinted models, the proliferation studies in HSMM could indicate that GelMA-AlgMA-fibrin induces the transition of myoblasts to a differentiated state.

The myogenic differentiation of human primary myoblasts in bioprinted rings was studied through the analysis of the genetic expression of early MRF (*MYF5*), late MRF (*MYOG*) and sarcomeric structural proteins (*ACTN2*, *MYH4* and *MYH7*) (Figure 3.14c). After 14 days in culture, MYF5 was downregulated, whereas MYOG was upregulated. The transition from early MRF to late MRF indicated that HSMM passed from a myoblast stage to a differentiated state. Concordantly, *ACTN2, MYH4* and *MYH7* sarcomeric proteins were noticeably upregulated, suggesting a late stage of differentiation. In the human models, the expression of type I slow myosin heavy chain (*MYH7*) was higher than type 2B fast myosin heavy chain (*MYH4*), which was opposite in murine models. The results agree with the differences in muscle fiber types among species [300]. It is known that small mammals contain a higher amount of fast anaerobic muscle fibers to perform fast and explosive movements, as escaping from predators. Instead, there is a low number of type 2B fast fibers in humans and a greater number of slow type I fibers.

The protein expression of α-actinin and myosin heavy chains was confirmed in immunostaining images (Figure 3.14d). Bioprinted rings showed multinucleated muscle fibers with high expression of sarcomeric proteins. Altogether, the results demonstrated that GelMA-AlgMA-fibrin biomaterial induced the differentiation of human primary myoblasts, thus it is a suitable candidate for the development of human *in vitro* muscle models. Nevertheless, immunostaining images also revealed a low density of muscle fibers. The limited proliferation of primary myoblasts impedes the formation of a packed tissue that promotes cell-cell contact, which hampers the fusion of myoblasts into multinucleated myotubes. Consequently, it is important to consider a high initial cell density in the printable biomaterials to achieve packed skeletal muscle tissue. Although the rings showed a low density of fibers, confocal images confirmed again the effect of extrusion bioprinting in the alignment of muscle fibers (Figure 3.14d).

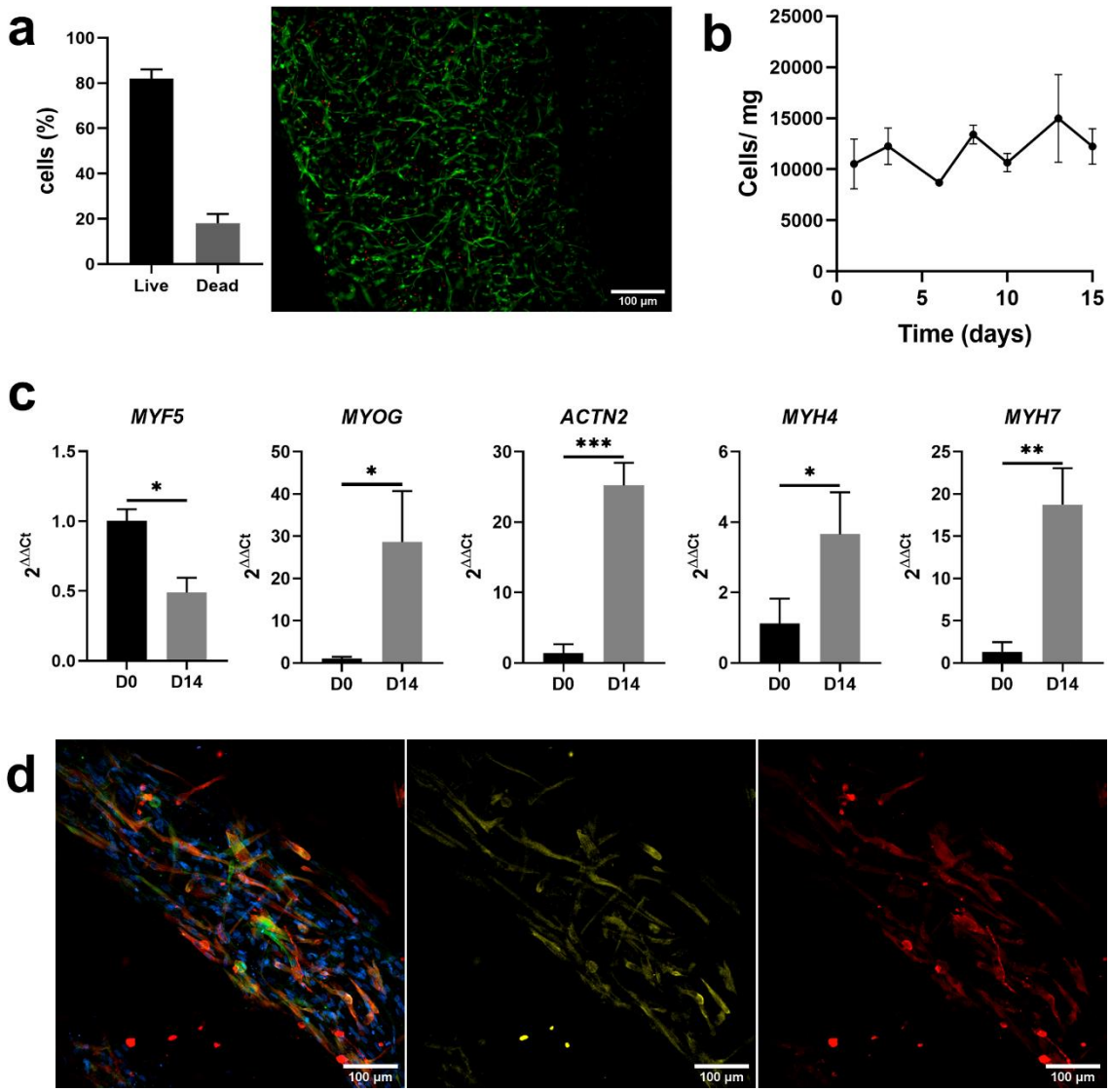

Figure 3.14. Fabrication and differentiation of human bioprinted muscle models. a) Immunostaining of live (green) and dead (red) HSMM in GelMA-AlgMA-Fib bioprinted rings cultured for 3 days. Scale bar = 100 µm. Cell viability was calculated from the percentage of live cells. b) Proliferation of HSMM calculated as the cells per mg of biomaterial obtained along 15 days cultured in complete medium (n=5). c) RTqPCR analysis of genes corresponding to myoblast stage (MYF5), early differentiation stage (MYOG) and late differentiation stage (ACTN2, MYH4 and MYH7) in bioprinted rings cultured in HSMM growth medium for 14 days (mean ± SD, t-test *p-value < 0.05, **p-value < 0.005 and ***p-value < 0.0005, n=5). d) Confocal images of HSMM differentiated fibers with stained F-actin (green), nuclei (blue), α-actinin (yellow) and MHC (red) in bioprinted rings after 14 days in culture. Scale bar = 100 µm.

3. Evaluation of the functionality of skeletal muscle models

3.1. Optimization of the parameters for electrical pulse stimulation

One of the main functions of skeletal muscle tissue is body locomotion, which is actuated by tissue contraction. Therefore, engineered muscles must have mature fibers with contractile capability. Contractile activity is indicative of the maturation state of muscle fibers, but it can be also used to evaluate muscle response to exercise, aging and drugs [16, 173, 269]. Due to their intrinsic role as natural motors, engineered muscles have been used to induce movement in soft robotics [172].

Muscle contraction can be activated by electrical pulses that induce the depolarization of the membrane depolarization and activation of the motor machinery of the cell. During the last years, several protocols for electrical pulse stimulation have been set up. There is considerable ambiguity in the literature in regard to the electrical parameters. Pulse amplitude, width and frequency range from 5 to 40 V, 1 to 20 ms and 0.5 to 100 Hz respectively [16, 120, 269, 301-303]. The controversy in the electrical parameters found in the literature is due to the particularities of each electrical pulse stimulation (EPS) system. Variations in the system resistance are defined by the distance between electrodes, medium composition and biomaterial conductivity, among others. In 2004, Marotta *et al*. designed a 6 well-plate in which they obtained synchronous contractions in square pulse voltages higher than 15 V and pulse durations longer than 1ms [302]. Later, it was demonstrated that 0.3V/mm amplitude, 4ms width and 1Hz resulted in 4.5-fold of contraction force [270], and that higher frequencies led to tetanic contraction and fiber break [303].

To adapt the electrical parameters to our stimulation system, first, the effect of electrical pulse stimulation (EPS) was evaluated in monolayer cultures of C2C12. As described by others, direct current (DC) in an aqueous medium yields high production of reactive oxygen species (ROS), which in long-term culture can acidify the medium and damage the cells [120]. In agreement with those studies, it was found a dramatic fall in cell survival near the anode (Figure 3.15a). In DC, electrical current is continuously flowing in the same direction, where electrons flow from the anode to the cathode. Electron release in the anode involves oxidative reactions that produce toxic compounds. To avoid cell damage by electrolysis byproducts, bipolar square pulses can be designed, where current changes its polarity (or electron direction) in each pulse and avoids the accumulation of electrons [120]. To counteract the electrolytic effect of direct current bipolar square pulses were designed, which allowed long-term stimulation experiments.

To set the optimum pulse amplitude, differentiated C2C12 were subjected to different voltages. It was found that pulse amplitudes below 10V induced the contraction of few fibers resulting in asynchronous movements. When amplitude increased to 20V, most fibers showed contraction activity that was accurately synchronized with pulse frequency (Figure 3.15b). Contraction amplitude was significantly reduced in voltages above 40V (Figure 3.15c). It was seen that at 80V most fibers ended their contraction activity after several minutes of EPS, probably due to induced damage and loss of contractile machinery architecture. Indeed, it is known that higher voltages can compromise muscle

integrity due to overheating and higher production of electrolysis byproducts [304]. Pulse frequency has a notable impact on contraction dynamics, since frequencies higher than 1Hz significantly reduced contraction amplitude (Figure 3.15d). Pulse width changes from 2 to 10 ms did not show highly significant changes (Figure 3.15e). Nevertheless, there was a decreasing tendency with increasing pulse width, which was particularly remarkable at 20 ms. To obtain synchronous contractions with the highest amplitudes, 20V, 4ms and 1Hz electrical parameters were selected.

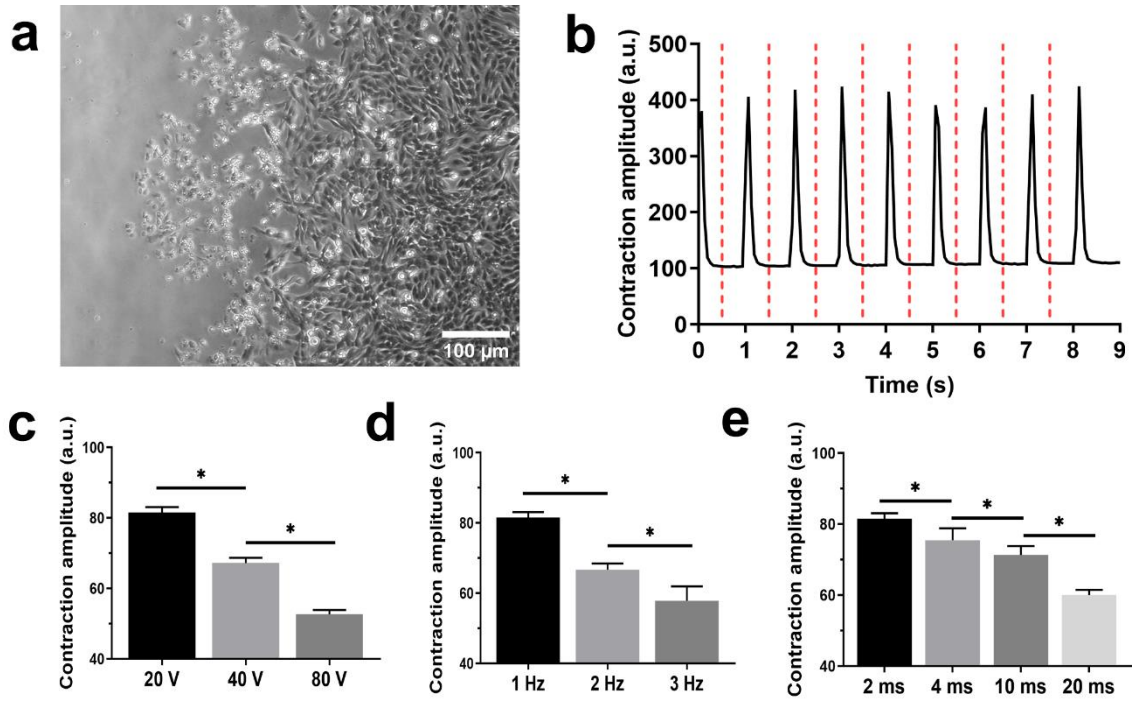

Figure 3.15. Setting of EPS parameters for muscle fiber stimulation. a) Bright field image of C2C12 myoblasts near the electrode after EPS with square monophasic pulses. b) electrogram of C2C12 differentiated fiber synchronous contraction amplitude subjected to 20V and 1Hz. Red dashed lines represent 1 s period. Effect of different a) voltages, d) frequencies and e) pulse amplitudes in the contraction amplitude of C2C12 fibers.

3.2. Effect of electrical pulse stimulation in monolayer cultures of C2C12 cells

To determine if the chosen electrical parameters were suitable for the development of skeletal muscle, the effect of EPS in C2C12 cultured in monolayer was studied. Video recordings of monolayer cultures revealed that 3 days of EPS for 1h increased the number of contractile fibers (Figure 3.16a). After 2 days of EPS, fiber contraction amplitude dramatically increased (Figure 3.16b). In concordance with results obtained by Ito *et al*. [270], the contraction amplitude of fibers increased after the first day of EPS training, suggesting an adaptation to EPS and progressive improvement of fiber sensitivity. After 2 days of EPS, fibers reached the maximum contractile amplitude, thus 3 days were considered enough for muscle culture adaptation to EPS.

Immunofluorescence images of monolayer cultures after 3 days of EPS showed upregulated expression of sarcomeric structural proteins α-actinin and MHC (Figure 3.16c). RTqPCR analysis confirmed those results, which showed upregulated expression of *Actn2* and *Myh7* (Figure 3.16d). However, fast type *Myh4* and *Tnnc2* did not show significant changes. It has been suggested that EPS induces a shift from fast type fiber to slow type fibers [305, 306], which is similar to changes in muscle found after routinary exercise *in vivo* [307]. These observations indicate that the chosen EPS parameters promote the differentiation of skeletal muscle fibers.

Confocal images also revealed the formation of sarcomeres, which are characteristic of differentiated fibers in an advanced maturation state (Figure 3.16c). Sarcomeres were distinguished by the reorganization of F-actin cytoskeleton into A-bands, which flanked the α-actinin bands that are part of Z-discs. Unstimulated monolayer cultures did not show sarcomere units. Therefore, EPS training of C2C12 with 20V, 2ms and 1Hz pulses enhance the reorganization of the cytoskeleton of skeletal muscle fibers into sarcomeres, achieving an advanced maturation and optimized contractile machinery.

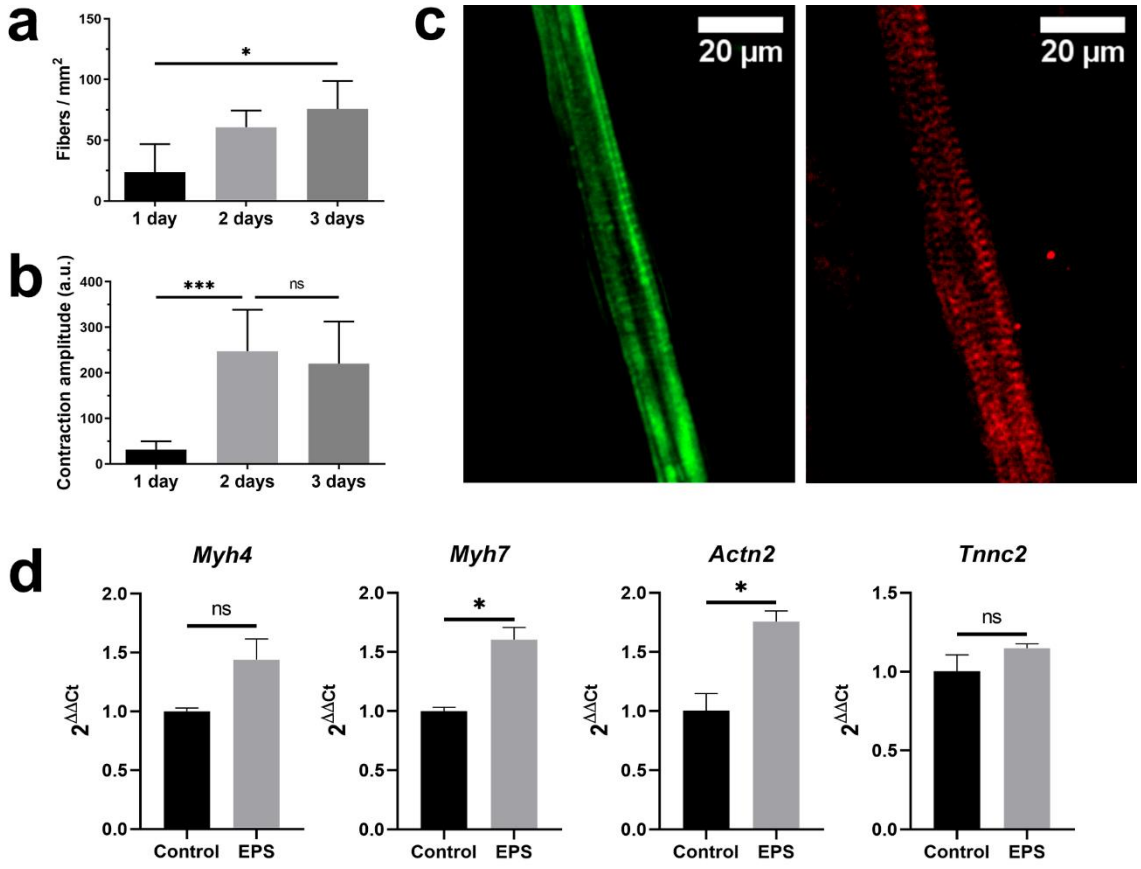

Figure 3.16. EPS effect in C2C12 differentiated monolayer cultures. a) Number of contracting fibers (n=5) and b) contraction amplitude (n=21) of fibers responding to EPS for 3 days. c) Confocal images of C2C12 fibers after 3 days of EPS showing stained F-actin (green) and α-actinin (red). Scale bar = 20 µm. d) Fold expression of muscle differentiation genes in fibers subjected to 3 days of EPS compared with non-stimulated (Control) (n=3). Data is presented as mean ± SD, one-way ANOVA and unpaired t-test *p-value < 0.05 and ***p-value < 0.0005.

3.3. Effect of electrical pulse stimulation in bioprinted rings

The designed EPS protocol enhanced the maturation of muscle fibers in monolayer culture. To study the functionality of skeletal muscle tissue in GelMA-AlgMA-fibrin 3D cultures, bioprinted rings with differentiated C2C12 fibers were stimulated with the same setup.

To avoid movement and vibrations during the life monitoring of bioprinted muscles, rings were anchored in silicon printed pillars (Figure 3.17a). Thanks to the high versatility of ring models, four silicon pillars were fabricated according to ring diameter and cured on cover glasses, which allowed their easy manipulation, sterilization and were optically compatible for microscopy techniques. Pillars were printed onto 24 x 24 mm coverslips, which allowed the stimulation of 24 rings simultaneously in a 6 well plate. Immobilized silicon pillars allowed to maintain muscle rings equidistantly between the two opposite carbon electrodes.

EPS training parameters in bioprinted rings provided strong and synchronous contraction of *in vitro* muscle fibers. They accurately responded to changes in pulse frequency, which could be used to modify the beats per second of the model (Figure 3.17b). Similar to 2D culture, fiber contraction amplitude in bioprinted rings increased after 3 days of EPS (Figure 3.17c). Although contraction amplitude significantly increased from the second day to the third day of EPS, the greatest impact occurred in the transition from the first day to the second day of EPS. The results suggested an adaptation and improvement of the contractile machinery over time, whose peak was found between the second and the third day of EPS training.

In contrast to monolayer cultures, EPS training for 3 days did not show significative effect in the genetic expression of structural proteins, except in *Tnnc2* (Figure 3.17d). Nevertheless, it was found that the genetic expression of *Myh7* was higher in 3D cultures than in non-stimulated and stimulated 2D cultures. The evidence suggested that Myh7 expression in bioprinted muscle fibers was already upregulated before EPS stimulation. Some studies demonstrated that mechanical tension had a similar effect on muscle tissue than electrical stimulation, which induced a fast-to-slow muscle fiber transition [308, 309, 310]. As a hypothesis, muscle fibers in a viscoelastic GelMA-AlgMA-Fib ring anchored in a silicon pillar could have a similar effect to induced mechanical stress. However, more extended studies will be needed to enlighten the effects of passive tension of pillars on the muscle fibers encapsulated in bioprinted rings.

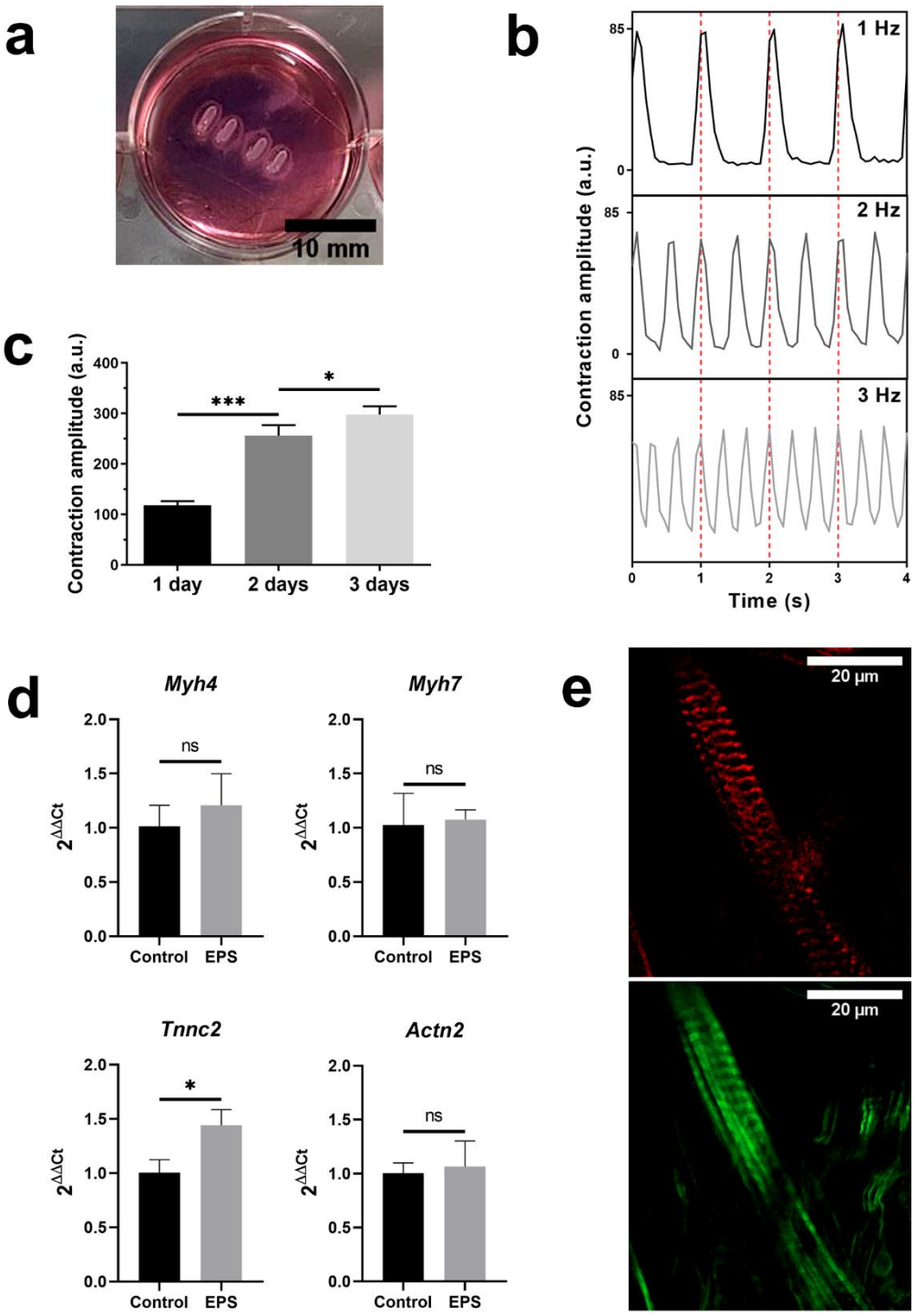

Figure 3.17. EPS effect in bioprinted rings a) anchored to bioprinted silicon pillars. b) Muscle fiber electrogram displaying the contraction amplitude at 1, 2 and 3 Hz pulse frequencies. Red dashed lines represent 1s periods. c) Contraction amplitude of fibers responding to EPS for 3 days. d) RTqPCR analysis of the expression of differentiation genes in samples electrically stimulated for 3 days vs non-stimulated (control) (n=3). e) Confocal images of C2C12 fibers after EPS treatment for 3 days showing sarcomeric bands of F-actin (green) and α-actinin (red). Scale bar = 20 µm. Data is presented as mean ± SD, one-way ANOVA and Unpaired t-test *p-value < 0.05 and ***p-value < 0.0005.

Unaltered genetic expression of sarcomeric proteins might suggest that the muscle maturation state in bioprinted rings was below the monolayer cultures. However, fluorescence staining of α-actinin and MHC revealed highly defined sarcomere units with strong protein expression (Figure 3.17e). During the 3 days of electrical pulse stimulation, fibers displayed similar steps to those observed in *Drosophila melanogaster* sarcomerogenesis [72, 103] (Figure 3.18a). F-actin in unstimulated fibers was aligned towards the longitudinal axis of the cell and showed low expression of α-actinin. Electrically stimulated fibers revealed a transitory state where F-actin appeared as punctuated disorganized mesh and images revealed increased expression of α-actinin. Finally, F-actin is reorganized into A-bands crosswise to the longitudinal axis. At the same time, α-actinin was concentrated in the Z-disks, forming intercalated bands with F-actin. The cytoskeleton reorganization resulted in the formation of sarcomeres with 2.8 µm separation between Z-disks (Figure 3.18b), which was in concordance with the assumed optimal sarcomere length for a 120º ankle angle in anesthetized mouse *in vivo* [311].

Together with the strong contractions found in the video recordings, it was demonstrated that murine muscle fibers in bioprinted GelMA-AlgMA-fibrin rings were functional and presented an advanced maturation state. The formation of sarcomeres in the absence of upregulated sarcomeric proteins suggested that muscle fibers achieved a more advanced maturation in GelMA-AlgMA-Fib rings prior to the EPS training, thus confirming the myogenic properties of the composite biomaterial.

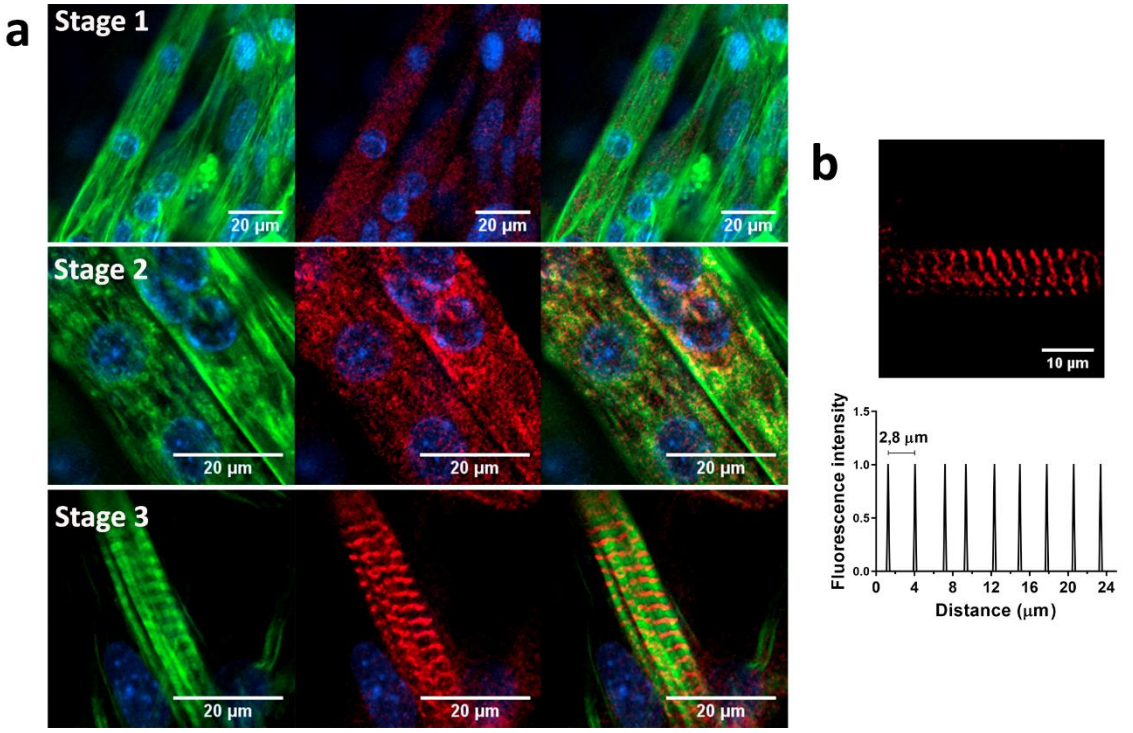

Figure 3.18. **Actin cytoskeleton rearrangement during sarcomerogenesis in bioprinted muscle rings.** a) Confocal images of the three visible stages of sarcomerogenesis displaying stained F-actin (green) and α-actinin (red). Scale bar 20 µm. b) Calculation of the distance between Z-disks (or sarcomere length) based on the fluorescence intensity of α-actinin stained samples. Scale bar 10 µm.

3.4. The role of EPS and nutrients in the hypertrophy of bioprinted muscles

Contractile activity of muscles is known to promote the synthesis of new proteins. Exercise is known to induce muscle hypertrophy through the activation of the mammalian target of rapamycin (mTOR) pathway, which is also involved in downregulating muscle atrophy pathways [312-315]. To evaluate the quality of the EPS system and study the response of bioprinted muscle rings, the activity of the mTOR pathway in stimulated models was analyzed. Furthermore, many studies underline the role of an appropriate aminoacid supplementation for the synthesis of proteins. AAs are used as direct substrates for the catabolic reaction, however, they also activate the mTOR signaling pathway by its recruitment to the lysosome surface, where they interact with Rheb GTPase and activate mTOR pathway [316]. Therefore, the response of bioprinted models to external biomolecules as aminoacids (AA) was also studied. To that end, the level of phosphorylated ribosomal protein S6 (p-rpS6) in paraffined sections was analyzed. rpS6 is a protein residing in the 40S ribosomal subunit. It is downstream of the mTOR pathway and plays an important role in mRNA translation [317].

Bioprinted rings were anchored, treated and removed from the EPS system for their posterior paraffination. Bioprinted rings cultured in GM and AA-depleted RPMI showed similar basal expression of p-rpS6, suggesting that conventional FBS and dialyzed FBS induced equivalent effects. Immunostaining images showed that bioprinted models stimulated with electrical pulses increased the protein expression levels of p-rpS6, whereas unstimulated models had low expression of the phosphorylated form (Figure 3.19). Increased signal of p-rpS6 indicated enhanced protein synthesis. Therefore, it was hypothesized that EPS mimicked the effects of exercise *in vivo* and promoted the hypertrophy of engineered muscles. In parallel, it was found that AA supplementation had a strong influence on the upregulation of p-rpS6 protein expression. The stained sections demonstrated that a suitable supplementation of aminoacids is required for the activation of the protein synthesis pathways. Thus, the availability and concentration of aminoacids in the medium play a key role in the hypertrophy process of engineered muscles.

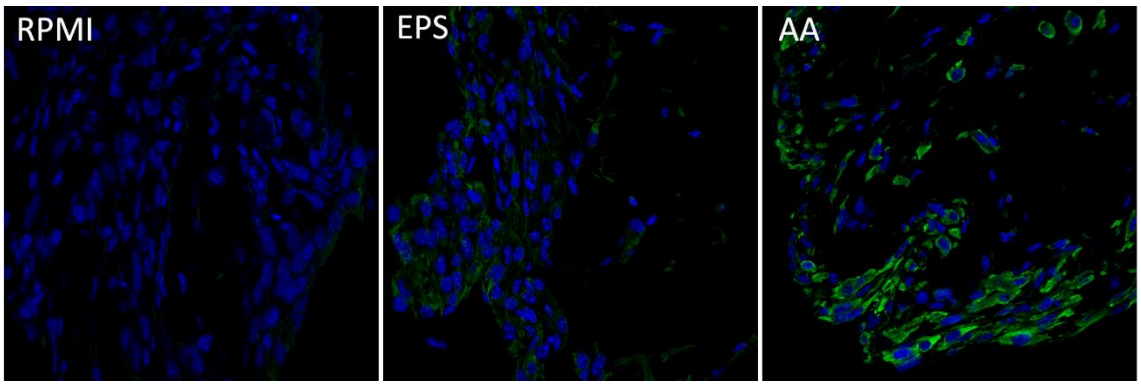

Figure 3.19. EPS and AA effect in protein synthesis of bioprinted rings. Paraffin sections of bioprinted rings treated with AA-depleted RPMI (RPMI), electrically stimulated for 1h (EPS) and supplemented with AAs for 15 minutes (AA). Images show nuclei stained in blue and rpS6 (Ser235/236) stained in green.

4. Applications of bioprinted rings as *in vitro* models of skeletal muscle tissue

4.1. Scalability of bioprinted muscle models for high-throughput screening devices to study the effects of β-carboline compounds in energy metabolism

In previous sections, it was demonstrated that bioprinted models of GelMA-AlgMA-fibrin biomaterial achieved functional and mature skeletal muscle tissue models. *In vitro* skeletal muscle models must recapitulate the response of native tissue to different stimuli. In that way, the results can be used to predict the effect of bioactive compounds in skeletal muscle tissue.

Metabolism and mitochondrial respiration dynamics are closely related to skeletal muscle conditions. Numerous pathologies are characterized by altered metabolism that can lead to muscle malfunction (i.e. diabetes) or arise as a secondary effect of the disease (i.e. DMD, cachexia). In fact, muscle metabolic diseases have been related to mitochondrial dysfunction [318-320]. Therefore, the mitochondrial metabolic flux of engineered muscles can be indicative of health status and function.

To analyze the metabolic activity of bioprinted rings, bioenergetic changes in response to electron transport chain (ETC) inhibitors were monitored. Thanks to the versatility of bioprinted rings, their size was adapted for the Seahorse XFe24 Flux Analyzer platform. The analyzer measured the extracellular oxygen concentration to determine the oxygen consumption rate (OCR). Engineered muscle ring models successfully responded to inhibitors and displayed the characteristic metabolic profile found in muscle fibers [321, 322]. Real-time analysis of the OCR revealed that basal respiration of C2C12 differentiated fibers in bioprinted rings was 3.5 pmol/min/ug of protein (Figure 3.20a). Oligomycin bound to the F0 subunit of the ATPase and blocked the ETC, which revealed the oxygen consumption originated from proton leakage and ROS production. It was found a scarce difference in OCR after the oligomycin and AA/Rot treatments, which meant a good ETC integrity and low proton leakage [323]. The addition of FCCP uncoupler with blocked ATPase revealed the capability of cells to adapt to increased oxygen demand. It was evidenced that engineered muscles successfully responded to consecutive doses of FCCP. Mitochondria of engineered fibers were able to adapt to high doses of FCCP, which increased the OCR over the basal respiration rate to meet the high oxygen demand. Under acute cellular stress or high bioenergetic demand conditions, cells must be capable of modulating the OCR to achieve enough substrate concentration to produce the needed ATP for cell survival [324]. In this line, engineered muscles showed good mitochondrial response to high energy demand situations, indicating good mitochondrial health and fitness.

The versatility of bioprinted rings and their adaptation to the Seahorse Analyzer provided a platform to study changes in the metabolic flux of engineered muscle models. Recent years of research have demonstrated different pharmacological effects of β-carboline compounds. They are found in a great variety of plants, and the derivatives are widely used in medicine because of their anti-inflammatory, antioxidant, antitumoral and

antibacterial effects [325]. It was found that controlled dosages of β-carbolines increased the respiratory chain activity in rat brains, which was suggested to counteract the age-related neurodegenerative effects and act as a neuroprotector [326]. However, different derivatives of β-carbolines can cause mitochondrial dysfunction and death in hepatocytes [327]. β-carbolines have potential applications in the pharmacological industry, however, there is a need to identify and study the effects of the different derivatives on each tissue type.

To study those effects in skeletal muscle tissue, bioprinted muscle rings were treated with one plant extract (PE) rich in β-carbolines and one of its isolated active ingredients (IAI) for 24h. Then, the OCR of the different treated models was analyzed after the addition of the electron transport chain inhibitors described before. The metabolic flux profile of bioprinted models treated with the isolated compound did not show significant differences from the control model (Figure 3.20b). In concordance, the values of basal respiration, maximal respiration, ATP production and spare respiration in IAI treatment were similar to control treatment (Figure 3.20c). In contrast, bioprinted models treated with the plant extract showed increased mitochondrial activity. The results displayed increased basal respiration, which meant an increase in total oxygen consumption that could be derived from higher ATP production rate, higher proton leak or increased production of non-mitochondrial ROS [326]. The addition of oligomycin and ATP synthesis blocking revealed an increased oxygen consumption rate, which was due to increased proton leak. However, the difference in oxygen consumption rate between basal state and oligomycin treatment revealed an increased ATP production. From those results, it can be deduced that plant extract increased the mitochondrial activity and ATP production, however, it could also compromise the membrane permeability.

The difference between basal respiration and maximal respiration is correlated with the plasticity of mitochondria and the capability to overcome stress situations avoiding an ATP crisis [327]. Engineered muscles treated with plant extract showed increased maximal respiration, which resulted in a higher spare respiratory capacity. Although differences were not statistically significant due to high variability, results suggested that plant extract improved the capability of muscle fibers to respond to acute stress, thus improving “mitochondrial fitness”. Several diseases lead to mitochondrial impairment in skeletal muscle tissue, which can result in accelerated atrophy of the fibers. Therefore, the β-carbolines present in the plant extract has potential pharmacological effects to improve the mitochondrial activity in skeletal muscle tissue. However, the β-carboline derivative analyzed in this study did not induce significant changes in mitochondrial activity. Thus, more extended studies are needed to identify the compounds of interest.

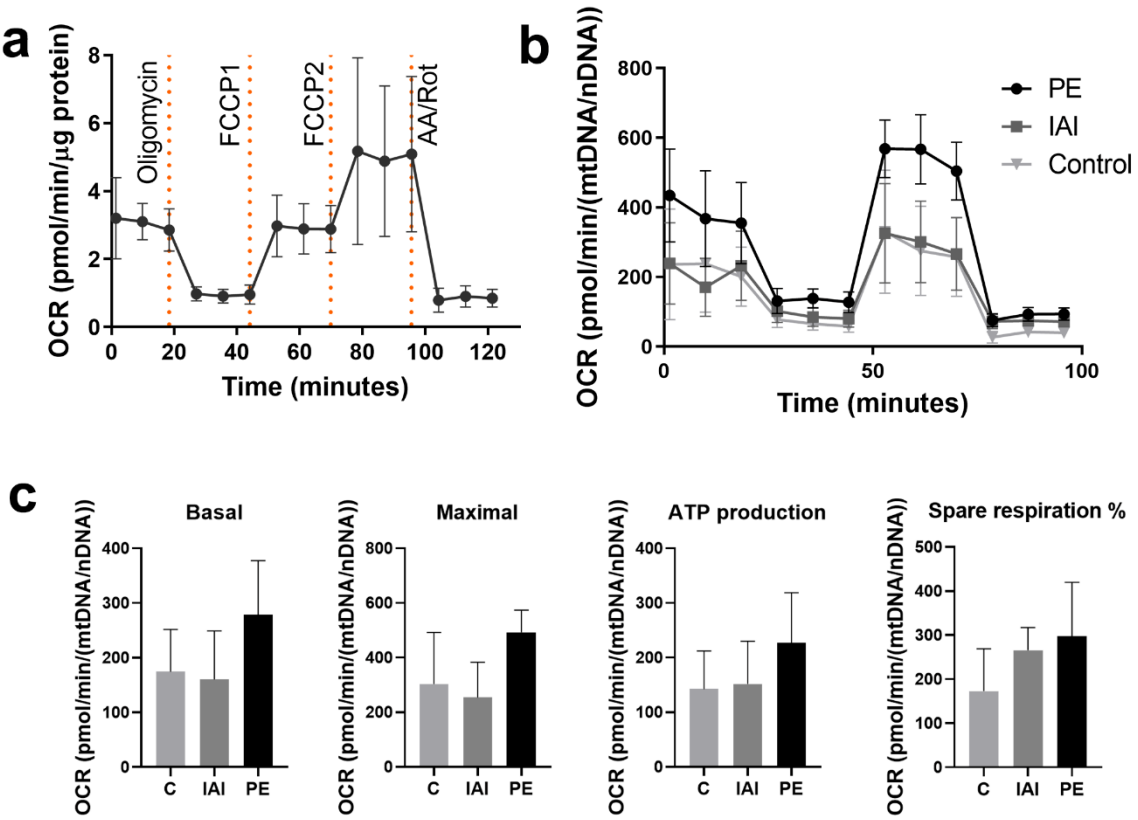

Figure 3.20. Mitochondrial respiration analysis of C2C12 muscle fibers in bioprinted rings using XFe24 Seahorse analyzer. a) Oxygen consumption rate (OCR) measured by Mito Stress Test after the application of Oligomycin, two doses of FCCP and antimycin/Rotenone (AA/Rot). b) OCR measured during Mito Stress Test in bioprinted rings treated with plant extract (PE) and isolated active ingredient (IAI), and c) the calculations of the resulting mitochondrial basal respiration (basal), maximal respiration (maximal), ATP production and spare respiration %.

4.2. Potential application of bioprinted models to study cancer cachexia-derived muscle wasting

Metabolic alterations of skeletal muscle tissue can be found in many types of disorders. Cachexia has been recently defined as a multifactorial syndrome characterized by the ongoing loss of skeletal muscle mass that cannot be fully reversed by conventional nutritional support and leads to functional impairment [328]. The pathophysiology of cachexia includes negative protein and energy balance, abnormal metabolism, and a weight loss greater than 5%, with or without the loss of fat mass. Cachexia is given in aging and several chronic diseases, particularly in cancer. Furthermore, cancer patients showing cachexia have a poor prognostic, worse response to cancer treatment and shortened lifespan.

There is no clear evidence that unveils the starting mechanisms of muscle wasting in cancer cachexia (CC) [118]. Nevertheless, it is known that muscle loss is mainly driven by an unbalanced protein turnover, where protein synthesis is downregulated and there is hyperactive proteolysis. Proteolytic activity in cancer cachexia is guided by the upregulation of the ubiquitin-proteasome pathway and altered autophagy pathway [329]. *Atrogin-1* (Fbxo32) and *MuRF1* (Trim63) are one of the main E3 ubiquitin ligases

participating in CC. They are responsible for the ubiquitination of sarcomeric structural proteins for their subsequent transport to the proteasome complex and degradation. Together with the unbalanced protein turnover, some studies showed altered mitochondrial dynamics, where muscle fibers presented an upregulated fission in mice with advanced cachexia [330]. Despite the importance of cachexia in cancer patients, there is still considerable controversy about the underlying molecular mechanisms, which explains the lack of treatments for this disease.

As a control, we first analyzed the effect of cancer cells-derived conditioned medium on monolayer cultures of C2C12 fibers was evaluated. Colon cancer is one of the diseases with the highest prevalence of cachexia. Therefore, colon cancer cell lines were chosen for the induction of muscle wasting. Conditioned medium (CM) was obtained after the culture of colon cancer cell lines in C2C12 growth medium for 48h. For the experiments in monolayer cultures, the conditioned medium was obtained from the supernatant of LS174T cell line culture.

Calcein staining of differentiated muscle fibers cultured in conditioned medium for 72h showed the characteristic phenotype of patients with cachexia. A decrease in muscle fiber diameter has been observed in patients with cancer cachexia and tumor-bearing mice models [331, 332]. The treated fibers were alive and did not show signs of toxicity or apoptosis. Instead, the diameter of muscle fibers decreased from 10 µm to 5 µm (Figure 3.21a). The cytoplasm of the fibers was shrunk to such an extent that the contour of the nuclei was visible.

The morphology of fibers was indicative of accelerated protein metabolism. To evaluate the effects of conditioned medium on the protein synthesis, the expression of sarcomeric proteins (*Acnt2, Tnnc2, Myh4, Myh1, Myh2* and *Myh7*) was studied. To study the changes in the proteolytic activity, the genetic expression of genes encoding for E3 ubiquitin ligases (*Trim63, Fbxo31* and *Fbxo32)* and mitochondrial fission (*Fis1*) were analyzed (Figure 3.21b).

The genetic expression of fibers cultured in conditioned medium highlighted strong downregulation of *Acnt2, Tnnc2, Myh4, Myh1* and *Myh2*. However, *Myh7* expression was unaltered (Figure 3.21b). As reported in many *in vitro* studies, CC is accompanied by the downregulation of protein synthesis pathways related to sarcomere structure [332, 333 334]. It was seen that Zip14 receptor could be involved in the blockade of *MyoD* and *Mef2c* expression, thus impeding the expression of myosin heavy chains [332]. Similarly, Nayak *et al.* found that SENP3 protein was degraded in the cachectic C2C12 line, which lead to a downregulation in MyHC-IIx (encoded by *Myh1*) at the mRNA and protein level [334].

In the last years, several studies demonstrated that the severity of CC effects differs among the fiber types [335]. Mendell and Engel described preferential atrophy of type II fast muscle fibers in cachexia [336], which was later confirmed by other authors [335, 337]. Indeed, higher degeneration of fast type fibers was in fasting, glucocorticoid administration, AIDS and aging, among others [338-341]. It was hypothesized that selective atrophy of skeletal muscle tissue could be related to the oxidative nature of fibers. PGC1α, which is required for oxidative metabolism and regulates the formation of oxidative type I fibers, was suggested to have a protective role against protein

degradation. In this way, it was proposed that higher content of PGC1α in slow-type fibers could result in better resistance to muscle atrophy than fast-type fibers [342]. However, overexpression of PGC1α had the opposite effect and led to muscle wasting [343]. As may be seen, there is still a big controversy concerning the fiber type selection in atrophy processes. Nevertheless, the gene expression results in C2C12 treated with CM were in concordance with previous studies of cancer cachexia, where slow-type fibers expressing *Myh7* were not affected.

The effect of CM in the upregulation of E3 ubiquitin ligases was studied (Figure 3.21b). As reported in previous works, *Fbxo32* (Atrogin 1) and *Fbxo31* E3 ubiquitin ligases were upregulated [332]. Oppositely, *Trim63* (MuRF1) was downregulated. Atrogin1 and MuRF1 have been described as universal factors involved different processes of muscle atrophy [344]. More specific studies confirmed that both Atrogin1 and MuRF1 were upregulated in cancer cachexia [345]. In contrast to those studies, muscle fibers treated with conditioned medium did not show upregulated expression of *Trim63* (MuRF1).

It was hypothesized that the control medium presented some effects of nutrient deprivation. In order to discard the effects of nutrient starvation due to the 48h of incubation, control samples received a similar treatment. The medium was collected from the supernatant of C2C12 cultured for 48h and used to treat C2C12 fibers for 72h. It was found that muscle fiber cultured in control medium upregulated the expression of *Trim63* (MuRF1), which suggested that nutrient starvation could have a stronger effect in MuRF1 upregulation and masked the effects of cancer-derived supernatant (Figure 3.22).

Muscle wasting in CC has been also associated with upregulated activity of autophagy and altered mitochondrial dynamics [329]. White *et al.* revealed downregulated expression of genes related to mitochondria fusion and upregulated expression of those related to fission in $Apc^{Min/+}$ cachectic mice models [346]. *Fis1* mitochondrial receptor was highly upregulated, which is involved in the activation of mitochondria fission. It is known that its activity is required to remove the damaged parts of mitochondria due to acute stress and induce apoptosis. Nevertheless, muscle fibers in monolayer treated with CM did not show upregulated expression of *Fis1*.

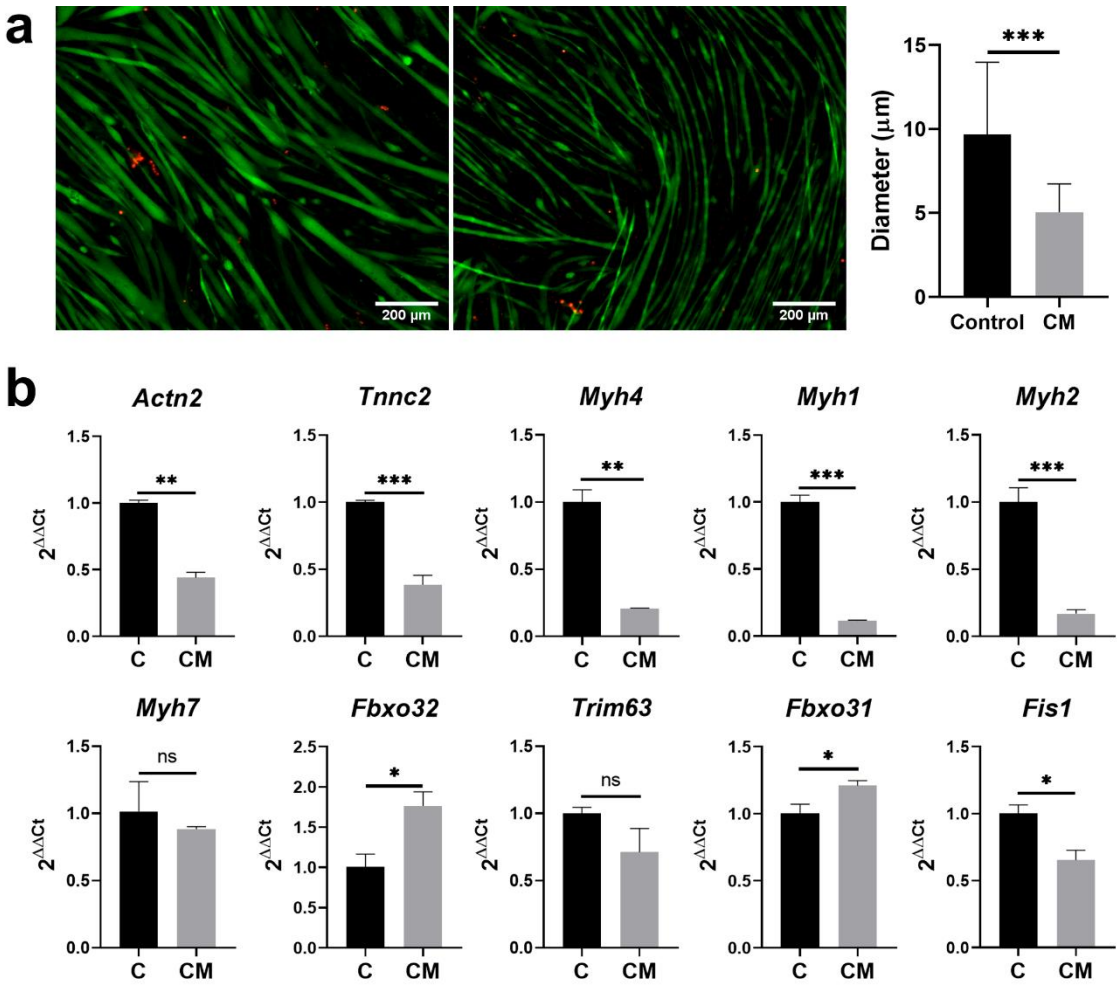

Figure 3.21. Effect of colon cancer cell-conditioned medium (CM) in C2C12 cultures. a) Confocal images of stained live (green) and dead (red) cells in control and cancer-cells conditioned medium (CM) for 72h. Scale bar 200 µm. Bar chart of fiber diameters in CM and control (n=42). b) Genetic expression fold change of control (C) vs monolayer cultures treated with LS174T conditioned medium (CM) (n=4). Data is presented as mean ± SD, Unpaired t-test, Two-way ANOVA *p-value < 0.05, **p-value < 0.005 and ***p-value < 0.0005.

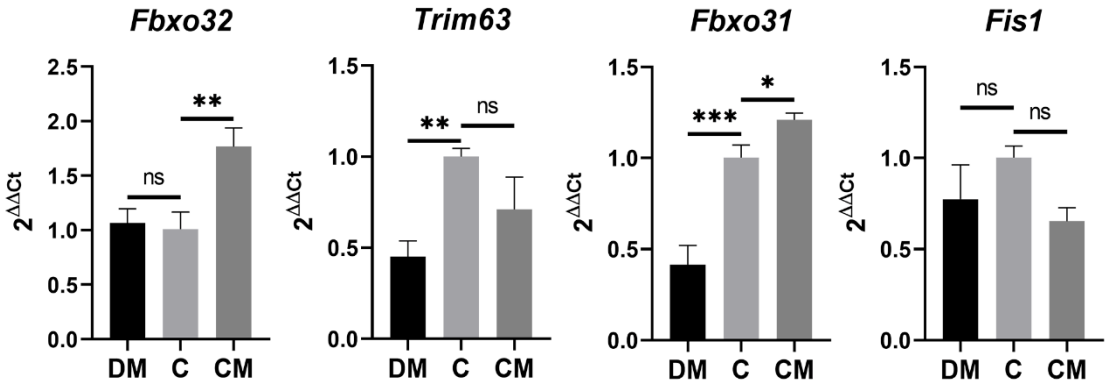

Figure 3.22. Effect of nutrient starving in C2C12 differentiated fibers. RTqPCR analysis of the genetic expression of E3 ubiquitin ligases and Fis1 after 72h in differentiation medium (DM),

C2C12 48h supernatant (C) and cancer cell 48h conditioned medium (CM) (mean ± SD, One-way ANOVA, *p-value < 0.05, **p-value < 0.005 and ***p-value < 0.0005, n = 4).

The results found in treated monolayer cultures of muscle fibers demonstrated that medium conditioned with colon cancer cells was a valuable strategy to induce cancer-induced cachexia in skeletal muscle tissue *in vitro*. Afterward, the effect of conditioned medium in bioprinted muscle models was studied. In these experiments, the effect of LS174T (LS) and HCT116 (HCT) cell lines supernatants was considered.

The morphology of muscle fibers in bioprinted rings treated with conditioned medium did not show noticeable changes in comparison with untreated fibers. In agreement with that finding, significant changes in fold expression of sarcomeric structural genes were only appreciable in *Actn2*, while genes encoding for myosin heavy chains were not significantly affected (Figure 3.23a). Intriguingly, *Myh1* and *Myh2* were upregulated in HCT treatment. All the conditioned mediums were collected at 80% of cell confluency, however, LS174T cells are often organized in clusters resulting in a higher number of total cells. Therefore, it could be thought that the supernatant of HCT116 preserved higher nutrient content, resulting in higher expression of sarcomeric proteins.

Since the morphology of fibers and the expression of genes related to myosin heavy chain proteins remained unchanged, it could be hypothesized that conditioned medium had a lower influence in 3D models than in 2D models. In contrast to that supposition, the expression of *Fbxo32, Fbxo31* and *Fis1* was dramatically upregulated in bioprinted rings (Figure 3.23a). In concordance with previous studies of cancer cachexia, Atrogin1 (*Fbxo32*) was the most upregulated E3 ubiquitin ligase [344]. Nevertheless, the conditioned medium of LS174T showed higher expression of Atrogin1 than HCT116.

To shed some light on the nature of those variabilities, the composition of several inflammatory factors of HCT and LS conditioned mediums were analyzed (Figure 3.23b). There is a considerable amount of literature about the role of inflammatory factors in muscle atrophy. Many studies suggest that cancer secreted factors as TNFα, IL-6 and IFNγ activate the signaling cascade of different pathways, as NFκB and STAT3, consequently upregulating the expression of E3 ubiquitin ligases and downregulating protein synthesis [347, 348]. The diversity of inflammatory factors in LS was found wider than in HCT. LS supernatant displayed upregulated expression of MIP-1δ, MIG, M-CSF, TNFRI and TNFRII, while HCT was mainly composed of IL6R, PDGF-BB and TNFRI. Among them, both presented remarkably higher expression of TNF receptor I (TNFRI), particularly in LS, which showed the highest concentration.

TNFRI is a transmembrane protein that binds TNFα through its extracellular domain and activates signaling pathways related to protein breakdown, apoptosis and inflammation [349]. In skeletal muscle, TNFRI-TNFα complex has shown a bimodal effect, where low concentrations of TNFα (< 0.05 ng/ml) demonstrated an essential role on muscle regeneration, while high concentrations (> 0.5 ng/ml) impaired myogenesis and differentiation [350, 351]. In tumor cells, TNFRI is cleaved from the membrane or secreted inside extracellular vesicles (EVs) to protect them from TNFα induced apoptosis. Indeed, high levels of soluble TNFRI (sTNFRI) in serum have been associated with late stages of CC and high mortality, thus suggesting TNFRI as a potential biomarker for CC

[352]. Clear evidence was observed after the analysis of TNFRI concentration in plasma of cachectic mice (mCC). The average concentration of soluble TNFRI in cachectic mice (mCC) was 2.9 ng/ml, which was two-fold higher than in healthy mice (C) (Figure 3.23c). In agreement with those results, LS conditioned medium, which presented higher TNFRI secretion, showed increased upregulation of Fbxo32 and Fbxo31, suggesting a greater influence in the activation of the proteasome pathway. The results suggested that medium conditioned with LS174T cells showed a more aggressive cachectic pathology.

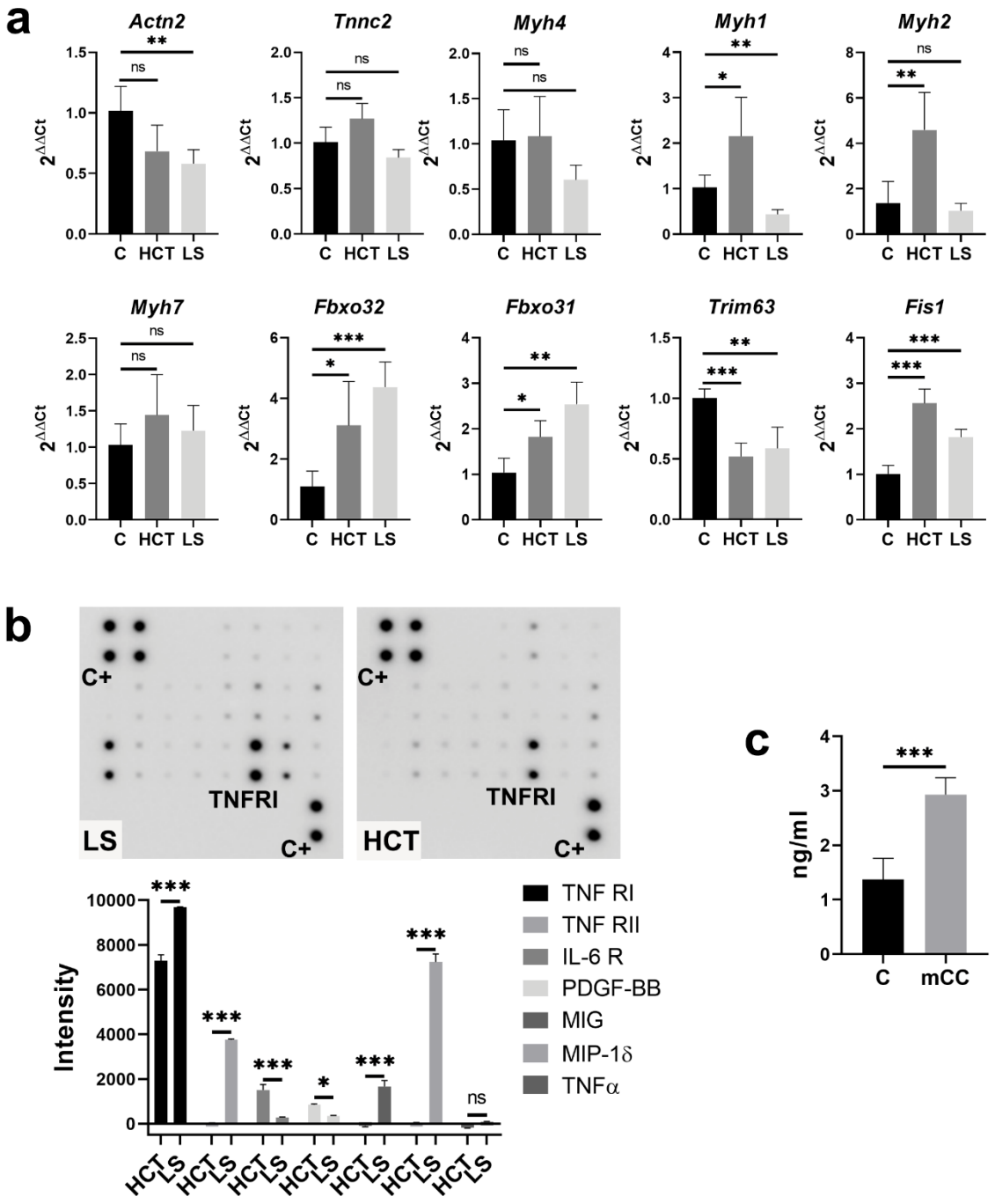

Figure 3.23. Effect of colon cancer cell-conditioned medium (CM) in bioprinted muscle rings. Conditioned mediums were prepared with HCT116 (HCT) and LS174T (LS) cell lines. a) RTqPCR analysis of the genetic fold expression of fiber differentiation genes (Actn2, Tnnc2,

Myh4, Myh1, Myh2 and Myh7), E3-ubiquitin ligases (Fbxo32, Trim 63 and Fbxo31) and autophagy related genes (Fis1) in non-treated (C) and treated bioprinted rings with LS and HCT for 72h (n=4). b) Array of inflammatory factors in HCT116 and LS174T CMs. The intensity of the most relevant dots was analyzed and displayed in a bar chart. C) TNFRI ng/ml in plasma of control (C) and 24 days tumour-bearing cachectic mice (mCC) (n=4). Data is presented as mean ± SD, One- and Two-way ANOVA, *p-value < 0.05, **p-value < 0.005 and ***p-value < 0.0005.

TNFRI upregulation was not accompanied by an upregulation of the TNFα factor (Figure 3.23b). Although TNFα has been described as a potential plasma biomarker of cachexia in colon cancer patients, the results indicated that nor HCT neither LS contained a notable amount of the soluble factor. Therefore, muscle wasting after the treatment with conditioned medium was not directly induced by soluble TNFα secreted from colon cancer cells. There is an increasing trend that associates skeletal muscle wasting in cancer cachexia with components of tumor cells secreted via extracellular vesicles (EVs). It was demonstrated that miRNAs and bioactive molecules like Hsp70/90 and adrenomedullin could be encapsulated in EVs, which enhanced their transport through the circulatory system [353, 354].

The role of cancer cells-secreted extracellular vesicles on the induction of muscle wasting in bioprinted rings were studied. Exosomes and microvesicles of LS174T and HCT116 conditioned mediums were isolated. The concentration of microvesicles and exosomes in LS was higher than in HCT, which contained 0.56 and 1.01 µg/µl, in front of 0.13 and 0.55 µg/µl respectively. For the life tracking of exosomes, they were stained with SYTO^{TM} RNASelect and the concentration was adjusted to 10µg in both treatments. Stained exosomes were filtered to remove the soluble marker. After 2h of incubation, C2C12 differentiated fibers in monolayer cultures showed green fluorescence, while there was no detectable signal in those cultures without exosomes (Figure 3.24a). However, muscle fibers treated with isolated EVs from LS174T and HCT116 conditioned mediums did not show a significant effect on their morphology and genetic expression (Figure 3.24b).

The experimental results suggested that muscle wasting on *in vitro* engineered muscle models were induced by soluble factors secreted by colon cancer cells, instead of encapsulated factors. However, more exhaustive studies are needed to unveil the factors and biological processes implicated in cancer-associated muscle wasting.

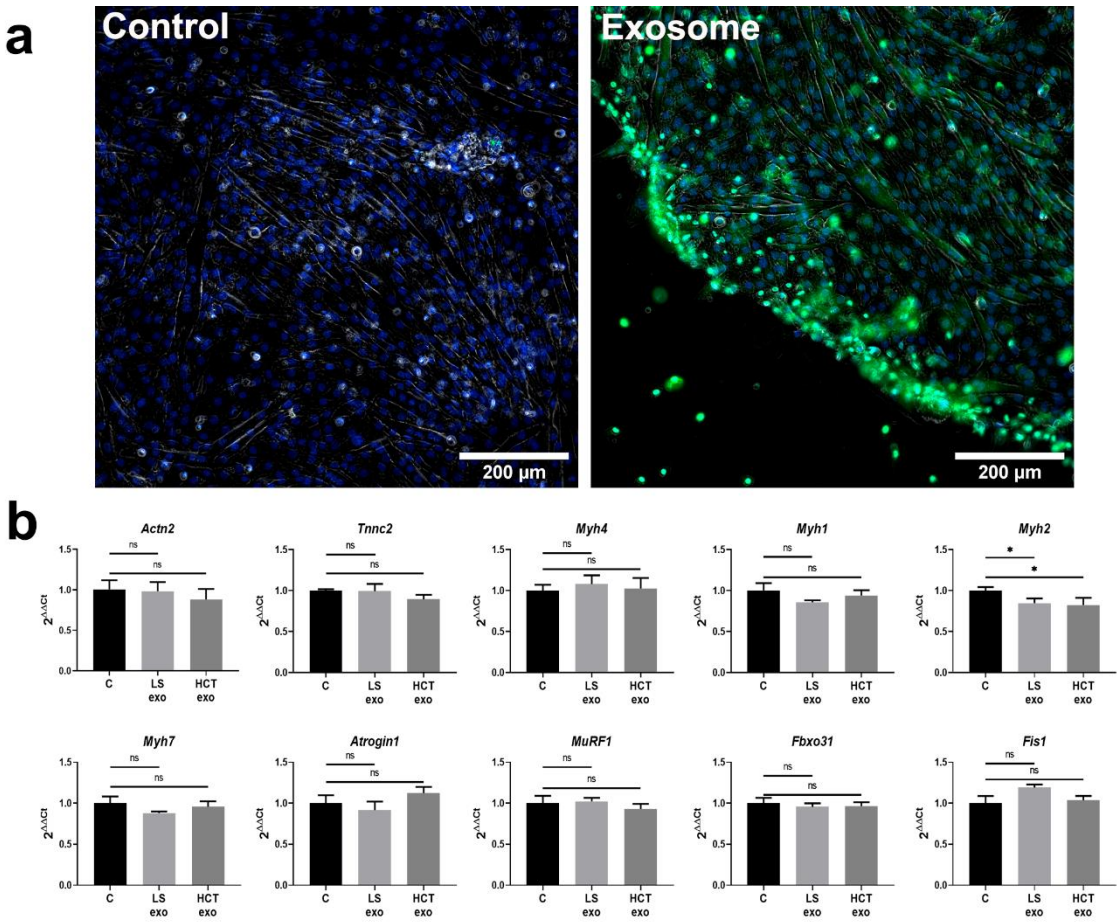

Figure 3.24. LS and HCT isolated exosome treatment effect in C2C12. A) Study of the exosome engulfment in C2C12 differentiated fibers. Exosome suspension and diluent alone (control) were stained with SYTO RNA marker (green) and filtered to remove the soluble marker. Control and exosome suspensions were incubated for 2h and observed at the microscope. Scale bar 200 µm. b) Genetic expression analysis of fiber differentiation genes (Actn2, Tnnc2, Myh4, Myh1, Myh2 and Myh7), E3-ubiquitin ligases (Fbxo32, Trim 63 and Fbxo31) and autophagy-related genes (Fis1) after 72h of exosome treatment (mean ± SD, One-way ANOVA, n = 3).

To validate the usability of bioprinted muscle rings (3D) for the study of muscle wasting in cancer cachexia, the genetic expression profile was compared with tumor-bearing mice (*in vivo*) and monolayer cultures (2D) (**Figure 3.*25***). To that end, mice were inoculated with melanoma cancer cells known to induce cachexia in skeletal muscle tissue. The genetic expression of sarcomeric structural genes was not significantly affected in cachectic mice. *Actn2, Tnnc2, Myh4, Myh1* and *Myh2* showed a decreasing trend, but it was not significant from control mice. As reported in KPP mouse models and C26 tumor-bearing mice, the mRNA content of MyHC in the quadriceps was not significantly altered, particularly in the case of slow and intermediate type fibers [119, 355]. In agreement with other studies of cachexia in mice, *in vivo* models showed a fast-to-slow fiber type transition with upregulated expression of *Myh7* [335]. Similarly, only fast type MyHCs were affected in bioprinted muscle models and *Myh7* was slightly upregulated, while all MyHC types were dramatically downregulated in 2D models.

The ubiquitin proteasome activity in cachectic mice models was enhanced, as demonstrated by *Fbxo32* (Atrogin1) and *Trim63* (MuRF1) expression upregulation, which is in line with previous studies [344]. It was found an increasing tendency of *Fbxo31* and *Fis1* expression, however, changes were not significant. Here again, bioprinted muscle models showed closer similarities to *in vivo* models than 2D cultures. The fold change of *Fbxo32* expression was found very similar between the *in vivo* and 3D models. It presented 4.5-fold higher expression than control mice, which was close to the 4-fold expression found in 3D. In contrast, 2D cultures presented a 1.7-fold upregulation. As explained before, the upregulation of MuRF1 was probably masked by the nutrient starving effect on *in vitro* cultures. Therefore, future experiments should consider a strategy to preserve high nutrient content during the treatment with conditioned medium. Intriguingly, the fold change of *Fbxo31* and *Fis1* was found higher in bioprinted models than in mice.

It is now known that the type of E3 ubiquitin ligases involved in the process of cachexia differs among the type of muscle group and the type of cancer. *Fbxo31* was upregulated in tibialis anterior and diaphragm muscles of mice with colon cancer-induced cachexia [332]. However, the results in mice bearing melanoma cells suggested that this type of cancer did not severely induce *Fbxo31* in mice. Similarly, it was seen an upregulated expression of Fis1 in colorectal cancer murine models, while melanoma models did not show significant alteration [346]. The findings point to variations in the gene expression pattern of the genes related to the protein degradation among different types of cancer, which should be considered in studies related to cancer cachexia. According to previous studies in cachexia derived from colorectal cancer, the response obtained in bioprinted muscle rings recapitulated the upregulation of E3 ubiquitin proteasomes and mitochondrial fission more faithfully than 2D models. Bioprinted models showed higher expression of *Fbxo32*, *Fbxo31* and *Fis1*, while they showed low expression of E3 ubiquitin ligases and downregulated expression of *Fis1* in 2D.

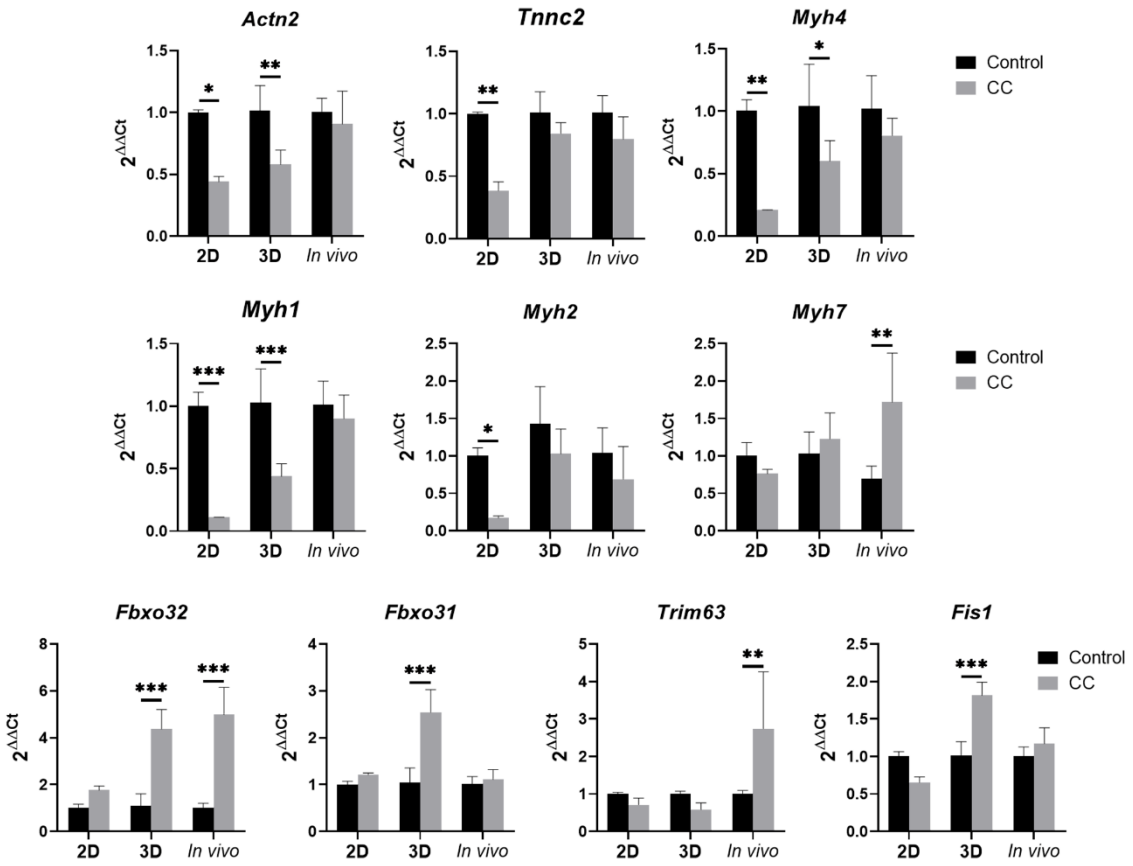

Figure 3.25. Genetic expression of cachexia-related genes in 2D, 3D and *in vivo* models. RTqPCR analysis of the genetic fold expression of sarcomeric proteins (Actn2, Tnnc2, Myh4, Myh1, Myh2 and Myh7), E3-ubiquitin ligases (Fbxo32, Trim 63 and Fbxo31) and autophagy related genes (Fis1). Comparison between muscle cachexia models (CC) of monolayer cultures (2D) and bioprinted rings (3D) treated with conditioned mediums of LS174T, and tumor-bearing mice (*in vivo*). Each group is compared with the corresponding non-treated controls (n=4). Data is presented as mean ± SD, One- and Two-way ANOVA, *p-value < 0.05, **p-value < 0.005 and ***p-value < 0.0005.

5. Other applications of GelMA-AlgMA biomaterial in tissue engineering: bioprinted neuroblastoma models

GelMA-AlgMA in combination with Fibrin was presented as a promising biomaterial to recapitulate the ECM of skeletal muscle tissue and develop mature and functional *in vitro* models. Afterward, it was explored the adaptability and potential applications of GelMA-AlgMA to engineer alternative tissues, as tumor models. The tumor microenvironment (TME) has been studied as one of the most important factors affecting tumor behavior and progression. TME is composed of cancer cells and stromal cells in an altered ECM, whose mechanical properties are usually modified resulting in stiffer matrices [356]. Higher elastic modulus has been associated with an aberrant and massive deposition of collagen and elastin fibers by cancer-associated fibroblasts and other stromal cells. In solid tumors like neuroblastoma, aberrant matrix deposition is one of the reasons for increased interstitial fluid pressure [357], which hampers drug arrival through the circulatory system and hinders the treatment. Indeed, high-risk tumors in neuroblastoma patients were characterized by high stiffness tissue formed by increased deposition of ECM fibers [358]. Therefore, tumor models must consist of biomaterials with high polymer fiber density and appropriate stiffness.

5.1. GelMA-AlgMA bioink modification to emulate high-risk neuroblastoma matrices

To study the effect of matrix stiffness in neuroblastoma cell clusters, a strategy to modulate the mechanical properties of the composite biomaterial was required. Previously, GelMA-AlgMA stiffness was increased by the addition of fibrin, while the porosity of the matrix was incremented by the reduction of photoinitiator concentration. The addition of low fibrin concentration did not significantly alter the porosity of the biomaterial. To better recapitulate the TME of neuroblastoma, increased stiffness had to be accompanied by a notable increase in matrix ECM fiber concentration. In this line, increasing the photoinitiator concentration resulted in biomaterials with higher stiffness, however, the concentration of the biopolymers remained constant.

A different strategy was focused on the modification of GelMA concentration. However, GelMA is one of the main components that determine the viscosity of the biomaterial, thus its modulation could compromise the printability of the bioink. As an alternative, the first modification of GelMA-AlgMA biomaterial to obtain higher stiffness was focused on the addition of higher AlgMA concentration. Compressive modulus results showed that stiffness increased with AlgMA concentration (Figure 3.8a). The addition of 1% and 2% AlgMA increased GelMA stiffness from 1.5 to 7.1 and 20.3 kPa respectively. As stated in previous results, AlgMA% also modulated biomaterial porosity (**Figure 3.*8***b). It was found that higher AlgMA concentration decreased biomaterial porosity. Consequently, SK-N-BE(2) and SH-SY5Y neuroblastoma cells were encapsulated in biomaterials of 5% (w/v) GelMA with 0, 1 and 2% (w/v) of AlgMA. Using those formulations, neuroblastoma cells were successfully encapsulated into bioprinted squares.

5.2. Evaluation of the effect of tissue stiffness in the evolution of neuroblastoma cell clusters *in vitro*

First, SK-N-BE(2) cells were cultured in GelMA with 0, 1 and 2% AlgMA bioprinted structures. After the fabrication process of 3D models, cells presented good viability and proliferated as clusters inside the biomaterial. The morphology, distribution and frequency of clusters were analyzed using paraffin sections of bioprinted squares stained with hematoxylin and eosin (Figure 3.26a). After 2 weeks of culture, SK-N-BE(2) clusters showed irregular morphology, spread cluster and poor cell density. In contrast, clusters in 1% and 2% AlgMA displayed more round morphology and cell density, particularly in 2% AlgMA, where clusters were smaller and more spherical. After 4 weeks of culture, AlgMA 0% showed a high number of clusters per mm^2 of small sizes, while clusters in AlgMA 2% were less numerous, but presented larger diameters.

To characterize the long-term effect of biomechanical properties on tumor aggressiveness, SK-N-BE(2) and SH-SY5Y cell lines were cultured over long time spans in soft (AlgMA 0%) and stiff (AlgMA 2%) gelatin-based hydrogels. Immunohistochemistry (IHC) staining of Ki67 showed that proliferation dynamics completely differ from one cell line to another (Figure 3.26b). SK-N-BE(2) cells appeared to be far more proliferative than SH-SY5Y cells in any condition studied, with a Ki67 proliferative index of 88.1% in stiff conditions at 4 weeks. In particular, proliferation indices of SK-N-BE(2) from the 2^{nd} to the 4^{th} week were raised from 17.9 to 70.1% and 34 to 88.1% in soft and stiff biomaterials respectively. Therefore, the proliferative index of SK-N-BE(2) was stiffness-dependent. In comparison, SH-SY5Y cells displayed lower proliferative indices than SK-N-BE(2) cells, as observed in 2D cultures (50 and 80% respectively), reaching up to 29.3% of proliferative cells in soft conditions at 6 weeks. SH-SY5Y cells in soft hydrogels achieved higher proliferative indices than in the stiffer ones, as opposed to SK-N-BE(2) cells.

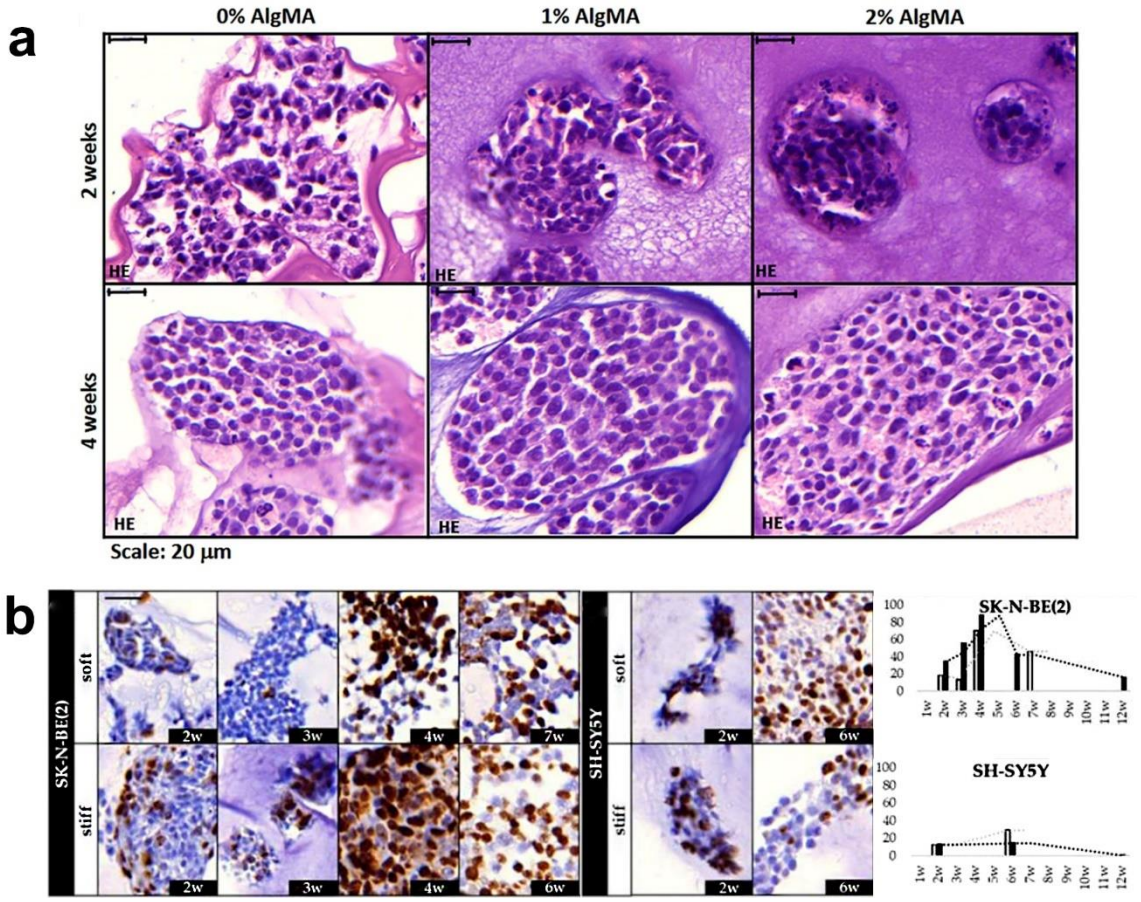

Figure 3.26. Neuroblastoma cluster morphology and proliferation in soft (0% AlgMA) and stiff (2% AlgMA) with GelMA biomaterials. a) Hydrogels hematoxylin-eosin stains (80×) studying the morphology of SK-N-BE(2) clusters after 2 and 4 weeks in culture. Scale bars 20 µm. b) Representative images of Ki67 expression at the time points studied (w: weeks) for each cell culture in soft and stiff biomaterials. The images on the left correspond to the SK-N-BE(2) cell line; the images on the right represent the SH-SY5Y cell line. Scale bar 25 µm at top left of the first image. Same scale bar is valid for all images. Bar chart quantification of Ki67 staining (% of positive cells) for SK-N-BE(2) (up) and (F) SH-SY5Y (down). White and black bars: soft and stiff scaffolds, respectively. Dashed lines indicate moving average per stiffness condition. X axis: time in weeks (w) and Y axis: % of Ki67 positive cells.

Neuroblastoma cluster aggressiveness was analyzed by the expression of polypyrimidine tract binding protein 1 (PTBP1) (Figure 3.27a). SK-N-BE(2) clusters in stiffest biomaterials presented the highest number of PTBP1 positive cells. The ratio of staining intensity and cell positivity was used to calculate H-score, which was higher in stiff (37.68) than in soft biomaterials (15.71). PTBP1 positive cells were dramatically increased from 2nd to 4th week, however, H-score again increased with stiffness (stiff: 277; soft: 257). Those results suggested that stiff biomaterials presented higher aggressiveness.

To study the apoptotic/antiapoptotic activity of cell clusters, the expression of Bcl2 antiapoptotic and Bax apoptotic markers were studied (Figure 3.27b). 2D cell cultures presented high Bcl2 expression (95% of positive cells) and intermediated Bax expression (40% of positive cells). In 3D cultures, Bcl2 expression was significantly lower in both

soft and stiff biomaterials, where the number of positive cells remained around 20% and 50%. Bax expression was also lower in 3D cultures, however, the number of positive cells differed between soft and stiff materials. It was found absent expression of Bax in soft materials, while the number of positive cells in stiff materials was up to 20%.

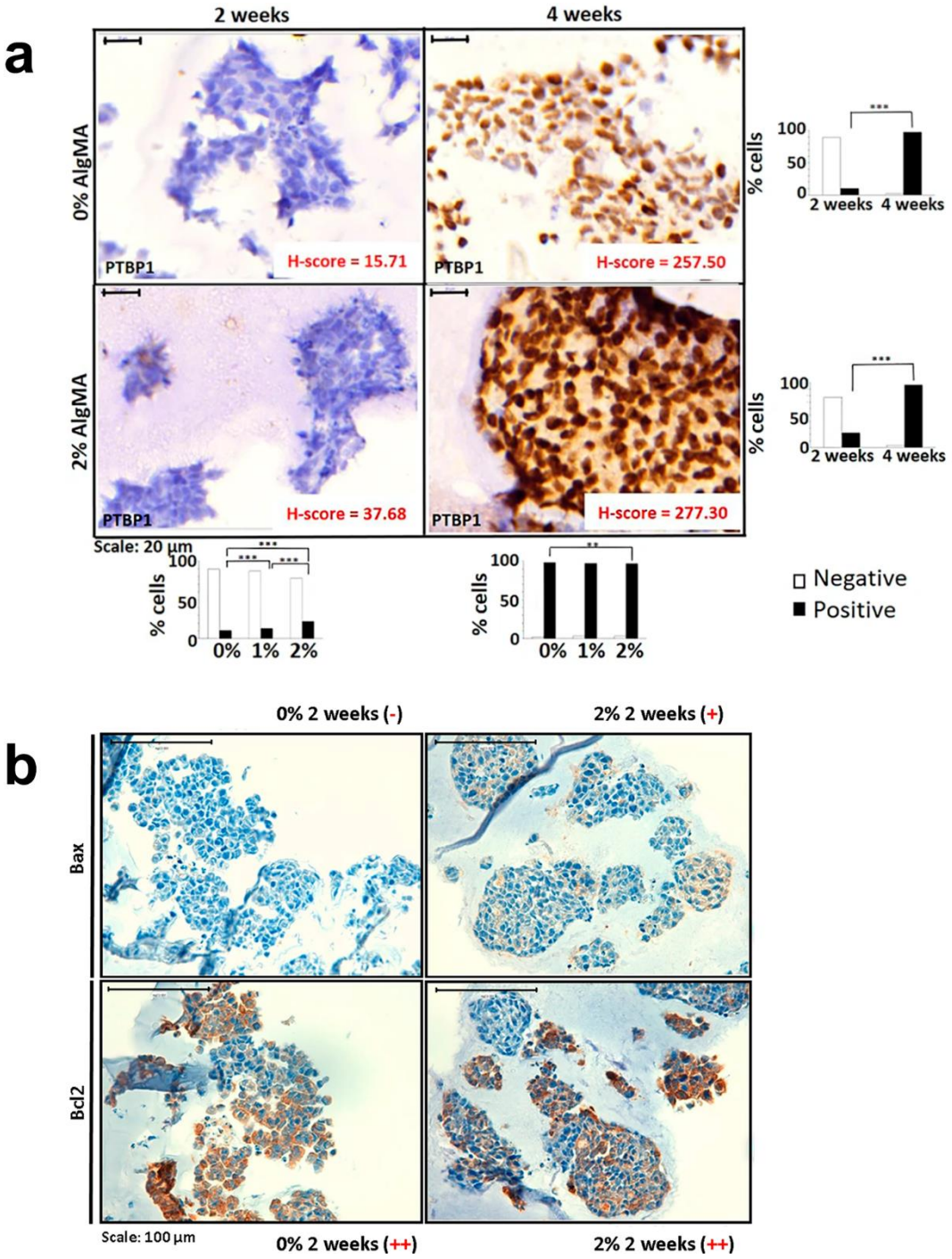

Figure 3.27. Study of SK-N-BE(2) aggressiveness and apoptosis in soft (0% AlgMA) and stiff (2% AlgMA) biomaterials. a) Immunohistochemistry images (80×), percentage of negative and positive cells and H-score for PTBP1. Scale bar 20 µm. Results expressed as percentage of cells represent total number of cells. White bars: negative cells; Black bars: positive cells. Statistical analysis using X2 test: **p-value < 0.01, ***p-value < 0.001. b) Immunohistochemistry images (40×) of Bax (apoptotic) and Bcl2 (antiapoptotic) markers. Optical microscopy analysis:

− Negative (<1% positive cells); + Low positive (1–20% positive cells); ++ Intermediate positive (20–50% positive cells). Scale bar 100 µm.

Territorial vitronectin (tVN) is associated with an aggressive neuroblastoma phenotype and is proposed as a drug target. Thus, its dynamics over time were characterized to complete the studies of neuroblastoma cluster aggressiveness in the different biomaterials (Figure 3.28). In 2D culture, only neuroblasts expressed low cytoplasmic staining for VN. When SK-N-BE(2) cells were grown in 3D conditions, they reached high tVN expression levels (86.0 and 88.5% in soft and stiff hydrogels at the 2nd week) followed by a decrease in both soft and stiff conditions. Although SH-SY5Y cells also increased their tVN expression when grown in 3D conditions (65.2 and 62.0% in soft and stiff hydrogels at the 2nd week), they mostly presented less tVN than SK-N-BE(2) cells. Interestingly, although SH-SY5Y stiff hydrogels followed a similar tVN expression dynamic as the SK-N-BE(2) ones over time, SH-SY5Y soft hydrogels slightly increased tVN expression from 2 to 6 weeks of cell culture (from 65.2 to 72.5%).

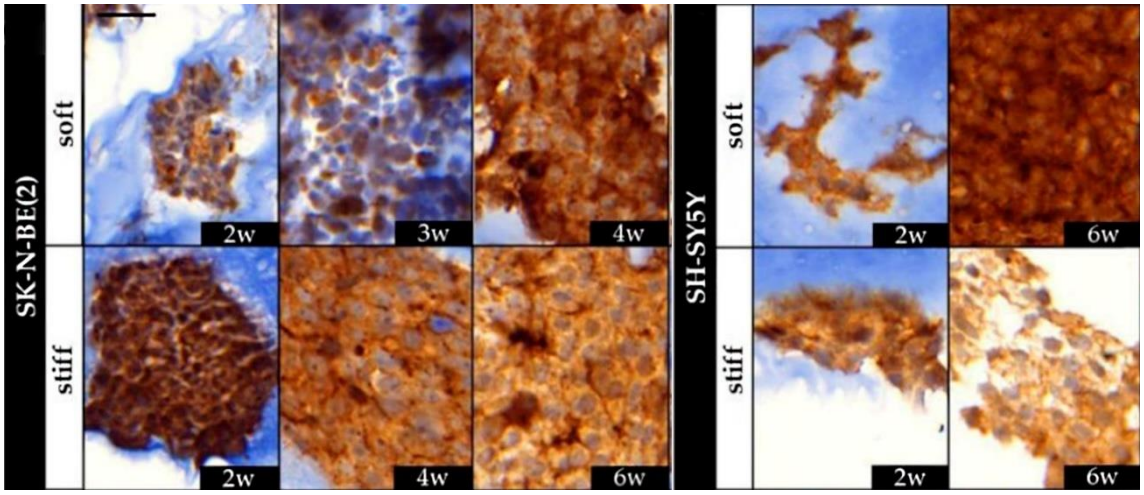

Figure 3.28. Vitronectin (VN) expression in SK-N-BE(2) and SH-SY5Y cell lines in soft (0% AlgMA) and stiff (2% AlgMA) biomaterials over time. The images on the left correspond to the SK-N-BE(2) cell line; the images on the right represent the SH-SY5Y cell line. Scale bar 25 µm at top left of the first image. Same scale bar is valid for all images.

The results found by Ki67 analyses indicated that SK-N-BE(2) cells in GelMA-AlgMA 2% (from here named stiff) biomaterials had a higher proliferative index than in AlgMA 0% (form here named soft) biomaterials. Furthermore, stiff materials showed larger, spherical and more packed clusters in comparison to the irregular and poorly dense clusters in soft materials. Going on with the analysis of SK-N-BE(2) clusters, it was found that stiff biomaterials induced higher expression of polypyrimidine tract-binding protein 1 (PTBP1) than soft biomaterials. PTBP1 is a member of the splicing proteins family in charge of processing pre-mRNA, which determines the final exon combination and consequently, the type of translated protein [359]. In several types of cancer, PTBP1 was associated with tumor initiation and progression, as in ovarian and glioma cancer [360,

361]. Zhang *et al*. correlated increased PTBP1 expression to high-risk metastatic neuroblastoma [361]. Considering those studies together with the proliferative results, it was suggested that stiff GelMA-AlgMA biomaterials with embedded SK-N-BE(2) cells were more suitable to replicate the aggressiveness of high-risk neuroblastoma patients [361, 362]. In contrast, 3D bioprinting of SH-SY5Y neuroblastoma cells did not show a high proliferative index in stiff GelMA-AlgMA biomaterials. Furthermore, they showed slightly increased proliferation in soft biomaterials after 6 weeks of culture, probably due to the higher permissibility of the matrix. The results indicated that GelMA-AlgMA stiffness had a greater effect in SK-N-BE(2) cells than in SH-SY5Y. Nevertheless, it was evidenced that GelMA-AlgMA biomaterial was not the most appropriate biomaterial to engineering neuroblastoma tumors based on SH-SY5Y cells and alternative materials could be more suitable for this type of model.

Despite the controversy found between the two neuroblastoma cell lines, their encapsulation and bioprinting in GelMA-AlgMA 3D cultures revealed significant differences with 2D cultures. SK-N-BE(2) in monolayer cultures showed a very high percentage of antiapoptotic marker (95% Bcl2 positive cells) and medium percentage of apoptotic marker (40% Bax positive cells). 3D cultures significantly reduced the percentage of the antiapoptotic marker, which ranged the 20-50% of positive cells regardless of matrix stiffness. Oppositely, matrix stiffness regulated the positivity of apoptotic cells, where soft matrices showed null expression while the positivity in stiff biomaterials was up to 20%. The results obtained in GelMA-AlgMA biomaterial were closer to the observations in neuroblastoma patients, in which the apoptotic markers did not exceed the 15% of positivity and the antiapoptotic markers positivity was around 50% [7, 363].

The encapsulation of SK-N-BE(2) and SH-SY5Y in GelMA-AlgMA biomaterial resulted in upregulated expression of territorial vitronectin tVN regardless of stiffness, while 2D cultures only showed low expression of cytoplasmatic vitronectin. Nevertheless, SK-N-BE(2) tVN expression was higher than SH-SY5Y. Previous studies proposed tVN as a relevant glycoprotein related to neuroblastoma aggressiveness and stiffness. Consequently, higher tVN expression indicated that the combination of SK-N-BE(2) with GelMA-AlgMA biomaterial could better recapitulate the aggressiveness of neuroblastoma cell clusters in patients. Altogether, GelMA-AlgMA provided durable biomaterials with tunable physical properties, which allowed to study the effect of stiffness *in vitro* for up to 6 weeks. Furthermore, using 3D bioprinting techniques it was possible to automatize the fabrication of numerous neuroblastoma 3D cultures.

Chapter 5

Discussion

The interest in three-dimensional *in vitro* models is continuously increasing. The conventional 2D models are becoming obsolete due to their inability to recapitulate all the environmental and functional parameters of the original tissues. The traditional workflow of drug testing begins from the preclinical trials, which can be separated into *in vitro* and *in vivo* studies. Before the use of animal models for *in vivo* studies, many drug candidates are discarded during the *in vitro* assays, which are used to identify highly toxic and genotoxic compounds. The *in vitro* assays are also used as a first approach to evaluate the effects of pharmacological compounds in the tissue of interest. However, the results found in monolayer cultures do not completely resemble the effects in living organisms, thus most of those drugs are rejected afterward in the *in vivo* studies. Furthermore, the species-specific differences between animal models and humans limit the predictive capability of the *in vivo* assays.

Many efforts are being made to develop *in vitro* models that faithfully resemble the physiological conditions of native tissue. These models are potential tools to overcome the gap between species, simplify the facility requirements, reduce the costs, reduce the use of animals and make pre-clinical studies reachable to many researchers. Those advantages are increasingly drawing biomedical companies. In a study of *Allied Market*, they estimated that as of 2015, the global 3D cell market was $765 million and expected to grow by 30% to $4691 million in 2022 [364]. Most of the commercialized three-dimensional models are based on organoids and spheroids. The technology of iPSCs has been exploited by *Cyprotex* to obtain multicellular 3D organoids of cardiac, hepatic and neural. Nevertheless, the fabrication of organoids is time-consuming, and the resulting products are delicate and have a short lifespan. Other companies have committed to biomaterial-based three-dimensional *in vitro* models, which made them scalable, reproducible and allowed to control their dimensions. Furthermore, the fabrication is less time-consuming, and the product is easier to handle. *Phenion* developed human skin and cornea 3D models to test cosmetics and drugs. Despite the recent growth of 3D *in vitro* models in the market, most models are related to dermal tissue, and there is a clear need to develop faithful models for different tissues.

The fabrication process of engineered tissues is highly complex and needs qualified personnel. Furthermore, most of the current strategies require manual processing, which increases the experimental variability due to human errors. Establishing automatized processes for the fabrication of engineered tissues will be a significant step forwards for the scaling-up and commercialization of these platforms. In this line, 3D bioprinting is a promising technique for the fabrication of biomaterial-based 3D *in vitro* models. Particularly, extrusion bioprinting allows the deposition of controlled volumes of biomaterial with encapsulated cells. The experiments performed in this project demonstrated that combining biomaterials science with extrusion bioprinting allowed the fabrication of highly defined 3D structures. Different shapes were selected according to the application and tissue type. For skeletal muscle tissue, 3D models were designed as rings to obtain easy-handling and anchorable engineered tissues. The size of the rings was changed and adapted to the different platforms. For example, the diameter of the rings was designed to fit the outer diameter of the 3D-printed pillars, while for the metabolic flux analyses the diameter was adapted to the size of the Seahorse analyzer wells. For the fabrication of neuroblastoma models, multiple layers of grids were designed to facilitate the medium absorption into squares with a considerable size. The results obtained in the

experiments using extrusion bioprinting demonstrated high reproducibility, meaning that the dimensions and volume of the 3D models were replicable. Therefore, extrusion bioprinting provided the automated fabrication of engineered tissues, which is of great interest for the scaling-up of *in vitro* models and future commercialization.

The main challenge of extrusion bioprinting is the design of printable formulations that meet the requisites of the technique. Printable materials are defined as those that enable the extrusion of the material through the printing nozzle and keep the fiber shape after the deposition [253]. Printable biomaterials are usually highly viscous formulations that enable extrusion in a wide range of pressures. However, those biomaterials often result in highly dense matrices with low porosity, which compromise the viability, proliferation, migration and differentiation of encapsulated cells. Thus, materials to fabricate *in vitro* models by extrusion bioprinting must have suitable rheological properties to be printable and yield highly porous matrices that promote the development of the targeted tissues.

Collagen is a structural protein present in the extracellular matrix of many tissues. The gelation of collagen is completed after several minutes at 37 °C, which forms a water-insoluble hydrogel. Therefore, this material is not the most appropriated for extrusion bioprinting, since the deposited layers of prepolymer will collapse and fuse, yielding 3D structures with poor definition. Furthermore, non-gelled collagen prepolymers use to be highly aqueous solutions. They are extruded as drops under pressure and can be classified as poorly printable materials. Companies like *Advanced BioMatrix* developed highly concentrated solutions of collagen, which significantly improves printability. Nevertheless, the polymer matrices are very dense and can hamper cell viability. Furthermore, once gelled, collagen is highly hydrophobic and generates separated solid precipitates that collapse the printing needle.

As an alternative, native collagen can be denaturalized into gelatin. Gelatin is a thermosensitive and highly hydrophilic biopolymer. The viscosity of the gelatin is temperature-dependent. This property makes gelatin a highly printable biomaterial even in considerably low concentrated solutions. However, gelatin is soluble in water, thus its original formulation is not suitable for the fabrication of hydrogels. The chemical modification of gelatin with methacrylic groups resulted in highly stable photocrosslinkable hydrogels. Using the same polymer concentration, the crosslinking degree of photocrosslinkable materials is determined by several parameters as the UV exposure time and the type and concentration of photoinitiator. However, the modulation of the physical properties by those parameters is limited to cell viability. Low photoinitiator concentrations and UV exposure times are desired to reduce the cytotoxic effects. In this work, LAP photoinitiator achieved photopolymerization processes of seconds at very low concentrations due to its high extinction coefficient at 365 nm. Fast photocrosslinking reactions allowed the immediate deposition of consecutive layers, avoiding the collapse of the 3D structure and significantly shortening the fabrication time.

Despite the photocrosslinked covalent bonds of gelatin methacryloyl (GelMA), they undergo a significant degradation in the presence of cells. Similar to collagen, they contain cell recognition motifs that promote cell-matrix interaction and renewal. In agreement with previous studies [269], the combination of GelMA with low concentrations of secondary polymers from plant sources significantly increased the

durability of 3D cultures *in vitro* and changed the physical properties of the final composite biomaterial. GelMA-AlgMA and GelMA-CMCMA presented high viability and showed opposite changes in biomaterial stiffness. The mechanical properties of biomaterials have shown highly significant effects on the behavior of encapsulated cells [130]. Therefore, GelMA-CMCMA composites could be used for the fabrication of bioprinted engineered soft tissues in the range of 1-2 kPa, while GelMA-AlgMA is appropriated for stiffer tissues.

GelMA-AlgMA biomaterial presented promising features for the fabrication of bioprinted *in vitro* models, as long-term stability, medium stiffness, and high viability. Nevertheless, the physical properties of GelMA-AlgMA must be adapted to the requirements of each tissue. The tunability of photocrosslinkable composite biomaterials provided a wide range of possible modifications to match the needs of the targeted tissue. Thus, GelMA-AlgMA can be used as the main component of printable biomaterial for tissue engineering, which can be combined with other polymers or modified by the modulation of photocrosslinking parameters.

Fibrin is the most extended biomaterial used for skeletal muscle tissue engineering [172-175]. In contrast to collagen, the crosslinking of fibrin is based on a fast enzymatic reaction. [293]. The combination of GelMA-AlgMA with fibrin provided customized bioprinted models for skeletal muscle tissue. The modulation of LAP photoinitiator concentration together with the combination of fibrin resulted in highly porous hydrogels that recapitulated the mechanical properties of skeletal muscle tissue. Higher porosity enhanced the proliferation of myoblasts that achieved high cellular density, which is necessary to promote cell-cell contacts and myoblast fusion during differentiation [100]. Despite the benefits of matrices with larger pores for skeletal muscle tissue engineering, it was demonstrated that porosity was not the main factor influencing the myogenic differentiation in GelMA-AlgMA-fibrin biomaterial.

Previous works postulated that muscle progenitor cells cultured on surfaces that mimicked the stiffness of skeletal muscle tissue displayed an advanced differentiation state [131]. The encapsulation of myoblasts in GelMA-AlgMA-fibrin biomaterials showed that, immediately after the printing process, cells started the myogenic commitment towards differentiated multinucleated muscle fibers. Therefore, the results confirmed that the stiffness of the biomaterial had a strong influence on the behavior of 3D cell cultures. What is more, GelMA-AlgMA-fibrin induced the spontaneous differentiation of myoblasts without additional chemical stimuli. The traditional protocol of myoblast differentiation *in vitro* is based on a sudden reduction of growth factors in highly confluent cultures, which induces the cell-fusion and myotube formation. This protocol has been also used in most of the 3D skeletal muscle models found in the literature [202, 223, 246]. However, few of them showed the negative effects of mediums with low serum content in the viability of 3D skeletal muscle cultures [365, 366]. Distler *et al.* defended that only medium containing more than 5% (v/v) of serum preserved high viability and enhanced muscle differentiation [260]. Coincidentally, they used a biomaterial based on a mixture of gelatin-oxidized alginate. They stated that high serum content could be necessary to ensure the diffusion of nutrients inside the bioprinted models. However, other studies achieved successful muscle differentiation in 3D cultures of different biomaterials using low serum [202, 223, 246]. Same as low concentrations of

dexamethasone induce muscle differentiation, whereas high concentration results in muscle atrophy [367], the overexposure of engineered muscles to differentiation signals could compromise muscle fiber viability. Considering the hypothesis that GelMA-AlgMA induces the spontaneous differentiation of encapsulated myoblasts, the addition of a complementary differentiation signal like serum starving may result in muscle atrophy. Furthermore, the biomaterial caused the same effect in encapsulated human primary myoblasts. After the incubation of human models in basal medium with high serum content, myoblasts were able to fuse and became differentiated muscle fibers with high expression of sarcomeric proteins. Based on previous works together with the results obtained in this work, it can be concluded that biomaterial mixtures of gelatin and alginate promote the spontaneous differentiation of muscle myoblasts in mediums with high serum content.

Human skeletal muscle tissue models are of great interest for the development of *in vitro* models that overcome the issues related to interspecies differences. GelMA-AlgMA-Fibrin could be used for the encapsulation and differentiation of human muscle precursor cells derived from patients to obtain mature skeletal muscle. These models could be useful in personalized medicine and complement the experiments in animal models for preclinical studies. Nevertheless, the proliferation of primary cells in bioprinted models was found scarce, which forces the encapsulation of a high density of precursor cells in the bioink to achieve the appropriate confluency for myoblast fusion and differentiation. However, high cell density can disturb the rheological properties of the bioink, which can lose printability properties [376]. Therefore, more extended studies are needed to determine the limits of cell density in the bioinks and to promote a higher proliferation in the bioprinted models. Concerning these limitations, the following experiments in this thesis to explore the potential applications of bioprinted models were performed with cell lines, which allowed a faster growth of muscle tissue.

Many 3D skeletal muscle *in vitro* models are fabricated using the passive tension technique. Cells are encapsulated inside soft biopolymers as collagen, fibrin and Matrigel and manually poured into plates or cylinder-shaped cavities. The main goal of those techniques is achieving unidirectional alignment of muscle fibers to mimic the tissue ultrastructure and promote organized and strong contraction [66]. Muscle differentiation in those models has been deeply studied. The effect of the distance between pillars, the biomaterial volume, or the size and shape of the molds in the myogenic process has been analyzed. To complement the skeletal muscle models, many works have studied the effect of electrical pulses in engineered tissues. Electrical pulses emulated the stimuli of the nervous system and promoted the differentiation and advanced maturation of muscle fibers, as well as they were used to validate the functionality of the engineered muscles.

As mentioned before, the fabrication-time of those models is manual and long, the physical properties of those biomaterials are difficult to control and, thus the scalability is limited. However, few examples of bioprinted skeletal muscle models achieved muscle fibers in a late differentiation state, and scarce researchers studied the effect of electrical stimulation in bioprinted models. Furthermore, the most successful bioprinted models are fabricated using sacrificial layers to improve the printability and stability of soft materials. To achieve the final models, they needed long gelation times and subsequent washing steps [261, 262]. Instead, those models fabricated with highly printable materials resulted in 3D cultures with low proliferation and poor muscle differentiation [256].

In contrast to previous works, skeletal muscle models of customized GelMA-AlgMA-fibrin designed with bioprinting techniques provided automatized and fast fabrication of 3D cultures with muscle fibers that displayed the characteristic phenotype and genotype of a late differentiation state. Furthermore, the morphology and orientation of muscle fibers in bioprinted models confirmed that extrusion bioprinting is a highly valuable tool for the alignment of cells in 3D cultures [257, 258]. In the case of skeletal muscle tissue engineering, extrusion bioprinting aligns the fibers towards the printing direction, which recapitulates the structure of the native tissue.

Very few works achieved successful muscle contraction in printable biomaterials as GelMA [368]. Indeed, the electrical stimulation of bioprinted muscle models using GelMA-alginate biomaterials did not achieve visible contraction beating [369]. The electrical parameters chosen to stimulate the GelMA-AlgMA-fibrin models induced the synchronized and strong contraction of the muscle models. On the one hand, the results reaffirmed that bioprinted muscle models presented a previous advanced maturation state. Furthermore, the electrical stimulation validated the capability of the bioprinted models to perform the basic functions of the tissue, the muscle contraction. On the other hand, it was confirmed that electrical stimuli can be used as a complementary system to the skeletal muscle *in vitro* model to enhance the formation of sarcomeres and improve the maturation of the muscle fibers. Some researchers are currently developing high-throughput platforms of electrically stimulated 3D cardiac muscle tissue using the passive tension technique [249]. In line with those examples, the electrical stimulation platforms developed for GelMA-AlgMA-fibrin bioprinted rings allowed the simultaneous stimulation of 24 samples. This platform could be a prototype for the high-throughput development of 3D *in vitro* skeletal muscle models.

One of the main goals of 3D *in vitro* models is to serve as complementary tools or replace animal models. To that end, the results obtained in 3D models should resemble the processes of native tissue. In recent years, many studies highlighted the advantages of 3D cultures in front of conventional 2D cultures to recapitulate the biological processes *in vitro* [370]. 3D models of neuromuscular junctions developed by Bakooshli *et al*. allowed the formation of more efficient and fast innervations than those observed in 2D cultures [371]. Using those 3D models, they were able to better replicate the effects of myasthenia gravis in neuromuscular junction than traditional monolayer cultures. Using iPSCs embedded in fibrin matrices, Maffioletti *et al*. obtained *in vitro* muscle models with similar characteristics to human skeletal muscle tissue [372]. They used this technology with iPSCs derived from patients with severe muscle dystrophies to fabricate reliable disease models of skeletal muscle laminopathies.

Acquired myopathies are poorly represented in 3D skeletal muscle models. Muscle atrophy has been modeled by the treatment of skeletal muscle fibers with glucocorticoids and inflammatory cytokines [373, 374]. However, these models only provide a general view of the effects of some factors during inflammatory processes in muscle. Bioprinted muscle rings treated with colon cancer-conditioned mediums showed the characteristic phenotype and genotype of cancer-cachexia in skeletal muscle tissue. It was found that the genetic expression of key genes involved in cancer cachexia was better represented in the 3D cultures than in the traditional monolayer cultures. Treated bioprinted rings showed similar features to tumor-bearing mice with advanced cachexia. These results

were another confirmation of the advantages of using 3D engineered tissues for disease modeling in front of 2D cultures. Therefore, GelMA-AlgMA-fibrin bioprinted muscles are great candidates for the development of skeletal muscle disease models. In fact, the experiments using those muscle models of cancer-cachexia stressed the complexity of this multifactorial syndrome [112]. The results led to the conclusion that muscle wasting was induced by soluble factors secreted by cancer cells. Among the studied soluble factors, TNFα receptor I (TNFRI) was the most upregulated one in both colon cancer cell lines. TNFRI has been found in the serum of patients with advanced muscle cachexia [352]. However, the direct relationship between TNFRI and skeletal muscle tissue has been poorly studied. The bioprinted models can be used as simplified systems to decipher the biological processes that are conducted in highly complex diseases as cancer cachexia-derived skeletal muscle wasting.

The advantages of bioprinted ring muscle models in front of traditional monolayer cultures were also highlighted when engineered muscles were exposed to bioactive compounds. Bioprinted ring models of GelMA-AlgMA-fibrin demonstrated a similar metabolic flux profile to native muscle single fibers. These models were useful tools to study the effects of β-carboline compounds in the metabolic activity of skeletal muscle tissue. Furthermore, it was seen that the results in bioprinted models could help to determine the main active ingredients of plant extracts involved in the improvement of the metabolic activity of muscle fibers. Consequently, bioprinted ring muscle models can be valuable platforms to perform drug screening tests *in vitro* as complementary studies of animal testing.

GelMA-AlgMA bioprintable material in combination with fibrin has broadly demonstrated its advantages for the development of *in vitro* skeletal muscle 3D cultures. Nevertheless, the versatility of GelMA-AlgMA biomaterial provides the freedom to customize printable materials for the engineering of different tissue models. In the last years, the importance of matrix composition and stiffness in tumors has been emphasized. Developing clinically relevant 3D *in vitro* models to recapitulate the complex interactions between tumor cells and tumor microenvironment is becoming one of the main issues in cancer research [57]. Zschenker *et al*. compared the cell behavior of different cancer cell lines in 3D Matrigel hydrogels [375]. They observed significant changes in the genetic expression profile of 3D and 2D cultures, which affected cell adhesion, immune system and defense response. They found that 3D cultures better replicated the chemoresistance found in patients than conventional monolayer cultures. However, the composition of that kind of soft matrices can vary among batches, and they do not provide the possibility to control the physical properties. In neuroblastoma, it was postulated that tumor stiffness was related to the aggressivity of the disease in patients [361, 362]. It was observed that aggressive tumors in patients with poor prognostic showed a high deposition of ECM fibers. In this sense, modifications in GelMA-AlgMA composition allowed to control the stiffness of the bioprinted neuroblastoma models. To better recapitulate the tumor microenvironment of neuroblastoma cancer, the concentration of AlgMA was modified, which provided matrices with higher or lower polymer densities, similar to those found in patients. In concordance with the results found in real tumors [362], GelMA-AlgMA biomaterials with the stiffest composition better recapitulated the behavior and protein expression profile of aggressive neuroblastoma tumors. Furthermore, 3D models presented similar expression and localization of vitronectin in neuroblastoma clusters,

which was not found in 2D cultures. In conclusion, bioprinted models of GelMA-AlgMA showed many advantages in front of 2D cultures to perform *in vitro* studies of neuroblastoma tumors.

To summarize, GelMA-AlgMA photocrosslinkable material is a highly valuable hydrogel for the automatized and fast fabrication of *in vitro* 3D models. This composite biomaterial is highly versatile and allows a wide range of modifications (composition, porosity, mechanical properties), without compromising the printability. In this sense, the properties of this bioink can be finely tuned to meet the physical requirements of different tissues. These features are of special interest to fabricate scalable models for the future commercialization of *in vitro* models, which have demonstrated special success in the field of skeletal muscle tissue engineering.

Chapter 6

Conclusions

1. Gelatin, alginate and cellulose natural biopolymers can be chemically modified with acrylic groups to obtain 3D meshes crosslinked with UV light.

2. Photocrosslinkable GelMA is a highly printable material with temperature-controlled viscosity, which should be set at 18°C for extrusion bioprinting at a concentration of 5% (w/v).

3. LAP photoinitiator presents higher photoactivation than I2959 at 365 nm UV light. LAP can be used at lower concentrations yielding a high crosslinking degree and improved cell viability.

4. UV exposure time and photoinitiator concentration are some of the most relevant factors affecting cell viability in photocrosslinkable hydrogels. 5 seconds of UV light and photoinitiator concentrations lower than 0.1 % (w/v) are optimal to obtain stable crosslinked 3D cultures with the highest viability.

5. CMCMA, AlgMA and PEGDA combination with GelMA results in uniform matrices with improved resistance to degradation and different physical properties. GelMA-CMCMA presented the lowest stiffness and GelMA-AlgMA the highest one, which ranged from 1.96 kPa to 5.53 kPa. Therefore, composite biomaterials can be chosen for different tissue engineering applications according to mechanical needs. Among them, GelMA-AlgMA is the composite biomaterial that better resembles the mechanical properties of muscle tissue.

6. CMCMA, AlgMA and PEGDA at 1% (w/v) do not alter the printability properties of GelMA and allows the printing of 3D cultures with encapsulated cells.

7. GelMA-CMCMA, GelMA-AlgMA and GelMA-PEGDA composite biomaterials support the differentiation of mouse muscle myoblasts into multinucleated myotubes. However, GelMA-PEGDA yields the lowest viability, which results in lower cell density and a poor number of muscle myotubes. Despite the highest viability in GelMA-CMCMA and GelMA-AlgMA, they present matrices with small pore sizes that limit the nutrient diffusion beyond 100 µm.

8. GelMA-AlgMA is a highly tunable material that provides several strategies to modify the physical properties of 3D *in vitro* cultures. The stiffness of the composite can be modified by the modulation of AlgMA concentration. Increasing AlgMA concentration to 2% (w/v) results in dense stiff matrices with higher mechanical properties.

9. Although the stiffness of GelMA-AlgMA2% is closer to the elastic modulus of skeletal muscle tissue, the porosity of the crosslinked matrices is extremely low and impedes cell migration and formation of multinucleated fibers.

10. An alternative strategy to modify the physical properties of GelMA-AlgMA is based on the modulation of LAP photoinitiator concentration. The porosity, swelling, degradation and stiffness are highly influenced by the photoinitiator concentration. A reduction of LAP from 0.1% to 0.02% (w/v) significantly increases biomaterial porosity, pore size and swelling, while preserves the stability of 3D structures in culture.

11. The addition of 0.5% (w/v) fibrin results in skeletal muscle tissue-like stiffness biomaterial, which reaches a compressive modulus of 11.4 kPa and improves the

resistance to degradation. Furthermore, fibrin addition preserves the porosity and swelling of GelMA-AlgMA biomaterial and does not compromise biomaterial printability.

12. Improved porosity of GelMA-AlgMA-Fib with 0.02% LAP results in 90% of cell viability in structures of more than 300 µm thickness, which shows high proliferation and ensures close cell-cell contact in C2C12 myoblasts to promote differentiation in 3D.

13. GelMA-AlgMA-Fib bioink is an excellent candidate for the generation of skeletal muscle tissue *in vitro* models. It induces the spontaneous differentiation of mouse and human myoblasts in basal growth medium into multinucleated muscle fibers with high expression of sarcomeric structural proteins.

14. The traditional protocol of myoblast differentiation using serum starvation is not suitable for mouse and human myoblasts culture in GelMA-AlgMA-Fibrin 3D cultures. In these models, the differentiation process must be performed in media containing high serum concentration to ensure correct nutrient supply.

15. Using extrusion bioprinting techniques allows the automated production of 3D models. Bioprinted rings are elastic and easy to handle, whose dimensions can be adapted to different platforms as an electrical stimulation system and Seahorse analyzer plates.

16. The extrusion bioprinting induces the alignment of the cells towards the printing direction, which is required to mimic the architecture of skeletal muscle tissue and obtain a coordinated muscle contraction. To ensure the effectiveness of the shear-stress is necessary to use needles with an inner diameter of 200 µm. The alignment effect is lost in the core of the extruded line in needles of wider inner diameter.

17. To avoid the toxic effects of electrolysis byproducts, muscle contraction must be induced with biphasic pulses.

18. Muscle training with electrical stimuli based in biphasic square pulses of 20V, 2ms and 1Hz enhances the formation of mature sarcomeres. EPS training can be used to emulate exercising muscle, since it induces a fast-to-slow fiber type transition and activates the protein synthesis pathways in 3D printed rings.

19. Electrical pulses and aminoacid supplementation increase the activity of mTOR pathway and protein synthesis in muscle.

20. Bioprinted models can be adapted to high-throughput platforms like Seahorse XF Analyzer. The models show a similar bioenergetic profile to isolated muscle fibers. This profile was affected by the treatment with plant extracts containing β-carbolines, which increased the maximal mitochondrial respiration and ATP synthesis.

21. GelMA-AlgMA-Fibrin bioprinted ring muscle models are contractile, functional and useful tools for the life-monitoring and molecular analysis of muscle metabolic alterations *in vitro*. This model is a promising alternative to animal testing for studying the effect of bioactive molecules in skeletal muscle tissue.

22. Differentiated muscle fibers treated with conditioned medium of colorectal cancer cells display similar morphology and activation of the ubiquitin-proteasome pathway than in cancer cachexia-derived muscle wasting.

23. High levels of soluble TNFRI in plasma are related to an advanced state of cancer cachexia. Among the studied inflammatory factors, soluble TNFRI is one of the most secreted by LS174T and HCT116 colorectal cancer cells.

24. LS174T cells secrete higher content of soluble TNFRI than HCT116 cells. They induce a more aggressive pathology with higher upregulation of the protein degradation pathways.

25. The treatment of differentiated muscle fibers with isolated extracellular vesicles from conditioned medium has no significant effects on the morphology and protein turnover. Therefore, the factors involved in the induction of muscle wasting are more likely to be secreted in a soluble form.

26. The transcription factors involved in the protein degradation pathways during cancer cachexia-induced muscle wasting differ between the different types of cancer. Nevertheless, *Fbxo32* (Atrogin1) is one of the most upregulated factors in cancer cachexia.

27. Bioprinted muscle rings treated with colorectal cancer cells-conditioned medium better recapitulate the pathology than traditional monolayer cultures. They display alterations in the genetic expression of sarcomeric proteins and the ubiquitin-proteasome pathway similar to tumor-bearing mouse models. Therefore, bioprinted rings of GelMA-AlgMA-Fibrin are proposed as a potential *in vitro* disease model to replace traditional 2D models of cancer cachexia-induced muscle wasting.

28. To study the effect of matrix stiffness on neuroblastoma cell clusters, the concentration of AlgMA can be modified. In the same way as in solid tumors, higher AlgMA content results in matrices with lower pores and higher stiffness.

29. Bioprinted models with 5% (w/v) GelMA and 2% (w/v) AlgMA (stiff models) with encapsulated SK-N-BE(2) cells show the characteristic proliferation and genetic expression of aggressive high-risk solid tumors in neuroblastoma patients. In contrast, soft models did not show an aggressive phenotype. Therefore, GelMA5%-AlgMA2% formulation is a candidate for the fabrication of bioprinted neuroblastoma models of SK-N-BE(2) cells. However, this behavior is not found in encapsulated SH-SY5Y cell clusters, which show poor proliferation. Thus, suitable biomaterial formulation should be adapted to the requirement of every neuroblastoma cell type.

30. Despite the different behavior of each neuroblastoma cell line, bioprinted models of neuroblastoma better recapitulated the antiapoptotic/apoptotic protein expression of neuroblastoma patients. Moreover, bioprinted neuroblastoma models showed high expression of territorial vitronectin, which is not found in monolayer cultures.

Chapter 7

Bibliography

1. Vacanti, J. P., & Langer, R. (1999). Tissue engineering: The design and fabrication of living replacement devices for surgical reconstruction and transplantation. Lancet, 354(SUPPL.1), 32–34. https://doi.org/10.1016/s0140-6736(99)90247-7
2. Sparrow, J., Hughes, S. M., & Segalat, L. (2008). Other model organisms for sarcomeric muscle diseases. Advances in Experimental Medicine and Biology, 642, 192–206. https://doi.org/10.1007/978-0-387-84847-1_14
3. Ericsson, A. C., Crim, M. J., & Franklin, C. L. (2013). A brief history of animal modeling. Missouri Medicine, 110(3), 201–205.
4. van Putten, M., Lloyd, E. M., de Greef, J. C., Raz, V., Willmann, R., & Grounds, M. D. (2020). Mouse models for muscular dystrophies: an overview. In Disease models & mechanisms (Vol. 13, Issue 2). NLM (Medline). https://doi.org/10.1242/dmm.043562
5. Grivel, J. C., & Margolis, L. (2009). Use of human tissue explants to study human infectious agents. Nature Protocols, 4(2), 256–269. https://doi.org/10.1038/nprot.2008.245
6. Leijendekker WJ, Elzinga G. Metabolic recovery of mouse extensor digitorum longus and soleus muscle. Pflugers Arch. 1990 Apr; 416(1–2):22–27. doi:10.1007/ bf00370217
7. Skardal, A. (2015). Bioprinting essentials of cell and protein viability. In Essentials of 3D Biofabrication and Translation (pp. 1–17). Elsevier Inc. https://doi.org/10.1016/B978-0-12-800972-7.00001-3
8. Chal, J. J., & Pourquié1, O. P. (2017). Making muscle: skeletal myogenesis in vivo and in vitro. https://doi.org/10.1242/dev.151035
9. Doss, M. X., & Sachinidis, A. (2019). Current Challenges of iPSC-Based Disease Modeling and Therapeutic Implications. Cells, 8(5), 403. https://doi.org/10.3390/cells8050403
10. Riedl, A., Schlederer, M., Pudelko, K., Stadler, M., Walter, S., Unterleuthner, D., Unger, C., Kramer, N., Hengstschläger, M., Kenner, L., Pfeiffer, D., Krupitza, G., & Dolznig, H. (2017). Comparison of cancer cells in 2D vs 3D culture reveals differences in AKT-mTOR-S6K signaling and drug responses. *Journal of Cell Science*, *130*(1), 203–218. https://doi.org/10.1242/jcs.188102
11. Kamei, K., Koyama, Y., Tokunaga, Y., Mashimo, Y., Yoshioka, M., Fockenberg, C., Mosbergen, R., Korn, O., Wells, C., & Chen, Y. (2016). Characterization of Phenotypic and Transcriptional Differences in Human Pluripotent Stem Cells under 2D and 3D Culture Conditions. Advanced Healthcare Materials, 5(22), 2951–2958. https://doi.org/10.1002/adhm.201600893
12. Soares, C. P., Midlej, V., Oliveira, M. E. W. de, Benchimol, M., Costa, M. L., & Mermelstein, C. (2012). 2D and 3D-Organized Cardiac Cells Shows Differences in Cellular Morphology, Adhesion Junctions, Presence of Myofibrils and Protein Expression. PLoS ONE, 7(5), e38147. https://doi.org/10.1371/journal.pone.0038147
13. Duval, K., Grover, H., Han, L. H., Mou, Y., Pegoraro, A. F., Fredberg, J., & Chen, Z. (2017). Modeling physiological events in 2D vs. 3D cell culture. In Physiology (Vol. 32, Issue 4, pp. 266–277). American Physiological Society. https://doi.org/10.1152/physiol.00036.2016
14. Baker, B. M., & Chen, C. S. (2012). Deconstructing the third dimension-how 3D culture microenvironments alter cellular cues. In Journal of Cell Science (Vol. 125, Issue 13, pp. 3015–3024). Company of Biologists. https://doi.org/10.1242/jcs.079509
15. Jensen, C., & Teng, Y. (2020). Is It Time to Start Transitioning From 2D to 3D Cell Culture? In Frontiers in Molecular Biosciences (Vol. 7, p. 33). Frontiers Media S.A. https://doi.org/10.3389/fmolb.2020.00033
16. Takahashi, H., Shimizu, T., & Okano, T. (2018). Engineered Human Contractile Myofiber Sheets as a Platform for Studies of Skeletal Muscle Physiology. Scientific Reports, 8(1). https://doi.org/10.1038/s41598-018-32163-1

17. Shimizu, T., Yamato, M., Akutsu, T., Shibata, T., Isoi, Y., Kikuchi, A., Umezu, M., & Okano, T. (2002). Electrically communicating three-dimensional cardiac tissue mimic fabricated by layered cultured cardiomyocyte sheets. Journal of Biomedical Materials Research, 60(1), 110–117. https://doi.org/10.1002/jbm.1284
18. Ikeda, K., Ito, A., Imada, R., Sato, M., Kawabe, Y., & Kamihira, M. (2017). In vitro drug testing based on contractile activity of C2C12 cells in an epigenetic drug model. Scientific Reports, 7(1), 44570. https://doi.org/10.1038/srep44570
19. Akkouch, A., Yu, Y., & Ozbolat, I. T. (2015). Microfabrication of scaffold-free tissue strands for three-dimensional tissue engineering. Biofabrication, 7(3), 031002. https://doi.org/10.1088/1758-5090/7/3/031002
20. Mittler, F., Obeïd, P., Rulina, A. V., Haguet, V., Gidrol, X., & Balakirev, M. Y. (2017). High-content monitoring of drug effects in a 3D spheroid model. Frontiers in Oncology, 7(DEC), 293. https://doi.org/10.3389/fonc.2017.00293
21. Shri, M., Agrawal, H., Rani, P., Singh, D., & Onteru, S. K. (2017). Hanging drop, a best three-dimensional (3D) culture method for primary buffalo and sheep hepatocytes. Scientific Reports, 7(1), 1–14. https://doi.org/10.1038/s41598-017-01355-6
22. Prunieras, M., Regnier, M., & Woodley, D. (1983). Methods for cultivation of keratinocytes with an air-liquid interface. Journal of Investigative Dermatology, 81(1 Suppl.), S28–S33. https://doi.org/10.1111/1523-1747.ep12540324
23. Freeman, A. E., Igel, H. J., Herrman, B. J., & Kleinfeld, K. L. (1976). Growth and characterization of human skin epithelial cell cultures. In Vitro, 12(5), 352–362. https://doi.org/10.1007/BF02796313
24. El Ghalbzouri, A., Commandeur, S., Rietveld, M. H., Mulder, A. A., & Willemze, R. (2009). Replacement of animal-derived collagen matrix by human fibroblast-derived dermal matrix for human skin equivalent products. Biomaterials, 30(1), 71–78. https://doi.org/10.1016/j.biomaterials.2008.09.002
25. Carlson, M. W., Alt-Holland, A., Egles, C., & Garlick, J. A. (2008). Three-Dimensional Tissue Models of Normal and Diseased Skin. Current Protocols in Cell Biology, 41(1), 19.9.1-19.9.17. https://doi.org/10.1002/0471143030.cb1909s41
26. Sheikh, F. A., Ju, H. W., Lee, J. M., Moon, B. M., Park, H. J., Lee, O. J., Kim, J. H., Kim, D. K., & Park, C. H. (2015). 3D electrospun silk fibroin nanofibers for fabrication of artificial skin. Nanomedicine: Nanotechnology, Biology, and Medicine, 11(3), 681–691. https://doi.org/10.1016/j.nano.2014.11.007
27. Sharif, S., Ai, J., Azami, M., Verdi, J., Atlasi, M. A., Shirian, S., & Samadikuchaksaraei, A. (2018). Collagen-coated nano-electrospun PCL seeded with human endometrial stem cells for skin tissue engineering applications. Journal of Biomedical Materials Research Part B: Applied Biomaterials, 106(4), 1578–1586. https://doi.org/10.1002/jbm.b.33966
28. Sadeghi, A. R., Nokhasteh, S., Molavi, A. M., Khorsand-Ghayeni, M., Naderi-Meshkin, H., & Mahdizadeh, A. (2016). Surface modification of electrospun PLGA scaffold with collagen for bioengineered skin substitutes. Materials Science and Engineering C, 66, 130–137. https://doi.org/10.1016/j.msec.2016.04.073
29. Pourchet, L. J., Thepot, A., Albouy, M., Courtial, E. J., Boher, A., Blum, L. J., & Marquette, C. A. (2017). Human Skin 3D Bioprinting Using Scaffold-Free Approach. Advanced Healthcare Materials, 6(4), 1601101. https://doi.org/10.1002/adhm.201601101
30. Van Kilsdonk, J. W. J., Van Den Bogaard, E. H., Jansen, P. A. M., Bos, C., Bergers, M., & Schalkwijk, J. (2013). An in vitro wound healing model for evaluation of dermal substitutes. Wound Repair and Regeneration, 21(6), 890–896. https://doi.org/10.1111/wrr.12086

31. Randall, M. J., Jüngel, A., Rimann, M., & Wuertz-Kozak, K. (2018). Advances in the biofabrication of 3D skin in vitro: Healthy and pathological models. In Frontiers in Bioengineering and Biotechnology (Vol. 6, Issue OCT, p. 154). Frontiers Media S.A. https://doi.org/10.3389/fbioe.2018.00154
32. Fernandez, T. L., Van Lonkhuyzen, D. R., Dawson, R. A., Kimlin, M. G., & Upton, Z. (2014). Characterization of a Human Skin Equivalent Model to Study the Effects of Ultraviolet B Radiation on Keratinocytes. Tissue Engineering Part C: Methods, 20(7), 588–598. https://doi.org/10.1089/ten.tec.2013.0293
33. Marconi, A., Quadri, M., Saltari, A., & Pincelli, C. (2018). Progress in melanoma modelling in vitro. Experimental Dermatology, 27(5), 578–586. https://doi.org/10.1111/exd.13670
34. Vidal, S. E. L., Tamamoto, K. A., Nguyen, H., Abbott, R. D., Cairns, D. M., & Kaplan, D. L. (2019). 3D biomaterial matrix to support long term, full thickness, immuno-competent human skin equivalents with nervous system components. Biomaterials, 198, 194–203. https://doi.org/10.1016/j.biomaterials.2018.04.044
35. Hopkins, A. M., DeSimone, E., Chwalek, K., & Kaplan, D. L. (2015). 3D in vitro modeling of the central nervous system. In Progress in Neurobiology (Vol. 125, pp. 1–25). Elsevier Ltd. https://doi.org/10.1016/j.pneurobio.2014.11.003
36. Watanabe, K., Nakamura, M., Okano, H., & Toyama, Y. (2007). Establishment of three-dimensional culture of neural stem/progenitor cells in collagen Type-1 Gel. In Restorative Neurology and Neuroscience (Vol. 25, Issue 2). IOS Press.
37. Ma, W., Fitzgerald, W., Liu, Q.-Y., O'shaughnessy, T. J., Maric, D., Lin, H. J., Alkon, D. L., & Barker, J. L. (2004). CNS stem and progenitor cell differentiation into functional neuronal circuits in three-dimensional collagen gels. https://doi.org/10.1016/j.expneurol.2003.10.016
38. Seidlits, S. K., Khaing, Z. Z., Petersen, R. R., Nickels, J. D., Vanscoy, J. E., Shear, J. B., & Schmidt, C. E. (2010). The effects of hyaluronic acid hydrogels with tunable mechanical properties on neural progenitor cell differentiation. Biomaterials, 31(14), 3930–3940. https://doi.org/10.1016/j.biomaterials.2010.01.125
39. Balgude, A. P., Yu, X., Szymanski, A., & Bellamkonda, R. V. (2001). Agarose gel stiffness determines rate of DRG neurite extension in 3D cultures. Biomaterials, 22(10), 1077–1084. https://doi.org/10.1016/S0142-9612(00)00350-1
40. Tsurkan, M. V., Chwalek, K., Prokoph, S., Zieris, A., Levental, K. R., Freudenberg, U., & Werner, C. (2013). Defined Polymer-Peptide Conjugates to Form Cell-Instructive starPEG-Heparin Matrices In Situ. Advanced Materials, 25(18), 2606–2610. https://doi.org/10.1002/adma.201300691
41. Tang-Schomer, M. D., White, J. D., Tien, L. W., Schmitt, L. I., Valentin, T. M., Graziano, D. J., Hopkins, A. M., Omenetto, F. G., Haydon, P. G., & Kaplan, D. L. (2014). Bioengineered functional brain-like cortical tissue. Proceedings of the National Academy of Sciences of the United States of America, 111(38), 13811–13816. https://doi.org/10.1073/pnas.1324214111
42. Khoshakhlagh, P., Sivakumar, A., Pace, L. A., Sazer, D. W., & Moore, M. J. (2018). Methods for fabrication and evaluation of a 3D microengineered model of myelinated peripheral nerve. Journal of Neural Engineering, 15(6), 64001–64012. https://doi.org/10.1088/1741-2552/aae129
43. Malheiro, A., Morgan, F., Baker, M., Moroni, L., & Wieringa, P. (2020). A three-dimensional biomimetic peripheral nerve model for drug testing and disease modelling. *Biomaterials*, *257*, 120230. https://doi.org/10.1016/j.biomaterials.2020.120230
44. Madison, R. D., Da Silva, C. F., & Dikkes, P. (1988). Entubulation repair with protein additives increases the maximum nerve gap distance successfully bridged with tubular

prostheses. Brain Research, 447(2), 325–334. https://doi.org/10.1016/0006-8993(88)91135-3

45. Cai, J., Peng, X., Nelson, K. D., Eberhart, R., & Smith, G. M. (2005). Permeable guidance channels containing microfilament scaffolds enhance axon growth and maturation. Journal of Biomedical Materials Research Part A, 75A(2), 374–386. https://doi.org/10.1002/jbm.a.30432
46. Itoh, S., Takakuda, K., Samejima, H., Ohta, T., Shinomiya, K., & Ichinose, S. (1999). Synthetic collagen fibers coated with a synthetic peptide containing the YIGSR sequence of laminin to promote peripheral nerve regeneration in vivo. Journal of Materials Science: Materials in Medicine, 10(3), 129–134. https://doi.org/10.1023/A:1008977221827
47. Schneeberger, K., Roth, S., Nieuwenhuis, E. E. S., & Middendorp, S. (2018). Intestinal epithelial cell polarity defects in disease: Lessons from microvillus inclusion disease. In DMM Disease Models and Mechanisms (Vol. 11, Issue 2). Company of Biologists Ltd. https://doi.org/10.1242/dmm.031088
48. Yi, B., Shim, K. Y., Ha, S. K., Han, J., Hoang, H. H., Choi, I., Park, S., & Sung, J. H. (2017). Three-dimensional in vitro gut model on a villi-shaped collagen scaffold. Biochip Journal, 11(3), 219–231. https://doi.org/10.1007/s13206-017-1307-8
49. Samy, K. E., Levy, E. S., Phong, K., Demaree, B., Abate, A. R., & Desai, T. A. (2019). Human intestinal spheroids cultured using Sacrificial Micromolding as a model system for studying drug transport. Scientific Reports, 9(1), 1–12. https://doi.org/10.1038/s41598-019-46408-0
50. Alzheimer, M., Svensson, S. L., König, F., Schweinlin, M., Metzger, M., Walles, H., & Sharma, C. M. (2020). A three-dimensional intestinal tissue model reveals factors and small regulatory RNAs important for colonization with Campylobacter jejuni. PLoS Pathogens, 16(2), e1008304. https://doi.org/10.1371/journal.ppat.1008304
51. Madden, L. R., Nguyen, T. V., Garcia-Mojica, S., Shah, V., Le, A. V., Peier, A., Visconti, R., Parker, E. M., Presnell, S. C., Nguyen, D. G., & Retting, K. N. (2018). Bioprinted 3D Primary Human Intestinal Tissues Model Aspects of Native Physiology and ADME/Tox Functions. IScience, 2, 156–167. https://doi.org/10.1016/j.isci.2018.03.015
52. Collins, S. D., Yuen, G., Tu, T., Budzinska, M. A., Spring, K., Bryant, K., & Shackel, N. A. (2019). In Vitro Models of the Liver: Disease Modeling, Drug Discovery and Clinical Applications. In Hepatocellular Carcinoma (pp. 47–67). Codon Publications. https://doi.org/10.15586/hepatocellularcarcinoma.2019.ch3
53. Kozyra, M., Johansson, I., Nordling, Å., Ullah, S., Lauschke, V. M., & Ingelman-Sundberg, M. (2018). Human hepatic 3D spheroids as a model for steatosis and insulin resistance. Scientific Reports, 8(1), 1–12. https://doi.org/10.1038/s41598-018-32722-6
54. Nudischer, R., Renggli, K., Hierlemann, A., Roth, A. B., & Bertinetti-Lapatki, C. (2020). Characterization of a long-term mouse primary liver 3D tissue model recapitulating innate-immune responses and drug-induced liver toxicity. PLOS ONE, 15(7), e0235745. https://doi.org/10.1371/journal.pone.0235745
55. Haque, T., Chen, H., Ouyang, W., Martoni, C., Lawuyi, B., Urbanska, A. M., & Prakash, S. (2005). In vitro study of alginate-chitosan microcapsules: An alternative to liver cell transplants for the treatment of liver failure. Biotechnology Letters, 27(5), 317–322. https://doi.org/10.1007/s10529-005-0687-3
56. Garreta, E., Prado, P., Tarantino, C., Oria, R., Fanlo, L., Martí, E., Zalvidea, D., Trepat, X., Roca-Cusachs, P., Gavaldà-Navarro, A., Cozzuto, L., Campistol, J. M., Izpisúa Belmonte, J. C., Hurtado del Pozo, C., & Montserrat, N. (2019). Fine tuning the extracellular environment accelerates the derivation of kidney organoids from human pluripotent stem cells. Nature Materials, 18(4), 397–405. https://doi.org/10.1038/s41563-019-0287-6

57. Rodrigues, J., Heinrich, M. A., Teixeira, L. M., & Prakash, J. (2021). 3D In Vitro Model (R)evolution: Unveiling Tumor–Stroma Interactions. In Trends in Cancer (Vol. 7, Issue 3, pp. 249–264). Cell Press. https://doi.org/10.1016/j.trecan.2020.10.009
58. Luca, A. C., Mersch, S., Deenen, R., Schmidt, S., Messner, I., Schäfer, K.-L., Baldus, S. E., Huckenbeck, W., Piekorz, R. P., Knoefel, W. T., Krieg, A., & Stoecklein, N. H. (2013). Impact of the 3D Microenvironment on Phenotype, Gene Expression, and EGFR Inhibition of Colorectal Cancer Cell Lines. PLoS ONE, 8(3), e59689. https://doi.org/10.1371/journal.pone.0059689
59. Melissaridou, S., Wiechec, E., Magan, M., Jain, M. V., Chung, M. K., Farnebo, L., & Roberg, K. (2019). The effect of 2D and 3D cell cultures on treatment response, EMT profile and stem cell features in head and neck cancer 11 Medical and Health Sciences 1112 Oncology and Carcinogenesis. Cancer Cell International, 19(1), 16. https://doi.org/10.1186/s12935-019-0733-1
60. Pavlou, M., Shah, M., Gikas, P., Briggs, T., Roberts, S. J., & Cheema, U. (2019). Osteomimetic matrix components alter cell migration and drug response in a 3D tumour-engineered osteosarcoma model. Acta Biomaterialia, 96, 247–257. https://doi.org/10.1016/j.actbio.2019.07.011
61. Taubenberger, A. V., Bray, L. J., Haller, B., Shaposhnykov, A., Binner, M., Freudenberg, U., Guck, J., & Werner, C. (2016). 3D extracellular matrix interactions modulate tumour cell growth, invasion and angiogenesis in engineered tumour microenvironments. Acta Biomaterialia, 36, 73–85. https://doi.org/10.1016/j.actbio.2016.03.017
62. Lam, C. R. I., Wong, H. K., Nai, S., Chua, C. K., Tan, N. S., & Tan, L. P. (2014). A 3D biomimetic model of tissue stiffness interface for cancer drug testing. Molecular Pharmaceutics, 11(7), 2016–2021. https://doi.org/10.1021/mp500059q
63. Casanellas, I., García-Lizarribar, A., Lagunas, A., & Samitier, J. (2018). Producing 3D Biomimetic Nanomaterials for Musculoskeletal System Regeneration. Frontiers in Bioengineering and Biotechnology, 6(SEP), 128. https://doi.org/10.3389/fbioe.2018.00128
64. Tzaphlidou, M. (2008). Bone architecture: Collagen structure and calcium/phosphorus maps. In Journal of Biological Physics (Vol. 34, Issues 1-2 SPEC. ISS., pp. 39–49). Springer. https://doi.org/10.1007/s10867-008-9115-y
65. Thorpe, C. T., & Screen, H. R. C. (2016). Tendon structure and composition. Advances in Experimental Medicine and Biology, 920, 3–10. https://doi.org/10.1007/978-3-319-33943-6_1
66. Gillies, A. R., & Lieber, R. L. (2011). Structure and function of the skeletal muscle extracellular matrix. In Muscle and Nerve (Vol. 44, Issue 3, pp. 318–331). NIH Public Access. https://doi.org/10.1002/mus.22094
67. Guimarães, C. F., Gasperini, L., Marques, A. P., & Reis, R. L. (2020). The stiffness of living tissues and its implications for tissue engineering. In Nature Reviews Materials (Vol. 5, Issue 5, pp. 351–370). Nature Research. https://doi.org/10.1038/s41578-019-0169-1
68. Heinemann, S., Heinemann, C., Wenisch, S., Alt, V., Worch, H., & Hanke, T. (2013). Calcium phosphate phases integrated in silica/collagen nanocomposite xerogels enhance the bioactivity and ultimately manipulate the osteoblast/osteoclast ratio in a human co-culture model. Acta Biomaterialia, 9(1), 4878–4888. https://doi.org/10.1016/j.actbio.2012.10.010
69. Bouet, G., Cruel, M., Laurent, C., Vico, L., Malaval, L., & Marchat, D. (2015). Validation of an in vitro 3D bone culture model with perfused and mechanically stressed ceramic scaffold. European Cells and Materials, 29, 250–267. https://doi.org/10.22203/eCM.v029a19

70. Kuo, C. K., & Tuan, R. S. (2008). Mechanoactive tenogenic differentiation of human mesenchymal stem cells. Tissue Engineering - Part A., 14(10), 1615–1627. https://doi.org/10.1089/ten.tea.2006.0415
71. Gehwolf, R., Spitzer, G., Wagner, A., Lehner, C., Weissenbacher, N., Tempfer, H., & Traweger, A. (2019). 3D-Embedded Cell Cultures to Study Tendon Biology. In Methods in Molecular Biology (Vol. 2045, pp. 155–165). Humana Press Inc. https://doi.org/10.1007/7651_2019_208
72. Lemke, S. B., & Schnorrer, F. (2017). Mechanical forces during muscle development. Mechanisms of Development, 144, 92–101. https://doi.org/10.1016/j.mod.2016.11.003
73. Geach, T. J., Hirst, E. M. A., & Zimmerman, L. B. (2015). Contractile activity is required for <scp>Z</scp> -disc sarcomere maturation in vivo. Genesis, 53(5), 299–307. https://doi.org/10.1002/dvg.22851
74. Kim, H., Kim, M. C., & Asada, H. H. (2019). Extracellular matrix remodelling induced by alternating electrical and mechanical stimulations increases the contraction of engineered skeletal muscle tissues. Scientific Reports, 9(1), 1–11. https://doi.org/10.1038/s41598-019-39522-6
75. Uzel, S. G. M., Platt, R. J., Subramanian, V., Pearl, T. M., Rowlands, C. J., Chan, V., Boyer, L. A., So, P. T. C., & Kamm, R. D. (2016). Microfluidic device for the formation of optically excitable, three-dimensional, compartmentalized motor units. Science Advances, 2(8), e1501429. https://doi.org/10.1126/sciadv.1501429
76. Heymsfield, S. B., Thomas, D. M., Bosy-Westphal, A., & Müller, M. J. (2019). The anatomy of resting energy expenditure: body composition mechanisms. In European Journal of Clinical Nutrition (Vol. 73, Issue 2, pp. 166–171). Nature Publishing Group. https://doi.org/10.1038/s41430-018-0319-3
77. Takeda, R., & Okazaki, K. (2018). Body Temperature Regulation During Exercise and Hyperthermia in Diabetics. In Diabetes and Its Complications. InTech. https://doi.org/10.5772/intechopen.74063
78. Charlotte, M., Severinsen, K., & Pedersen, B. K. (2020). Muscle-Organ Crosstalk: The Emerging Roles of Myokines. https://doi.org/10.1210/endrev/bnaa016
79. Kelley, D. E., Mokan, M., Simoneau, J. A., & Mandarino, L. J. (1993). Interaction between glucose and free fatty acid metabolism in human skeletal muscle. Journal of Clinical Investigation, 92(1), 91–98. https://doi.org/10.1172/JCI116603
80. Lancaster, G. I., & Febbraio, M. A. (2014). The immunomodulating role of exercise in metabolic disease. In Trends in Immunology (Vol. 35, Issue 6, pp. 262–269). Elsevier Ltd. https://doi.org/10.1016/j.it.2014.02.008
81. Penna, F., Ballarò, R., Beltrà, M., De Lucia, S., Castillo, L. G., & Costelli, P. (2019). The skeletal muscle as an active player against cancer cachexia. In Frontiers in Physiology (Vol. 10, Issue FEB, p. 41). Frontiers Media S.A. https://doi.org/10.3389/fphys.2019.00041
82. Steinmetz, P. R. H., Kraus, J. E. M., Larroux, C., Hammel, J. U., Amon-Hassenzahl, A., Houliston, E., Wörheide, G., Nickel, M., Degnan, B. M., & Technau, U. (2012). Independent evolution of striated muscles in cnidarians and bilaterians. *Nature*, *487*(7406), 231–234. https://doi.org/10.1038/nature11180
83. Kachur, T. M., & Pilgrim, D. B. (2008). Myosin assembly, maintenance and degradation in muscle: Role of the chaperone UNC-45 in myosin thick filament dynamics. In *International Journal of Molecular Sciences* (Vol. 9, Issue 9, pp. 1863–1875). Multidisciplinary Digital Publishing Institute (MDPI). https://doi.org/10.3390/ijms9091863

84. Squire, J. M. (2016). Muscle contraction: Sliding filament history, sarcomere dynamics and the two Huxleys. Global Cardiology Science and Practice, 2016(2). https://doi.org/10.21542/gcsp.2016.11 Sweeney, H. L., & Houdusse, A. (2010). Structural and Functional Insights into the Myosin Motor Mechanism. *Annual Review of Biophysics*, *39*(1), 539–557. https://doi.org/10.1146/annurev.biophys.050708.133751

85. Purves, D., Augustine, G. J., Fitzpatrick, D., Katz, L. C., LaMantia, A.-S., McNamara, J. O., & Williams, S. M. (2001). Motor Neuron-Muscle Relationships.

86. *Molecular Mechanisms of Neurotransmitter Release*. (2008). https://doi.org/10.1007/978-1-59745-481-0

87. Mukund, K., & Subramaniam, S. (2019). Skeletal muscle: A review of molecular structure and function, in health and disease. *Wiley Interdisciplinary Reviews: Systems Biology and Medicine*, *12*(1). https://doi.org/10.1002/wsbm.1462

88. Dulhunty, A. F., Haarmann, C. S., Green, D., Laver, D. R., Board, P. G., & Casarotto, M. G. (2002). Interactions between dihydropyridine receptors and ryanodine receptors in striated muscle. In *Progress in Biophysics and Molecular Biology* (Vol. 79, Issues 1–3, pp. 45–75). Pergamon. https://doi.org/10.1016/S0079-6107(02)00013-5

89. Needham, D. M. (1926). RED AND WHITE MUSCLE. Physiological Reviews, 6(1), 1–27. https://doi.org/10.1152/physrev.1926.6.1.1

90. Schiaffino S, Hanzlikova V, Pierobon S. Relations between structure and function in rat skeletal muscle fibers. J Cell Biol 47: 107–119, 1970.

91. DeNardi C, Ausoni S, Moretti P, Gorza L, Velleca M, Buckingham M & Schiaffino S (1993) Type 2X-myosin heavy chain is coded by a muscle fiber type-specific and developmentally regulated gene. J Cell Biol 123, 823– 835.

92. Allen, D. L., Harrison, B. C., Maass, A., Bell, M. L., Byrnes, W. C., & Leinwand, L. A. (2001). Cardiac and skeletal muscle adaptations to voluntary wheel running in the mouse. *Journal of Applied Physiology*, *90*(5), 1900–1908. https://doi.org/10.1152/jappl.2001.90.5.1900

93. Ørtenblad, N., Nielsen, J., Boushel, R., Söderlund, K., Saltin, B., & Holmberg, H.-C. (2018). The Muscle Fiber Profiles, Mitochondrial Content, and Enzyme Activities of the Exceptionally Well-Trained Arm and Leg Muscles of Elite Cross-Country Skiers. *Frontiers in Physiology*, *9*(AUG), 1031. https://doi.org/10.3389/fphys.2018.01031

94. Scott, W., Stevens, J., & Binder-Macleod, S. A. (2001). Human skeletal muscle fiber type classifications. In Physical Therapy (Vol. 81, Issue 11, pp. 1810–1816). American Physical Therapy Association. https://doi.org/10.1093/ptj/81.11.1810

95. Pette, D., & Staront, R. S. (1997). Mammalian skeletal muscle fiber type transitions. *International Review of Cytology*, *170*, 143–223. https://doi.org/10.1016/s0074-7696(08)61622-8

96. Bentzinger, C. F., Wang, Y. X., & Rudnicki, M. A. (2012). Building muscle: molecular regulation of myogenesis. In *Cold Spring Harbor perspectives in biology* (Vol. 4, Issue 2). Cold Spring Harbor Laboratory Press. https://doi.org/10.1101/cshperspect.a008342

97. Du, C., Jin, Y. Q., Qi, J. J., Ji, Z. X., Li, S. Y., An, G. S., Jia, H. T., & Ni, J. H. (2012). Effects of myogenin on expression of late muscle genes through myoD-Dependent chromatin remodeling ability of myogenin. *Molecules and Cells*, *34*(2), 133–142. https://doi.org/10.1007/s10059-012-2286-1

98. Berkes, C. A., & Tapscott, S. J. (2005). MyoD and the transcriptional control of myogenesis. *Seminars in Cell & Developmental Biology*, *16*, 585–595. https://doi.org/10.1016/j.semcdb.2005.07.006

99. Bondesen, B. A., Jones, K. A., Glasgow, W. C., & Pavlaoi, G. K. (2007). Inhibition of myoblast migration by prostacyclin is associated with enhanced cell fusion. *The FASEB Journal*, *21*(12), 3338–3345. https://doi.org/10.1096/fj.06-7070com

100. Abmayr, S. M., & Pavlath, G. K. (2012). Myoblast fusion: Lessons from flies and mice. In *Development* (Vol. 139, Issue 4, pp. 641–656). Company of Biologists. https://doi.org/10.1242/dev.068353

101. Mann, C. J., Perdiguero, E., Kharraz, Y., Aguilar, S., Pessina, P., Serrano, A. L., & Muñoz-Cánoves, P. (2011). Aberrant repair and fibrosis development in skeletal muscle. In *Skeletal Muscle* (Vol. 1, Issue 1, p. 21). BioMed Central. https://doi.org/10.1186/2044-5040-1-21

102. Weitkunat, M., Kaya-Çopur, A., Grill, S. W., & Schnorrer, F. (2014). Tension and force-resistant attachment are essential for myofibrillogenesis in drosophila flight muscle. *Current Biology*, *24*(7), 705–716. https://doi.org/10.1016/j.cub.2014.02.032

103. Spletter, M. L., Barz, C., Yeroslaviz, A., Zhang, X., Lemke, S. B., Bonnard, A., Brunner, E., Cardone, G., Basler, K., Habermann, B. H., & Schnorrer, F. (2018). A transcriptomics resource reveals a transcriptional transition during ordered sarcomere morphogenesis in flight muscle. *ELife*, *7*. https://doi.org/10.7554/eLife.34058

104. Brown D, & Williams K, & Cuccurullo S (2014). Myopathies. Maitin I.B., & Cruz E(Eds.), CURRENT Diagnosis & Treatment: Physical Medicine & Rehabilitation. McGraw-Hill. https://accessmedicine-mhmedical-com.sire.ub.edu/content.aspx?bookid=1180&sectionid=70378701

105. Chad, D. A. (2003). Neuromuscular Disorders, Overview. In Encyclopedia of the Neurological Sciences (pp. 494–500). Elsevier. https://doi.org/10.1016/b0-12-226870-9/00844-3

106. Gilbreath, H. R., Castro, D., & Iannaccone, S. T. (2014). Congenital myopathies and muscular dystrophies. In Neurologic Clinics (Vol. 32, Issue 3, pp. 689–703). W.B. Saunders. https://doi.org/10.1016/j.ncl.2014.04.006

107. Berardo, A., DiMauro, S., & Hirano, M. (2010). Diagnostic algorithm for metabolic myopathies. In Current Neurology and Neuroscience Reports (Vol. 10, Issue 2, pp. 118–126). NIH Public Access. https://doi.org/10.1007/s11910-010-0096-4

108. Pasnoor, M., Barohn, R. J., & Dimachkie, M. M. (2014). Toxic myopathies. In Neurologic Clinics (Vol. 32, Issue 3, pp. 647–670). W.B. Saunders. https://doi.org/10.1016/j.ncl.2014.04.009

109. Crum-Cianflone, N. F. (2008). Bacterial, fungal, parasitic, and viral myositis. In Clinical Microbiology Reviews (Vol. 21, Issue 3, pp. 473–494). American Society for Microbiology (ASM). https://doi.org/10.1128/CMR.00001-08

110. Sharma, V., Borah, P., Basumatary, L. J., Das, M., Goswami, M., & Kayal, A. K. (2014). Myopathies of endocrine disorders: A prospective clinical and biochemical study. Annals of Indian Academy of Neurology, 17(3), 298–302. https://doi.org/10.4103/0972-2327.138505

111. Chawla, J. (2011). Stepwise approach to myopathy in systemic disease. Frontiers in Neurology, AUG. https://doi.org/10.3389/fneur.2011.00049

112. Argilés, J. M., Busquets, S., Stemmler, B., & López-Soriano, F. J. (2014). Cancer cachexia: Understanding the molecular basis. In Nature Reviews Cancer (Vol. 14, Issue 11, pp. 754–762). Nature Publishing Group. https://doi.org/10.1038/nrc3829

113. Strassmann G, Fong M, Kenney JS, Jacob CO. Evidence for the involvement of interleukin 6 in experimental cancer cachexia. J Clin Invest. (1992) 89:1681–4. doi: 10.1172/JCI115767

114. Guttridge DC, MayoMW, Madrid LV, Wang CY, Baldwin AS Jr. NF-kappaB-induced loss of MyoD messenger RNA: possible role in muscle decay and cachexia. Science. (2000) 289:2363–6. doi: 10.1126/science.289.5488.2363

115. Zimmers TA, Davies MV, Koniaris LG, Haynes P, Esquela AF, Tomkinson KN, et al. Induction of cachexia in mice by systemically administered myostatin. Science. (2002) 296:1486–8. doi: 10.1126/science.1069525

116. Okugawa Y, Toiyama Y, Hur K, Yamamoto A, Yin C, Ide S, et al. Circulating miR-203 derived from metastatic tissues promotes myopenia in colorectal cancer patients. J Cachexia Sarcopenia Muscle. (2019) 10:536–48. doi: 10.1002/jcsm.12403

117. Zhang G, Liu Z, Ding H, Zhou Y, Doan HA, Sin KWT, et al. Tumor induces muscle wasting in mice through releasing extracellular Hsp70 and Hsp90. Nat Commun. (2017) 8:589. doi: 10.1038/s41467-017-00726-x

118. Marceca, G. P., Londhe, P., & Calore, F. (2020). Management of Cancer Cachexia: Attempting to Develop New Pharmacological Agents for New Effective Therapeutic Options. In Frontiers in Oncology (Vol. 10, p. 298). Frontiers Media S.A. https://doi.org/10.3389/fonc.2020.00298

119. Talbert, E. E., Cuitiñ, M. C., Ladner, K. J., Dillhoff, M. E., Schmidt, C. R., & Guttridge Correspondence, D. C. (2019). Modeling Human Cancer-induced Cachexia Gene ontology of cachectic muscles from KPP mice resembles that of PDA patients. *CellReports*, *28*, 1612-1622.e4. https://doi.org/10.1016/j.celrep.2019.07.016

120. Khodabukus, A., Madden, L., Prabhu, N. K., Koves, T. R., Jackman, C. P., Muoio, D. M., & Bursac, N. (2019). Electrical stimulation increases hypertrophy and metabolic flux in tissue-engineered human skeletal muscle. Biomaterials, 198, 259–269. https://doi.org/10.1016/j.biomaterials.2018.08.058

121. Yim, E. K. F., & Sheetz, M. P. (2012). Force-dependent cell signaling in stem cell differentiation. In *Stem Cell Research and Therapy* (Vol. 3, Issue 5, pp. 1–12). BioMed Central. https://doi.org/10.1186/scrt132

122. Casanellas, I., Lagunas, A., Vida, Y., Pérez-Inestrosa, E., Andrades, J. A., Becerra, J., & Samitier, J. (2019). Matrix Nanopatterning Regulates Mesenchymal Differentiation through Focal Adhesion Size and Distribution According to Cell Fate. *Biomimetics*, *4*(2), 43. https://doi.org/10.3390/biomimetics4020043

123. Graham, Z. A., Gallagher, P. M., & Cardozo, C. P. (2015). Focal adhesion kinase and its role in skeletal muscle. In *Journal of Muscle Research and Cell Motility* (Vol. 36, Issues 4–5, pp. 305–315). Springer International Publishing. https://doi.org/10.1007/s10974-015-9415-3

124. Ahumada, M., Jacques, E., Calderon, C., & Martínez-Gómez, F. (2018). Porosity in Biomaterials: A Key Factor in the Development of Applied Materials in Biomedicine. In *Handbook of Ecomaterials* (pp. 1–20). Springer International Publishing. https://doi.org/10.1007/978-3-319-48281-1_162-1

125. Zdravkov, B. D., Cermák, J. J. ˇ, Sefara, M., & Janků, J. (2007). Pore classification in the characterization of porous materials: A perspective. *CEJC*, *5*(2), 385–395. https://doi.org/10.2478/s11532-007-0017-9

126. Caliari, S. R., & Harley, B. A. C. (2011). Collagen-GAG materials. In *Comprehensive Biomaterials* (Vol. 2, pp. 279–302). Elsevier. https://doi.org/10.1016/b978-0-08-055294-1.00075-1

127. Pelham, R. J., & Wang, Y.-L. (1997). Cell locomotion and focal adhesions are regulated by substrate flexibility. In *Cell Biology* (Vol. 94). www.pnas.org.

128. Engler, A., Bacakova, L., Newman, C., Hategan, A., Griffin, M., & Discher, D. (2004). Substrate Compliance versus Ligand Density in Cell on Gel Responses. *Biophysical Journal*, *86*(1 I), 617–628. https://doi.org/10.1016/S0006-3495(04)74140-5

129. Evans, E., Leung, A., & Zhelev, D. (1993). Synchrony of cell spreading and contraction force as phagocytes engulf large pathogens. *Journal of Cell Biology*, *122*(6), 1295–1300. https://doi.org/10.1083/jcb.122.6.1295

130. Engler, A. J., Sen, S., Sweeney, H. L., & Discher, D. E. (2006). Matrix Elasticity Directs Stem Cell Lineage Specification. *Cell*, *126*(4), 677–689. https://doi.org/10.1016/j.cell.2006.06.044

131. Engler, A. J., Griffin, M. A., Sen, S., Bönnemann, C. G., Sweeney, H. L., & Discher, D. E. (2004). Myotubes differentiate optimally on substrates with tissue-like stiffness: Pathological implications for soft or stiff microenvironments. *Journal of Cell Biology*, *166*(6), 877–887. https://doi.org/10.1083/jcb.200405004

132. Jiwlawat, N., Lynch, E. M., Napiwocki, B. N., Stempien, A., Ashton, R. S., Kamp, T. J., Crone, W. C., & Suzuki, M. (2019). Micropatterned substrates with physiological stiffness promote cell maturation and Pompe disease phenotype in human induced pluripotent stem cell-derived skeletal myocytes. *Biotechnology and Bioengineering*, *116*(9), 2377–2392. https://doi.org/10.1002/bit.27075

133. Barnes, J. M., Przybyla, L., & Weaver, V. M. (2017). Tissue mechanics regulate brain development, homeostasis and disease. *COMMENTARY SPECIAL ISSUE: 3D CELL BIOLOGY*. https://doi.org/10.1242/jcs.191742

134. Heljak, M. K., Swieszkowski, W., & Kurzydlowski, K. J. (2014). Modeling of the degradation kinetics of biodegradable scaffolds: The effects of the environmental conditions. *Journal of Applied Polymer Science*, *131*(11), n/a-n/a. https://doi.org/10.1002/app.40280

135. Se, H. O., Soung, G. K., & Jin, H. L. (2006). Degradation behavior of hydrophilized PLGA scaffolds prepared by melt-molding particulate-leaching method: Comparison with control hydrophobic one. *Journal of Materials Science: Materials in Medicine*, *17*(2), 131–137. https://doi.org/10.1007/s10856-006-6816-2

136. Bramfeldt, H., Sarazin, P., & Vermette, P. (2008). Blends as a strategy towards tailored hydrolytic degradation of poly(ε-caprolactone-co-d,l-lactide)-poly(ethylene glycol)-poly(ε-caprolactone-co-d,l-lactide) co-polymers. *Polymer Degradation and Stability*, *93*(4), 877–882. https://doi.org/10.1016/j.polymdegradstab.2008.01.023

137. Wang, L., Wu, S., Cao, G., Fan, Y., Dunne, N., & Li, X. (2019). Biomechanical studies on biomaterial degradation and co-cultured cells: mechanisms, potential applications, challenges and prospects. *Journal of Materials Chemistry B*, *7*(47), 7439–7459. https://doi.org/10.1039/c9tb01539f

138. Lam, C. X. F., Hutmacher, D. W., Schantz, J. T., Woodruff, M. A., & Teoh, S. H. (2009). Evaluation of polycaprolactone scaffold degradation for 6 months in vitro and in vivo. *Journal of Biomedical Materials Research. Part A*, *90*(3), 906–919. https://doi.org/10.1002/jbm.a.32052

139. McKeon-Fischer, K. D., Flagg, D. H., & Freeman, J. W. (2011). Coaxial electrospun poly(ε-caprolactone), multiwalled carbon nanotubes, and polyacrylic acid/polyvinyl alcohol scaffold for skeletal muscle tissue engineering. *Journal of Biomedical Materials Research Part A*, *99A*(3), 493–499. https://doi.org/10.1002/jbm.a.33116

140. Merceron, T. K., Burt, M., Seol, Y. J., Kang, H. W., Lee, S. J., Yoo, J. J., & Atala, A. (2015). A 3D bioprinted complex structure for engineering the muscle-tendon unit. *Biofabrication*, *7*(3), 35003. https://doi.org/10.1088/1758-5090/7/3/035003

141. Huang, N. F., Patel, S., Thakar, R. G., Wu, J., Hsiao, B. S., Chu, B., Lee, R. J., & Li, S. (n.d.). *Myotube Assembly on Nanofibrous and Micropatterned Polymers*. https://doi.org/10.1021/nl060060o

142. Ricotti, L., Taccola, S., Pensabene, V., Mattoli, V., Fujie, T., Takeoka, S., Menciassi, A., & Dario, P. (2010). Adhesion and proliferation of skeletal muscle cells on single layer poly(lactic acid) ultra-thin films. *Biomedical Microdevices*, *12*(5), 809–819. https://doi.org/10.1007/s10544-010-9435-0

143. McKeon-Fischer, K. D., & Freeman, J. W. (2011). Characterization of electrospun poly(L-lactide) and gold nanoparticle composite scaffolds for skeletal muscle tissue engineering. *Journal of Tissue Engineering and Regenerative Medicine*, *5*(7), 560–568. https://doi.org/10.1002/term.348

144. Kim, M. J., Choi, Y. S., Yang, S. H., Hong, H. N., Cho, S. W., Cha, S. M., Pak, J. H., Kim, C. W., Kwon, S. W., & Park, C. J. (2006). Muscle regeneration by adipose tissue-derived adult stem cells attached to injectable PLGA spheres. *Biochemical and Biophysical Research Communications*, *348*(2), 386–392. https://doi.org/10.1016/j.bbrc.2006.07.063

145. Aviss, K. J., Gough, J. E., & Downes, S. (2010). Aligned electrospun polymer fibres for skeletal muscle regeneration. *European Cells and Materials*, *19*, 193–204. https://doi.org/10.22203/eCM.v019a19

146. Levenberg, S., Rouwkema, J., Macdonald, M., Garfein, E. S., Kohane, D. S., Darland, D. C., Marini, R., Van Blitterswijk, C. A., Mulligan, R. C., D'Amore, P. A., & Langer, R. (2005). Engineering vascularized skeletal muscle tissue. *Nature Biotechnology*, *23*(7), 879–884. https://doi.org/10.1038/nbt1109

147. Vannozzi, L., Ricotti, L., Santaniello, T., Terencio, T., Oropesa-Nunez, R., Canale, C., Borghi, F., Menciassi, A., Lenardi, C., & Gerges, I. (2017). *3D porous polyurethanes featured by different mechanical properties: Characterization and interaction with skeletal muscle cells*. https://doi.org/10.1016/j.jmbbm.2017.07.018

148. Liao, I.-C., Liu, J. B., Bursac, N., & Leong, K. W. (2008). Effect of Electromechanical Stimulation on the Maturation of Myotubes on Aligned Electrospun Fibers. *Cellular and Molecular Bioengineering*, *1*(2–3), 133–145. https://doi.org/10.1007/s12195-008-0021-y

149. Riboldi, S. A., Sadr, N., Pigini, L., Neuenschwander, P., Simonet, M., Mognol, P., Sampaolesi, M., Cossu, G., & Mantero, S. (2008). Skeletal myogenesis on highly orientated microfibrous polyesterurethane scaffolds. *Journal of Biomedical Materials Research Part A*, *84A*(4), 1094–1101. https://doi.org/10.1002/jbm.a.31534

150. Siepe, M., Giraud, M.-N., Liljensten, E., Nydegger, U., Menasche, P., Carrel, T., & Tevaearai, H. T. (2007). Construction of Skeletal Myoblast-Based Polyurethane Scaffolds for Myocardial Repair. *Artificial Organs*, *31*(6), 425–433. https://doi.org/10.1111/j.1525-1594.2007.00385.x

151. Milton Harris, J., & Chess, R. B. (2003). Effect of pegylation on pharmaceuticals. In *Nature Reviews Drug Discovery* (Vol. 2, Issue 3, pp. 214–221). Nature Publishing Group. https://doi.org/10.1038/nrd1033

152. Ensing, B., Tiwari, A., Tros, M., Hunger, J., Domingos, S. R., Pérez, C., Smits, G., Bonn, M., Bonn, D., & Woutersen, S. (2019). On the origin of the extremely different solubilities of polyethers in water. *Nature Communications*, *10*(1), 1–8. https://doi.org/10.1038/s41467-019-10783-z

153. Kolesky, D. B., Truby, R. L., Sydney Gladman, A., Busbee, T. A., Homan, K. A., Lewis, J. A., Kolesky, D. B., Truby, R. L., Gladman, A. S., Busbee, T., Homan, K.

A., & Lewis, J. A. (n.d.). *3D Bioprinting of Vascularized, Heterogeneous Cell-Laden Tissue Constructs*. https://doi.org/10.1002/adma.201305506

154. H.-W. Kang, S.J. Lee, I.K. Ko, C. Kengla, J.J. Yoo, A. Atala, A 3D bioprinting system to produce human-scale tissue constructs with structural integrity, Nat. Biotechnol. (2016), http://dx.doi.org/10.1038/nbt.3413

155. Mao, H., Wang, C., Chang, X., Cao, H., Shan, G., Bao, Y., & Pan, P. (2018). Poly(lactic acid)/poly(ethylene glycol) stereocomplexed physical hydrogels showing thermally-induced gel-sol-gel multiple phase transitions. *Materials Chemistry Frontiers*, *2*(2), 313–322. https://doi.org/10.1039/c7qm00502d

156. Guo, M., Pitet, L. M., Wyss, H. M., Vos, M., Dankers, P. Y. W., & Meijer, E. W. (2014). Tough stimuli-responsive supramolecular hydrogels with hydrogen-bonding network junctions. *Journal of the American Chemical Society*, *136*(19), 6969–6977. https://doi.org/10.1021/ja500205v

157. Liu, L., Feng, X., Pei, Y., Wang, J., Ding, J., & Chen, L. (2018). α-Cyclodextrin concentration-controlled thermo-sensitive supramolecular hydrogels. *Materials Science and Engineering C*, *82*, 25–28. https://doi.org/10.1016/j.msec.2017.08.045

158. O'Donnell, K., Boyd, A., & Meenan, B. J. (2019). Controlling Fluid Diffusion and Release through Mixed-Molecular-Weight Poly(ethylene) Glycol Diacrylate (PEGDA) Hydrogels. *Materials*, *12*(20), 3381. https://doi.org/10.3390/ma12203381

159. Rich, M. H., Lee, M. K., Marshall, N., Clay, N., Chen, J., Mahmassani, Z., Boppart, M., & Kong, H. (2015). Water-Hydrogel Binding Affinity Modulates Freeze-Drying-Induced Micropore Architecture and Skeletal Myotube Formation. *Biomacromolecules*, *16*(8), 2255–2264. https://doi.org/10.1021/acs.biomac.5b00652

160. García-Lizarribar, A., Fernández-Garibay, X., Velasco-Mallorquí, F., Castaño, A. G., Samitier, J., & Ramon-Azcon, J. (2018). Composite Biomaterials as Long-Lasting Scaffolds for 3D Bioprinting of Highly Aligned Muscle Tissue. *Macromolecular Bioscience*, 1800167. https://doi.org/10.1002/mabi.201800167

161. Ziemkiewicz, N., Talovic, M., Madsen, J., Hill, L., Scheidt, R., Patel, A., Haas, G., Marcinczyk, M., Zustiak, S. P., & Garg, K. (2018). Laminin-111 functionalized polyethylene glycol hydrogels support myogenic activity in vitro. *Biomedical Materials (Bristol)*, *13*(6), 065007. https://doi.org/10.1088/1748-605X/aad915

162. Han, W. M., Mohiuddin, M., Anderson, S. E., García, A. J., & Jang, Y. C. (2019). Co-delivery of Wnt7a and muscle stem cells using synthetic bioadhesive hydrogel enhances murine muscle regeneration and cell migration during engraftment. *Acta Biomaterialia*, *94*, 243–252. https://doi.org/10.1016/j.actbio.2019.06.025

163. Browe, D. P., Wood, C., Sze, M. T., White, K. A., Scott, T., Olabisi, R. M., & Freeman, J. W. (2017). Characterization and optimization of actuating poly(ethylene glycol) diacrylate/acrylic acid hydrogels as artificial muscles. *Polymer*, *117*, 331–341. https://doi.org/10.1016/j.polymer.2017.04.044

164. Hosseinzadeh, S., Rezayat, S. M., Giaseddin, A., Aliyan, A., & Soleimani, M. (2018). Microfluidic system for synthesis of nanofibrous conductive hydrogel and muscle differentiation. *Journal of Biomaterials Applications*, *32*(7), 853–861. https://doi.org/10.1177/0885328217744377

165. Villa, C., Martello, F., Erratico, S., Tocchio, A., Belicchi, M., Lenardi, C., & Torrente, Y. (2017). P(NIPAAM-co-HEMA) thermoresponsive hydrogels: an alternative approach for muscle cell sheet engineering. *Journal of Tissue Engineering and Regenerative Medicine*, *11*(1), 187–196. https://doi.org/10.1002/term.1898

166. Bačáková, L., Filová, E., Rypáček, F., Švorčík, V., & Starý, V. (2004). Cell Adhesion on Artificial Materials for Tissue Engineering. *Physiol. Res*, *53*, 35–45. http://www.biomed.cas.cz/physiolres

167. Dinescu, S., Albu Kaya, M., Chitoiu, L., Ignat, S., Kaya, D. A., & Costache, M. (2018). *Collagen-Based Hydrogels and Their Applications for Tissue Engineering and Regenerative Medicine* (pp. 1–21). Springer, Cham. https://doi.org/10.1007/978-3-319-76573-0_54-1

168. Rao, L., Qian, Y., Khodabukus, A., Ribar, T., & Bursac, N. (2018). Engineering human pluripotent stem cells into a functional skeletal muscle tissue. *Nature Communications*, *9*(1), 1–12. https://doi.org/10.1038/s41467-017-02636-4

169. Kim, W. J., & Kim, G. H. (2019). A functional bioink and its application in myoblast alignment and differentiation. *Chemical Engineering Journal*, *366*, 150–162. https://doi.org/10.1016/j.cej.2019.02.071

170. Kattula, S., Byrnes, J. R., & Wolberg, A. S. (2017). Fibrinogen and Fibrin in Hemostasis and Thrombosis. In *Arteriosclerosis, Thrombosis, and Vascular Biology* (Vol. 37, Issue 3, pp. e13–e21). Lippincott Williams and Wilkins. https://doi.org/10.1161/ATVBAHA.117.308564

171. Jackson, M. R. (2001). Fibrin sealants in surgical practice: An overview. *American Journal of Surgery*, *182*(2 SUPPL. 1), S1–S7. https://doi.org/10.1016/S0002-9610(01)00770-X

172. Cvetkovic, C., Raman, R., Chan, V., Williams, B. J., Tolish, M., Bajaj, P., Sakar, M. S., Asada, H. H., Saif, M. T. A., & Bashir, R. (2014). Three-dimensionally printed biological machines powered by skeletal muscle. *Proceedings of the National Academy of Sciences*, *111*(28), 10125–10130. https://doi.org/10.1073/pnas.1401577111

173. Rajabian, N., Shahini, A., Asmani, M., Vydiam, K., Choudhury, D., Nguyen, T., … Andreadis, S. T. (2020). Bioengineered Skeletal Muscle as a Model of Muscle Aging and Regeneration. *Tissue Engineering Part A*. https://doi.org/10.1089/ten.tea.2020.0005

174. Martin, N. R. W., Passey, S. L., Player, D. J., Mudera, V., Baar, K., Greensmith, L., & Lewis, M. P. (2015). Neuromuscular junction formation in tissue-engineered skeletal muscle augments contractile function and improves cytoskeletal organization. *Tissue Engineering - Part A*, *21*(19–20), 2595–2604. https://doi.org/10.1089/ten.tea.2015.0146

175. Khodabukus, A., Kaza, A., Wang, J., Prabhu, N., Goldstein, R., Vaidya, V. S., & Bursac, N. (2020). Tissue-engineered human myobundle system as a platform for evaluation of skeletal muscle injury biomarkers. *Toxicological Sciences*, *176*(1), 124–136. https://doi.org/10.1093/toxsci/kfaa049

176. Nikkhah, M., Akbari, M., Paul, A., Memic, A., Dolatshahi-Pirouz, A., & Khademhosseini, A. (2016). Gelatin-Based Biomaterials For Tissue Engineering And Stem Cell Bioengineering. In *Biomaterials from Nature for Advanced Devices and Therapies* (pp. 37–62). John Wiley & Sons, Inc. https://doi.org/10.1002/9781119126218.ch3

177. Bigi, A., Cojazzi, G., Panzavolta, S., Rubini, K., & Roveri, N. (2001). Mechanical and thermal properties of gelatin films at different degrees of glutaraldehyde crosslinking. *Biomaterials*, *22*(8), 763–768. https://doi.org/10.1016/S0142-9612(00)00236-2

178. Bertoldo, M., Bronco, S., Gragnoli, T., & Ciardelli, F. (2007). Modification of Gelatin by Reaction with 1,6-Diisocyanatohexane. *Macromolecular Bioscience*, *7*(3), 328–338. https://doi.org/10.1002/mabi.200600215

179. Draye, J. P., Delaey, B., Van De Voorde, A., Van Den Bulcke, A., Bogdanov, B., & Schacht, E. (1998). In vitro release characteristics of bioactive molecules from dextran dialdehyde cross-linked gelatin hydrogel films. *Biomaterials*, *19*(1–3), 99–107. https://doi.org/10.1016/S0142-9612(97)00164-6

180. Kim, H. W., Knowles, J. C., & Kim, H. E. (2005). Hydroxyapatite and gelatin composite foams processed via novel freeze-drying and crosslinking for use as temporary hard tissue scaffolds. *Journal of Biomedical Materials Research - Part A*, *72*(2), 136–145. https://doi.org/10.1002/jbm.a.30168

181. Vargas, G., Acevedo, J. L., López, J., & Romero, J. (2008). Study of cross-linking of gelatin by ethylene glycol diglycidyl ether. *Materials Letters*, *62*(21–22), 3656–3658. https://doi.org/10.1016/j.matlet.2008.04.020

182. Bertoni, F., Barbani, N., Giusti, P., & Ciardelli, G. (2006). Transglutaminase reactivity with gelatine: Perspective applications in tissue engineering. *Biotechnology Letters*, *28*(10), 697–702. https://doi.org/10.1007/s10529-006-9046-2

183. Aubin, H., Nichol, J. W., Hutson, C. B., Bae, H., Sieminski, A. L., Cropek, D. M., Akhyari, P., & Khademhosseini, A. (2010). Directed 3D cell alignment and elongation in microengineered hydrogels. *Biomaterials*, *31*(27), 6941–6951. https://doi.org/10.1016/j.biomaterials.2010.05.056

184. Hosseini, V., Ahadian, S., Ostrovidov, S., Camci-Unal, G., Chen, S., Kaji, H., Ramalingam, M., & Khademhosseini, A. (n.d.). *Engineered Contractile Skeletal Muscle Tissue on a Microgrooved Methacrylated Gelatin Substrate*. https://doi.org/10.1089/ten.tea.2012.0181

185. Meinert, C., Kaemmerer, E., Martine, L. C., Yue, K., Levett, P. A., Klein, T. J., W Melchels, F. P., Loessner, D., Khademhosseini, A., & Hutmacher, D. W. (2016). *Functionalization, preparation and use of cell-laden gelatin methacryloyl–based hydrogels as modular tissue culture platforms*. https://doi.org/10.1038/nprot.2016.037

186. Laternser, S., Keller, H., Leupin, O., Rausch, M., Graf-Hausner, U., & Rimann, M. (2018). A Novel Microplate 3D Bioprinting Platform for the Engineering of Muscle and Tendon Tissues. *SLAS Technology*, *23*(6), 599–613. https://doi.org/10.1177/2472630318776594

187. Calve, S., & Simon, H. (2012). Biochemical and mechanical environment cooperatively regulate skeletal muscle regeneration. *The FASEB Journal*, *26*(6), 2538–2545. https://doi.org/10.1096/fj.11-200162

188. Calve, S., Isaac, J., Gumucio, J. P., & Mendias, C. L. (2012). Hyaluronic acid, HAS1, and HAS2 are significantly upregulated during muscle hypertrophy. *American Journal of Physiology-Cell Physiology*, *303*(5), C577–C588. https://doi.org/10.1152/ajpcell.00057.2012

189. Leach, J. B., Bivens, K. A., Collins, C. N., & Schmidt, C. E. (2004). Development of photocrosslinkable hyaluronic acid-polyethylene glycol-peptide composite hydrogels for soft tissue engineering. *Journal of Biomedical Materials Research*, *70A*(1), 74–82. https://doi.org/10.1002/jbm.a.30063

190. Feroz, S., Muhammad, N., Ranayake, J., & Dias, G. (2020). Keratin - Based materials for biomedical applications. In *Bioactive Materials* (Vol. 5, Issue 3, pp. 496–509). KeAi Communications Co. https://doi.org/10.1016/j.bioactmat.2020.04.007

191. Feng, X., & Coulombe, P. A. (2015). A role for disulfide bonding in keratin intermediate filament organization and dynamics in skin keratinocytes. *Journal of Cell Biology*, *209*(1), 59–72. https://doi.org/10.1083/jcb.201408079

192. Tomblyn, S., Pettit Kneller, E. L., Walker, S. J., Ellenburg, M. D., Kowalczewski, C. J., Van Dyke, M., Burnett, L., & Saul, J. M. (2016). Keratin hydrogel carrier system for simultaneous delivery of exogenous growth factors and muscle progenitor cells. *Journal of Biomedical Materials Research Part B: Applied Biomaterials*, *104*(5), 864–879. https://doi.org/10.1002/jbm.b.33438

193. Baker, H. B., Passipieri, J. A., Siriwardane, M., Ellenburg, M. D., Vadhavkar, M., Bergman, C. R., Saul, J. M., Tomblyn, S., Burnett, L., & Christ, G. J. (2017). Cell and Growth Factor-Loaded Keratin Hydrogels for Treatment of Volumetric Muscle Loss in a Mouse Model. *Tissue Engineering Part A*, *23*(11–12), 572–584. https://doi.org/10.1089/ten.tea.2016.0457

194. Passipieri, J. A., Baker, H. B., Siriwardane, M., Ellenburg, M. D., Vadhavkar, M., Saul, J. M., Tomblyn, S., Burnett, L., & Christ, G. J. (2017). Keratin Hydrogel Enhances *In Vivo* Skeletal Muscle Function in a Rat Model of Volumetric Muscle Loss. *Tissue Engineering Part A*, *23*(11–12), 556–571. https://doi.org/10.1089/ten.tea.2016.0458

195. Saldin, L. T., Cramer, M. C., Velankar, S. S., White, L. J., & Badylak, S. F. (2017). Extracellular matrix hydrogels from decellularized tissues: Structure and function. In *Acta Biomaterialia* (Vol. 49, pp. 1–15). Elsevier Ltd. https://doi.org/10.1016/j.actbio.2016.11.068

196. Baiguera, S., Del Gaudio, C., Di Nardo, P., Manzari, V., Carotenuto, F., & Teodori, L. (2020). 3D Printing Decellularized Extracellular Matrix to Design Biomimetic Scaffolds for Skeletal Muscle Tissue Engineering. In *BioMed Research International* (Vol. 2020). Hindawi Limited. https://doi.org/10.1155/2020/2689701

197. Urciuolo, A., Urbani, L., Perin, S., Maghsoudlou, P., Scottoni, F., Gjinovci, A., Collins-Hooper, H., Loukogeorgakis, S., Tyraskis, A., Torelli, S., Germinario, E., Fallas, M. E. A., Julia-Vilella, C., Eaton, S., Blaauw, B., Patel, K., & De Coppi, P. (2018). Decellularised skeletal muscles allow functional muscle regeneration by promoting host cell migration. *Scientific Reports*, *8*(1), 1–20. https://doi.org/10.1038/s41598-018-26371-y

198. Choi, Y. J., Jun, Y. J., Kim, D. Y., Yi, H. G., Chae, S. H., Kang, J., Lee, J., Gao, G., Kong, J. S., Jang, J., Chung, W. K., Rhie, J. W., & Cho, D. W. (2019). A 3D cell printed muscle construct with tissue-derived bioink for the treatment of volumetric muscle loss. *Biomaterials*, *206*, 160–169. https://doi.org/10.1016/j.biomaterials.2019.03.036

199. Kim, W. J., Lee, H., Lee, J. U., Atala, A., Yoo, J. J., Lee, S. J., & Kim, G. H. (2020). Efficient myotube formation in 3D bioprinted tissue construct by biochemical and topographical cues. *Biomaterials*, *230*, 119632. https://doi.org/10.1016/j.biomaterials.2019.119632

200. Patel, K. H., Dunn, A. J., Talovic, M., Haas, G. J., Marcinczyk, M., Elmashhady, H., Kalaf, E. G., Sell, S. A., & Garg, K. (2019). Aligned nanofibers of decellularized muscle ECM support myogenic activity in primary satellite cells in vitro. *Biomedical Materials (Bristol)*, *14*(3), 35010. https://doi.org/10.1088/1748-605X/ab0b06

201. Hong, Y., Huber, A., Takanari, K., Amoroso, N. J., Hashizume, R., Badylak, S. F., & Wagner, W. R. (2011). Mechanical properties and in vivo behavior of a biodegradable synthetic polymer microfiber-extracellular matrix hydrogel biohybrid scaffold. *Biomaterials*, *32*(13), 3387–3394. https://doi.org/10.1016/j.biomaterials.2011.01.025

202. Neal, D., Sakar, M. S., Ong, L. L. S., & Harry Asada, H. (2014). Formation of elongated fascicle-inspired 3D tissues consisting of high-density, aligned cells using sacrificial outer molding. *Lab on a Chip*, *14*(11), 1907–1916. https://doi.org/10.1039/c4lc00023d

203. Bian, W., Liau, B., Badie, N., & Bursac, N. (2009). Mesoscopic hydrogel molding to control the 3d geometry of bioartificial muscle tissues. *Nature Protocols*, *4*(10), 1522–1534. https://doi.org/10.1038/nprot.2009.155

204. Lee, K. Y., & Mooney, D. J. (2012). Alginate: Properties and biomedical applications. In *Progress in Polymer Science (Oxford)* (Vol. 37, Issue 1, pp. 106–126). Elsevier Ltd. https://doi.org/10.1016/j.progpolymsci.2011.06.003

205. Liling, G., Di, Z., Jiachao, X., Xin, G., Xiaoting, F., & Qing, Z. (2016). Effects of ionic crosslinking on physical and mechanical properties of alginate mulching films. *Carbohydrate Polymers*, *136*, 259–265. https://doi.org/10.1016/j.carbpol.2015.09.034

206. Krzywoszyńska, K., Witkowska, D., Swiatek-kozlowska, J., Szebesczyk, A., & Kozłowski, H. (2020). General aspects of metal ions as signaling agents in health and disease. In *Biomolecules* (Vol. 10, Issue 10, pp. 1–30). MDPI AG. https://doi.org/10.3390/biom10101417

207. Jeon, O., Bouhadir, K. H., Mansour, J. M., & Alsberg, E. (2009). Photocrosslinked alginate hydrogels with tunable biodegradation rates and mechanical properties. *Biomaterials*, *30*(14), 2724–2734. https://doi.org/10.1016/j.biomaterials.2009.01.034

208. Bidarra, S. J., Barrias, C. C., & Granja, P. L. (2014). Injectable alginate hydrogels for cell delivery in tissue engineering. In *Acta Biomaterialia* (Vol. 10, Issue 4, pp. 1646–1662). Elsevier BV. https://doi.org/10.1016/j.actbio.2013.12.006

209. Chou, A. I., Akintoye, S. O., & Nicoll, S. B. (2009). Photo-crosslinked alginate hydrogels support enhanced matrix accumulation by nucleus pulposus cells in vivo. *Osteoarthritis and Cartilage*, *17*(10), 1377–1384. https://doi.org/10.1016/j.joca.2009.04.012

210. Fenn, S. L., Miao, T., Scherrer, R. M., & Oldinski, R. A. (2016). Dual-Cross-Linked Methacrylated Alginate Sub-Microspheres for Intracellular Chemotherapeutic Delivery. *ACS Applied Materials and Interfaces*, *8*(28), 17775–17783. https://doi.org/10.1021/acsami.6b03245

211. Chandler, E. M., Berglund, C. M., Lee, J. S., Polacheck, W. J., Gleghorn, J. P., Kirby, B. J., & Fischbach, C. (2011). Stiffness of photocrosslinked RGD-alginate gels regulates adipose progenitor cell behavior. *Biotechnology and Bioengineering*, *108*(7), 1683–1692. https://doi.org/10.1002/bit.23079

212. Tommila, M., Jokilammi, A., Penttinen, R., & Ekholm, E. (2013). Cellulose - A Biomaterial with Cell-Guiding Property. In Cellulose - Medical, Pharmaceutical and Electronic Applications. InTech. https://doi.org/10.5772/54436

213. Hickey, R. J., & Pelling, A. E. (2019). Cellulose biomaterials for tissue engineering. In Frontiers in Bioengineering and Biotechnology (Vol. 7, Issue MAR, p. 45). Frontiers Media S.A. https://doi.org/10.3389/fbioe.2019.00045

214. Kabir, S. M. F., Sikdar, P. P., Haque, B., Bhuiyan, M. A. R., Ali, A., & Islam, M. N. (2018). Cellulose-based hydrogel materials: chemistry, properties and their prospective applications. Progress in Biomaterials, 7(3), 153–174. https://doi.org/10.1007/s40204-018-0095-0

215. Capanema, N. S. V., Mansur, A. A. P., de Jesus, A. C., Carvalho, S. M., de Oliveira, L. C., & Mansur, H. S. (2018). Superabsorbent crosslinked carboxymethyl cellulose-PEG hydrogels for potential wound dressing applications. *International Journal of Biological Macromolecules*, *106*, 1218–1234. https://doi.org/10.1016/j.ijbiomac.2017.08.124

216. Mali, K. K., Dhawale, S. C., Dias, R. J., Dhane, N. S., & Ghorpade, V. S. (2018). Citric acid crosslinked carboxymethyl cellulose-based composite hydrogel films for drug delivery. Indian Journal of Pharmaceutical Sciences, 80(4), 657–667. https://doi.org/10.4172/pharmaceutical-sciences.1000405

217. Leonardis, M., Palange, A., Dornelles, R. F. V., & Hund, F. (2010). Use of cross-linked carboxymethyl cellulose for soft-tissue augmentation: preliminary clinical studies. *Clinical Interventions in Aging*, *5*, 317–322. https://doi.org/10.2147/cia.s13813

218. Velasco-Mallorquí, F., Fernández-Costa, J. M., Neves, L., & Ramón-Azcón, J. (2020). New volumetric CNT-doped gelatin-cellulose scaffolds for skeletal muscle tissue engineering. Nanoscale Advances, 2(7), 2885–2896. https://doi.org/10.1039/d0na00268b

219. Zarrintaj, P., Manouchehri, S., Ahmadi, Z., Saeb, M. R., Urbanska, A. M., Kaplan, D. L., & Mozafari, M. (2018). Agarose-based biomaterials for tissue engineering. In Carbohydrate Polymers (Vol. 187, pp. 66–84). Elsevier Ltd. https://doi.org/10.1016/j.carbpol.2018.01.060

220. Guaccio, A., Borselli, C., Oliviero, O., & Netti, P. A. (2008). Oxygen consumption of chondrocytes in agarose and collagen gels: A comparative analysis. *Biomaterials*, *29*(10), 1484–1493. https://doi.org/10.1016/j.biomaterials.2007.12.020

221. Bagher, Z., Atoufi, Z., Alizadeh, R., Farhadi, M., Zarrintaj, P., Moroni, L., Setayeshmehr, M., Komeili, A., & Kamrava, S. K. (2019). Conductive hydrogel based on chitosan-aniline pentamer/gelatin/agarose significantly promoted motor neuron-like cells differentiation of human olfactory ecto-mesenchymal stem cells. Materials Science and Engineering C, 101, 243–253. https://doi.org/10.1016/j.msec.2019.03.068

222. Strobel, H. A., Calamari, E. L., Alphonse, B., Hookway, T. A., & Rolle, M. W. (2018). Fabrication of custom agarose wells for cell seeding and tissue ring self-assembly using 3D-printed molds. Journal of Visualized Experiments, 2018(134), 56618. https://doi.org/10.3791/56618

223. Tanaka, T., Hattori-Aramaki, N., Sunohara, A., Okabe, K., Sakamoto, Y., Ochiai, H., Hayashi, R., & Kishi, K. (2014). Alignment of Skeletal Muscle Cells Cultured in Collagen Gel by Mechanical and Electrical Stimulation. International Journal of Tissue Engineering, 2014, 1–5. https://doi.org/10.1155/2014/621529

224. Pollot, B. E., Rathbone, C. R., Wenke, J. C., & Guda, T. (2018). Natural polymeric hydrogel evaluation for skeletal muscle tissue engineering. Journal of Biomedical Materials Research Part B: Applied Biomaterials, 106(2), 672–679. https://doi.org/10.1002/jbm.b.33859

225. Bandyopadhyay, A., Chowdhury, S. K., Dey, S., Moses, J. C., & Mandal, B. B. (2019). Silk: A Promising Biomaterial Opening New Vistas Towards Affordable Healthcare Solutions. In Journal of the Indian Institute of Science (Vol. 99, Issue 3, pp. 445–487). Springer International Publishing. https://doi.org/10.1007/s41745-019-00114-y

226. Manchineella, S., Thrivikraman, G., Khanum, K. K., Ramamurthy, P. C., Basu, B., & Govindaraju, T. (2016). Pigmented Silk Nanofibrous Composite for Skeletal Muscle Tissue Engineering. Advanced Healthcare Materials, 5(10), 1222–1232. https://doi.org/10.1002/adhm.201501066

227. Zhang, M., & Guo, B. (2017). Electroactive 3D Scaffolds Based on Silk Fibroin and Water-Borne Polyaniline for Skeletal Muscle Tissue Engineering. *Macromolecular Bioscience*, *17*(9), 1700147. https://doi.org/10.1002/mabi.201700147

228. Chaturvedi, V., Naskar, D., Kinnear, B. F., Grenik, E., Dye, D. E., Grounds, M. D., Kundu, S. C., & Coombe, D. R. (2017). Silk fibroin scaffolds with muscle-like elasticity support in vitro differentiation of human skeletal muscle cells. Journal of Tissue Engineering and Regenerative Medicine, 11(11), 3178–3192. https://doi.org/10.1002/term.2227

229. Ren, Y. J., Zhou, Z. Y., Liu, B. F., Xu, Q. Y., & Cui, F. Z. (2009). Preparation and characterization of fibroin/hyaluronic acid composite scaffold. *International Journal of Biological Macromolecules*, *44*(4), 372–378. https://doi.org/10.1016/j.ijbiomac.2009.02.004

230. Zhou, J., Cao, C., Ma, X., & Lin, J. (2010). Electrospinning of silk fibroin and collagen for vascular tissue engineering. *International Journal of Biological Macromolecules*, *47*(4), 514–519. https://doi.org/10.1016/j.ijbiomac.2010.07.010

231. Mandal, B. B., Kapoor, S., & Kundu, S. C. (2009). Silk fibroin/polyacrylamide semi-interpenetrating network hydrogels for controlled drug release. *Biomaterials*, *30*(14), 2826–2836. https://doi.org/10.1016/j.biomaterials.2009.01.040

232. Jiang, T., James, R., Kumbar, S. G., & Laurencin, C. T. (2014). Chitosan as a Biomaterial: Structure, Properties, and Applications in Tissue Engineering and Drug Delivery. In *Natural and Synthetic Biomedical Polymers* (pp. 91–113). Elsevier Inc. https://doi.org/10.1016/B978-0-12-396983-5.00005-3

233. Akpan, E. I., Gbenebor, O. P., Adeosun, S. O., & Cletus, O. (2020). Solubility, degree of acetylation, and distribution of acetyl groups in chitosan. In *Handbook of Chitin and Chitosan* (pp. 131–164). Elsevier. https://doi.org/10.1016/b978-0-12-817970-3.00005-5

234. Dai, T., Tanaka, M., Huang, Y. Y., & Hamblin, M. R. (2011). Chitosan preparations for wounds and burns: Antimicrobial and wound-healing effects. In *Expert*

Review of Anti-Infective Therapy (Vol. 9, Issue 7, pp. 857–879). NIH Public Access. https://doi.org/10.1586/eri.11.59

235. Cooper, A., Jana, S., Bhattarai, N., & Zhang, M. (2010). Aligned chitosan-based nanofibers for enhanced myogenesis. *Journal of Materials Chemistry*, *20*(40), 8904–8911. https://doi.org/10.1039/c0jm01841d

236. Kheradmandi, M., Vasheghani-Farahani, E., Ghiaseddin, A., & Ganji, F. (2016). Skeletal muscle regeneration via engineered tissue culture over electrospun nanofibrous chitosan/PVA scaffold. *Journal of Biomedical Materials Research Part A*, *104*(7), 1720–1727. https://doi.org/10.1002/jbm.a.35702

237. Junkin, M., Leung, S. L., Whitman, S., Gregorio, C. C., & Wong, P. K. (2011). Cellular self-organization by autocatalytic alignment feedback. *Journal of Cell Science*, *124*(24), 4213–4220. https://doi.org/10.1242/jcs.088898

238. Vajanthri, K. Y., Sidu, R. K., & Mahto, S. K. (2020). Micropatterning and Alignment of Skeletal Muscle Myoblasts Using Microflowed Plasma Process. *IRBM*, *41*(1), 48–57. https://doi.org/10.1016/j.irbm.2019.08.003

239. Almonacid Suarez, A. M., Zhou, Q., Rijn, P., & Harmsen, M. C. (2019). Directional topography gradients drive optimum alignment and differentiation of human myoblasts. *Journal of Tissue Engineering and Regenerative Medicine*, *13*(12), 2234–2245. https://doi.org/10.1002/term.2976

240. Zhao, Y., Zeng, H., Nam, J., & Agarwal, S. (2009). Fabrication of skeletal muscle constructs by topographic activation of cell alignment. *Biotechnology and Bioengineering*, *102*(2), 624–631. https://doi.org/10.1002/bit.22080

241. Ahadian, S., Ramón-Azcón, J., Ostrovidov, S., Camci-Unal, G., Hosseini, V., Kaji, H., … Matsue, T. (2012). Interdigitated array of Pt electrodes for electrical stimulation and engineering of aligned muscle tissue. *Lab on a Chip*, *12*(18), 3491–3503. https://doi.org/10.1039/c2lc40479f

242. Sun, Y., Duffy, R., Lee, A., & Feinberg, A. W. (2013). *Optimizing the structure and contractility of engineered skeletal muscle thin films*. https://doi.org/10.1016/j.actbio.2013.04.036

243. Choi, J. S., Lee, S. J., Christ, G. J., Atala, A., & Yoo, J. J. (2008). The influence of electrospun aligned poly(ε-caprolactone)/collagen nanofiber meshes on the formation of self-aligned skeletal muscle myotubes. *Biomaterials*, *29*(19), 2899–2906. https://doi.org/10.1016/j.biomaterials.2008.03.031

244. MacQueen, L. A., Alver, C. G., Chantre, C. O., Ahn, S., Cera, L., Gonzalez, G. M., O'Connor, B. B., Drennan, D. J., Peters, M. M., Motta, S. E., Zimmerman, J. F., & Parker, K. K. (2019). Muscle tissue engineering in fibrous gelatin: implications for meat analogs. *Npj Science of Food*, *3*(1), 1–12. https://doi.org/10.1038/s41538-019-0054-8

245. Smoak, M. M., Han, A., Watson, E., Kishan, A., Grande-Allen, K. J., Cosgriff-Hernandez, E., & Mikos, A. G. (2019). Fabrication and characterization of electrospun decellularized muscle-derived scaffolds. *Tissue Engineering - Part C: Methods*, *25*(5), 276–287. https://doi.org/10.1089/ten.tec.2018.0339

246. Bansai, S., Morikura, T., Onoe, H., & Miyata, S. (2019). Effect of cyclic stretch on tissue maturation in myoblast-laden hydrogel fibers. *Micromachines*, *10*(6). https://doi.org/10.3390/mi10060399

247. Dado, D., & Levenberg, S. (2009). Cell-scaffold mechanical interplay within engineered tissue. In *Seminars in Cell and Developmental Biology* (Vol. 20, Issue 6, pp. 656–664). Elsevier Ltd. https://doi.org/10.1016/j.semcdb.2009.02.001

248. Vandenburgh, H., Shansky, J., Benesch-Lee, F., Barbata, V., Reid, J., Thorrez, L., … Crawford, G. (2008). Drug-screening platform based on the contractility of tissue-engineered muscle. *Muscle and Nerve*, *37*(4), 438–447. https://doi.org/10.1002/mus.20931

249. Iuliano, A., van der Wal, E., Ruijmbeek, C. W. B., in 't Groen, S. L. M., Pijnappel, W. W. M. P., de Greef, J. C., & Saggiomo, V. (2020). Coupling 3D Printing and Novel Replica Molding for In House Fabrication of Skeletal Muscle Tissue Engineering Devices. *Advanced Materials Technologies*, *5*(9). https://doi.org/10.1002/admt.202000344

250. Morimoto, Y., Onoe, H., & Takeuchi, S. (2018). Biohybrid robot powered by an antagonistic pair of skeletal muscle tissues. Science Robotics, 3(18), 4440. https://doi.org/10.1126/scirobotics.aat4440

251. Gillispie, G., Prim, P., Copus, J., Fisher, J., Mikos, A. G., Yoo, J. J., Atala, A., & Lee, S. J. (2020). Assessment methodologies for extrusion-based bioink printability. In Biofabrication (Vol. 12, Issue 2, p. 022003). Institute of Physics Publishing. https://doi.org/10.1088/1758-5090/ab6f0d

252. Kyle, S., Jessop, Z. M., Al-Sabah, A., & Whitaker, I. S. (2017). 'Printability'' of Candidate Biomaterials for Extrusion Based 3D Printing: State-of-the-Art.' Advanced Healthcare Materials, 6(16), 1700264. https://doi.org/10.1002/adhm.201700264

253. Ouyang, L., Yao, R., Zhao, Y., & Sun, W. (2016). Effect of bioink properties on printability and cell viability for 3D bioplotting of embryonic stem cells. Biofabrication, 8(3), 035020. https://doi.org/10.1088/1758-5090/8/3/035020

254. Paxton, N., Smolan, W., Böck, T., Melchels, F., Groll, J., & Jungst, T. (2017). Proposal to assess printability of bioinks for extrusion-based bioprinting and evaluation of rheological properties governing bioprintability. *Biofabrication*, *9*(4). https://doi.org/10.1088/1758-5090/aa8dd8

255. Hafezi, F., Shorter, S., Tabriz, A. G., Hurt, A., Elmes, V., Boateng, J., & Douroumis, D. (2020). Bioprinting and preliminary testing of highly reproducible novel bioink for potential skin regeneration. *Pharmaceutics*, *12*(6), 1–21. https://doi.org/10.3390/pharmaceutics12060550

256. Blaeser, A., Duarte Campos, D. F., Puster, U., Richtering, W., Stevens, M. M., & Fischer, H. (2016). Controlling Shear Stress in 3D Bioprinting is a Key Factor to Balance Printing Resolution and Stem Cell Integrity. Advanced Healthcare Materials, 5(3), 326–333. https://doi.org/10.1002/adhm.201500677

257. Costantini, M., Testa, S., Mozetic, P., Barbetta, A., Fuoco, C., Fornetti, E., … Gargioli, C. (2017). Microfluidic-enhanced 3D bioprinting of aligned myoblast-laden hydrogels leads to functionally organized myofibers in vitro and in vivo. Biomaterials, 131, 98–110. https://doi.org/10.1016/j.biomaterials.2017.03.026

258. Mozetic, P., Giannitelli, S. M., Gori, M., Trombetta, M., & Rainer, A. (2017). Engineering muscle cell alignment through 3D bioprinting. *Journal of Biomedical Materials Research Part A*, *105*(9), 2582–2588. https://doi.org/10.1002/jbm.a.36117

259. Kim, H., Jang, J., Park, J., Lee, K. P., Lee, S., Lee, D. M., Kim, K. H., Kim, H. K., & Cho, D. W. (2019). Shear-induced alignment of collagen fibrils using 3D cell printing for corneal stroma tissue engineering. Biofabrication, 11(3), 035017. https://doi.org/10.1088/1758-5090/ab1a8b

260. Distler, T., Solisito, A. A., Schneidereit, D., Friedrich, O., Detsch, R., & Boccaccini, A. R. (2020). 3D printed oxidized alginate-gelatin bioink provides guidance for C2C12 muscle precursor cell orientation and differentiation via shear stress during bioprinting. Biofabrication, 12(4), 045005. https://doi.org/10.1088/1758-5090/ab98e4

261. Kang, H. W., Lee, S. J., Ko, I. K., Kengla, C., Yoo, J. J., & Atala, A. (2016). A 3D bioprinting system to produce human-scale tissue constructs with structural integrity. Nature Biotechnology, 34(3), 312–319. https://doi.org/10.1038/nbt.3413

262. Kim, J. H., Seol, Y. J., Ko, I. K., Kang, H. W., Lee, Y. K., Yoo, J. J., … Lee, S. J. (2018). 3D Bioprinted Human Skeletal Muscle Constructs for Muscle Function Restoration. Scientific Reports, 8(1). https://doi.org/10.1038/s41598-018-29968-5

263. Ngan, C., Quigley, A., O'Connell, C., Kita, M., Bourke, J., Wallace, G. G., … Kapsa, R. M. I. (2020). 3D Bioprinting and Differentiation of Primary Skeletal Muscle Progenitor Cells. In Methods in Molecular Biology (Vol. 2140, pp. 229–242). Humana Press Inc. https://doi-org.sire.ub.edu/10.1007/978-1-0716-0520-2_15

264. Seyedmahmoud, R., Çelebi-Saltik, B., Barros, N., Nasiri, R., Banton, E., Shamloo, A., … Ahadian, S. (2019). Three-dimensional bioprinting of functional skeletal muscle tissue using gelatin methacryloyl-alginate bioinks. Micromachines, 10(10). https://doi.org/10.3390/mi10100679

265. Mestre, R., Patiño, T., Barceló, X., Anand, S., Pérez-Jiménez, A., & Sánchez, S. (2019). Force Modulation and Adaptability of 3D-Bioprinted Biological Actuators Based on Skeletal Muscle Tissue. Advanced Materials Technologies, 4(2). https://doi.org/10.1002/admt.201800631

266. Choi, Y. J., Kim, T. G., Jeong, J., Yi, H. G., Park, J. W., Hwang, W., & Cho, D. W. (2016). 3D Cell Printing of Functional Skeletal Muscle Constructs Using Skeletal Muscle-Derived Bioink. Advanced Healthcare Materials, 5(20), 2636–2645. https://doi.org/10.1002/adhm.201600483

267. Cvetkovic, C., Rich, M. H., Raman, R., Kong, H., & Bashir, R. (2017). A 3D-printed platform for modular neuromuscular motor units. Microsystems & Nanoengineering, 3(1), 1–9. https://doi.org/10.1038/micronano.2017.15

268. Morimoto, Y., Kato-Negishi, M., Onoe, H., & Takeuchi, S. (2013). Three-dimensional neuron-muscle constructs with neuromuscular junctions. Biomaterials, 34(37), 9413–9419. https://doi.org/10.1016/j.biomaterials.2013.08.062

269. Ortega, M. A., Fernández-Garibay, X., Castaño, A. G., De Chiara, F., Hernández-Albors, A., Balaguer-Trias, J., & Ramón-Azcón, J. (2019). Muscle-on-a-chip with an on-site multiplexed biosensing system for: In situ monitoring of secreted IL-6 and TNF-α. Lab on a Chip, 19(15), 2568–2580. https://doi.org/10.1039/c9lc00285e

270. Ito, A., Yamamoto, Y., Sato, M., Ikeda, K., Yamamoto, M., Fujita, H., Nagamori, E., Kawabe, Y., & Kamihira, M. (2015). Induction of functional tissue-engineered skeletal muscle constructs by defined electrical stimulation. Scientific Reports, 4(1), 4781. https://doi.org/10.1038/srep04781

271. J. Visser, F. P. Melchels, J. E. Jeon, E. M. van Bussel, L. S. Kimpton, H. M. Byrne, W. J. Dhert, P. D. Dalton, D. W. Hutmacher, & Malda, J. (2015). Reinforcement of hydrogels using three-dimensionally printed microfibres. Nature Communications, 6, 6933. https://doi.org/10.1038/ncomms7933

272. Reeves, R., Ribeiro, A., Lombardo, L., Boyer, R., & Leach, J. B. (2010). Synthesis and characterization of carboxymethylcellulose-methacrylate hydrogel cell scaffolds. Polymers, 2(3), 252–264. https://doi.org/10.3390/polym2030252

273. Nichol, J. W., Koshy, S. T., Bae, H., Hwang, C. M., Yamanlar, S., & Khademhosseini, A. (2010). Cell-laden microengineered gelatin methacrylate hydrogels. Biomaterials, 31(21), 5536–5544. https://doi.org/10.1016/j.biomaterials.2010.03.064

274. Yin, J., Yan, M., Wang, Y., Fu, J., & Suo, H. (2018). 3D Bioprinting of Low-Concentration Cell-Laden Gelatin Methacrylate (GelMA) Bioinks with a Two-Step Cross-linking Strategy. https://doi.org/10.1021/acsami.7b16059

275. Wong, D. Y., Ranganath, T., & Kasko, A. M. (2015). Low-dose, long-wave UV light does not affect gene expression of human mesenchymal stem cells. PLoS ONE, 10(9). https://doi.org/10.1371/journal.pone.0139307

276. Lin, R.-Z., Chen, Y.-C., Moreno-Luna, R., Khademhosseini, A., & Melero-Martin, J. M. (2013). Transdermal regulation of vascular network bioengineering using a photopolymerizable methacrylated gelatin hydrogel. https://doi.org/10.1016/j.biomaterials.2013.05.060

277. Hensman, C., Hanna, G. B., Drew, T., Moseley, H., & Cuschieri, A. (1998). Total radiated power, infrared output, and heat generation by cold light sources at the distal end of endoscopes and fiber optic bundle of light cables. Surgical Endoscopy, 12(4), 335–337. https://doi.org/10.1007/s004649900665

278. Fairbanks, B. D., Schwartz, M. P., Bowman, C. N., & Anseth, K. S. (2009). Photoinitiated polymerization of PEG-diacrylate with lithium phenyl-2,4,6-trimethylbenzoylphosphinate: polymerization rate and cytocompatibility. Biomaterials. https://doi.org/10.1016/j.biomaterials.2009.08.055

279. Leonhardt, S., Klare, M., Scheer, M., Fischer, T., Cordes, B., & Eblenkamp, M. (2016). Biocompatibility of photopolymers for additive manufacturing. Current Directions in Biomedical Engineering, 2(1), 113–116. https://doi.org/10.1515/cdbme-2016-0028

280. Wei, D., Xiao, W., Sun, J., Zhong, M., Guo, L., Fan, H., & Zhang, X. (2015). Materials Chemistry B A biocompatible hydrogel with improved stiffness and hydrophilicity for modular tissue engineering assembly. 3(14), 2745–2910. www.rsc.org/MaterialsB

281. Berger, A. J., Linsmeier, K. M., Kreeger, P. K., & Masters, K. S. (2017). Decoupling the effects of stiffness and fiber density on cellular behaviors via an interpenetrating network of gelatin-methacrylate and collagen. Biomaterials, 141, 125–135. https://doi.org/10.1016/j.biomaterials.2017.06.039

282. Janmaleki, M., Liu, J., Kamkar, M., Azarmanesh, M., Sundararaj, U., & Nezhad, A. S. (2021). Role of temperature on bio-printability of gelatin methacryloyl bioink in two-step cross-linking strategy for tissue engineering applications. Biomedical Materials (Bristol), 16(1), 015021. https://doi.org/10.1088/1748-605X/abbcc9

283. Li, M., Tian, X., Schreyer, D. J., & Chen, X. (2011). Effect of needle geometry on flow rate and cell damage in the dispensing-based biofabrication process. Biotechnology Progress, 27(6), 1777–1784. https://doi.org/10.1002/btpr.679

284. Chang, R., Nam, J., & Sun, W. (n.d.). Effects of Dispensing Pressure and Nozzle Diameter on Cell Survival from Solid Freeform Fabrication-Based Direct Cell Writing. https://doi.org/10.1089/ten.a.2007.0004

285. Fedorovich, N. E., Kuipers, E., Gawlitta, D., Dhert, W. J. A., & Alblas, J. (2011). Scaffold porosity and oxygenation of printed hydrogel constructs affect functionality of embedded osteogenic progenitors. Tissue Engineering - Part A, 17(19–20), 2473–2486. https://doi.org/10.1089/ten.tea.2011.0001

286. Aparnathi, M. K., & Patel, J. S. (2016). Effect of gel porosity and stiffness on culture of HepG2 cells encapsulated in gelatin methacrylate hydrogels. Thomson Reuters ISI ESC and Crossref Indexed Journal NAAS Journal Score, 9(3), 463–470. www.bbrc.in/

287. Karande, T. S., Ong, J. L., & Agrawal, C. M. (2004). Diffusion in musculoskeletal tissue engineering scaffolds: Design issues related to porosity, permeability, architecture, and nutrient mixing. Annals of Biomedical Engineering, 32(12), 1728–1743. https://doi.org/10.1007/s10439-004-7825-2

288. Duchi, S., Onofrillo, C., O'Connell, C. D., Blanchard, R., Augustine, C., Quigley, A. F., Kapsa, R. M. I., Pivonka, P., Wallace, G., Di Bella, C., & Choong, P. F. M. (2017). Handheld Co-Axial Bioprinting: Application to in situ surgical cartilage repair. Scientific Reports, 7(1), 1–12. https://doi.org/10.1038/s41598-017-05699-x

289. Wittmer, C. R., Phelps, J. A., Saltzman, W. M., & Van Tassel, P. R. (2007). Fibronectin terminated multilayer films: Protein adsorption and cell attachment studies. Biomaterials, 28(5), 851–860. https://doi.org/10.1016/j.biomaterials.2006.09.037

290. Han, N., Johnson, J. K., Bradley, P. A., Parikh, K. S., Lannutti, J. J., & Winter, J. O. (2012). Cell Attachment to Hydrogel-Electrospun Fiber Mat Composite Materials. Journal of Functional Biomaterials, 3(3), 497–513. https://doi.org/10.3390/jfb3030497

291. Grzelkowska-Kowalczyk, K. (2016). The Importance of Extracellular Matrix in Skeletal Muscle Development and Function. In Composition and Function of the Extracellular Matrix in the Human Body. InTech. https://doi.org/10.5772/62230

292. Caccamo, A. E., Scaltriti, M., Caporali, A., D'Arca, D., Scorcioni, F., Astancolle, S., Mangiola, M., & Bettuzzi, S. (2004). Cell detachment and apoptosis induction of immortalized human prostate epithelial cells are associated with early accumulation of a 45 kDa nuclear isoform of clusterin. Biochemical Journal, 382(1), 157–168. https://doi.org/10.1042/BJ20040158

293. de Melo, B. A. G., Jodat, Y. A., Cruz, E. M., Benincasa, J. C., Shin, S. R., & Porcionatto, M. A. (2020). Strategies to use fibrinogen as bioink for 3D bioprinting fibrin-based soft and hard tissues. In Acta Biomaterialia (Vol. 117, pp. 60–76). Acta Materialia Inc. https://doi.org/10.1016/j.actbio.2020.09.024

294. Abelseth, E., Abelseth, L., De La Vega, L., Beyer, S. T., Wadsworth, S. J., & Willerth, S. M. (2018). 3D Printing of Neural Tissues Derived from Human Induced Pluripotent Stem Cells Using a Fibrin-Based Bioink. https://doi.org/10.1021/acsbiomaterials.8b01235

295. Blomb7ck, B., & Bark, N. (2004). Fibrinopeptides and fibrin gel structure. https://doi.org/10.1016/j.bpc.2004.07.013

296. Tanaka, K., Sato, K., Yoshida, T., Fukuda, T., Hanamura, K., Kojima, N., Shirao, T., Yanagawa, T., & Watanabe, H. (2011). Evidence for cell density affecting C2C12 myogenesis: Possible regulation of myogenesis by cell-cell communication. Muscle and Nerve, 44(6), 968–977. https://doi.org/10.1002/mus.22224

297. Chowdhury, S. R., Muneyuki, Y., Takezawa, Y., Kino-oka, M., Saito, A., Sawa, Y., & Taya, M. (2010). Growth and differentiation potentials in confluent state of culture of human skeletal muscle myoblasts. Journal of Bioscience and Bioengineering, 109(3), 310–313. https://doi.org/10.1016/j.jbiosc.2009.09.042

298. Yoshiko, Y., Hirao, K., & Maeda, N. (2002). Differentiation in C 2 C 12 myoblasts depends on the expression of endogenous IGFs and not serum depletion. American Journal of Physiology-Cell Physiology, 283(4), C1278–C1286. https://doi.org/10.1152/ajpcell.00168.2002

299. Ruijtenberg, S., & Heuvel, S. van den. (2016). Coordinating cell proliferation and differentiation: Antagonism between cell cycle regulators and cell type-specific gene expression. Cell Cycle, 15(2), 196. https://doi.org/10.1080/15384101.2015.1120925

300. Pellegrino, M. A., Canepari, M., Rossi, R., D'Antona, G., Reggiani, C., & Bottinelli, R. (2003). Orthologous myosin isoforms and scaling of shortening velocity with body size in mouse, rat, rabbit and human muscles. The Journal of Physiology, 546(3), 677–689. https://doi.org/10.1113/jphysiol.2002.027375

301. Gerard, C., Forest, M. A., Beauregard, G., Skuk, D., & Tremblay, J. P. (2012). Fibrin gel improves the survival of transplanted myoblasts. Cell Transplantation, 21(1), 127–137. https://doi.org/10.3727/096368911X576018

302. Marotta, M., Bragós, R., & Gómez-Foix, A. M. (2004). Design and performance of an electrical stimulator for long-term contraction of cultured muscle cells. BioTechniques, 36(1), 68–73. https://doi.org/10.2144/04361ST01

303. Orfanos, Z., Gödderz, M. P. O., Soroka, E., Gödderz, T., Rumyantseva, A., van der Ven, P. F. M., Hawke, T. J., & Fürst, D. O. (2016). Breaking sarcomeres by in vitro exercise. Scientific Reports, 6(1), 19614. https://doi.org/10.1038/srep19614

304. Nikolić, N., & Aas, V. (2019). Electrical pulse stimulation of primary human skeletal muscle cells. In Methods in Molecular Biology (Vol. 1889, pp. 17–24). Humana Press Inc. https://doi.org/10.1007/978-1-4939-8897-6_2

305. Langelaan, M. L. P., Boonen, K. J. M., Rosaria-Chak, K. Y., van der Schaft, D. W. J., Post, M. J., & Baaijens, F. P. T. (2011). Advanced maturation by electrical stimulation: Differences in response between C2C12 and primary muscle progenitor cells. Journal of Tissue Engineering and Regenerative Medicine, 5(7), 529–539. https://doi.org/10.1002/term.345

306. Nedachi, T., Fujita, H., & Kanzaki, M. (2008). Contractile C2C12 myotube model for studying exercise-inducible responses in skeletal muscle. American Journal of Physiology - Endocrinology and Metabolism, 295(5), 1191–1204. https://doi.org/10.1152/ajpendo.90280.2008

307. Gregory, P., Low, R. B., & Stirewalt, W. S. (1986). Changes in skeletal-muscle myosin isoenzymes with hypertrophy and exercise. Biochemical Journal, 238(1), 55–63. https://doi.org/10.1042/bj2380055

308. Goldspink, D. F., Easton, J., Winterburn, S. K., Williams, P. E., & Goldspink, G. E. (1991). The role of passive stretch and repetitive electrical stimulation in preventing skeletal muscle atrophy while reprogramming gene expression to improve fatigue resistance. Journal of Cardiac Surgery, 6(1 SUPPL.), 218–224. https://doi.org/10.1111/jocs.1991.6.1s.218

309. Sakiyama, K., Abe, S., Tamatsu, Y., & Ide, Y. (2005). Effects of stretching stress on the muscle contraction proteins of skeletal muscle myoblasts. In Biomedical Research (Vol. 26, Issue 2).

310. Candiani, G., Riboldi, S. A., Sadr, N., Lorenzoni, S., Neuenschwander, P., Montevecchi, F. M., & Mantero, S. (2010). Cyclic mechanical stimulation favors myosin heavy chain accumulation in engineered skeletal muscle constructs. Journal of Applied Biomaterials and Biomechanics, 8(2), 68–75. https://doi.org/10.1177/228080001000800202

311. Llewellyn, M. E., Barretto, R. P. J., Delp, S. L. & Schnitzer, M. J. Minimally invasive high-speed imaging of sarcomere contractile dynamics in mice and humans. Nature 454, 784–788 (2008).

312. Fyfe, J. J., Bishop, D. J., Bartlett, J. D., Hanson, E. D., Anderson, M. J., Garnham, A. P., & Stepto, N. K. (2018). Enhanced skeletal muscle ribosome biogenesis, yet attenuated mTORC1 and ribosome biogenesis-related signalling, following short-term concurrent versus single-mode resistance training. Scientific Reports, 8(1), 1–21. https://doi.org/10.1038/s41598-017-18887-6

313. Miyatake, S., Hino, K., Natsui, Y., Ebisu, G., & Fujita, S. (2020). Protein Supplementation Enhances the Effects of Intermittent Loading on Skeletal Muscles by Activating the mTORC1 Signaling Pathway in a Rat Model of Disuse Atrophy. Nutrients, 12(9), 2729. https://doi.org/10.3390/nu12092729

314. Bodine, S. C., Stitt, T. N., Gonzalez, M., Kline, W. O., Stover, G. L., Bauerlein, R., Zlotchenko, E., Scrimgeour, A., Lawrence, J. C., Glass, D. J., & Yancopoulos, G. D. (2001). Akt/mTOR pathway is a crucial regulator of skeletal muscle hypertrophy and can prevent muscle atrophy in vivo. Nature Cell Biology, 3(11), 1014–1019. https://doi.org/10.1038/ncb1101-1014

315. Deldicque, L., Theisen, D., & Francaux, M. (2005). Regulation of mTOR by amino acids and resistance exercise in skeletal muscle. In European Journal of Applied Physiology (Vol. 94, Issues 1–2, pp. 1–10). Springer. https://doi.org/10.1007/s00421-004-1255-6

316. Bar-Peled, L., & Sabatini, D. M. (2014). Regulation of mTORC1 by amino acids. Trends Cell Biol, 24(7), 400–406. https://doi.org/10.1016/j.tcb.2014.03.003

317. Ruvinsky, I., & Meyuhas, O. (2006). Ribosomal protein S6 phosphorylation: from protein synthesis to cell size. In Trends in Biochemical Sciences (Vol. 31, Issue 6, pp. 342–348). Elsevier. https://doi.org/10.1016/j.tibs.2006.04.003

318. Kelley, D. E., He, J., Menshikova, E. V., & Ritov, V. B. (2002). Dysfunction of mitochondria in human skeletal muscle in type 2 diabetes. Diabetes, 51(10), 2944–2950. https://doi.org/10.2337/diabetes.51.10.2944

319. Moore, T. M., Lin, A. J., Strumwasser, A. R., Cory, K., Whitney, K., Ho, T., Ho, T., Lee, J. L., Rucker, D. H., Nguyen, C. Q., Yackly, A., Mahata, S. K., Wanagat, J., Stiles, L., Turcotte, L. P., Crosbie, R. H., & Zhou, Z. (2020). Mitochondrial Dysfunction Is an Early Consequence of Partial or Complete Dystrophin Loss in mdx Mice. Frontiers in Physiology, 11, 690. https://doi.org/10.3389/fphys.2020.00690

320. Hughes, M. C., Ramos, S. V., Turnbull, P. C., Rebalka, I. A., Cao, A., Monaco, C. M. F., Varah, N. E., Edgett, B. A., Huber, J. S., Tadi, P., Delfinis, L. J., Schlattner, U., Simpson, J. A., Hawke, T. J., & Perry, C. G. R. (2019). Early myopathy in Duchenne muscular dystrophy is associated with elevated mitochondrial H2O2 emission during impaired oxidative phosphorylation. Journal of Cachexia, Sarcopenia and Muscle, 10(3), 643–661. https://doi.org/10.1002/jcsm.12405

321. Schuh, R. A., Jackson, K. C., Schlappal, A. E., Spangenburg, E. E., Ward, C. W., Park, J. H., Dugger, N., Shi, G. L., & Fishman, P. S. (2014). Mitochondrial oxygen consumption deficits in skeletal muscle isolated from an Alzheimer's disease-relevant murine model. BMC Neuroscience, 15(1), 24. https://doi.org/10.1186/1471-2202-15-24

322. Schuh, R. A., Jackson, K. C., Khairallah, R. J., Ward, C. W., & Spangenburg, E. E. (2012). Measuring mitochondrial respiration in intact single muscle fibers. American Journal of Physiology - Regulatory Integrative and Comparative Physiology, 302(6), 712–719. https://doi.org/10.1152/ajpregu.00229.2011

323. Hill, B. G., Benavides, G. A., Lancaster, J. J. R., Ballinger, S., Dell'Italia, L., Zhang, J., & Darley-Usmar, V. M. (2012). Integration of cellular bioenergetics with mitochondrial quality control and autophagy. Biological Chemistry, 393(12), 1485–1512. https://doi.org/10.1515/hsz-2012-0198

324. Marchetti, P., Fovez, Q., Germain, N., Khamari, R., & Kluza, J. (2020). Mitochondrial spare respiratory capacity: Mechanisms, regulation, and significance in non-transformed and cancer cells. In FASEB Journal (Vol. 34, Issue 10, pp. 13106–13124). John Wiley and Sons Inc. https://doi.org/10.1096/fj.202000767R

325. Moloudizargari, M., Mikaili, P., Aghajanshakeri, S., Asghari, M. H., & Shayegh, J. (2013). Pharmacological and therapeutic effects of Peganum harmala and its main alkaloids. Pharmacognosy Reviews, 7(14), 199. https://doi.org/10.4103/0973-7847.120524

326. Rommelspacher, H., Frenzel, M., & Dencher, N. A. (2012). β-Carbolines Increase the Performance of the Respiratory Chain in Mitochondria. Isoquinolines And Beta-Carbolines As Neurotoxins And Neuroprotectants: New Vistas In Parkinson's Disease Therapy, 125–131. https://doi.org/10.1007/978-1-4614-1542-8_8

327. Y, N., T, S., H, I., A, O., & D, N. (2010). Mitochondrial dysfunction and biotransformation of β-carboline alkaloids, harmine and harmaline, on isolated rat hepatocytes. Chemico-Biological Interactions, 188(3), 393–403. https://doi.org/10.1016/J.CBI.2010.09.004

328. Fearon, K., Strasser, F., Anker, S. D., Bosaeus, I., Bruera, E., Fainsinger, R. L., Jatoi, A., Loprinzi, C., MacDonald, N., Mantovani, G., Davis, M., Muscaritoli, M., Ottery, F., Radbruch, L., Ravasco, P., Walsh, D., Wilcock, A., Kaasa, S., & Baracos, V. E. (2011). Definition and classification of cancer cachexia: An international consensus. In The Lancet Oncology (Vol. 12, Issue 5, pp. 489–495). Elsevier. https://doi.org/10.1016/S1470-2045(10)70218-7

329. Fearon, K. C. H., Glass, D. J., & Guttridge, D. C. (2012). Cell Metabolism Review Cancer Cachexia: Mediators, Signaling, and Metabolic Pathways. Cell Metabolism, 16, 153–166. https://doi.org/10.1016/j.cmet.2012.06.011

330. White, J. P., Puppa, M. J., Sato, S., Gao, S., Price, R. L., Baynes, J. W., Kostek, M. C., Matesic, L. E., & Carson, J. A. (2012). IL-6 regulation on skeletal muscle mitochondrial remodeling during cancer cachexia in the ApcMin/+ mouse. Skeletal Muscle, 2(1), 14. https://doi.org/10.1186/2044-5040-2-14

331. Johns, N., Hatakeyama, S., Stephens, N. A., Degen, M., Degen, S., Frieauff, W., Lambert, C., Ross, J. A., Roubenoff, R., Glass, D. J., Jacobi, C., & Fearon, K. C. H. (2014). Clinical Classification of Cancer Cachexia: Phenotypic Correlates in Human Skeletal Muscle. PLoS ONE, 9(1), e83618. https://doi.org/10.1371/journal.pone.0083618

332. Wang, G., Biswas, A. K., Ma, W., Kandpal, M., Coker, C., Grandgenett, P. M., Hollingsworth, M. A., Jain, R., Tanji, K., López-Pintado, S., Borczuk, A., Hebert, D., Jenkitkasemwong, S., Hojyo, S., Davuluri, R. V., Knutson, M. D., Fukada, T., & Acharyya, S. (2018). Metastatic cancers promote cachexia through ZIP14 upregulation in skeletal muscle. Nature Medicine, 24(6), 770–781. https://doi.org/10.1038/s41591-018-0054-2

333. Acharyya, S., Ladner, K. J., Nelsen, L. L., Damrauer, J., Reiser, P. J., Swoap, S., & Guttridge, D. C. (2004). Cancer cachexia is regulated by selective targeting of skeletal muscle gene products. Journal of Clinical Investigation, 114(3), 370–378. https://doi.org/10.1172/jci20174

334. Nayak, A., Lopez-Davila, A. J., Kefalakes, E., Holler, T., Kraft, T., & Amrute-Nayak, M. (2019). Regulation of SETD7 Methyltransferase by SENP3 Is Crucial for Sarcomere Organization and Cachexia. https://doi.org/10.1016/j.celrep.2019.04.107

335. Ciciliot, S., Rossi, A. C., Dyar, K. A., Blaauw, B., & Schiaffino, S. (2013). Muscle type and fiber type specificity in muscle wasting. In International Journal of Biochemistry and Cell Biology (Vol. 45, Issue 10, pp. 2191–2199). Elsevier Ltd. https://doi.org/10.1016/j.biocel.2013.05.016

336. Mendell, J. R., & Engel, W. K. (1971). The fine structure of type II muscle fiber atrophy. Neurology, 21(4), 358–365. https://doi.org/10.1212/wnl.21.4.358

337. Adamiak, K., & Sionkowska, A. (2020). Current methods of collagen cross-linking: Review. In International Journal of Biological Macromolecules (Vol. 161, pp. 550–560). Elsevier B.V. https://doi.org/10.1016/j.ijbiomac.2020.06.075

338. Li, J. B., & Goldberg, A. L. (1976). Effects of food deprivation on protein synthesis and degradation in rat skeletal muscles. American Journal of Physiology, 231(2), 441–448. https://doi.org/10.1152/ajplegacy.1976.231.2.441

339. Goldberg, A. L., & Goodman, H. M. (1969). Relationship between cortisone and muscle work in determining muscle size. The Journal of Physiology, 200(3), 667–675. https://doi.org/10.1113/jphysiol.1969.sp008715

340. Serrano, A. L., Jardi, M., Suelves, M., Klotman, P. E., & Munoz-Canoves, P. (2008). HIV-1 transgenic expression in mice induces selective atrophy of fast-glycolytic skeletal muscle fibers. In Frontiers in Bioscience (Vol. 13, Issue 8, pp. 2797–2805). https://doi.org/10.2741/2886

341. Evans, W. J., & Lexell, J. (1995). Human Aging, Muscle Mass, and Fiber Type Composition. The Journals of Gerontology Series A: Biological Sciences and Medical Sciences, 50A(Special), 11–16. https://doi.org/10.1093/gerona/50A.Special_Issue.11

342. Wang, Y., & Pessin, J. E. (2013). Mechanisms for fiber-type specificity of skeletal muscle atrophy. In Current Opinion in Clinical Nutrition and Metabolic Care (Vol. 16, Issue 3, pp. 243–250). NIH Public Access. https://doi.org/10.1097/MCO.0b013e328360272d

343. Miura, S., Tomitsuka, E., Kamei, Y., Yamazaki, T., Kai, Y., Tamura, M., Kita, K., Nishino, I., & Ezaki, O. (2006). Overexpression of peroxisome proliferator-activated receptor γ co-activator-1α leads to muscle atrophy with depletion of ATP. American Journal of Pathology, 169(4), 1129–1139. https://doi.org/10.2353/ajpath.2006.060034

344. Bodine, S. C., Latres, E., Baumhueter, S., Lai, V. K. M., Nunez, L., Clarke, B. A., Poueymirou, W. T., Panaro, F. J., Erqian Na, Dharmarajan, K., Pan, Z. Q., Valenzuela, D. M., Dechiara, T. M., Stitt, T. N., Yancopoulos, G. D., & Glass, D. J. (2001). Identification of ubiquitin ligases required for skeletal Muscle Atrophy. Science, 294(5547), 1704–1708. https://doi.org/10.1126/science.1065874

345. Sukari, A., Muqbil, I., Mohammad, R. M., Philip, P. A., & Azmi, A. S. (2016). F-BOX proteins in cancer cachexia and muscle wasting: Emerging regulators and therapeutic opportunities. In Seminars in Cancer Biology (Vol. 36, pp. 95–104). Academic Press. https://doi.org/10.1016/j.semcancer.2016.01.002

346. White, J. P., Baltgalvis, K. A., Puppa, M. J., Sato, S., Baynes, J. W., & Carson, J. A. (2011). Muscle oxidative capacity during IL-6-dependent cancer cachexia. American Journal of Physiology - Regulatory Integrative and Comparative Physiology, 300(2), R201–R211. https://doi.org/10.1152/ajpregu.00300.2010

347. Glass, D. J. (2010). Signaling pathways perturbing muscle mass. Current Opinion in Clinical Nutrition and Metabolic Care, 13(3), 225–229. https://doi.org/10.1097/MCO.0b013e32833862df

348. Baracos, V. E., Martin, L., Korc, M., Guttridge, D. C., & Fearon, K. C. H. (2018). Cancer-associated cachexia. In Nature Reviews Disease Primers (Vol. 4, Issue 1, pp. 1–18). Nature Publishing Group. https://doi.org/10.1038/nrdp.2017.105

349. Li, J., Yi, X., Yao, Z., Chakkalakal, J. V, Xing, L., & Boyce, B. F. (2020). TNF Receptor-Associated Factor 6 Mediates TNFα-Induced Skeletal Muscle Atrophy in Mice During Aging. Journal of Bone and Mineral Research, 35(8), 1535–1548. https://doi.org/10.1002/jbmr.4021

350. Chen, S. E., Jin, B., & Li, Y. P. (2007). TNF-α regulates myogenesis and muscle regeneration by activating p38 MAPK. American Journal of Physiology - Cell Physiology, 292(5), 1660–1671. https://doi.org/10.1152/ajpcell.00486.2006

351. Zhan, M., Jin, B., Chen, S. E., Reecy, J. M., & Li, Y. P. (2007). TACE release of TNF-α mediates mechanotransduction-induced activation of p38 MAPK and myogenesis. Journal of Cell Science, 120(4), 692–701. https://doi.org/10.1242/jcs.03372

352. Aderka, D., Engelmann, H., Hornik, V., Skornick, Y., Levo, Y., Wallach, D., & Kushtai, G. (1991). Increased Serum Levels of Soluble Receptors for Tumor Necrosis Factor in Cancer Patients. Cancer Research, 51(20).

353. Marceca, G. P., Nigita, G., Calore, F., & Croce, C. M. (2020). MicroRNAs in Skeletal Muscle and Hints on Their Potential Role in Muscle Wasting During Cancer Cachexia. In Frontiers in Oncology (Vol. 10, p. 2604). Frontiers Media S.A. https://doi.org/10.3389/fonc.2020.607196

354. Chitti, S. V., Fonseka, P., & Mathivanan, S. (2018). Emerging role of extracellular vesicles in mediating cancer cachexia. In Biochemical Society Transactions (Vol. 46, Issue 5, pp. 1129–1136). Portland Press Ltd. https://doi.org/10.1042/BST20180213

355. Molinari, F., Pin, F., Gorini, S., Chiandotto, S., Pontecorvo, L., Penna, F., Rizzuto, E., Pisu, S., Musarò, A., Costelli, P., Rosano, G., & Ferraro, E. (2017). The mitochondrial metabolic reprogramming agent trimetazidine as an 'exercise mimetic' in cachectic C26-bearing mice. Journal of Cachexia, Sarcopenia and Muscle, 8(6), 954–973. https://doi.org/10.1002/jcsm.12226

356. Brassart-Pasco, S., Brézillon, S., Brassart, B., Ramont, L., Oudart, J. B., & Monboisse, J. C. (2020). Tumor Microenvironment: Extracellular Matrix Alterations Influence Tumor Progression. In Frontiers in Oncology (Vol. 10, p. 397). Frontiers Media S.A. https://doi.org/10.3389/fonc.2020.00397

357. Heldin, C. H., Rubin, K., Pietras, K., & Östman, A. (2004). High interstitial fluid pressure - An obstacle in cancer therapy. In Nature Reviews Cancer (Vol. 4, Issue 10, pp. 806–813). Nature Publishing Group. https://doi.org/10.1038/nrc1456

358. Tadeo, I., Berbegall, A. P., Castel, V., García-Miguel, P., Callaghan, R., Påhlman, S., Navarro, S., & Noguera, R. (2016). Extracellular matrix composition defines an ultra-high-risk group of neuroblastoma within the high-risk patient cohort. British Journal of Cancer, 115(4), 480–489. https://doi.org/10.1038/bjc.2016.210

359. Cheung, H. C., Hai, T., Zhu, W., Baggerly, K. A., Tsavachidis, S., Krahe, R., & Cote, G. J. (2009). Splicing factors PTBP1 and PTBP2 promote proliferation and migration of glioma cell lines. Brain, 132(8), 2277–2288. https://doi.org/10.1093/brain/awp153

360. He, X., Pool, M., Darcy, K. M., Lim, S. B., Auersperg, N., Coon, J. S., & Beck, W. T. (2007). Knockdown of polypyrimidine tract-binding protein suppresses ovarian tumor cell growth and invasiveness in vitro. Oncogene, 26(34), 4961–4968. https://doi.org/10.1038/sj.onc.1210307

361. Zhang, S., Wei, J. S., Li, S. Q., Badgett, T. C., Song, Y. K., Agarwal, S., Coarfa, C., Tolman, C., Hurd, L., Liao, H., He, J., Wen, X., Liu, Z., Thiele, C. J., Westermann, F., Asgharzadeh, S., Seeger, R. C., Maris, J. M., Guidry Auvil, J. M., … Khan, J. (n.d.). Original Articles MYCN controls an alternative RNA splicing program in high-risk metastatic neuroblastoma. https://doi.org/10.1016/j.canlet.2015.11.045

362. Gestblom, C., Hoehner, J. C., & Påhlman, S. (1995). Proliferation and apoptosis in neuroblastoma: subdividing the mitosis-karyorrhexis index. European Journal of Cancer, 31(4), 458–463. https://doi.org/10.1016/0959-8049(95)00006-5

363. Liu, X., Zuo, Y., Sun, J., Guo, Z., Fan, H., & Zhang, X. (2017). Degradation regulated bioactive hydrogel as the bioink with desirable moldability for microfluidic biofabrication. Carbohydrate Polymers, 178, 8–17. https://doi.org/10.1016/j.carbpol.2017.09.014

364. P. Jaiswal, “Allied Market Research, 3D Cell culture Market, Report code LI171474.,” 2017.

365. Yaffe, D., & Saxel, O. (1977). Serial passaging and differentiation of myogenic cells isolated from dystrophic mouse muscle. Nature 1977 270:5639, 270(5639), 725–727. https://doi.org/10.1038/270725A0

366. Carosio, S., Barberi, L., Rizzuto, E., Nicoletti, C., Prete, Z. Del, & Musarò, A. (2013). Generation of eX vivo-vascularized Muscle Engineered Tissue (X-MET). Scientific Reports 2013 3:1, 3(1), 1–9. https://doi.org/10.1038/srep01420

367. C., S., W., V., & M., L. (2016). Effects of Dexamethasone on Satellite Cells and Tissue Engineered Skeletal Muscle Units. Https://Home-Liebertpub-Com.Sire.Ub.Edu/Tea, 22(5–6), 480–489. https://doi.org/10.1089/TEN.TEA.2015.0545

368. Laternser, S., Keller, H., Leupin, O., Rausch, M., Graf-Hausner, U., & Rimann, M. (2018). A Novel Microplate 3D Bioprinting Platform for the Engineering of Muscle and Tendon Tissues: Https://Doi.Org/10.1177/2472630318776594, 23(6), 599–613. https://doi.org/10.1177/2472630318776594

369. Seyedmahmoud, R., Çelebi-Saltik, B., Barros, N., Nasiri, R., Banton, E., Shamloo, A., Ashammakhi, N., Dokmeci, M. R., & Ahadian, S. (2019). Three-Dimensional Bioprinting of Functional Skeletal Muscle Tissue Using Gelatin Methacryloyl-Alginate Bioinks. Micromachines 2019, Vol. 10, Page 679, 10(10), 679. https://doi.org/10.3390/MI10100679

370. Liu, C., Oikonomopoulos, A., Sayed, N., & Wu, J. C. (2018). Modeling human diseases with induced pluripotent stem cells: from 2D to 3D and beyond. Development, 145(5). https://doi.org/10.1242/DEV.156166

371. Bakooshli, M. A., Lippmann, E. S., Mulcahy, B., Iyer, N., Nguyen, C. T., Tung, K., Stewart, B. A., Van Den Dorpel, H., Fuehrmann, T., Shoichet, M., Bigot, A., Pegoraro, E., Ahn, H., Ginsberg, H., Zhen, M., Ashton, R. S., & Gilbert, P. M. (2019). A 3d culture model of innervated human skeletal muscle enables studies of the adult neuromuscular junction. ELife, 8. https://doi.org/10.7554/ELIFE.44530

372. Maffioletti, S. M., Sarcar, S., Henderson, A. B. H., Mannhardt, I., Pinton, L., Moyle, L. A., Steele-Stallard, H., Cappellari, O., Wells, K. E., Ferrari, G., Mitchell, J. S., Tyzack, G. E., Kotiadis, V. N., Khedr, M., Ragazzi, M., Wang, W., Duchen, M. R., Patani, R., Zammit, P. S., … Tedesco, F. S. (2018). Three-Dimensional Human iPSC-Derived Artificial Skeletal Muscles Model Muscular Dystrophies and Enable Multilineage Tissue Engineering. Cell Reports, 23(3), 899–908. https://doi.org/10.1016/j.celrep.2018.03.091

373. Menconi, M., Gonnella, P., Petkova, V., Lecker, S., & Hasselgren, P. O. (2008). Dexamethasone and corticosterone induce similar, but not identical, muscle wasting responses in cultured L6 and C2C12 myotubes. Journal of Cellular Biochemistry, 105(2), 353–364. https://doi.org/10.1002/jcb.21833

374. Archer-Lahlou, E., Lan, C., & Jagoe, R. T. (2018). Physiological culture conditions alter myotube morphology and responses to atrophy treatments: implications for in vitro research on muscle wasting. Physiological Reports, 6(12). https://doi.org/10.14814/phy2.13726

375. O, Z., T, S., S, H., & N, C. (2012). Genome-wide gene expression analysis in cancer cells reveals 3D growth to affect ECM and processes associated with cell adhesion but not DNA repair. PloS One, 7(4). https://doi.org/10.1371/JOURNAL.PONE.0034279

376. Gillispie, G. J., Han, A., Uzun-Per, M., Fisher, J., Mikos, A. G., Niazi, M. K. K., Yoo, J. J., Lee, S. J., & Atala, A. (2020). The Influence of Printing Parameters and Cell Density on Bioink Printing Outcomes. Https://Home-Liebertpub-Com.Sire.Ub.Edu/Tea, 26(23–24), 1349–1358. https://doi.org/10.1089/TEN.TEA.2020.0210

Development of tunable bioinks to fabricate 3D-printed *in vitro* models:

a special focus on skeletal muscle models with potential applications in metabolic alteration studies

Programa de Doctorat de Biomedicina

Universitat de Barcelona

Tesis realitzada en el Institut de Bioenginyeria de Catalunya (IBEC)

PhD candidate

Andrea García Lizarribar

Director

Josep Samitier Martí

Firmado por 38424107P JOSEP SAMITIER (R: G64045719) el día 24/09/2021 con un certificado emitido por AC Representación

IBEC Institute for Bioengineering of Catalonia

EXCELENCIA SEVERO OCHOA

UNIVERSITAT DE BARCELONA